Particle acceleration with beam driven plasma wakefield

Thèse de doctorat de l'Université Paris-Saclay
préparée à l'école Polytechnique

École doctorale n°572 : ondes et matières (EDOM)
Spécialité de doctorat: optique et physique des plasmas

Thèse présentée et soutenue à Palaiseau, le 09 Mars 2018, par
Antoine DOCHE

Composition du Jury :

M. Patrick MORA, Directeur de recherche CPhT, école Polytechnique - CNRS	Président du jury
M. Philippe BALCOU, Directeur de recherche CELIA, CEA – CNRS – Université de Bordeaux	Rapporteur
M. Emmanuel D'HUMIERES, Directeur de recherche CELIA, CEA – CNRS – Université de Bordeaux	Rapporteur
Mme. Edda GSCHWENDTNER, Directrice de recherche CERN, Engineering Department	Examinatrice
M. Sébastien CORDE, Maitre de conférence LOA, École Polytechnique	Co-directeur de thèse
M. Victor MALKA, Directeur de recherche LOA, École Polytechnique	Directeur de thèse

Remerciements - Acknowledgements

Avant toute chose, il faut préciser que différents acteurs ont rendu possible les campagnes expérimentales sur lesquelles repose ce travail et la rédaction de ce manuscrit. Eux seuls méritent tous les honneurs qui découlent des accomplissements scientifiques présentés dans ce texte, et pour leur temps, leur aide et leur confiance je tiens à les remercier individuellement.

Je souhaite remercier en tout premier lieu mon directeur de thèse, Victor Malka pour son accueil au Laboratoire d'Optique Appliquée dès février 2014. C'est grâce à lui que ce manuscrit a pu être écrit, grâce à son soutien face aux difficultés, et à ses conseils quant à la direction à prendre à chaque moment important. J'exprime donc beaucoup de reconnaissance pour ses enseignements scientifiques et humains, pour toutes les opportunités qu'il a rendues possibles, notamment pour partir étudier sous d'autres horizons.

Je remercie à présent vivement Sébastien Corde, mon co-encadrant de thèse depuis Août 2015. Le difficile parcours scientifique qu'a constitué cette thèse n'a été possible que grâce à son intervention. Je souhaite exprimer mes remerciements pour la patiente infinie dont il a fait preuve, ses efforts incessants de pédagogie, son enthousiasme pour les discussions scientifiques et son sens inné du partage. Outre l'opportunité qu'il m'a offerte de partir découvrir la recherche scientifique outre-Atlantique, il restera un modèle de précision scientifique et plus largement de rigueur intellectuelle dans le travail. Il a sans aucun doute redonné de l'enthousiasme à cette thèse, et pour son action auprès des étudiants et de ces collègues il mérite plus largement toute la reconnaissance et l'estime des membres du laboratoire dans lequel cette thèse a eu lieu.

L'expérience d'accélération d'un paquet distinct de positron dans un accélérateur par onde de sillage plasma est avant tout la récompense du travail de la collaboration E200 au sein de la plateforme FACET, au SLAC. Pour cela je tiens à remercier les différentes personnes qui ont rendu cette expérience possible, qui m'ont transmis d'innombrables savoir-faire, en même temps que beaucoup de nouveaux concepts scientifiques. Merci avant tout à Michael « Mike » Litos pour sa bonne humeur, sa passion communicative pour la physique et son enseignement dispensé avec patience. Merci à Spencer Gessner qui restera un modèle, par son efficacité dans le travail et sa passion pour les sciences. Merci à Mark Hogan pour son soutien bienveillant au cours des expériences, très important dans les moments de doute. Merci également au Professeur Chan Joshi pour ses conseils, remarques et enseignements, il oriente avec brio la collaboration E200, sa bienveillance et son influence sont une chance pour tous les étudiants. Merci à tous les gens qui ont partagé leur savoir sans compter, m'ont spontanément aidé à faire face aux imprévus divers : Carl Lindstrøm qui comme moi se bat pour défendre une thèse, Brendan O'Shea pour son aide face à l'inextricable système informatique de FACET, Kenneth « Ken » Marsh pour avoir partagé sans compter son savoir-faire expérimental, Christine Clarke et Selina Green pour leur disponibilité et leur soutien logistique quelle que soit l'heure du jour ou de la nuit. Je voudrais remercier également Christopher « Chris » Clayton pour sa motivation

communicative pendant les runs, ses discussions fort intéressantes pendant les pauses, Navid Vafaei pour son soutien moral quand les résultats tardaient à arriver… Merci à Chris Beekman pour les bons moments passés en Californie comme en France au cours de ce travail intensif. Merci à Erik Adli pour ses enseignements, son invitation à Oslo également, et merci à James Allen et Rafal Zgadzaj pour leur amitié, et pour le temps passé à travailler dans la bonne humeur. Merci à tous les autres personnels du SLAC qui ont rendu ce travail possible.

L'essentiel du travail présenté ici a été accompli grâce à l'héritage scientifique et au personnel du Laboratoire d'Optique Appliquée. Pour cela, des remerciements appuyés doivent être adressés aux différents membres de groupes de recherche FLEX et SPL. Merci à Alessandro Flacco, qui a co-encadré mon travail de thèse pendant les 8-10 premiers mois, son habileté technique et son sens physique ont été une source d'inspiration pendant l'ensemble de ces trois années. Merci à Julien Gautier, Amar Tafzi, Jean-Philippe Godet, Jean-Philippe Rousseau, Stéphane Sebban, Fabien Tissandier, Antoine Rousse, Davide Boschetto, Benoit Mahieu, Guillaume Lambert, Agustin Lifschitz, Pascal Rousseau, Boris Vodungbo et Cédric Thaury, pour leur bonne humeur, leurs conseils et leur aide. Merci à Jean-Marcel Rax pour toutes les discussions passées ensembles, et toutes les questions générales de physique au sujet desquelles il a pu éclairer le groupe des étudiants. Mille mercis aux gars de la mécanique, Jean-lou « Charly » Charles, Mickaël Martinez, Bernard Allali et Florian Oper. Merci également au personnel du secrétariat pour leur soutien, leur disponibilité et leur bonne humeur : Sandrine Tricaud, Octavie Verdun, Lucie Huguet, Catherine Buljore, Patricia Toullier, merci.

Pendant trois années au LOA, j'ai pu côtoyer d'autres étudiants, des camarades d'infortune que je n'oublierai pas. Merci donc à Dan Lévy, Viacheslav Smartsev, Adrien Despresseux, Safir Lazar, Antonin Siciak, Carla Da Silva Alves, Francesco Massimo, Olivier Delmas, Florian Mollica, Gaël Massé, Emilie Bayart, Evgeny Chelnokov, Igor Andriyash, Julien Ferri, Hermine Danvy, Flavien Museur, Chris Beekman, Benjamin Vauzour, Clément Caizergues, Emilien Guillaume, Andreas Döpp et Marc. Pour tous les moments passés ensemble à travailler, discuter, s'amuser, merci beaucoup, ce fut une belle aventure.

Par ailleurs, beaucoup d'autres personnes méritent des remerciements. Merci beaucoup à Nicolas Panel, Joris Guery, Pierre Chopin, Olga Chashchina et Raphael Deswartes, un remerciement également de la part de tous les étudiants du campus de l'École polytechnique pour le temps qu'ils leur ont consacré. Merci à Benjamin Madon et Pascal Delange pour leur amitié. Merci à mes parents et à ma sœur, ainsi qu'aux autres membres de ma famille proche. Ce manuscrit est dédié à la mémoire de Loys et Laurent Doche, qui auraient bien aimé découvrir son sujet. Merci beaucoup à Liu Jia pour son soutien et sa compréhension face au chronophage travail que constitue la rédaction d'un manuscrit de thèse. Merci à tous mes amis du campus de Polytechnique, Shen Yixin, Weiran Zhang, Lei Yu, Lawrence Das Sourav, Guilhem Beaussoleil, François Deloche et tous les autres.

Introduction

Context

Particle accelerators have tremendous impact in academic research together with many important societal applications for example for cancer treatments. In the context of fundamental research, they have been built to probe materials and to study fundamental interactions by colliding beams of energetic particles with extreme luminosity. For this purpose, particle beams (also named particle bunches in this manuscript) can reach a speed close to *c*, the speed of light. More compact machines, that deliver lower energy particle beams became indispensable for several activities in our modern societies, they even contribute to fight cancer and save lives by providing particular ionizing radiations to treat tumors.

The current accelerators in use are said to be *radiofrequency* accelerators, as the particle beams are moving in cavities in which devices called klystrons produce the electromagnetic wave that the particles "surf" to gain energy. A fundamental limitation, the electric breakdown, occurs when the field in the electromagnetic cavity becomes too high. When the maximum admissible electric field is reached, the metallic cavity can be destroyed. As a consequence of this limited value of the electric field of the order of 100 MV/m, scientists have to build longer and larger facilities to increase the final energy of the particle beams. For fundamental research, progresses in theoretical models require always higher energy beams, that is why a new technology is now needed, to provide a sustainable alternative to the limitations of "conventional" accelerators.

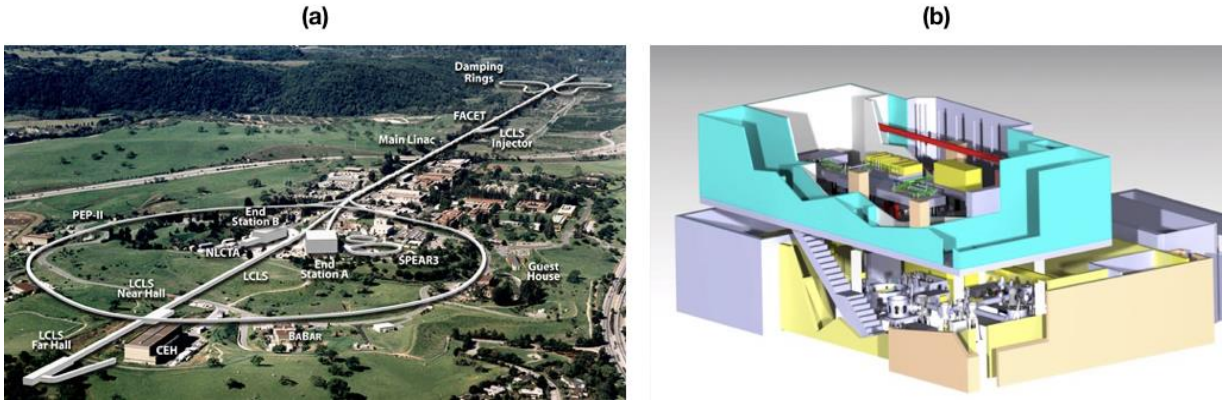

Figure 0.1: (a) A conventional accelerator: SLAC National Accelerator facility. The total length of the linear accelerator is 3 km. (b) An experimental platform dedicated to LWFA: Salle Jaune at Laboratoire d'Optique Appliquée, Palaiseau France, the length of each room is typically 30 m.

Plasmas as they are ionized media, are not limited by electrical breakdown, which explains why this medium has been investigated as an alternative to metallic cavities. By controlling the collective motion of electrons with lasers, accelerating fields of the order of hundreds of GeV/m have been demonstrated [**Malka 02].** Such high gradients are more than three orders of magnitude higher than the best accelerating gradient of conventional facilities. The difference in sizes between conventional and plasma-based accelerators can be seen in Fig. 0.1: although the specific experiment (b) does not provide particles of GeV energy yet as the massive SLAC facility (a) does, conventional and plasma-based accelerators typically have this size ratio. Among the four plasma-based schemes **[Joshi 03]**, my thesis will deal with two of them: Laser Wakefield Acceleration (LWFA) **[Tajima 79]** and Plasma Wakefield Acceleration (PWFA) **[Fainberg 56, Chen 85]**. In these two concepts, an electron density wave is excited in a plasma. The wave driver – either a laser pulse (LWFA, Fig. 0.2 (a)) or a bunch of particles (PWFA, Fig. 0.2 (b)) - deposits energy in the medium as it excites the wave. The accelerated beam extracts this energy.

Both the LWFA and the PWFA schemes have focused the attention of the scientific community, and many breakthrough results were theoretically and experimentally achieved. Plasma-based acceleration techniques started with the precursor article by Tajima and Dawson **[Tajima 79]**. Four schemes were suggested, of whom PWFA and LWFA have bright prospects. The PWFA scheme was built theoretically **[Ruth 85, Katsouleas 86]** before the first experimental demonstrations for electrons **[Rosenzweig 88, 89, Blumenfeld 07, Litos 14]** and positrons **[Blue 03, Corde 15]** drive beams. The LWFA acceleration scheme allows the excitation of an intense plasma wave by a laser pulse of a few joules and a few

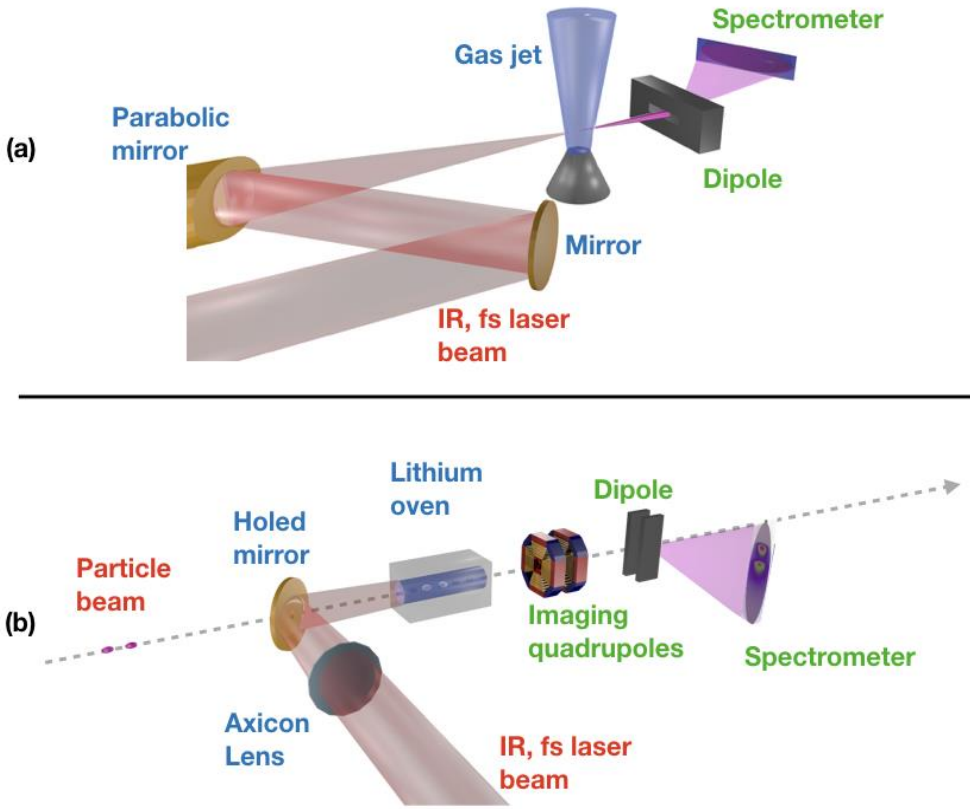

Figure 0.2: (a) A typical laser wakefield experiment, a parabolic mirror focuses a laser beam into a gas jet. The emerging electron beam is characterized by a spectrometer. (b) A plasma wakefield experiment, in which two particle bunches are sent into a laser pre-ionized plasma. A spectrometer displays the energy of the particle bunch emerging from the plasma. This experiment can be carried out with electron or positron bunches.

tens of femtoseconds. This is why this scheme can be accomplished in limited size and low cost facilities such as the Salle Jaune at Laboratoire d'Optique Appliquée (Fig. 0.1 (b)). The first experimental demonstration of quasi-monoenergetic electron beam generation in LWFA was accomplished in 2004 **[Mangles 04, Faure 04, Geddes 04]**, before further improvement of the beam properties was made **[Faure 06].** Multi-GeV electron acceleration was recently reached with modern pettawatt laser technologies **[Kim 13, Leemans 14, Wang 13]**. LWFA and PWFA rely on the transfer of energy to a beam of particles, thanks to plasma electron density waves. The driver energy deposition in the plasma is therefore the first physical phenomenon that needs to be understood and optimized to build a plasma-based accelerator. Apart from plasma electron density waves driving, another major challenge occupies most of the research community: the injection of particles into the accelerating cavity to extract its energy. In fact, the energy contained in the excited wave can either be sampled by some particles in the beam driving the wake itself, or from a second, externally produced beam, or else by electrons from the plasma **[Joshi 03]**.

LWFA and PWFA scientific communities past experiments have already set up many milestones in the production of high quality, high-energy particle bunches. These two schemes already led to multi-GeV particle bunches, with a very high quality: low divergence, high brightness and low energy spread of the particle beams. Therefore, some medical and industrial non-destructive imaging applications can already be considered with the beam quality plasma-based facilities provide. Moreover, plasma accelerators open very promising prospects towards compact and very high-energy colliders. This last application that is extremely challenging requires many improvements of the beam properties and to overcome several technological limitations. First, the challenge of staging PWFA or LWFA accelerators is to be solved, second, beam quality has to be preserved when wakefields are used to "boost" externally produced particle beams. Last, the total accelerated charge should be increased further.

Objective of this thesis

As demonstrated in the previous paragraph, hopes lie on plasma-based acceleration experiments towards the realization of compact and cost-efficient electron-positron colliders. This is true even if several technological challenges still require to be overcome before such a facility is built. Regarding the staging of plasma modules, accelerator stages would be used to further accelerate a distinct bunch of particles, independently of the accelerating cavity generation. This requires to master a scheme in which a distinct bunch of particles extracts energy from a plasma accelerating cavity. This was accomplished already with electrons **[Litos 14]**, but is yet to be demonstrated with positrons. The important milestone of accelerating a distinct bunch of positrons independently of the technique employed to drive the plasma accelerating cavity will be the prime objective of my thesis.

Moreover, beam driven plasma wakes experiments still require huge conventional facilities to take place: at SLAC for instance, FACET plasma wakefield experiments use the 20.35 GeV electron or positron beams accelerated by the radiofrequency facility to drive plasma waves. This is a serious limitation to the number of experiments that can simultaneously take place in the world. In the long run, it is a limitation to scientific progresses accomplished by the community of researchers. The second part of my thesis will therefore be dedicated to the realization of a hybrid LWFA-PWFA scheme at the Laboratoire d'Optique Appliquée in Palaiseau, France. This experiment is expected to demonstrate that plasma waves can be

driven in a gas jet, using a LWFA-produced electron beam. Obtaining a clear evidence of the excitation of an accelerating cavity in this hybrid setup is the second objective of the work presented here. In addition, manipulating LWFA produced electron beams in optics laboratories was driven by the interest for x-ray Betatron sources. The hybrid scheme introduced above opens prospects regarding the optimization of such x-ray sources. That is why we will study x-ray light emission as well in this second experiment.

Outline of the manuscript

Part I provides first a brief presentation of the history of particle accelerators and of their applications in Chapter 1. Second, useful concepts in laser and beam physics are introduced in both Chapter 1 and Chapter 2. In Chapter 3, theoretical details are given about LWFA and PWFA. The driving of plasma waves by a particle beam or a laser pulse is derived in detail in the "linear" regime case and some qualitative details about the "nonlinear" or "blow-out" regime are provided. In addition, a comprehensive description of the propagation of a laser pulse and of an electron bunch in a plasma is made.

Part II is dedicated to the main experimental result, the demonstration of the acceleration of a trailing positron bunch in a plasma wakefield accelerator. Chapter 4 and Chapter 5 introduce the experimental setup of the experiment that took place at the FACET (Facility for Advanced aCcelerator Experimental Tests) facility at SLAC National Accelerator Laboratory. The different experimental diagnostics and methods are then described in further details. Chapter 5 reports the results of the experiment and the simulations performed to obtain further insight into the acceleration process underlying this experimental achievement. Part II is concluded by a study of the wakefield regime driven in the plasma during the experiment.

Part III presents the hybrid LWFA-PWFA experiments accomplished at Laboratoire d'Optique Appliquée. Chapter 6 is dedicated to the experimental campaign of 2017 in which a LWFA-produced electron beam was used to drive plasma waves in a gas jet. In this experimental study, an electron beam created by laser-plasma interaction is refocused by particle bunch-plasma interaction in a second gas jet. A study of some physical phenomena associated to this hybrid LWFA-PWFA platform is then accomplished. Chapter 7 reports the work accomplished in 2016 to exploit the hybrid LWFA-PWFA scheme in order to enhance the X-ray emission produced by the LWFA electron beam. The first experimental realization of this last scheme is reported, and its promising results are discussed.

Part I

Chapter 1

Particle accelerators, laser and beam physics

This introductory chapter begins with a short history of particle accelerators. First is a chronological presentation of **particle accelerator facilities** and their corresponding **applications**. The second and third sections of this chapter provide a brief introduction to **laser and beam physics**, by introducing the main concepts of these fields that will be used throughout the manuscript. These sections introduce the formalism and the conventions used in the rest of the text as well.

Contents

1. Particle accelerators: technology and applications

a. A century-long history

Accelerators and particle colliders have a long history made of many successive innovations; new facilities emerged all along the 20th century. Several particle acceleration schemes were used, however only two of them are still in use in world-class facilities.

The very first accelerators were electrostatic ones, such as the Van de Graaff accelerator invented in the late 1920s **[Van de Graaf 33]**. These machines were using a static electric field set up between two electrodes to accelerate electrons. However, electrostatic accelerators were strongly limited by electrical breakdown that could easily destroy the setup; the maximal energy that the particles could reach was limited to 20-30 MeV **[Humphries 02]**.

Starting from the 1930s, accelerators become radio-frequency (RF) electromagnetic machines. Although they are called radio-frequency accelerators, most of these devices work with microwave electromagnetic fields. Guiding cavities sustain the oscillations of an electromagnetic wave with a wavelength ranging from a few centimeters to a few tens of centimeters and a phase velocity close to the velocity of the accelerated particles. Particle energies were then pushed higher thanks to the invention of a circular acceleration scheme: cyclotrons that would produce electron or proton beams from the 1930s on. **[Lawrence 32]** These circular facilities force accelerated particles to circle several times in an electromagnetic field before exiting the device. Cyclotrons were using magnetic fields to force the particles to move on two half-circle orbits and were accelerating them in between where the particles would see an electric field. Increasing slowly their energy each time they circle through the machine, the particles would rotate at a radius that becomes larger and larger until they escape from the ring. Particle energies in these machines were limited to a few tens of MeV at first, until a new generation of circular accelerators was invented: synchrocyclotrons. Facilities of this generation, some of whom are still being built nowadays, accelerate individual bunches of particles only, and match the radio-frequency electromagnetic field frequency with the bunches energy. This strategy needs the magnetic field amplitude to compensate for the energy gain by bending accordingly more the particles trajectories, leading to more turns inside the accelerator ring and therefore to particles with a higher final energy. This technology is still common for proton medical accelerators, as it is

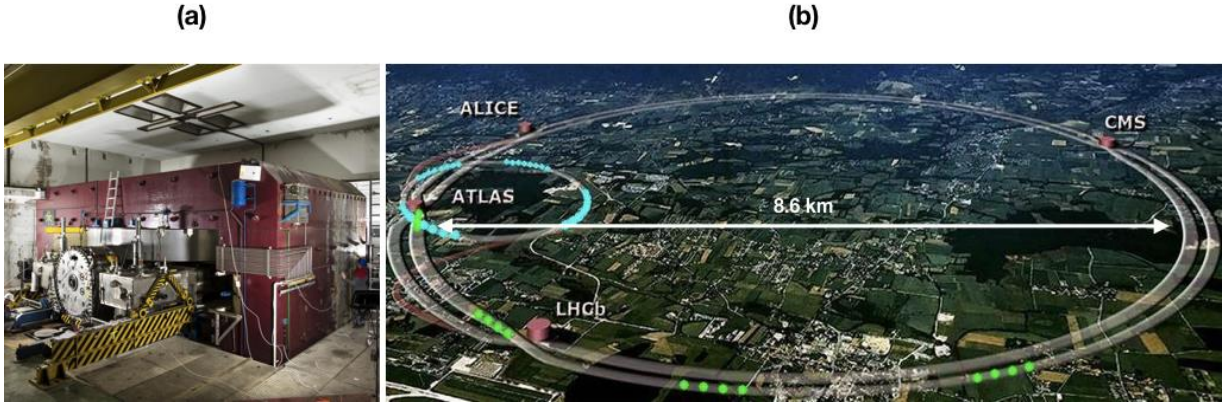

Figure 1.1: (a) CERN 1956 synchrocyclotron producing bunches of protons with an energy of 600 MeV. (b) The Large Hadron Collider facility nowadays, that can provide 7 TeV particles. As displayed on the figure, the main ring has a diameter of 8.6 km. From CERN.

an efficient and repeatable way to produce proton bunches of 70 to 250 MeV for instance. An example of one of the first synchrocyclotron ever built can be seen in Fig. 1.1 (a). A modern facility used for proton therapy is displayed in Fig. 1.3 (a). This last picture is the treatment room of Orsay proton therapy center, a facility which relies on a synchrocyclotron to produce the ionizing radiations. The main technology for fundamental physics accelerators is the synchrotron **[Veksler 44]**, used for instance at the Large Electron-Positron Collider from 1989 to 2000 **[Myers 90]** and at the Large Hadron Collider (LHC, Fig. 1.1 (b)) until now. Synchrotrons are modified cyclotrons in which the magnetic field amplitude increases with the increasing particle energy so that the particles can maintain their orbit inside the circular accelerator and reach very high energies. The LHC accelerates protons up to 7 TeV, the highest particle energy value ever obtained in an experiment; it led to the discovery of the Higgs boson **[LHC 12]**.

Although circular facilities flourished around the world, driven by their multiple applications, linear accelerators were not abandoned. Indeed, the energy lost by synchrotron radiation in circular accelerators, makes their uses for high-energy (greater than hundreds of GeV) electron-positron colliders non-relevant. Only linear acceleration prevents such loses. With accelerating fields limited by the electric breakdown, the size of these facilities has to become higher and higher to reach high energies. Two different linear RF based accelerator technologies exist. Linear induction accelerators were invented in the early 1960s, and were using a phenomenon called induction isolation to maintain the potential differences in the facilities low, while the net electric potential on the axis of the beam line would efficiently accelerate particles **[Christophilos 64]**. Linear induction accelerators were not the first devices to use magnetic induction to transmit energies to particles. The Betatron, a circular accelerator invented in 1935 was already inductively accelerating particles in a torus shaped vacuum chamber. The most widespread kind of linear accelerators are the electromagnetic radio-frequency accelerators, based on a scheme that was suggested as early as 1924 **[Ising 24]**. Stanford Linear Accelerator (SLAC National Accelerator Laboratory) for instance is such an accelerator, and opened in 1966 **[Neal 68]**. It led three of its users to obtain a Nobel Prize, in 1976 for the discovery of the charm quark, in 1990 for the quark structure and in 1995 for the discovery of the tau lepton. Successive upgrades led SLAC accelerator energy to increase twice in its history. Two major linear accelerator facilities have been proposed for the next decades. The International Linear Collider (ILC) first, whose particles will reach the energy of $250\ GeV$ and which may be built in Japan **[ILC 07]**. Its footprint is estimated to be 30 km. Another major project is the Compact Linear International Collider (CLIC), which is to accelerate particles to the energy of $1.5\ TeV$ **[CLIC 12]**.

Accelerator	Technology	Date	Particles	Energy
Van De Graaf acc.	Electrostatic	1929	e^-	$25\ MeV$
Betatron acc.	Induction	1935	e^-	$300\ MeV$
Linear Induction acc.	Induction	1962	e^-	$50\ MeV$
SLAC	Linear RF	1966	e^-/e^+	$50\ GeV$
LEP	Circular RF	1989	e^-/e^+	$25-105\ GeV$
LHC	Circular RF	2008	p	$7\ TeV$
ILC	Linear RF	-	e^-/e^+	$250\ GeV$
CLIC	Linear RF	-	e^-/e^+	$1.5\ TeV$

Figure 1.2: Comparison of accelerators and facilities that set up milestone in experimental physics.

In Fig. 1.2 are summarized the different accelerators discussed in the previous paragraph along with their energy. The three first accelerators describe a general kind of devices, in contrast with the last five that are unique world-class facilities or proposed colliders. As can be seen, linear induction accelerators did not increase the maximal energy reached by particle bunches, however, they were able to produce the highest current bunches at the time they were invented. Large scale facilities, involving many countries and built in the late 20th and 21st century (LEP, LHC, ILC and CLIC) reach much higher energies than their predecessors.

b. Particle beams and applications

Accelerator facilities are built for different purposes: they are used either for fundamental research, medical or industrial uses.

With an annual market of few billions of euros with an annual increase of about 10%, the accelerators industry is a very flourishing activity. These applications concern cancer therapy, ion implementation, electron cutting and welding, electron beam and X rays irradiators, radio-isotope production, ion beam analysis, neutron generators, to cite the more important. In medicine, the effects of radiations on human bodies were discovered at the end of the 19th and at the beginning of the 20th century, along with the interest cancer research had for ionizing radiations **[Pusey 00]**. The first era of radiation medicine considered only using gamma-rays, emitted by natural radioactive elements or by x-ray tubes. The discovery of the nuclear reactor made the production of artificial radioactive isotopes easier and boosted x-ray therapy development. However, from the early 1900s to the 1940s therapists were still fumbling on the use of radiations **[Coutard 37]**. X-ray therapies are now quite common to treat most kind of cancers, even if the defects of this technology fueled scientific research about other kinds of radiations: particle beams. Particle therapy started during World War II and is still widely used nowadays **[Thwaites 06]**. Electron therapy has been considered **[Klein 08]**, but proton therapy seems more promising **[Levin 05]**. Facilities such as the synchrocyclotron of Orsay, France (Fig. 1.3 (a) and (b)) perform proton therapy. Hadrontherapy appears to be more interesting than classical x-ray therapy because the later has side effects such as provoking burns, and revealed itself to be less effective in several situations. The high costs and large footprints of particle therapy facilities fuel the need for

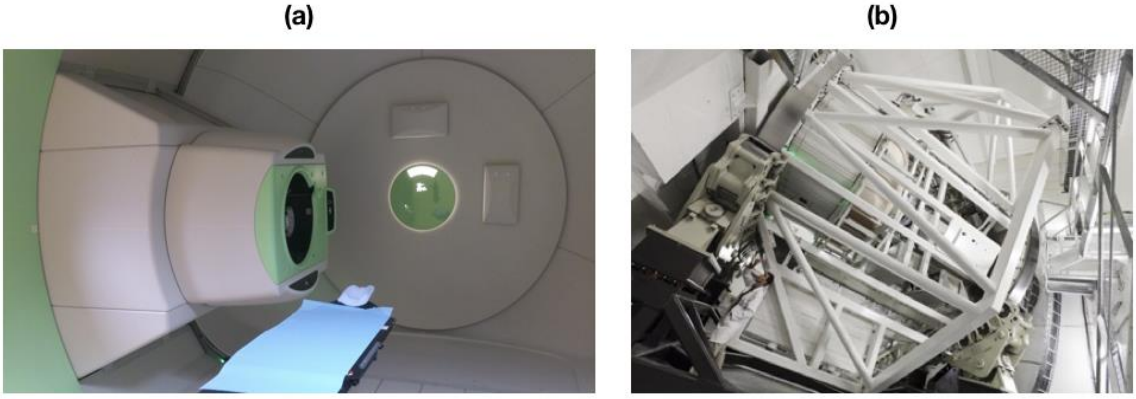

Figure 1.3: (a) Gantry of the proton therapy center in Orsay, France. The patient lies on the bed (center), the ionizing radiations flow from the mobile green and white device (left). (b) Moving structure of the gantry. The chamber (a) is inside the circular shape on the top left. The grey device on the bottom of the picture is one of the brake of the moving structure. Its total height is approximately 4m. Courtesy of E. Bayard

new particle sources. Plasma-based acceleration techniques appear to be promising solutions on that point of view **[Malka 08]**. Both radiobiology experiments **[Pommarel 17]** and simulations (as in Fig. 1.4 (a)) to optimize treatments are carried out from plasma-based particle beams.

Particle colliders are also the primary experimental apparatus of fundamental physics research. To study the fine structure of matter, researchers need to collide particles with higher and higher energies in order to study smaller and smaller subdivisions of their constituents. The LHC for instance is a 27 km in circumference torus shaped facility that accelerates protons to 7 TeV and led to the discovery of the Higgs boson **[LHC 12]**. The colossal footprint of the LHC can be seen in Fig. 1.1 (b). Its total cost is estimated to be of about 10 billion euros, which makes it one of the most expensive scientific machines ever built. Future colliders listed in Fig. 1.2 are also expected to operate with particle energies exceeding the TeV, and therefore their sizes will grow accordingly: the ILC is expected to measure 30 km **[ILC 07]**. The cost and footprint of modern facilities also suggest that a new kind of technology should be considered to accelerate more efficiently particle beams. CERN director Fabiola Gianotti emphasized the challenge for the scientific community: "High-energy accelerators have been our most powerful tools of exploration in particle physics, so we cannot abandon them. What we have to do is push the research and development in accelerator technology, so that we will be able to reach higher energy with compact accelerators" **[Gibney 15]**. Plasma-based accelerators also appear to be very promising on that point of view: the size of the future conventional ILC facility is correlated with the maximal accelerating field achievable due to electrical breakdown limit, 100 MV/m. Plasma-based acceleration offers three orders of magnitude higher accelerating fields: 100 GV/m can be achieved **[Malka 02]**. Although accelerator physicists still face many challenges, a plasma-based facility design has already been considered **[Adli 13]**.

Laser-plasma accelerators should contribute in the near future to medical and security particle beams applications. For security purpose, LWFA bremsstrahlung gamma-ray beams, that allow non-destructive inspection with a high spatial resolution, could become prime tools of nuclear facilities or astronautic companies. Indeed, actors from these fields need non-

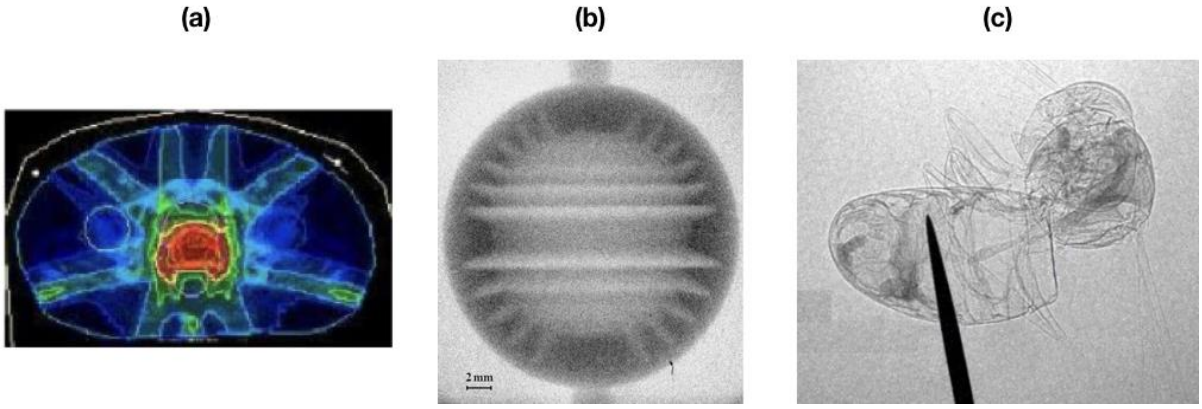

Figure 1.4: Examples of applications of particle beams, some of which can already be accomplished with plasma-based particle accelerators. (a) Simulation of an electron beam dose deposition for cancer treatment. Research is being done on the use of the different kinds of particles, here electron beams burn also the body (blue and green areas) around the tumor (red area). (b) Gamma-ray internal imaging of a metallic sample accomplished at LOA. From ***[Ben-Ismail 11]*** *(c) Imaging of a bee body using x-rays from a plasma-based accelerator particle beam accomplished at the ALLS facility of the INRS-EMT laboratory. From* ***[Fourmaux 11]***

destructive testing techniques to study material fatigue, to ensure safety and to perform quality control **[Cartz 95]**. **SourceLab, a start-up, spin-off of LOA** for instance is developing such sources to identify cracks spreading on materials. For the application of non-destructive testing, plasma-based acceleration could provide a cheaper and more efficient solution for all users **[Malka 08]**. Betatron X-ray beam delivered by LWFA is another pertinent source for imaging application. The spatial coherence and the small dimension of the source allow to perform phase contrast X-ray imaging of biological object with a resolution of tens of micrometer **[Corde 13]**. This opens the possibility to detect breast cancer tumor at earlier stage with a moderate dose deposition. Direct use of very high energy electrons (in the 100 to 300 MeV) is envisaged for cancer treatments. It was shown that in the case of prostate cancer, this approach should reduce by 20% the dose delivered in safe tissues and sensitive organs compared to the dose deposited by X-MRT (modulated photon radiotherapy). These near-term applications are illustrated in Fig. 1.4.

2. Laser physics concepts and formalism

LWFA and PWFA both rely on concepts of plasma and laser physics. This section and the next introduce the formalism and the conventions used in these two fields of physics that will be used in the whole manuscript.

a. Laser fields and Gaussian pulses

Gaussian beams are preeminent in physics. In fact, Gaussian beams are laser fields solution of the Helmholtz equation, under the hypothesis of the paraxial approximation. Gaussian beams describe therefore the behaviour of a laser field propagating through an isotropic medium under the paraxial approximation. This is the realistic solution (as opposed for instance to the plane wave description, simpler but unrealistic) of the equation that describes accurately the beams scientists use in their experiments. In the rest of the manuscript, when an explicit form is needed for the laser field used in the experiments, we will consider a Gaussian beam.

For a Gaussian electromagnetic pulse the complex vector potential reads:

$$\boldsymbol{A}(r,z,t) = A_0 \frac{w_0}{w(z)} e^{-\frac{r^2}{w(z)^2}} e^{-2\ln(2)\frac{(ct-z)^2}{c^2\tau_0^2}} e^{i\omega t} e^{-i\left(kz+\frac{kr^2}{2R(z)}-\psi(z)\right)} \boldsymbol{u} \qquad \textbf{(1.1)}$$

Where the parameters are the following:

ω is the angular frequency of the laser pulse.

$k = \frac{2\pi}{\lambda}$ is the wave vector of the laser pulse.

w_0 is the waist dimension of the laser pulse.

z is the algebraic distance to the beam focal spot.

$\psi(z) = \arctan(\frac{z}{z_R})$ is the Gouy phase, an additional phase term that contributes to shift the phase near the focal spot, but that is constant far from it. This term is responsible for the π-phase shift at focus.

$c\tau_0$ is the laser pulse length in vacuum, measured as the Full Width at Half Maximum of the beam in the propagation direction z.

$\frac{kr^2}{2R(z)}$ where $R(z) = z\left(1 + \frac{z_R^2}{z^2}\right)$ is the curvature radius. This is an additional quadratic term that takes into account the curvature of the phase front at distance z from the focal spot.

$w(z) = w_0\sqrt{1 + \frac{z^2}{z_R^2}}$ is the transverse size of the laser pulse. The graph $(z, w(z))$ is ploted in Fig. 1.5, where the asymptotic evolution of the waist dimension appears clearly.

Formula **(1.1)** describes a laser pulse that has a Gaussian shape in the z direction, whose envelope is given by the term $e^{-2\ln(2)\frac{(ct-z)^2}{c^2\tau_0^2}}$. The z direction is also the direction of propagation in the formula written above. The pulse has a Gaussian shape in the transverse direction, given by the term $e^{-\frac{r^2}{w(z)^2}}$.

In the LWFA experiments described in this manuscript, the laser final focus is often accomplished with a parabolic mirror that focuses an initially well-collimated beam of diameter $D = 6\ cm$, and that has a focal length of typically $f = 1\ m$. The convergence angle $\theta \sim \frac{D}{2f}$ of the beam enables to compare the waist w_0 with the parameters of the parabola. We have $\frac{w(z)}{z} \sim \frac{\lambda}{\pi w_0}$ far from the focal spot. For small angles, one also has: $\frac{\lambda}{\pi w_0} \sim \frac{D}{2f}$. Therefore, the waist is typically: $w_0 \sim \frac{2\lambda f}{\pi D}$. The laser spot size is therefore for a perfect beam of the order of ten micrometres.

The transverse size of the laser beam is given by $w(z) = w_0\sqrt{1 + \frac{z^2}{z_R^2}}$, where w_0 is the waist dimension, the minimal transverse size of the beam. The Rayleigh length z_R is the distance over which the laser intensity is reduced by a factor of 2, it also corresponds to the distance after which the transverse size is increased by a factor $\sqrt{2}$, starting from the waist: $z_R = \frac{\pi w_0^2}{\lambda}$.

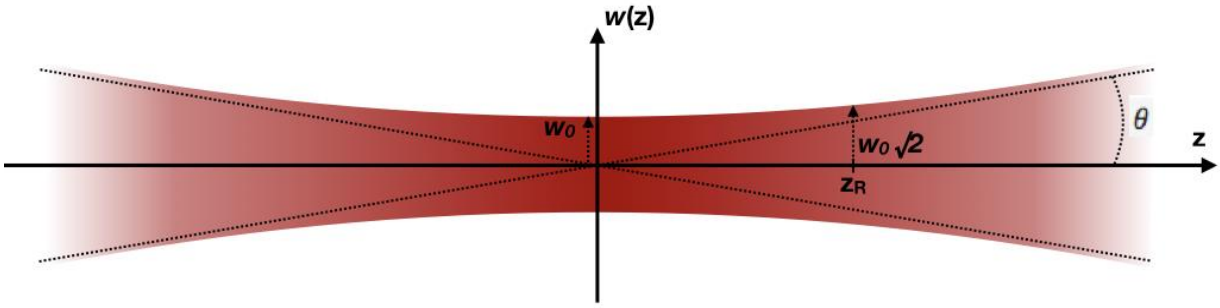

Figure 1.5: A Gaussian beam, near its focus. The plot represents the waist dimension, as a function of the position z. The meanings of the parameters w_0, θ and z_R are also visible.

By definition, the E and B fields can be deduced from the relations:

$$\boldsymbol{E} = -\frac{\partial \boldsymbol{A}}{\partial t} \quad \textbf{(1.2)}$$

$$\boldsymbol{B} = \nabla \times \boldsymbol{A} \quad \textbf{(1.3)}$$

The intensity of the Gaussian laser pulse reads:

$$I(r,z,t) = I_0 \frac{w_0^2}{w^2(z)} e^{-\frac{2r^2}{w(z)^2}} e^{-4\ln(2)\frac{(ct-z)^2}{c^2\tau_0^2}} \quad \textbf{(1.4)}$$

b. Relativistic regime

When the quiver velocity of an electron in the electric field of an electromagnetic wave reaches a value close to c, we say that the laser field is relativistic. Studying the motion of particles in such fields will be important in the rest of the manuscript. A parameter is often used to discuss whether a laser beam is relativistic: the normalized vector potential a_0. We will introduce it in a simpler case that illustrates clearly how particles behave in extreme electromagnetic fields.

To simplify the derivation, we consider the simpler case of a particle in a plane electromagnetic wave. In the non-relativistic limit, in which the magnetic force can be neglected, the equation of motion of the particle writes:

$$\frac{d\boldsymbol{p}}{dt} = q\boldsymbol{E_0} e^{i(\omega_0 t - k.z)}$$

As by definition, $\boldsymbol{E} = i\omega\boldsymbol{A}$, one can write:

$$\boldsymbol{p} = \gamma m \boldsymbol{v_{quiver}} = q\boldsymbol{A}$$

When the momentum is of order of mc, it is necessary to consider the relativistic correction to the motion of the electron, the non-relativistic approximation is not correct anymore. Therefore, it is common to define the normalized vector potential of the laser pulse to distinguish non-relativistic and relativistic regimes directly from this dimensionless parameter:

$$a_0 = \frac{eA_0}{mc}$$

When $a_0 \ll 1$, the regime is non-relativistic, and when $a_0 > 1$, the regime is said to be relativistic.

One last formula may be of interest in the following, it is the expression of a_0 in terms of the wavelength of the electromagnetic wave and of its intensity:

$$a_0 = \frac{eA_0}{mc} = \frac{eE_0}{mc\omega_0} = \left[\frac{e^2}{2\pi^2\epsilon_0 m^2 c^5}\lambda^2 I_0\right]^{\frac{1}{2}}$$

$$= 0.86\,\lambda[\mu m]\sqrt{I[10^{18} W/cm^2]} \quad \textbf{(1.5)}$$

We have $a_0 \propto \sqrt{I_0}\lambda$. The square root of *I* in equation **(1.5)** was expected, as the intensity of a laser field grows as the square of the amplitude of the electric field, directly related to a_0.

c. Maxwell equations

The propagation of an electromagnetic wave in a medium is described by Maxwell equations:

$$\boldsymbol{\nabla} \times \boldsymbol{E} = -\frac{\partial \boldsymbol{B}}{\partial t} \quad \textbf{(1.6)}$$

$$\boldsymbol{\nabla} . (\epsilon \boldsymbol{E}) = \rho/\epsilon_0 \quad \textbf{(1.7)}$$

$$\boldsymbol{\nabla} \times \boldsymbol{B} = \mu_0 \boldsymbol{J} + \mu_0 \epsilon_r \epsilon_0 \frac{\partial \boldsymbol{E}}{\partial t} \quad \textbf{(1.8)}$$

$$\boldsymbol{\nabla} . \boldsymbol{B} = 0 \quad \textbf{(1.9)}$$

One can define for the rest of the manuscript the relative permittivity by $\epsilon_r(\omega) = I + \chi(\omega)$. The relation between the current density in the medium and the electric susceptibility χ is given by:

$$\boldsymbol{j}(\boldsymbol{r}) = i\omega\epsilon_0\chi(\omega)\boldsymbol{E}(\boldsymbol{r}) \quad \textbf{(1.10)}$$

By combining Maxwell equations, one can easily obtain the equation of propagation for the field $\boldsymbol{E}$ for the case of a monochromatic wave with a time dependence $e^{i\omega t}$:

$$\Delta \boldsymbol{E} - \boldsymbol{\nabla}(\boldsymbol{\nabla}.\mathbf{E}) + \frac{\omega^2}{c^2}\epsilon_r(\omega)\boldsymbol{E} = 0 \quad \textbf{(1.11)}$$

Note that throughout the manuscript, ϵ will describe the emittance of a particle beam and only in the context of Maxwell equations ϵ is the electric permittivity.

d. Chirped pulse amplification

The field of laser interaction with matter opened many prospects to physicists for example in creating new matter conditions such as warm and dense matter, in triggering nuclear fusion reaction, in reproducing in laboratories the state of matter of stars, or in offering the possibility to produce energy thanks to inertial confinement fusion. These examples were performed with long and energetic laser pulse at intensities lower than $10^{15} W/cm^2$. Since the invention of the "Chirped pulse amplification (CPA)" technique accomplished by Strickland and Mourou **[Strickland 85]**, laser intensities greater than $10^{18} W/cm^2$ have been reached, with a record today of a few $10^{21}\ W/cm^2$. Such high intensities made laboratory laser-produced plasmas achievable, while keeping the experimental devices dimensions limited. CPA laser systems provided to researchers enough physical phenomena to study for several decades, along with many potential applications.

Before "CPA" was invented, physicists were facing a limitation in further increasing the power of their laser systems: during laser light production, the beam passes through an amplifying media and is reflected by several optical components. However, when the intensity inside the amplification media or on the optics becomes too high, the beam faces nonlinear effects that distort the spatial and spectral profile of the pulses **[Maine 88]**. This ruins any hope to reach a higher power. CPA made possible to overcome this technological limitation. A schematic of a Chirped Pulse Amplification laser system is displayed in Fig. 1.6.

From an initial low-energy ultra-short pulse of a few femtosecond, a first grating pair stretches it to hundreds of picoseconds by adding a linear component to the pulse group delay. The stretched pulse is then amplified by many orders of magnitude over the whole spectrum, before being recompressed by suppressing the linear part of the group delay with the second grating pair. Amplification occurs when the beam is stretched, therefore the intensity in the amplifying media stays moderate.

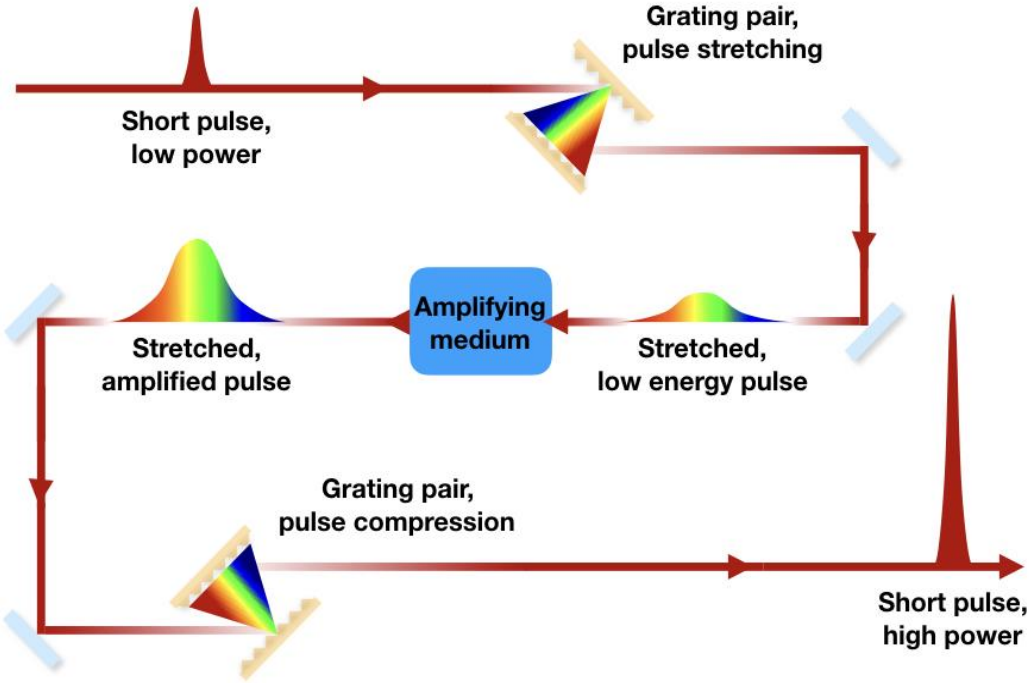

Figure 1.6: Schematic of the chirped pulse amplification technique.

The initial technology was using optical fibers as a stretcher and a grating pair to recompress the pulses. The reason for this is that CPA was developed in the context of radar research. The technology in use nowadays for high power laser facilities relies on grating pairs both for the stretcher and the compressor.

In particle accelerators, beams have to be transported over hundreds of meters, and reshaped to have the dimension and divergence required by the experiments. Several concepts and conventions in beam physics are necessary to discuss how LWFA and PWFA experiments set requirements on beam parameters. These concepts are introduced in the following section.

3. Beam physics concepts and formalism

Electron particle beams in conventional accelerators are usually produced by a diode **[Humphries 02]**. Particles flow from the cathode, are accelerated by the potential gradient between the two electrodes and emerge through holes in the anode. The beam is then spatially and spectrally shaped downstream in the facility. Positron bunches are produced by sending a high-energy electron beam on a thick tungsten alloy target. Electron/positron pairs are generated and positrons are selected and accelerated in the facility **[Humphries 02]**. Quantifying the beam quality is a matter of first importance for the different applications: a plasma-based collider requires high **luminosity** and therefore beams with large numbers of particles and with very small bunch sizes. As can be understood from this example, a low divergence and a low transverse beam size are the requirements for a good transverse quality beam. A figure of merit for this quality, the **emittance**, will be introduced in this section, then the **Twiss parameters** that describe the beam and its propagation along the beamline of a

particle accelerator will be introduced, as well as **matrix formalism** of beam physics. From these concepts, the equation of the beam envelope in a focusing field will be derived. The **trace-space** shape of the beam and its evolution will be commented in further detail in the third paragraph, with a discussion regarding the sources of emittance growth, that degrade the beam quality.

a. Emittance

We consider in the following a beam propagating in the z direction, whose transverse dimensions are labeled xy. In the x dimension, the angle of the particle is $x' = \frac{dx}{dz} \approx \frac{P_x}{P}$. From the particle distribution, we define the **geometrical emittance**:

$$\epsilon_x = \sqrt{\bar{x}^2 \bar{x}'^2 - \overline{x x'}^2} \qquad \textbf{(1.12)}$$

Where $\bar{x}$ indicate the mean of the quantity x over all the particles in the beam. This quantity is defined for each axis of the transverse plane, ϵ_x and ϵ_y. It is often called the Root Mean Square (RMS) emittance **[Reiser 08]**.

The plane $x - x'$ is sometimes called the **trace-space** and is usually used in the beam physics community. The $x - p_x$ plane is more common in classical and quantum mechanics and is called the **phase-space**.

Ideal beams are made of particles moving exactly in the same direction. No trajectory crossing can occur in these beams, that is why they are also called "laminar beams". In the $x - x'$ trace-space, for a given x, all particules have the same angle x'. Therefore, the RMS emittance is null, and the $x - x'$ profile is a line. Beams can be either converging (for example when there are being focused by a lens), or diverging (for example after they passed their waist during a free drift).

The product mean $\overline{x x'}$ over all the particles in a bunch describes the correlation in trace-space between the parameters x and x'. If all the transverse forces on the beamline are linear, there should not be any nonlinearity in the bunch representation in trace-space and the emittance should be approximately equal to the area of the beam in trace-space $x - x'$. In the rest of the manuscript, the linear transverse force assumption will be made.

In the particular case of a beam focused by a quadrupole lens, the term $\overline{x x'}$ represents the inward or outward flow. This term is null at the waist of the beam. At the waist, the emittance can be written: $\epsilon_x = \sigma_0 \Theta$ where $\sigma_0 = \sqrt{\bar{x}^2}$ is the transverse RMS size and $\Theta = \sqrt{\bar{x}'^2}$ the RMS divergence.

However, from the definition **(1.12)**, x' and ϵ_x will decrease when the beam energy increases in the accelerator. To compare the emittances of beams with energies different from each other, we need to take into account the energy dependence and therefore define the normalized emittance:

$$\epsilon_{n,x} = \beta \gamma \epsilon_x$$

This definition will be implicitly used in the rest of the manuscript. While the geometrical emittance measures the area in the trace-space, the normalized emittance measures the area in the normalized phase-space.

Liouville's theorem ensures that the emittance is invariant under ideal accelerating conditions **[Lejeune 80]**. To improve the beam emittance, one can consider improving the generation process of the particle beam. In order to produce beams of lower initial emittance, one can also focus on mitigating all possible sources of emittance growth during the acceleration and transport of the beam, last one can also rely on cooling mechanisms such as damping rings.

The transport of a beam is a process of fundamental importance in particle accelerators and can be easily described using the formalism presented now.

b. Transfer matrices, transport

For a single particle, when the particle drifts in free space along the beamline of an accelerator facility or moves through a quadrupole magnet, its position in trace-space evolves. The displacement between two z positions labeled 1 and 2 in trace-space can be conveniently described by a transfer matrix M: $\begin{pmatrix} x \\ x' \end{pmatrix}_2 = M \begin{pmatrix} x \\ x' \end{pmatrix}_1$.

For a drift in free space $M = \begin{pmatrix} 1 & L \\ 0 & 1 \end{pmatrix}$, where L is the distance between the two positions.

For a quadrupole in the thin-lens approximation i.e. if the quadrupole length is much smaller than the focal lengths: $M = \begin{pmatrix} 1 & 0 \\ -\frac{1}{f_2} & \frac{f_1}{f_2} \end{pmatrix}$. In general, f_1 and f_2, the distances to the principal planes of the quadrupole are chosen identical.

The drift space transfer matrix and the thin-lens matrix both apply to describe the evolution of the beam envelope in phase-space. The general form of the transfer matrix without the thin-lens approximation is more complex, and it is not indispensable for the work reported in this thesis. Furthermore, thick lens matrices cannot be applied to the beam envelope coordinates, but rather to individual particle motion.

The matrix description is a convenient way to calculate the effect of quadrupoles on the beam. Quadrupoles are the equivalent of lenses in optics, that is why in beam physics it is common to call them lenses. They are often used to image the beam from one point of the beam line onto a screen. An example of such a system is given for the FACET energy spectrometer diagnostic in Part II.

c. Twiss parameters and beam envelope equation

Along with the emittance, three parameters conveniently describe the propagation of the beam in the beamline, noted α, β and γ and called the **Twiss parameters**. Their definitions provide a direct insight into their meanings:

$$\hat{\beta} = \frac{\langle x^2 \rangle}{\epsilon} \quad \textbf{(1.13)}$$

$$\hat{\alpha} = -\frac{\langle xx' \rangle}{\epsilon} \quad \textbf{(1.14)}$$

$$\hat{\gamma} = \frac{\langle x'^2 \rangle}{\epsilon} \quad \textbf{(1.15)}$$

There is the relation $\hat{\gamma}\hat{\beta} - \hat{\alpha}^2 = 1$ between them, by definition of the RMS emittance ϵ. $\hat{\beta}$ expresses the RMS spatial width in the x direction $R = \sqrt{\langle x^2 \rangle}$, while $\hat{\gamma}$ expresses the RMS angle of the distribution of particles in the x dimension $\theta = \sqrt{\langle x'^2 \rangle}$. $\hat{\alpha}$ contains the correlations between the first two parameters. A Gaussian distribution in the trace-space would write **[Frederico 16]**:

$$\rho(x, x') = \frac{1}{2\pi\epsilon} e^{-\frac{\hat{\gamma}x^2 + 2\hat{\alpha}xx' + \hat{\beta}x'^2}{2\epsilon}} \qquad \textbf{(1.16)}$$

Such a distribution is plotted as an example in Fig. 1.7. The R and θ parameters appear as plotted. In this trace-space, the distribution of the particles in the beam will be an ellipse whose equation is: $\hat{\gamma}x^2 + 2\hat{\alpha}xx' + \hat{\beta}x'^2 = \epsilon$. It is easy to understand that the RMS emittance is the area of the ellipse drawn on the trace-space plane, by definition.

Twiss parameters are very convenient for beam physicists as their evolution when the beam propagates along the beam line is described by differential equations simpler than the equations of the couple (R, θ). However, we will derive the equation of evolution of the beam envelope R as well from the equations over $\hat{\alpha}$ and $\hat{\beta}$. This equation will be useful to study the evolution of the beam in a plasma wakefield accelerator. The following calculation is accurate whenever individual particles in the beam face a linear focusing force: $x'' = -\kappa x$.

Starting from the definition **(1.13)** – **(1.15)** and keeping in mind the relation $x'' = -\kappa x$ for individual particles, we have:

$$\hat{\alpha}' = -\frac{\langle x'^2 + xx'' \rangle}{\epsilon} = -\hat{\gamma} + \kappa\hat{\beta}$$
$$\hat{\beta}' = 2\frac{\langle xx' \rangle}{\epsilon} = -2\hat{\alpha}$$

These first order equations describe the evolution of α and β along the beam line. One can reach the independent second order equations over α and β:

$$\hat{\alpha}'' = 2\kappa\frac{\langle xx' \rangle}{\epsilon} - 2\hat{\alpha}\kappa = -4\kappa\hat{\alpha}$$

$$\hat{\beta}'' = -2\hat{\alpha}' = 2\hat{\gamma} - 2\kappa\hat{\beta} = 2\frac{1 + \frac{\hat{\beta}'^2}{4}}{\hat{\beta}} - 2\kappa\hat{\beta}$$

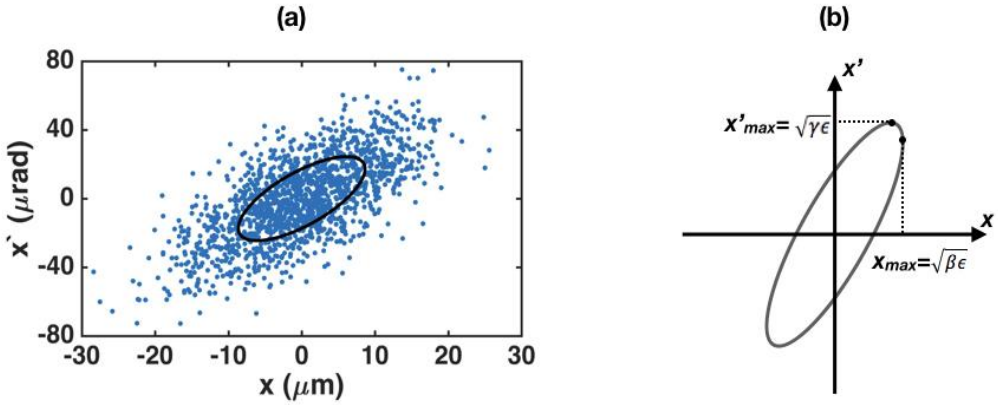

Figure 1.7: (a) Particle distribution in trace-space. The black line is the ellipse whose equation is given above. Its area is πϵ. (b) Dimensions of the ellipse expressed with the Twiss parameters.

We want now to derive the envelope equation for R, we have to recall the definition of $\hat{\beta}$ in terms of the RMS extent of the beam in the x dimension. As said earlier $R^2 = \hat{\beta}\epsilon$ (as shown in Fig. 1.7 (b)), and ϵ is a constant during the evolution of the beam, therefore:

$$\hat{\beta} = \frac{R^2}{\epsilon}$$
$$\hat{\beta}' = \frac{2RR'}{\epsilon}$$
$$\hat{\beta}'' = \frac{2}{\epsilon}(RR'' + R'^2)$$

The second order equation over $\hat{\beta}$ writes for R:

$$R'' + \kappa R - \frac{\epsilon^2}{R^3} = 0 \qquad \textbf{(1.17)}$$

Equation **(1.17)** describes the evolution of the envelope of the beam, the RMS value of the beam size in x. In this equation, R'' is the term of evolution of the envelope, κR is the focusing linear force, while $\frac{\epsilon^2}{R^3}$ is often called the "emittance force" **[Humphries 02]**. The "emittance force" acts as if the beam was being forced to spread transversally. This spreading would be due to the beam emittance, and it opposes the external focusing force.

d. Evolution of the trace-space ellipse in free space

The evolution of the ellipse in trace-space illustrates the role of the Twiss parameters as well. For a drift in free space, we have from the previous paragraphs the transfer matrix $M = \begin{pmatrix} 1 & z \\ 0 & 1 \end{pmatrix}$. The relation for the evolution of $\begin{pmatrix} x(z) \\ x'(z) \end{pmatrix} = M \begin{pmatrix} x_0 \\ x_0' \end{pmatrix}$ compared to the ellipse equation leads to the matrix relation **[Reid 91]**:

$$\begin{pmatrix} \beta(z) \\ \alpha(z) \\ \gamma(z) \end{pmatrix} = \begin{pmatrix} 1 & -2z & z^2 \\ 0 & 1 & -z \\ 0 & 0 & 1 \end{pmatrix} \begin{pmatrix} \beta_0 \\ \alpha_0 \\ \gamma_0 \end{pmatrix}$$

Choosing the origin of the z axis at the beam waist leads to: $\begin{pmatrix} \beta(z) \\ \alpha(z) \end{pmatrix} = \begin{pmatrix} \beta_0 + \frac{z^2}{\beta_0} \\ -\frac{z}{\beta_0} \end{pmatrix}$. β_0 is the analogous of the Rayleigh length z_R for a Gaussian laser beam.

The evolution of parameters **(1.13) – (1.15)** for a beam propagating in free space is as follows: for a converging beam, initially we have $\alpha > 0$, at focus $\alpha = 0$ and after focus when the beam diverges $\alpha < 0$. The beam emittance (area of the ellipse in trace-space) is constant. Before focus, a particle that has $x > 0$ must also have $x' < 0$ (the beam converges, Fig. 1.8 (a)). After focus, it is the opposite (Fig. 1.8 (c)). At focus ($\alpha = 0$, Fig. 1.8 (b)) the beam reaches its minimal possible size in x: the ellipse is "upright".

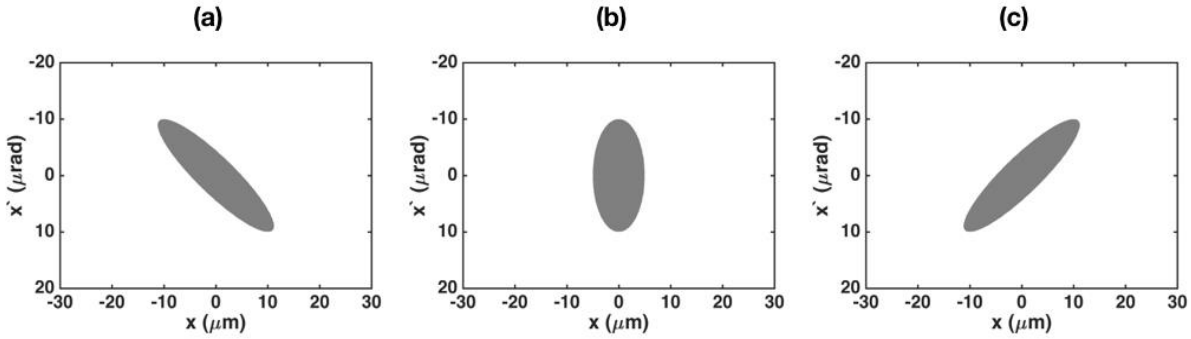

Figure 1.8: Evolution of the trace-space ellipse of a particle beam moving in real space without focusing force, when the beam crosses a focal spot. (a) Before focus. (b) At focus. (c) After focus. The area of the ellipse stays constant, so does the extremum of x'.

e. Periodic focusing systems

In conventional accelerators particle beams are transported along the beam lines over kilometers. A periodic set of lenses maintains the beam close to the axis by refocusing it regularly. In real space, each particle undergoes pseudo harmonic oscillations with a wavelength $\lambda = \frac{2\pi}{\sqrt{\kappa}}$. In trace-space, the beam ellipse accomplishes complete rotations around the origin **[Humphries 02]**. Scientists define the **phase advance** per cell $\boldsymbol{\sigma}$ as the fraction of the complete rotation of the beam ellipse in trace-space between two consecutive lenses. In Fig. 1.9 is plotted a particle trajectory in a periodic focusing system, along with the envelope evolution. We can say that the beam is correctly **matched** if the envelope oscillations are stable, such as in Fig. 1.9. A stability threshold can be found from the derivation of the parameters **(1.13) – (1.15) [Humphries 02]**. This **matching condition** is the requirement to be able to maintain the beam close to the axis of the beam line, while keeping a constant emittance over the full length of the accelerator.

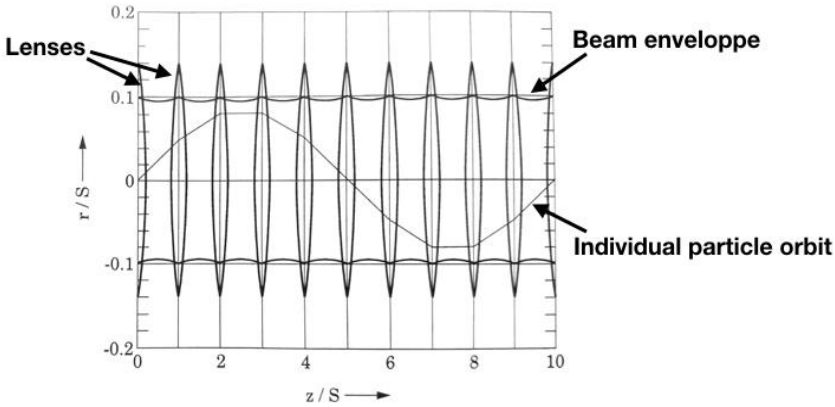

*Figure 1.9: Periodic focusing system. The abscise is the position along the line, normalized to the distance between two consecutive lenses, the vertical axis represents the transverse dimension of the beam. From **[Humpries 02].***

f. Sources of emittance growth

Preserving the normalized emittance during acceleration and transport along the beam line is a major and well-known issue. Focusing components provide linear forces that do preserve

the emittance. SLAC National Accelerator Laboratory provides for instance a beam with typical x and y normalized emittances of $100\,mm.mrad \times 10\,mm.mrad$ at the experimental area, for a minimal beam size of $30\,\mu m$.

Several phenomena are sources of emittance growth, some of them, occurring in Plasma Wakefield Acceleration experiments are listed below with further details.

Nonlinear focusing forces:

Beams facing nonlinear focusing forces such as in the wakefield seen by large transverse size bunches in a plasma wakefield accelerator do not conserve their emittance. Such focusing fields distort the ellipsoidal shape of the beam in trace-space. For perfectly harmonic forces, the trace-space beam ellipse rotates without any distortion.

In plasma or laser wakefield accelerator schemes, Betatron oscillations can occur to all accelerated particles **[Rousse 04]**. In the case of a highly nonlinear blowout regime, the focusing force due to the ion cavity is perfectly linear in r (the distance of the electron undergoing Betatron motion to the axis). However, far from the axis the focusing force can become higher than the linear force close to the axis. Therefore, outer particles phase in trace-space can evolve faster. This is directly responsible for distortion of the ellipse in trace-space. Particle will spread in phase-space and form a uniform circular shape with a higher area than the initial ellipse.

This phenomenon occurs also in conventional accelerators beam lines, in which periodic focusing quadrupole doublets are used to transport the beam (when matching conditions are met, nonlinearity has the smallest effect, while it can be very strong when mismatched). The ellipse in trace-space therefore rotates as the beam propagates in the line. If the focusing forces are nonlinear, outer particle phase advance will evolve faster as well. In that case, the trace-space beam ellipse will be distorted.

Linear forces dependent on the beam longitudinal coordinate

If the force depends on the longitudinal coordinate, emittance growth will occur. This phenomenon can happen for instance in the linear regime of PWFA or LWFA. If the plasma wave is sampled by a beam whose longitudinal size is of the same order as the variation length of the wakefield in the longitudinal direction, then the particles will rotate with different speeds in trace-space **[Mehrling 12]**.

Chromaticity spread

Beam energy spread implies a variation of the emittance. If one considers Betatron oscillations of particles in the blow-out regime of Plasma Wakefield Acceleration, particles in trace-space $x - x'$ rotate around the origin at the frequency $\omega_b = \omega_p/\sqrt{2\gamma}$ **[Lu 06b, Corde 13]**. ω_b depends on gamma, therefore particles with different energies will rotate at different velocities. As many Betatron oscillations occur during the acceleration process, this will contribute to distort the beam ellipse in trace-space **[Michel 06]**.

The first chapter was an introduction to particle accelerators and to the technologies underlying particle energy gain in these facilities. Examples of applications were given and the necessary increase in acceleration gradient to push fundamental research further was illustrated. A solution to this issue could be plasma based acceleration. Two sections of the first chapter were dedicated to some of the physics concepts useful in the manuscript: laser and particle beam physics. The next chapter is dedicated to the presentation of plasma physics results, results necessary to derive the theory behind plasma acceleration of particles.

Chapter 2

Introduction to plasma physics

Plasma-based acceleration techniques rely on several important concepts of **plasma physics** that will be presented here. After the introduction of the basic concepts and parameters, a simple model of **electromagnetic waves propagation** in plasmas is derived and the **fluid description** of a plasma and its formalism are introduced.

Contents

1. Plasmas

Plasma is the most common state of matter in the visible universe. A gaseous medium is called "plasma" if the presence of free charged particles is in proportion high enough for collective phenomenon to take place in it. Charged particles in the gas interact with all others through the Coulomb force. Globally, any change in the charge distribution leads to an increase of the electrostatic energy. Such a state is therefore unstable and particles are quickly dispatched to reach a lower energy state. As a consequence, matter tends to be globally quasi-neutral with as many positive and negative charges everywhere. Disequilibrium only takes place on a very short time scale whose duration will be discussed in this chapter.

In most phenomenon studied in physics laboratories almost all atoms are partially or fully ionized with all of them having lost at least an electron. This is the case in all the experiments described in this manuscript.

a. Electronic plasma frequency

The most important parameter that characterizes the displacements of electrons in a plasma is called the **electronic plasma frequency**. It appears naturally when one considers an electrostatic wave in a plasma. In this model as in all this manuscript, ions are supposed to be immobile on the time scale of electron motion.

To study collective oscillations of plasma electrons in 1-D, the common model relies on an initially homogeneous and neutral gas plasma with an electron density n_0. We consider now a planar sheath of electrons, initially at $x = x_0$, whose position is perturbed of a quantity $\xi(x_0, t)$. Such a perturbation is displayed in Fig. 2.1, where a sheath of electrons is displaced of the quantity ξ in the dimension x. To maintain a fluid description for this model, we have to assume that during the oscillations, slices of electrons at different initial positions do not cross each other during their motion.

n_0 is the plasma ion/electron density, before the perturbation occurs.

Poisson equation writes:

$$\Delta\phi = -\frac{\rho}{\epsilon_0} \qquad \textbf{(2.1)}$$

In one dimension $\Delta\phi = \frac{\partial^2\phi}{\partial x^2} = -\frac{\partial E}{\partial x}$, and integrating equation **(2.1)** between $-\infty$ and $x_0 + \xi$ writes:

$$\int_{-\infty}^{x_0+\xi} -\frac{\partial E}{\partial x} dx = \int_{-\infty}^{x_0+\xi} \frac{(n_e(x) - n_0(x))e}{\epsilon_0} dx$$

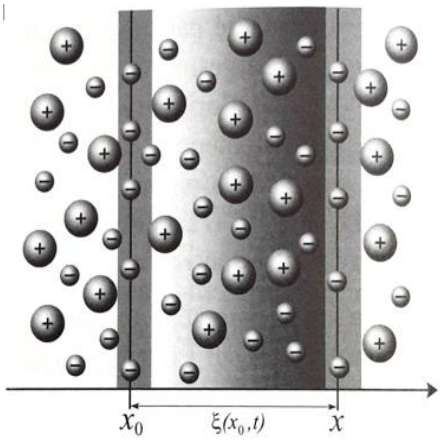

*Figure 2.1: Electronic perturbation in one dimension. From **[Rax 05]**.*

At $-\infty$ the E field is considered null. All the electrons between x_0 and $x_0 + \xi$ are displaced to positions $x > x_0 + \xi$ (to satisfy the hypothesis that slices of electrons at different initial positions do not cross). The previous integral becomes:

$$E(x_0 + \xi) = \frac{n_0 e}{\epsilon_0}\xi$$

The equation above, injected into Newton's second law of motion, becomes:

$$\ddot{\xi} = -\frac{e}{m}E = -\frac{e^2 n_0}{m\epsilon_0}\xi$$

This is the equation of a harmonic oscillator, whose frequency writes:

$$\omega_p = \left(\frac{e^2 n_0}{m\epsilon_0}\right)^{\frac{1}{2}} \qquad \textbf{(2.2)}$$

Parameter **(2.2)** describes the collective oscillations of electrons in a plasma after they have faced a small perturbation around their equilibrium positions. It is the equation associated to an electrostatic wave in a cold plasma, whose dispersion relation writes therefore:

$$\omega = \omega_p \qquad \textbf{(2.3)}$$

This parameter sets the time scale of relaxation of internal electrostatic perturbations: ω_p^{-1}. Parameter **(2.2)** has a major role in plasma physics **[Rax 05]**. The simple 1-D model and the definition given of ω_p provide enough details to introduce the models of LWFA and PWFA. We call parameter **(2.2)** the **plasma frequency**.

As can be seen in the definition of the plasma frequency, $\omega_p^{-1} \sim n_0^{-\frac{1}{2}}$. This indicates that the denser a plasma is, the faster the electrostatic interaction will pull the electrons back to their initial equilibrium.

b. Debye Length

Another important parameter to describe collective phenomena in plasma physics is the **Debye length**. This parameter is defined as the product between the thermal speed of plasma electrons and the typical time length of electron oscillations in a neutral plasma ω_p^{-1}:

$$\lambda_D = \frac{v_{Te}}{\omega_p}$$
$$= \left(\frac{k_B T_e}{m}\right)^{\frac{1}{2}} . \frac{1}{\omega_p} = \left(\frac{\epsilon_0 k_B T_e}{n_0 e^2}\right)^{\frac{1}{2}}$$

This parameter is also the typical damping length of electrostatic phenomena in plasmas **[Debye 23]**. When the electrostatic equilibrium is broken, after a typical distance of λ_D, the effects of the electrostatic perturbation are strongly damped. As can be seen in the definition of the Debye length, $\lambda_D \sim n_0^{-\frac{1}{2}}$, the denser a plasma is, the stronger the electrostatic perturbation is screened.

After this brief introduction, it is necessary to describe the physical phenomenon underlying the production of laboratory plasmas used in LWFA and PWFA experiments.

2. Ionization

To set up both LWFA and PWFA experiments, it is necessary to produce plasmas in a repeatable way. For PWFA it is crucial to produce a long and stable homogeneous plasma. The use of intense and very short laser pulses is a reliable solution. Plasma production from a laser pulse occurs after a total ionization of the gas on the laser path. Several phenomena explain the ionization of a gas atom when it is exposed to a laser field, they are detailed below.

a. Low-Field Ionization: the photoelectric effect

When the intensity of the laser field is small, $E_L < 10^{11}\ V/m$, the regime of ionization is called Low-Field Ionization. Examining Bohr model gives an insight into the ionization process. In a low intensity laser field, if the laser photons have an energy high enough to hit gas atoms and pull their valence electron out, ionization occurs. To be specific, this process occurs when photons energy is greater than the ionization potential U_I of the atom as depicted in Fig 2.2 (b). The final energy of the pulled-out electron is given by the very well-known Einstein formula for the photoelectric effect:

$$E_f = \hbar\omega - U_I$$

The ionization rate depends on the cross section of the atoms and of the flux of photons. This technique is not used to create laboratory plasmas. It is hard to produce photons of energy high enough (typically a few eV) to reach the Low-Field Ionization regime. On the contrary, very high power pulses can be achieved with photons of more moderate energy.

For very high fields, and photons of lower energy, several more complex physical mechanisms lead to ionization of a gas when it is hit by a femtosecond laser pulse: Multi-Photon Ionization, Barrier Suppression Ionization and Field Ionization.

b. Multi-Photon Ionization

This phenomenon is similar to the simple photoelectric effect described earlier in the low-field regime, where a photon directly pulls out an electron from the atom. In case of Multi-Photon Ionization, several photons simultaneously contribute to ionize an atom, as seen in Fig. 2.2 (c). In a gas, Multi-Photon Ionization is dominant at intensities of 10^{11} to 10^{13} W/cm^2**[Agostini 68]**. One of the assumptions made in the Multi-Photon Ionization model is that the laser field does not modify the atomic potential the electron sees, which is not the case of some of the processes described below. Einstein formula can be adapted to the case of Multi-Photon Ionization, and becomes:

$$E_f = n\hbar\omega - E_I$$

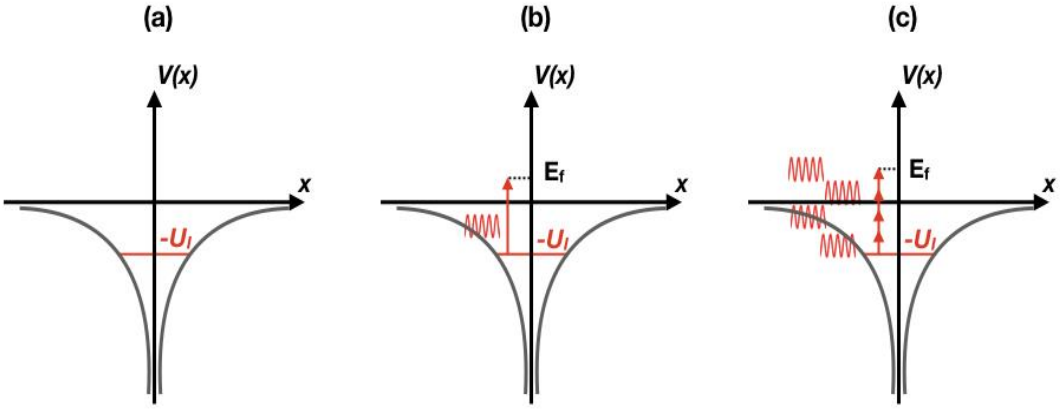

Figure 2.2: Ionization processes (a) Coulomb potential of an atom, the valence electron has an ionization energy U_I. (b) Low-Field Ionization process, the energy of the incoming photon is high enough to ionize the atom. (c) Multi-Photon Ionization: the atom is ionized under the combined effect of multiple photons. When the total energy of the photons is U_I the process is called Multi-Photon Ionization. In the specific case where the total energy is higher than U_I, the process is called Above-Threshold Ionization, case (c).

c. Tunnel Ionization and Barrier Suppression Ionization

These two processes of ionization are two regimes of the same phenomenon. The model comes from the intuitive idea that when the electric field of the laser is high enough, it suppresses the electric field generated by the nucleus of the atom that valence electrons see. **[Gibbon 05]** provides an intuitive derivation of the laser field needed to totally ionize a gas by suppressing the barrier potential.

The model for Barrier Suppression Ionization is obtained from a coulomb potential by adding the laser field to the potential **[Bethe 57]**, where Z is the atomic number of the gas molecules:

$$V(r) = -\frac{1}{4\pi\epsilon_0}\frac{Ze^2}{r} - eEr$$

The barrier potential is lowered on the right of the atom as shown in Fig. 2.3 (b).

If the maximum value of the potential on the right side in Fig. 2.3 (b) is lowered below U_I, the regime is called Barrier Suppression Ionization and ionization occurs directly. From **[Faure 07]**, the laser intensity required for Barrier Suppression Ionization to occur is:

$$I_{sb}[W\ cm^{-2}] = 4\ 10^{9}\frac{E_i^4}{Z^2}$$

In the case of hydrogen ionization, it is $I_{sb} = 1.4\ 10^{14}\ W\ cm^{-2}$.

However, Tunnel Ionization can lower this threshold, and ensure that ionization occurs below this limit. In fact, the theory of quantum mechanics shows that there is a probability for the electron to tunnel through the barrier potential although the minimum of $V(r)$ is still larger than U_I.

The transition from Multi-Photon Ionization to Tunnel Ionization - Barrier Suppression Ionization is smooth. Tunnel and Multi-Photon Ionization were first studied by Keldysh, who defined the so-called Keldysh parameter **[Keldysh 65]**:

$$\gamma = \sqrt{\frac{U_I}{2U_p}}$$

where U_I is the ionization potential, as seen above and U_p is the ponderomotive potential. U_p is the energy associated to the quiver motion of an electron in a laser field. The Keldysh parameter distinguishes the Tunnel and Multi-Photon regimes. When $\gamma \ll 1$, Tunnel Ionization is dominant, while Multi-Photon Ionization is significant for $\gamma \gg 1$.

This paragraph introduced the different phenomenon that lead to laser produced plasmas. It is now important to present the formalism in use to describe plasmas in most PWFA and LWFA experiments.

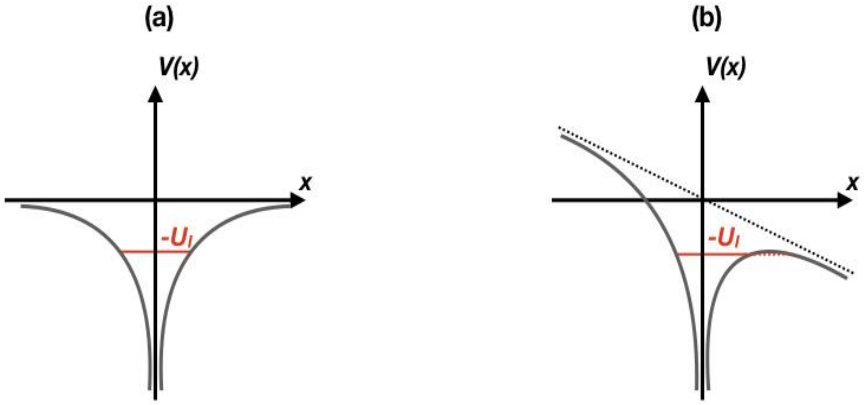

Figure 2.3: Ionization processes (a) Coulomb potential of an atom, the valence electron has an ionization energy U_I. (b) Tunnel Ionization, when the laser field is strong enough the potential is tilted and makes the tunneling effect (transition through the barrier depicted with a red dashed line) possible. For extremely strong fields, the potential bends enough to permit the suppression of the potential barrier.

3. Fluid description of a plasma

A full description of a plasma has to take into account the position and speed of each of the N particles composing the plasma. Such a description is called a **kinetic model** and takes into account an immense number of parameters as the systems studied in laboratories are macroscopic. A set of equations describe the behaviour of particles in the plasma. Each particle evolution follows Newton's second law of motion. Maxwell equations describe the evolution of the E and B fields in the system.

Solving a problem using a kinetic model implies to use the tools of statistical mechanics, as too many parameters are necessary to describe the particles individually. A kinetic model to solve a plasma physics problem relies on the distribution function $f_j(\boldsymbol{r}, \boldsymbol{v}, t)$ which represents the mean number of particle j at time t in a unit volume of the phase-space at position $(\boldsymbol{r}, \boldsymbol{v})$. The mean values of $\boldsymbol{r}$ and $\boldsymbol{v}$ are obtained by averaging over many evolutions of the system. The particles j can be electrons or ions. In this section, we note it j but we will see that only electrons will be considered in the following chapters.

In the context of laser and plasma wakefield experiments, we will neglect the collisions between particles **[Mora 13]**. Under that hypothesis, a study of the mean number of particles in an arbitrary volume leads to the continuity equation **[Mora 13]**:

$$\frac{\partial f_j}{\partial t} + \nabla \cdot \left(f_j \boldsymbol{V}\right) = 0 \qquad \textbf{(2.4)}$$

where V is a 6-element vector of the phase-space, whose first 3 elements correspond to the usual velocity and the last 3 elements correspond to the acceleration. When one separates the position and speed components of equation (2.4), one reaches the Vlasov equation:

$$\frac{\partial f_j}{\partial t} + \boldsymbol{v}.\nabla_{\boldsymbol{r}}\left(f_j\right) + \frac{q_j}{m_j}(\boldsymbol{E} + \boldsymbol{v} \times \boldsymbol{B}) \cdot \nabla_{\boldsymbol{v}}\left(f_j\right) = 0 \qquad \textbf{(2.5)}$$

Along with Maxwell equations and the definitions: $\rho = \sum_i q_j \int f_j(\boldsymbol{v}) d\boldsymbol{v}$ and $\boldsymbol{j} = \sum_i q_j \int \boldsymbol{v}.f_j(\boldsymbol{v}) d\boldsymbol{v}$ (where j distinguishes the classes of particle, electrons or ions, and i is the indices with which the particles in the class are listed) this system of equations forms the **Vlasov-Maxwell equations** system. To reach this system, one has to neglect the differences between the mean fields (the $\boldsymbol{E}$ and $\boldsymbol{B}$ fields in the equations) and the fields in the plasma for each realisation of the evolution of the system.

Maxwell-Vlasov system of equations is written using the distribution function. To go further in the study of the behaviour of a plasma, physicists often have to consider mean values of the parameters of the system. We will therefore integrate the previous system to make the mean value and moments of the distribution function appear. Such a model is called a **fluid description** of a plasma. Each fluid parameter is the integral over the velocity of the distribution function multiplied by the corresponding fluid parameter. Examples are given below:

The particle density is defined as:

$$n_j(\boldsymbol{r}, t) = \int f_i(\boldsymbol{r}, \boldsymbol{v}, t) d\boldsymbol{v} \qquad \textbf{(2.6)}$$

The fluid velocity is defined as:

$$n_j(\boldsymbol{r},t).\boldsymbol{v}_j(\boldsymbol{r},t) = \int \boldsymbol{v}.f_i(\boldsymbol{r},\boldsymbol{v},t)d\boldsymbol{v} \quad \textbf{(2.7)}$$

The pressure tensor is defined as:

$$P_j(\boldsymbol{r},t) = m_j \int \Big(\boldsymbol{v} - \boldsymbol{v}_j(\boldsymbol{r},\boldsymbol{v},t)\Big)\Big(\boldsymbol{v} - \boldsymbol{v}_j(\boldsymbol{r},\boldsymbol{v},t)\Big) f_i(\boldsymbol{r},\boldsymbol{v},t)d\boldsymbol{v} \quad \textbf{(2.8)}$$

Where m_j is the mass of constituent j.

Integrating equation **(2.5)** over $\boldsymbol{v}$ leads to the particle number conservation equation for the j particles in the fluid:

$$\frac{\partial n_j}{\partial t} + \nabla \cdot \big(n_j \boldsymbol{v_j}\big) = 0 \quad \textbf{(2.9)}$$

The first moment of equation (2.5) leads to Euler equation, also called momentum conservation equation:

$$\Big(\frac{\partial}{\partial t} + \big(\boldsymbol{v}_j \cdot \nabla_r\big)\Big)\boldsymbol{v_j} = -\frac{\nabla \,.\, P_j}{m_j n_j} + \frac{q_j}{m_j}\big(\boldsymbol{E} + \boldsymbol{v_j} \times \boldsymbol{B}\big) \quad \textbf{(2.10)}$$

This equation introduces a new parameter in spite of the fluid velocity: the pressure. The third order moment of Vlasov equation would provide a new equation involving P_j, however, it would also introduce a new fluid parameter such as the heath flux. So would the fourth order moment of Vlasov equation do. Physicists usually rely on a closing hypothesis to put an end to this endless suite of equations. The cold plasma hypothesis ($P_j = 0$) is a common hypothesis and the one used in the following chapters.

The previous paragraph introduced the main concepts and the formalism in use in plasma physics. In the following chapters, the physics of electromagnetic waves in a plasma will be of prime importance in the models. We derive therefore in this section a fundamental concept regarding the propagation of electromagnetic waves in a plasma: the **critical density**.

4. Electromagnetic waves in plasmas

To study how electromagnetic waves propagate in plasmas, one has to start from equation **(1.11).** For a monochromatic wave of frequency ω:

$$\nabla\,(\nabla \cdot \boldsymbol{E}) - \Delta\boldsymbol{E} - \frac{\omega^2}{c^2}\epsilon_r(\omega)\boldsymbol{E} = \boldsymbol{0}$$

We recall the relation between $\boldsymbol{E}$ and $\boldsymbol{j}$: $\boldsymbol{j}(\boldsymbol{r}) = i\omega\epsilon_0\chi(\omega)\boldsymbol{E}(\boldsymbol{r})$, with $\epsilon_r(\omega) = 1 + \chi(\omega)$.

We will now go further in the model than equation **(1.11)** does, by combining equation **(1.11)** with the equation of motion for the fluid particles **(2.10).** For a non-collisional cold plasma, equation (2.10), writes for electrons:

$$\frac{\partial \boldsymbol{v}}{\partial t} + (\boldsymbol{v}.\nabla)\boldsymbol{v} = -\frac{e}{m}(\boldsymbol{E} + \boldsymbol{v} \times \boldsymbol{B})$$

A perturbative expansion gives at first order in $\boldsymbol{v}$:

$$\boldsymbol{v} = -\frac{e\boldsymbol{E}}{i\omega m} \quad \textbf{(2.11)}$$

The definition of χ along with the last equation writes:

$$i\omega\epsilon_0\chi(\omega)\boldsymbol{E}(\boldsymbol{r}) = \frac{e^2 n_0 \boldsymbol{E}(\boldsymbol{r})}{i\omega m}$$

And we obtain for $\epsilon_r(\omega)$:

$$\epsilon_r(\omega) = 1 - \frac{\omega_p^2}{\omega^2}$$

Purely electromagnetic waves verify $\nabla \cdot \boldsymbol{E} = 0$, so that equation **(1.11)** becomes:

$$\Delta\boldsymbol{E} + \frac{\omega^2}{c^2}\epsilon_r(\omega)\boldsymbol{E} = \boldsymbol{0} \qquad \textbf{(2.12)}$$

Inserting the plane wave expression for E, $E = E_0 e^{i(\omega t - kr)}$, equation **(2.12)** leads to the **dispersion relation** for electromagnetic waves in a cold, non-collisional plasma:

$$\omega^2 = \omega_p^2 + k^2 c^2 \qquad \textbf{(2.13)}$$

Equation **(2.13)** indicates in particular that the wave vector **k**, which appears in $\boldsymbol{E} = \boldsymbol{E_0} exp(i(\omega t - \boldsymbol{k}.\boldsymbol{r}))$ has an imaginary part if $\omega < \omega_p$. In that case, the **E** field is exponentially damped and therefore the electromagnetic wave cannot propagate in the plasma, it is an evanescent wave. In Fig 2.4 is plotted the dispersion relation in the (k, ω) plane.

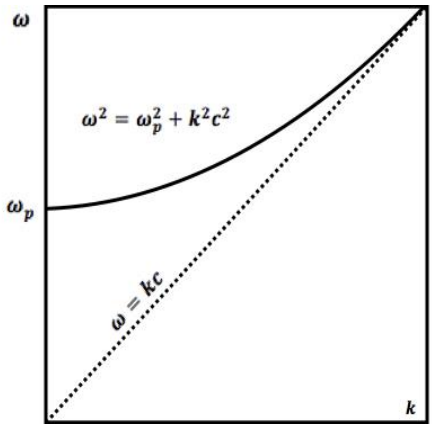

Figure 2.4: Dispersion diagram for electromagnetic waves in a plasma. ω_p appears as the cut-off frequency. Waves of frequency inferior to ω_p cannot propagate in the plasma ***[Rax 05].***

The discussion above indicates that ω_p is the limit between two regimes:

- If $\omega_p > \omega$ the electromagnetic wave cannot propagate, the plasma is said to be **overdense**.
- If $\omega_p < \omega$ the electromagnetic wave can propagate, the plasma is **underdense**.

In this thesis, we only consider the second kind of plasmas and electromagnetic fields. In terms of density, for a fixed electromagnetic wavelength, one has: $\omega_p < \omega \Leftrightarrow n_e < n_c = \frac{\omega^2 m \epsilon_0}{e^2}$. When the electron density is lower than the critical density for the frequency of the electromagnetic wave, then the wave can propagate.

This conclude the preliminary results necessary to derive the theory of wakefield excitation by a drive beam, in a plasma. The linear theory will be presented in details in the following chapter, starting from the conventions and concepts introduced so far.

Chapter 3

Plasma-based accelerators

The plasma-based acceleration schemes LWFA and PWFA can be understood as the combination of three physical phenomena. First is the **excitation of a plasma wave**, which is the accelerating structure of plasma-based accelerators. Second is the **injection** of particles in this accelerating structure. Injected particles can come from the drive particle bunch itself (in PWFA), from electrons of the plasma, or from an externally injected "trailing bunch". And third is the **acceleration** of the injected particles by the accelerating structure. To accurately describe the excitation of plasma waves along the full length of the plasma accelerator, it is also necessary to know how drive beams (laser pulse in LWFA, particle beam in PWFA) **propagate and evolve** while moving through a plasma. We will see as well that depending on the parameters of the drivers, plasma waves can be excited in **two different regimes**, a linear one which has an analytical solution, and a **nonlinear "blow-out"** regime.

Contents

1. Propagation of the driver in a plasma

a. Laser pulses propagation in a plasma

Several processes occur to a laser pulse propagating in a plasma. First is presented a relativistic correction to equation **(2.12)**, significant for very intense drivers. Second is a description of self-focusing and guiding of laser pulses, a phenomenon responsible for the efficient propagation and driving of plasma waves by high power laser pulses. Last, a short paragraph discusses the phase velocity of the plasma wave driven by a laser pulse propagating in a plasma, which will be important in the following.

Relativistic transparency

When a relativistic electromagnetic wave propagates in a plasma, the response of the medium depends on the polarization of the wave. Only in the case of a circularly polarized beam a simple solution exists. We will briefly derive in this section the dispersion relation of a relativistic electromagnetic plane wave with a circular polarization **[Mora 13]**.

Using normalized quantities, in particular $\boldsymbol{a} = e\boldsymbol{A}/mc$ and $\boldsymbol{u} = \boldsymbol{p}/mc$, and using Maxwell-Ampere equation, the Coulomb gauge $\boldsymbol{\nabla}.\boldsymbol{a} = 0$ and the relativistic equation of motion for an electron fluid element, we have:

$$\Delta\boldsymbol{a} - \frac{1}{c^2}\frac{\partial^2}{\partial t^2}\boldsymbol{a} = -e\mu_0\boldsymbol{j}_\perp/mc \qquad \textbf{(3.1)}$$

$$\boldsymbol{u}_\perp = \boldsymbol{a} \qquad \textbf{(3.2)}$$

$$\boldsymbol{j}_\perp = -en_0\boldsymbol{u}_\perp c/\gamma \qquad \textbf{(3.3)}$$

Inserting (3.3) into (3.1) leads to:

$$\left(\frac{\partial^2}{\partial z^2} - \frac{1}{c^2}\frac{\partial^2}{\partial t^2}\right)\boldsymbol{a} = \frac{\omega_p^2}{\gamma c^2}\boldsymbol{a} \qquad \textbf{(3.4)}$$

Inserting the expression of a plane wave $\boldsymbol{a}(\boldsymbol{r},t) = \boldsymbol{a_0}e^{i(\omega t - kr)}$ into (3.4), we obtain:

$$\omega^2 = \frac{\omega_p^2}{\gamma} + k^2c^2 \qquad \textbf{(3.5)}$$

Under the condition $n_0 < \gamma n_c$, the wave vector k is real, which means that the wave can propagate in the plasma. To conclude, in the relativistic regime, the wave can propagate through plasmas of higher densities than the critical density **(2.13)**.

Self-focusing

Due to the perturbation of the refractive index they induce, laser pulses can self-focus when they propagate into plasmas **[Sprangle 92]**. In fact, when the refractive index has a maximum on-axis, the phase front of a laser propagating along the axis bends and self-focuses **[Esarey 97]**. For intense laser pulses, relativistic effects must be taken into account, **[Litvak 69, Sprangle 87]**.

The refractive index can be deduced from $\eta = c/v_\phi$. The phase velocity $v_\phi = \omega/k$ is obtained from equation **(3.5)**. Linearizing v_ϕ and expressing the local plasma frequency (that takes into account the local plasma electron density $n_p = n_0 + \delta n$ instead of n_0) as a function of $\omega_p^2 = n_0e^2/m\epsilon_0$ leads to **[Esarey 96b]**:

$$\eta(\omega) = 1 - \frac{\omega_p^2}{2\omega^2}\left(1 - \frac{a^2}{2} + \frac{\delta n}{n_0}\right) \quad \textbf{(3.6)}$$

The term $\frac{a^2}{2}$ in **(3.6)** is responsible for relativistic optical guiding **[Sprangle 87]** and the term $\frac{\delta n}{n_0}$ is due to the plasma density perturbation induced by the laser pulse in the plasma **[Sun 87]**.

If the laser intensity is peaked on axis, equation **(3.6)** satisfies the requirements of self-focusing. In addition, in that case the paraxial equation of the laser in the plasma takes the form of an equation with a third-order nonlinearity, as in nonlinear optics. Therefore, self-focusing will occur when the power of the laser exceeds a critical power: P_c. **[Sprangle 87]** The theory of relativistic optical guiding provides the result: $P_c[GW] = 17.4(\omega/\omega_p)^2$.

When $P < P_c$, beam diffraction dominates the behavior of the pulse: the laser quickly defocuses. On the contrary, when $P > P_c$, a focusing effect will occur and guided propagation will not be possible neither. Last, when $P = P_c$ optical guiding occurs: in Fig 3.1 (a), (iii) the laser beam radius has an initial "plateau", compared to the case $P < P_c$ (ii). The curve (iv) shows that a preformed plasma channel is extremely interesting as the channel guides the laser over many Rayleigh lengths.

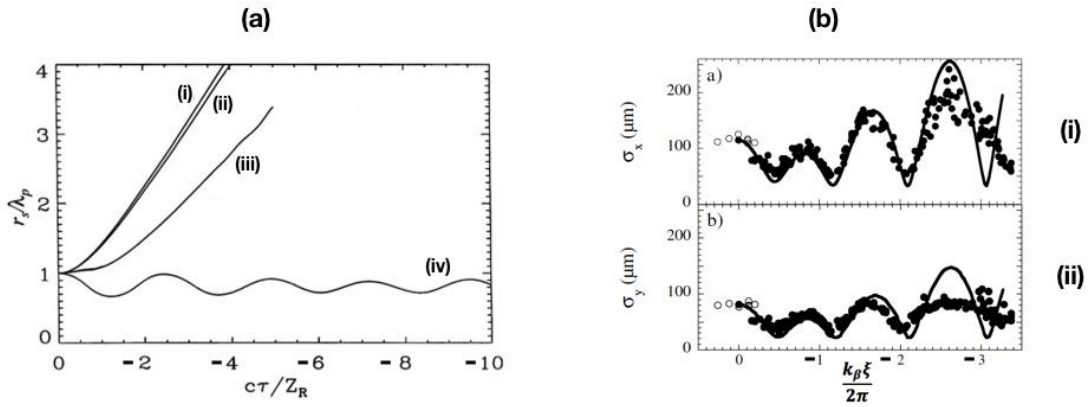

*Figure 3.1: (a) Laser spot size as a function of the normalized propagation distance in the plasma. (i) Vacuum diffraction (ii) $L=\frac{\lambda_p}{4}$ (iii) $L=\frac{\lambda_p}{4}$, $P = P_c$, $a_0 = 0.9$ and $\lambda_p = 0.03$ cm (iv) Guiding in a preformed plasma channel, from **[Sprangle 92, Esarey 09]** (b) Betatron oscillations of the drive beam of an electron driven PWFA experiment. Transverse beam dimensions as a function of the phase advance (i) Beam spot size in the horizontal plane (σ_x) (ii) Beam spot size in the vertical plane (σ_y), from **[Clayton 02]**.*

Phase velocity of the plasma wave

Knowing the phase velocity of a laser-driven plasma wave is of prime importance to discuss how particles can be "trapped" inside the wave and increase their energy by staying in the accelerating E_z field. The dispersion relation **(2.13)** gives access to the group velocity of the laser, and thus to the phase velocity of the plasma wave in the linear regime. One gets for the group velocity: $v_g = \frac{d\omega}{dk} = c\sqrt{1 - \frac{\omega_p^2}{\omega^2}}$. Corrections have to be made to this formula in the case of very strong laser drivers **[Decker 94]**.

b. Electron beam propagation in a gas plasma

When an electron beam propagates into a plasma, several physical phenomena perturb its evolution. Although these processes are far different from the processes occurring to a laser pulse, the experimental observables are quite similar **[Joshi 02]**. An electron beam entering into a plasma expels plasma electrons close to its propagation axis. In turn, the induced charge density in the plasma perturbs the balance between the self-magnetic and self-electric forces of the beam. If $n_b < n_0$, the beam is self-pinched by the self-magnetic force, the focusing is highly nonlinear **[Geraci 00, Humphries 02]**. On the contrary, if $n_b > n_0$ (also called the underdense condition for an electron beam) the beam expels the electrons in its wake creating an ion cavity. This cavity is responsible for beam focusing, the focusing force can be linear in this regime and its effect can be described in more details. Some of the processes are listed below.

Beam focusing

The first effect of the plasma on the beam is a strong focusing due to the cavity transverse force introduced above. Before any description of the exact longitudinal structure of the ion cavity, if plasma electrons are fully expelled, it can be noticed that the transverse force will be linear in r. As said in chapter 2, a linear focusing force does not create any aberration, and does not induce emittance growth.

Betatron oscillations of the beam envelope

In the case evocated above, when a strong focusing happens with a linear force, the beam can undergo several oscillations called Betatron oscillations of the beam envelope. **[Clayton 02]** This process is due to the successive effects of the emittance term and of the linear focusing term that appear in **(1.17)**. When the particles oscillate in the plasma, equation **(1.17)** writes:

$$\sigma_r''(z) + \left[\frac{\omega_p^2}{(2\gamma)c^2} - \frac{{\epsilon_n}^2}{\gamma^2\sigma_r^4(z)}\right]\sigma_r(z) = 0 \qquad \textbf{(3.7)}$$

Where σ_r is the transverse radius of the beam and $k_\beta = \sqrt{\frac{\omega_p^2}{(2\gamma)c^2}}$ is the Betatron wavenumber. The beam is said to be **matched** in the plasma when $\beta = 1/k_\beta = \lambda_\beta/2\pi$ and $\alpha = 0$. If this condition is fulfilled, the beam will propagate along the whole plasma without any evolution of its radius because the focusing force is exactly balanced by the emittance term. The corresponding matched beam radius is:

$$\sigma_r = \left(\frac{\epsilon_n}{\gamma k_\beta}\right)^{\frac{1}{2}} \qquad \textbf{(3.8)}$$

The spatial period of the envelope oscillations is $\lambda_\beta/2$. The beams used in PWFA experiments do not always have a circular symmetry in the transverse plane, therefore their sizes and emittances can differ in transverse directions. Fig. 3.1 (b) illustrates these oscillations.

Electron hosing stability

Going further in the details, we have to discuss the electron hosing instability. For long beams, there is a coupling between the beam electrons and the electrons at the border of the ion cavity **[Whittum 91]**. This coupling leads to growing transverse perturbations of the

beam, a growth that can lead to a transverse breaking of the bunch. The beam centroids of the bunch longitudinal slices will undergo harmonic oscillations due to this coupling. The equations describing the coupling can be numerically solved and describe oscillations whose amplitudes grow quickly.

Some of the phenomena occurring to a bunch of electrons propagating in a plasma were described. A comprehensive description would also include other phenomena such as the individual Betatron oscillations and radiation emission of particles, or the collective refraction of the beam if it encounters a plasma boundary **[Muggli 01, Joshi 03]**. Individual Betatron oscillations will be discussed in further details in Part III as they were an important concept for the hybrid experiment carried out at LOA and reported in this thesis. The description of these other phenomena are not needed to understand the experiment of part II and III.

Regarding positron bunches, the problem of their propagation is more complex and no theoretical model explains the evolution of a positron bunch in a plasma. However, some phenomena have already been identified and described **[Hogan 03]** and will be introduced in Part II of this manuscript.

After the introduction of the phenomena occurring to some drivers when they propagate in a plasma, we can now describe the main concept of this chapter: the driving of plasma waves.

2. Solution of plasma waves in the linear regime

a. Plasma wave excitation

In this section, we wish to derive first a general equation for laser or beam excitation of charge density waves in a plasma. This will be a general introduction to the two schemes studied in the work reported here. The derivation uses the fluid approximation for electrons and assumes immobile ions and a cold plasma. The following notations with be used throughout the manuscript: n_0 is the unperturbed plasma density, $n_p = n_0 + \delta n$ is the perturbed plasma electron density, n_b is the drive particle beam density, q its particle charge (for the PWFA case), and $\boldsymbol{v}$ the velocity of the plasma electron fluid element. The definitions for the electromagnetic potentials read:

$$\boldsymbol{E} = -\nabla V - \frac{\partial \boldsymbol{A}}{\partial t} \quad \textbf{(3.9)}$$

$$\boldsymbol{B} = \nabla \times \boldsymbol{A} \quad \textbf{(3.10)}$$

Coulomb gauge is a convenient gauge choice for plasmas and lasers related problems, which we will use in the following: $\nabla \cdot \boldsymbol{A} = 0$. Furthermore, we will introduce the plasma wave vector $k_p = \frac{\omega_p}{c} = \sqrt{\frac{n_0 e^2}{m\epsilon_0}}.\frac{1}{c}$ and use in this section the normalized scalar and vector potentials $\phi = \frac{eV}{mc^2}$ and $\boldsymbol{a} = \frac{e\boldsymbol{A}}{mc}$ whenever it is possible to normalize and simplify an equation.

When a beam propagates in a plasma, Poisson equation writes:

$$\nabla^2 \phi = -k_p^2 \left(\frac{q}{e}\frac{n_b}{n_0} - \frac{\delta n}{n_0} \right) \quad \textbf{(3.11)}$$

The first term in the right-hand side is the source term due to the particle drive beam. The linearity of equation **(3.10)** allows to define the potential associated to the beam particles only: ϕ_b. In fact, when the beam propagates in free space, Poisson equation is $\nabla^2\phi_b = -\frac{k_p^2}{n_0}\frac{q}{e}n_b$. The remaining term in the right-hand side of **(3.10)** describes the charge density arising from the ion background and the perturbed electron density of the plasma.

We now need to express the motion of an electron fluid element of the plasma. Defining the normalized momentum $\boldsymbol{u} = \frac{\boldsymbol{p}}{mc}$ and replacing **(3.8)** and **(3.9)** into **(2.10)** leads to:

$$\begin{aligned}\frac{\partial \boldsymbol{u}}{\partial t} &= -(\boldsymbol{v}\cdot\nabla_{\boldsymbol{r}})\boldsymbol{u} + \boldsymbol{c\nabla}\phi + \frac{\partial \boldsymbol{a}}{\partial t} - \boldsymbol{v}\times\boldsymbol{\nabla}\times\boldsymbol{a} \\ &= \frac{\partial \boldsymbol{a}}{\partial t} + c\boldsymbol{\nabla}(\phi - \gamma)\end{aligned} \qquad \textbf{(3.12)}$$

It can be shown that if $\boldsymbol{v}\times\boldsymbol{\nabla}\times(\boldsymbol{u}-\boldsymbol{a})$ is initially null, it stays null when the system evolves **[Gorbunov 97].** This remark and the identity $\boldsymbol{c\nabla}\gamma = \frac{c}{\gamma}\boldsymbol{\nabla}\frac{\boldsymbol{u}^2}{\boldsymbol{2}} = (\boldsymbol{v}\cdot\nabla_{\boldsymbol{r}})\boldsymbol{u} + \boldsymbol{v}\times\boldsymbol{\nabla}\times\boldsymbol{u}$ were used to simplify the second line.

The term $c\boldsymbol{\nabla}\phi$ is the electric force due to the charge density of the plasma and of the drive particle beam (PWFA case) and the term $-c\boldsymbol{\nabla}\gamma$ is the relativistic laser ponderomotive force (LWFA case) which pushes the plasma electrons towards the regions of lower γ. The next derivations are performed by **linearizing** these two terms. $a = |\boldsymbol{a}|$ and n_b/n_0 are supposed to be small compared to 1, and the induced perturbation of the electron density $\delta n = n_p - n_0$ is assumed to be small compared to n_0. In particular the LWFA source term can be rewritten: $c\boldsymbol{\nabla}\gamma = \boldsymbol{c\nabla}(a^2/2)$. Under these assumptions, the regime of excitation of plasma waves will be called the **linear regime**.

Linearizing equation (2.9) and taking the time derivative leads to:

$$\frac{\partial^2\delta n}{\partial t^2} + n_0 c\nabla\cdot\left(\frac{\partial \boldsymbol{a}}{\partial t} + c\boldsymbol{\nabla}\left(\phi - \frac{a^2}{2}\right)\right) = 0$$

Coulomb gauge ensures $\nabla\cdot\boldsymbol{a} = 0$, therefore, one gets by replacing ϕ using Poisson equation **(3.10):**

$$\left(\frac{\partial^2}{\partial t^2} + \omega_p^2\right)\frac{\delta n}{n_0} = \omega_p^2\frac{q}{e}\frac{n_b}{n_0} + c^2\nabla^2\frac{a^2}{2} \qquad \textbf{(3.13)}$$

This equation describes the excitation of a plasma wave by a particle beam (first term of the right-hand side) or a laser (second term of the right-hand side), and shows the similarity of the laser-driven (LWFA) and beam-driven (PWFA) schemes in the linear regime.

To help readers imagine how we can excite plasma waves in a real experiment, details of a LWFA experiment are depicted in Fig. 3.2. The laser pulse (orange) of typical transverse dimension $20\ \mu m$ drives a plasma wave in its wake as seen in Fig 3.2 (a). Each bucket has a size of order λ_p (for instance $n_0 = 10^{18} cm^{-3}$ corresponds to $\lambda_p \sim 30\ \mu m$). The wave displayed on picture (a) is magnified compared to image (b), and picture (a) comes from a numerical simulation. LWFA experiments such as the ones carried out at LOA take place as depicted in Fig 3.2 (b): an intense and femtosecond laser pulse is focused into a gas jet.

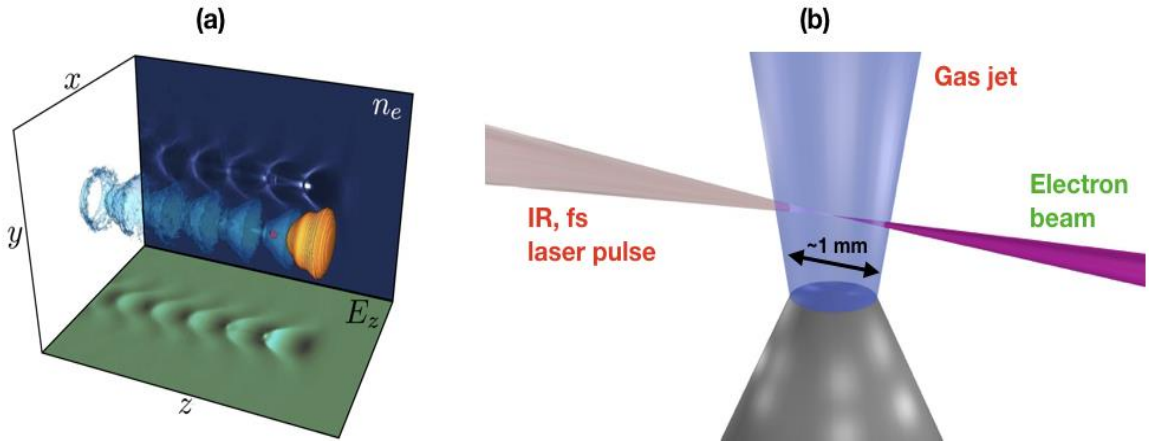

*Figure 3.2: (a) A plasma electron density wave driven by a laser pulse (orange). A bunch of accelerated electrons extracts energy from the accelerating cavity (red) PIC simulation, from **[Réchatin 10]** (b) Details of the LWFA setup of Fig. 0.2 a. The plasma density wave is driven in the gas jet. Each ion cavity has a typical dimension of $\lambda_p \sim 30\ \mu m$ for $n_0 = 10^{18}\ cm^{-3}$.*

b. Beam driven plasma density waves

Equation **(3.12)** relates $\delta n/n_0$ with the source terms for both particle and laser drivers. As we shall see in the next section for laser driven waves, equation **(3.12)** leads directly to an equation over ϕ that can be solved for a Gaussian laser driver and thus the $\boldsymbol{E}$ and $\boldsymbol{B}$ fields can be derived directly in that case. For a particle driver, deriving the electromagnetic fields is more difficult and requires to write and solve directly the equations over $\boldsymbol{E}$ and $\boldsymbol{B}$. This is done in this section, by following the calculation first published by Keinigs and Jones **[Keinigs 86]**.

The outline of the derivation is the following: we write first the equations describing the evolution of the $\boldsymbol{E}$ and $\boldsymbol{B}$ fields. Then we will switch to Fourier space for the longitudinal variable. The Fourier transformed equations can then be solved for a point-like source, which leads to the corresponding Green function solution. Coming back to real space with an inverse Fourier transform, a convolution of the solution for a point-like source with the real drive beam profile will lead to the general solution. This strategy will be applied to the E_z field, to the transverse force $W = E_r - cB_\theta$ and to the electron density in the plasma n_p.

In this section, ρ is the charge density of the problem: $\rho = en_0 - en_p + qn_b = -e\delta n + qn_b$, the velocity of the beam is v_b and there is no laser.

Applying operator ∇ to Poisson equation and operator $\frac{\partial}{\partial t}$ to the Maxwell-Ampere equation written for the vector potential leads to the following two equations:

$$-\Delta(\boldsymbol{\nabla} V) = \frac{\boldsymbol{\nabla}\rho}{\epsilon_0} \qquad \textbf{(3.14)}$$

$$-\Delta \frac{\partial \boldsymbol{A}}{\partial t} = \mu_0 \frac{\partial \boldsymbol{j}}{\partial t} + \frac{1}{c^2}\frac{\partial^2 \boldsymbol{E}}{\partial t^2} \qquad \textbf{(3.15)}$$

The sum of (3.13) and (3.14), along with the relation $\boldsymbol{E} = -\boldsymbol{\nabla} V - \frac{\partial \boldsymbol{A}}{\partial t}$ leads to:

$$\left(\Delta - \frac{1}{c^2}\frac{\partial^2}{\partial t^2}\right)\boldsymbol{E} = \mu_0 \frac{\partial(\boldsymbol{j_b}+\boldsymbol{j_p})}{\partial t} + \frac{\boldsymbol{\nabla}\rho}{\epsilon_0} \quad \textbf{(3.16)}$$

The expression of $\boldsymbol{j} = \boldsymbol{j_b} + \boldsymbol{j_p}$ still contains a component of which $\boldsymbol{E}$ is a parameter: $\boldsymbol{j_p}$. The term $\mu_0 \frac{\partial}{\partial t}(\boldsymbol{j_p})$ can be written explicitly by replacing $\boldsymbol{v}$ from equation **(2.11):**

$$\mu_0 \frac{\partial}{\partial t}(\boldsymbol{j_p}) = \mu_0 \frac{\partial}{\partial t}(-en_0\boldsymbol{v}) = \frac{\mu_0 n_0 e^2}{m}\boldsymbol{E} = \frac{\omega_p^2}{c^2}\boldsymbol{E} \quad \textbf{(3.17)}$$

The equation for $\boldsymbol{E}$ can therefore be rewritten:

$$\left(\Delta - \frac{\omega_p^2}{c^2} - \frac{1}{c^2}\frac{\partial^2}{\partial t^2}\right)\boldsymbol{E} = \mu_0 \frac{\partial \boldsymbol{j_b}}{\partial t} + \frac{\boldsymbol{\nabla}\rho}{\epsilon_0} \quad \textbf{(3.18)}$$

The curl of equation (3.17) along with Maxwell-Faraday equation leads to the equation for $\boldsymbol{B}$:

$$\left(\Delta - \frac{\omega_p^2}{c^2} - \frac{1}{c^2}\frac{\partial^2}{\partial t^2}\right)\boldsymbol{B} = -\mu_0 \boldsymbol{\nabla} \times \boldsymbol{j_b} \quad \textbf{(3.19)}$$

These two equations describe the evolution of the fields in the plasma, the source terms appear on the right. The $\boldsymbol{B}$ field evolution depends only on the drive beam current, in contrast with the electric field $\boldsymbol{E}$ evolution. It means that in the linear regime, the response of the plasma will be purely electrostatic.

An important approximation is needed at that point, we assume now that the fields in the wake only depend on the variable $\xi = v_b t - z$. This assumption is called the "**quasistatic approximation**" and means that the drive beam envelope evolves much slower than plasma electrons move. The change of variables from (t, z) to $\xi = v_b t - z$, leads to the following equations:

$$\left(\Delta_\perp - \frac{\omega_p^2}{c^2} + \frac{1}{\gamma_b^2}\frac{\partial^2}{\partial \xi^2}\right)\boldsymbol{E} = \mu_0 \frac{\partial \boldsymbol{j_b}}{\partial t} + \frac{\boldsymbol{\nabla}\rho}{\epsilon_0} \quad \textbf{(3.20)}$$

$$\left(\Delta_\perp - \frac{\omega_p^2}{c^2} + \frac{1}{\gamma_b^2}\frac{\partial^2}{\partial \xi^2}\right)\boldsymbol{B} = -\mu_0 \boldsymbol{\nabla} \times \boldsymbol{j_b} \quad \textbf{(3.21)}$$

With the assumption of cylindrical symmetry, the right-hand term of equation **(3.19)** can be written:

$$\mu_0 \frac{\partial(\boldsymbol{j_b})}{\partial t} + \frac{\boldsymbol{\nabla}\rho}{\epsilon_0} = \frac{1}{\epsilon_0}\frac{\partial}{\partial \xi}\left(q\left(\left(\frac{v_b}{c}\right)^2 - 1\right)n_b + e\delta n\right)\boldsymbol{u_z} + \frac{1}{\epsilon_0}\frac{\partial}{\partial r}(qn_b - e\delta n)\boldsymbol{u_r} \quad \textbf{(3.22)}$$

Besides the linearization of the equations, we can make another assumption to go further into the demonstration: it can be assumed that $v_b = c$ and therefore, $\gamma_b = \infty$. Under this assumption:

$$(\Delta_\perp - k_p^2)\boldsymbol{E} = \frac{e}{\epsilon_0}\frac{\partial \delta n}{\partial \xi}\boldsymbol{u_z} + \frac{e}{\epsilon_0}\frac{\partial}{\partial r}\left(\frac{q}{e}n_b - \delta n\right)\boldsymbol{u_r} \quad \textbf{(3.23)}$$

$$(\Delta_\perp - k_p^2)\boldsymbol{B} = \frac{q}{c\epsilon_0}\frac{\partial n_b}{\partial r}\,\boldsymbol{u_\theta} \quad \textbf{(3.24)}$$

The limit we just considered here illustrates an important property of relativistic particle beams: before considering the relativistic limit, there was a term containing n_b in the equation for E_z, which disappeared when $v_b \to c$. This means that the $\boldsymbol{E}$ field of a relativistic beam has the shape of a disk, or a pancake, it is purely transversal, and in the case of a cylindrically symmetric beam, it is also cylindrically symmetric.

To solve equations **(3.22)** and **(3.23)**, we now have to switch to Fourier space, and replace the operators according to the rule $\frac{\partial}{\partial \xi} \to -ik\,\cdot$. If ξ is the variable in real space, we consider variable k in Fourier space.

Equations **(3.22)** and **(3.23)** can be written in Fourier space for the components of the fields with cylindrical symmetry:

$$\left(\Delta_\perp - k_p^2\right)\hat{E}_z = -\frac{e}{\epsilon_0} ik\widehat{\delta n} \quad \textbf{(3.25)}$$

$$\left(\Delta_\perp - \frac{1}{r^2} - k_p^2\right)\hat{E}_{\boldsymbol{r}} = \frac{e}{\epsilon_0}\frac{\partial}{\partial r}\left(\frac{q}{e}\hat{n}_b - \widehat{\delta n}\right) \quad \textbf{(3.26)}$$

$$\left(\Delta_\perp - \frac{1}{r^2} - k_p^2\right)\hat{B}_{\boldsymbol{\theta}} = \frac{q}{c\epsilon_0}\frac{\partial \hat{n}_b}{\partial r} \quad \textbf{(3.27)}$$

We need to express the right-hand side of all three equations **(3.25) – (3.27)** using only $\hat{n}_b$, therefore, we express $\widehat{\delta n}$ using equation **(3.12)**:

$$\left(\frac{\partial^2}{\partial \xi^2} + k_p^2\right)\delta n = k_p^2 \frac{q}{e} n_b \to \left(k_p^2 - k^2\right)\widehat{\delta n} = k_p^2 \frac{q}{e}\hat{n}_b$$

Therefore, $\widehat{\delta n}$ can be replaced by $\frac{k_p^2}{k_p^2 - k^2}\frac{q}{e}\hat{n}_b$ in the equations over $\boldsymbol{E}$:

$$\left(\Delta_\perp - k_p^2\right)\hat{E}_z = \frac{q}{\epsilon_0}\frac{ikk_p^2}{k^2 - k_p^2}\hat{n}_b \quad \textbf{(3.28)}$$

$$\left(\Delta_\perp - \frac{1}{r^2} - k_p^2\right)\hat{E}_{\boldsymbol{r}} = \frac{k^2}{k^2 - k_p^2}\frac{q}{\epsilon_0}\frac{\partial \hat{n}_b}{\partial r} \quad \textbf{(3.29)}$$

The equation over B_θ can be replaced by a more interesting one, over the transverse force F_r (divided by the elementary charge here) on the beam, that can be evaluated thanks to the Lorentz force expression:

$$\frac{F_r}{e} = (\boldsymbol{E} + v_b \boldsymbol{u_z} \times \boldsymbol{B}).\boldsymbol{u_r}$$

The source is a beam whose speed is considered in the relativistic limit: $\boldsymbol{v_b} = c\boldsymbol{u_z}$**.** Therefore, the transverse force is:

$$W = \frac{F_r}{e} = E_r - cB_\theta \quad \textbf{(3.30)}$$

Combining the equations for E_r and B_θ, gives:

$$\left(\Delta_\perp - \frac{1}{r^2} - k_p^2\right)\widehat{W} = \frac{k_p^2}{k^2 - k_p^2}\frac{q}{\epsilon_0}\frac{\partial \hat{n}_b}{\partial r} \quad \textbf{(3.31)}$$

We are now going to replace the source term by a point-like source, the solution of the corresponding equation is the Green function of our problem. We will then convolve this solution with the general source profile to reach the general solution of the problem.

The point-like source term written in cylindrical coordinates with azimuthal symmetry, has the following expression:

$$n_b(r,\xi) = \frac{\delta(r - r')}{2\pi r}\delta(\xi) \to \hat{n}_b(r,k) = \frac{\delta(r - r')}{2\pi r}$$

The equations are now:

$$\left(\Delta_\perp - k_p^2\right)\hat{E}_z = \frac{q}{\epsilon_0}\frac{ikk_p^2}{k^2 - k_p^2}\frac{\delta(r - r')}{2\pi r} \quad \textbf{(3.32)}$$

$$\left(\Delta_\perp - \frac{1}{r^2} - k_p^2\right)\widehat{W} = \frac{q}{\epsilon_0}\frac{k_p^2}{k^2-k_p^2}\frac{\partial}{\partial r}\left(\frac{\delta(r-r')}{2\pi r}\right) \quad \textbf{(3.33)}$$

$$\widehat{\delta n} = \frac{q}{e}\frac{k_p^2}{k_p^2-k^2}\frac{\delta(r-r')}{2\pi r} \quad \textbf{(3.34)}$$

Solution for E_z

Following the derivation from **[Jackson 62]**, §3.11, the solution for radial equation **(3.32)** is a linear combination of Bessel modified functions. To keep Jackson's notation, let's denote ψ the solution, combination of I_m and K_m the modified Bessel functions. Two solutions will coexist, ψ_1 that satisfies the boundary conditions for $r < r'$ and ψ_2 that satisfies the boundary conditions for $r > r'$. As demonstrated in **[Appendix 1]**, the Green function is symmetric in r, r', which implies that ψ_1 and ψ_2 can be exchanged. Therefore, the solution of the equation **[Jackson 62]**:

$$\left(\Delta_\perp - k_p^2\right)g_0 = -\frac{4\pi}{r}\delta(r-r') \quad \textbf{(3.35)}$$

is $g_0(r,r') = 4\pi I_0(k_p r_<)K_0(k_p r_>)$, where I_0 and K_0 are Bessel modified functions and the normalization factor 4π is given by the discontinuity of the equation at r' and where $r_< = \min(r,r')$ and $r_> = \max(r,r')$.

Therefore, the most general solution for $\hat{E}_{z,G}$ will be:

$$\hat{E}_{z,G}(k,r) = -\frac{q}{\epsilon_0}\frac{ikk_p^2}{k^2-k_p^2}\frac{1}{2\pi}I_0(k_p r_<)K_0(k_p r_>) \quad \textbf{(3.36)}$$

The inverse Fourier transform of the solution writes:

$$E_{z,G}(r,\xi) = -\frac{q}{\epsilon_0}\frac{I_0(k_p r_<)K_0(k_p r_>)}{2\pi}\, p.v.\int_{-\infty}^{+\infty}\frac{ikk_p^2}{k^2-k_p^2}e^{ik\xi}dk \quad \textbf{(3.37)}$$

The usual method to calculate the integral term uses the Residue theorem, with a well-chosen contour. The contour integral must take into account the two real poles of the function, and have this contour enlarged to the whole complex plane. Our contour γ is depicted in Fig. 3.3 (a). For positive values of ξ, the complex exponential $e^{ik\xi}$ will decay at infinity when $\mathcal{I}(k) > 0$. We therefore choose the contour as depicted in Fig. 3.3 (a).

The poles of $\frac{ik}{k^2-k_p^2}$ are not included in this contour, the integral over the contour is null. $p.v.\int_{-\infty}^{+\infty}\frac{ik}{k^2-k_p^2}e^{ik\xi}dk$ can then be calculated thanks to the Residue Theorem, which writes with the contour of Fig 3.3 (a), for any values of R and ϵ, assuming $\xi > 0$:

$$\oint_\gamma \frac{ik}{k^2-k_p^2}e^{ik\xi}dk = 0$$

Using $I = [-R;\ R]\backslash\left(\left[-k_p-\epsilon;-k_p+\epsilon\right]\cup\left[k_p-\epsilon;k_p+\epsilon\right]\right)$, this integral can be divided into the sum of four terms, whose limits are:

$$\lim_{R\to\infty}\int_0^\pi \frac{\left(iRe^{i\theta}\right)^2}{(Re^{i\theta})^2-k_p^2}e^{-R(\sin(\theta)-i\cos(\theta))\xi}d\theta = 0$$

$$\lim_{\epsilon\to 0}\int_{\pi}^{0}\frac{i\left(\pm k_p+\epsilon e^{i\theta}\right)}{\left(\pm k_p+\epsilon e^{i\theta}\right)^2-k_p^2}e^{i\left(\pm k_p+\epsilon e^{i\theta}\right)\xi}i\epsilon e^{i\theta}d\theta=-i\pi\left[\frac{i}{2}\left(e^{ik_p\xi}+e^{-ik_p\xi}\right)\right]$$

$$\lim_{\epsilon\to 0}\int_{I}\frac{ik}{k^2-k_p^2}e^{ik\xi}dk=p.v.\int_{-\infty}^{+\infty}\frac{ik}{k^2-k_p^2}e^{ik\xi}dk$$

As a result:

$$p.v.\int_{-\infty}^{+\infty}\frac{ik}{k^2-k_p^2}e^{ik\xi}dk=-\pi\cos(k_p\xi)$$

The Green function solution is therefore in real space, with H the Heaviside function:

$$E_{z,G}(r',\xi)=\frac{q}{2\epsilon_0}k_p^2I_0\left(k_pr_<\right)K_0\left(k_pr_>\right)\cos\left(k_p\xi\right)H(\xi) \qquad \textbf{(3.38)}$$

The general solution is the convolution between the solution (3.38) and the real source profile:

$$E_z(r,\xi)=\frac{q}{2\epsilon_0}k_p^2\int_{-\infty}^{\infty}\int_{0}^{\infty}n_b(r',\xi')I_0\left(k_pr_<\right)K_0\left(k_pr_>\right)\cos\left(k_p(\xi-\xi')\right)H(\xi-\xi')r'dr'\,d\xi'$$

If we consider a source profile of the form: $n_b=\frac{N}{(2\pi)^{3/2}\sigma_r^2\sigma_z}e^{-r^2/2\sigma_r^2}e^{-\xi^2/2\sigma_z^2}$, where N is the bunch particle number, σ_r σ_z the transverse and longitudinal extents of the bunch, we obtain:

$$E_z(r,\xi)=\frac{q}{\epsilon_0}k_p^2\frac{N}{2(2\pi)^{\frac{3}{2}}\sigma_r^2\sigma_z}\int_{-\infty}^{\xi}e^{-\frac{\xi'^2}{2\sigma_z^2}}\cos\left(k_p(\xi-\xi')\right)d\xi'\int_{0}^{\infty}e^{-r'^2/2\sigma_r^2}I_0\left(k_pr_<\right)K_0\left(k_pr_>\right)r'dr' \qquad \textbf{(3.39)}$$

The solution **(3.39)** is plotted in Fig. 3.3 (b), in the linear regime, the E_z field in the wakefield appears with the cosines shape. The wave period is given by the plasma wavelength λ_p, we will see in the following that the transverse extent of E_z is larger than the electron density of the plasma.

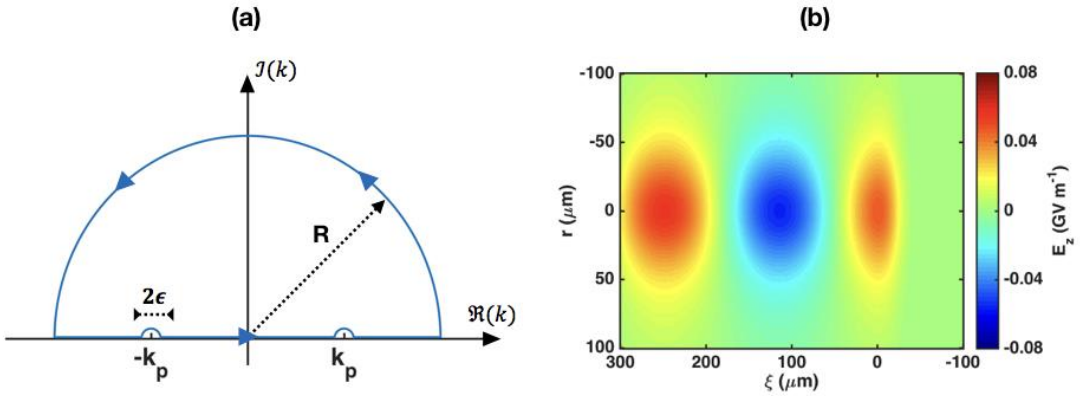

Figure 3.3: (a) Contour γ for the calculation of $p.v.\int_{-\infty}^{+\infty}\frac{ik_p^2}{k^2-k_p^2}e^{ik\xi}dk$. (b) Longitudinal electric field in the wakefield in the linear regime of a positron driven plasma wakefield. Parameters are $n_0=10^{16}cm^{-3}, N=10^8, \sigma_z=15\ \mu m, \sigma_r=20\ \mu m$.

Solution for W:

The equation for W is the following:

$$\frac{1}{r}\frac{\partial}{\partial r}\left(r\frac{\partial}{\partial r}\widehat{W}\right)-\left(\frac{1}{r^2}+k_p^2\right)\widehat{W}\ =\frac{k_p^2}{k^2-k_p^2}\frac{q}{\epsilon_0}\frac{\partial\hat{n}_b}{\partial r} \qquad \textbf{(3.40)}$$

Because of the additional term $\frac{1}{r^2}$, the solution is a combination of Bessel modified functions of first order, I_1 and K_1. The general solution for a point-like source writes **[Jackson 62]**:

$$g_1(r,r_0)=I_1\left(k_p r_<\right)K_1(k_p r_>)$$
$$\widehat{W_G}=-\frac{q}{\epsilon_0}\frac{k_p^2}{k^2-k_p^2}\frac{1}{2\pi}I_1\left(k_p r_<\right)K_1(k_p r_>) \qquad \textbf{(3.41)}$$

where $r_<=\min(r,r')$ and $r_>=\max(r,r')$.

To calculate the inverse Fourier transform, we should consider the same contour as for E_z, and we obtain the following expression:

$$W_G=-\frac{q}{\epsilon_0}\frac{1}{2\pi}k_p^2 I_1\left(k_p r_<\right)K_1\left(k_p r_>\right)\ p.v.\int_{-\infty}^{+\infty}\frac{e^{ik\xi}}{k^2-k_p^2}dk$$

The complex integral is:

$$p.v.\int_{-\infty}^{+\infty}\frac{e^{ik\xi}}{k^2-k_p^2}dk\ =-\frac{\pi}{k_p}\sin(k_p\xi)$$

The solution yields in real space, with H the Heaviside function:

$$W_G=\frac{q}{2\epsilon_0}k_p I_1\left(k_p r_<\right)K_1(k_p r_>)\sin(k_p\xi)H(\xi) \qquad \textbf{(3.42)}$$

The convolution formula for W_G and the whole source distribution is the following:

$$W(r,\xi)=-\frac{q}{2\epsilon_0}k_p\int_{-\infty}^{\xi}\int_0^{\infty}\frac{\partial n_b}{\partial r}(r',\xi')I_1\left(k_p r_<\right)K_1\left(k_p r_>\right)\sin\left(k_p(\xi-\xi')\right)r'dr'\,d\xi'$$

which is a more explicit formula for W. Replacing the source profile we chose to consider, $n_b=\frac{N}{(2\pi)^{3/2}\sigma_r^2\sigma_z}e^{-r^2/2\sigma_r^2}e^{-\xi^2/2\sigma_z^2}$, the previous equation writes:

$$W(r,\xi)=\frac{q}{\epsilon_0}k_p\frac{N}{4(2\pi)^{\frac{3}{2}}\sigma_r^4\sigma_z}\int_{-\infty}^{\xi}e^{-\frac{\xi'^2}{2\sigma_z^2}}\sin\left(k_p(\xi-\xi')\right)d\xi'$$
$$\int_0^{\infty}r'^2e^{-r'^2/2\sigma_r^2}I_1\left(k_p r_<\right)K_1\left(k_p r_>\right)dr' \qquad \textbf{(3.43)}$$

W is plotted in Fig. 3.4 (a), the force has a symmetry with respect to the propagation axis z. The integral term in formula **(3.43)** different from the integral in **(3.39)** explains the sign difference on each side of the axis. The sinusoidal shape is visible, the wakefield has alternative focusing and defocusing region for the accelerated particles.

Solution for δn:

The derivation for the plasma electron density is more direct, from equation (3.34):

$$\widehat{\delta n}(r,k)=\frac{k_p^2}{k_p^2-k^2}\frac{q}{e}\hat{n}_b \qquad \textbf{(3.44)}$$

$$\delta n_G(r,\xi) = -\frac{q}{e}\frac{1}{2\pi}k_p^2\, p.v.\int_{-\infty}^{+\infty}\frac{e^{ik\xi}}{k^2-k_p^2}dk$$

The same calculation, with the same contour as performed for E_z and W leads to:

$$p.v.\int_{-\infty}^{+\infty}\frac{e^{ik\xi}}{k^2-k_p^2}dk = -\frac{\pi}{k_p}\sin(k_p\xi)$$

Therefore, the solution for a point-like (in ξ) source writes, with H the Heaviside function:

$$\delta n_G(r,\xi,\xi') = \frac{q}{2e}k_p\sin\left(k_p\xi\right)H(\xi) \qquad \textbf{(3.45)}$$

Replacing the source distribution profile $n_b = \frac{1}{(2\pi)^{3/2}\sigma_r^2\sigma_z}e^{-r^2/2\sigma_r^2}e^{-\xi^2/2\sigma_z^2}$ and convolving the Green function with the source profile:

$$\delta n(r,\xi) = \frac{q}{e}k_p\frac{Ne^{-\frac{r^2}{2\sigma_r^2}}}{2(2\pi)^{3/2}\sigma_r^2\sigma_z}\int_{-\infty}^{+\infty}\mathrm{e}^{-\frac{\xi'^2}{2\sigma_z^2}}\sin\left(k_p(\xi-\xi')\right)H(\xi-\xi')d\xi'$$

$$\delta n(r,\xi) = \frac{q}{e}k_p\frac{Ne^{-\frac{r^2}{2\sigma_r^2}}}{2(2\pi)^{3/2}\sigma_r^2\sigma_z}\int_{-\infty}^{\xi}\mathrm{e}^{-\frac{\xi'^2}{2\sigma_z^2}}\sin\left(k_p(\xi-\xi')\right)d\xi' \qquad \textbf{(3.46)}$$

Formula **(3.46)** is the plasma electron density, displayed in Fig. 3.4 (b). The radial extent of the density perturbation is more limited than the extent of the E_z field. The E_z field also lags the density perturbation by a quarter period, or a 90° phase.

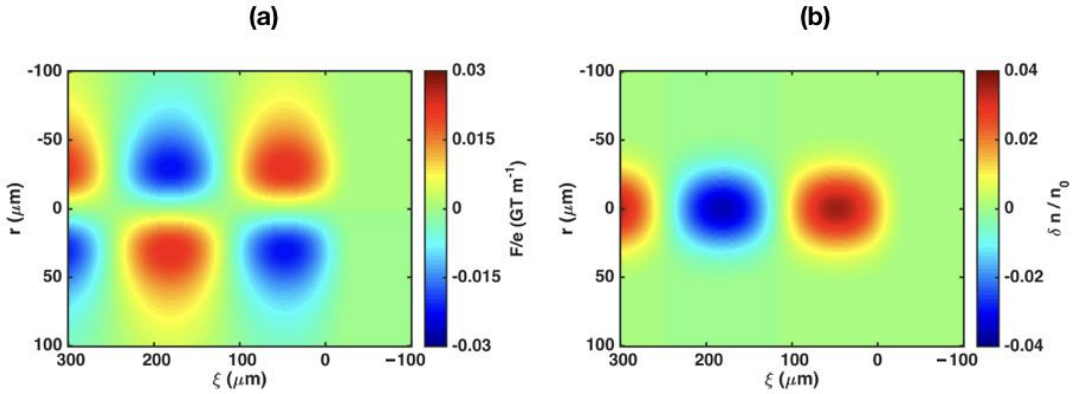

Figure 3.4: (a) Transverse force in the wakefield in the linear regime of plasma wakefield generation. (b) Plasma electron density perturbation in the linear regime of plasma wakefield generation. Parameters are $n_0 = 10^{16}cm^{-3}, N = 10^8, \sigma_z = 15\ \mu m, \sigma_r = 20\ \mu m$.

c. Laser driven plasma electron density waves

Laser driven linear wakefields have been studied through many articles and thesis reports **[Glinec 06, Rechatin 10, Corde 12, Lehe 14]**. The calculation of the fields is simpler in the case of LWFA. In fact, the equation over ϕ, **(3.48)** is straightforward to reach from the equation over δn **(3.13)**. For a Gaussian laser pulse (and a Gaussian source term $c^2\nabla^2\frac{a^2}{2}$), it is possible to solve the equation over ϕ directly. From the explicit formula of ϕ, the fields can be obtained easily. In this section, the results are recalled briefly.

Combining equation **(3.10)** and **(3.12)** with $n_b = 0$ leads to:

$$\left(\frac{\partial^2}{\partial t^2} + \omega_p^2\right)\phi = \omega_p^2 \frac{\boldsymbol{a^2}}{2} \quad \textbf{(3.47)}$$

For a Gaussian shaped pulse, $\boldsymbol{a} = \Re\left(\boldsymbol{a_0} e^{-\frac{r^2}{w_0}} e^{-\frac{\xi^2}{l^2}} e^{-i(\omega t - kz)}\right)$ with $l = \frac{c\tau_0}{\sqrt{2\ln(2)}}$, where τ_0 is the FWHM duration of the Gaussian laser pulse. After averaging the source term over a laser period, one obtains for ϕ when $\xi \gg c\tau_0$:

$$\phi(r,\xi) = -\frac{k_p}{4}\int_{-\infty}^{+\infty} \boldsymbol{a}^2 \sin\left(k_p(\xi - \xi')\right) d\xi'$$

$$\phi(r,\xi) = -\frac{k_p}{4}\int_{-\infty}^{+\infty} \boldsymbol{a}^2 \left(\cos(k_p\xi')\sin(k_p\xi) + \cos(k_p\xi)\sin(k_p\xi')\right) d\xi'$$

$$\phi(r,\xi) = -a_0^2 \frac{k_p}{4} e^{-\frac{2r^2}{w_0^2}} \int_{-\infty}^{+\infty} e^{-\frac{\xi'^2}{l^2}} \cos(k_p\xi')\sin(k_p\xi)\, d\xi' \quad \textbf{(3.48)}$$

as the integral of the term containing $sin(k_p\xi')$ is null. The result is:

$$\phi(r,\xi) = -\sqrt{\pi} a_0^2 \frac{k_p l}{4} e^{-\frac{2r^2}{w_0^2}} e^{-\frac{k_p^2 l^2}{4}} \sin(k_p\xi)$$

Therefore, Poisson equation **(3.10)** leads to the density in the wake of the laser pulse:

$$\frac{\delta n}{n_0} = -\sqrt{\pi} a_0^2 \frac{k_p l}{4} e^{-\frac{k_p^2 l^2}{4}} e^{-\frac{2r^2}{w_0^2}} \sin(k_p\xi) \quad \textbf{(3.49)}$$

One gets also the E_z and E_r fields after the laser pulse thanks to the electrostatic potential:

$$E_z = -\frac{\partial\left(\frac{mc^2\phi}{e}\right)}{\partial\xi} = \frac{mc\omega_p}{e}\left(\sqrt{\pi} a_0^2 \frac{k_p l}{4}\right) e^{-\frac{k_p^2 l^2}{4}} e^{-\frac{2r^2}{w_0^2}} \cos(k_p\xi) \quad \textbf{(3.50)}$$

$$E_r = -\frac{\partial\left(\frac{mc^2\phi}{e}\right)}{\partial r} = -\frac{mc\omega_p}{e}\left(\sqrt{\pi} a_0^2 \frac{l\, r}{w_0^2}\right) e^{-\frac{k_p^2 l^2}{4}} e^{-\frac{2r^2}{w_0^2}} \sin(k_p\xi) \quad \textbf{(3.51)}$$

The density perturbation, as the electrostatic potential depends on ξ as $\propto \sin(k_p\xi)$.

In many experiments, the drive beams are very strong and the wakefield regime is not linear anymore, the description above does not hold anymore, the regime is nonlinear. Furthermore, the nonlinear regime of wakefield acceleration has interesting properties for the applications of particle beams.

3. One-dimensional solution of plasma waves in the nonlinear regime

The relativistic nonlinear theory of laser driven plasma waves can be solved analytically in one dimension **[Akhiezer 56, Dawson 59]**.

Regarding **laser driven waves**, from the general equation of motion in the relativistic case (3.4), in the quasi-static approximation, we can reach the following equation for ϕ, with $\beta_p = \frac{v_p}{c}$, $\gamma_p = \left(1-\beta_p^2\right)^{-\frac{1}{2}}$ and v_p the phase velocity of the plasma wave:

$$\frac{\partial^2\phi}{\partial\xi^2} = k_p^2\left\{\gamma_p^2\left[\beta_p\left(1-\frac{1+<a^2>}{\gamma_p^2(1+\phi)^2}\right)^{-\frac{1}{2}}-1\right]\right\} \cong \frac{k_p^2}{2}\left[\frac{1+<a^2>}{(1+\phi)^2}-1\right] \qquad \textbf{(3.52)}$$

In this specific one-dimensional case, equation **(3.52)** has been extensively studied **[Dalla 93, Dalla 94, Teychenné 94]**. The solution for the potential, the corresponding longitudinal field E_z and the density perturbation $\frac{\delta n}{n_0}$ are plotted in Fig. 3.5 (a). The shape of the longitudinal electric field is not sinusoidal anymore, but it has a saw tooth typical shape, with steep gradients. Its plasma wavelength, λ_{NL} depends on the intensity of the driver. The plasma electron density profile has peaks of high amplitude at the points where the electric field sign changes. At these very points, plasma electrons have velocities close to the plasma wave velocity, and therefore they stay in these regions for a long time. This behaviour is in clear contrast with the behaviour of electrons in the regions where $\frac{\delta n}{n_0}$ is minimal whose velocities are close to $-v_p$.

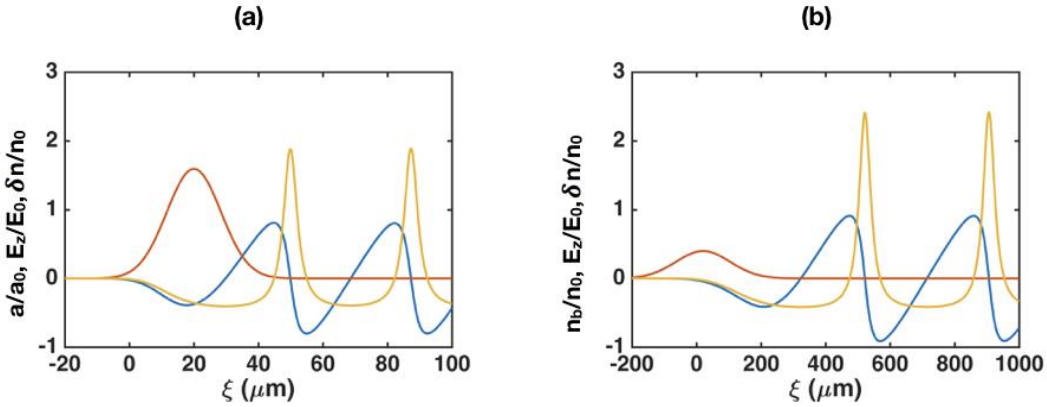

Figure 3.5: (a) Laser driven nonlinear plasma density wave. (red) Laser field (a/a_0), (blue) longitudinal electric field on axis (E_z/E_0), (yellow) plasma electron density n_p/n_0 $(a_0 = 2)$. (b) Electron beam driven nonlinear density wave. (red) Beam Current n_b/n_0 (blue) E_z/E_0 field on axis, (yellow) plasma electron density n_p/n_0. $(n_0 = 10^{16} cm^{-3})$.

Regarding **beam driven waves**, in the linear regime, formulas **(3.39)**, **(3.43)** and **(3.46)** are identical for positrons and electrons. In fact, the charge of the drive beam particles in each of the explicit formulas for n_p, W and E_z only appears as a pre-factor. In both electron and positron driven wakefields, the beam gives an initial kick to plasma electrons either by pulling or pushing them. In addition, the initial displacement is quite weak. When the beam density increases, the excited waves will not be described by the linear model and the formulas above will not hold any more. The difference in the interaction for positrons and electrons leads to very non-symmetrical behaviours of plasma electrons.

In electron driven nonlinear waves, a one-dimensional model provides an equation over β, the speed of the plasma electrons, first derived in 1959 **[Akhiezer 59]**:

$$n_p = \frac{n_0}{1-\beta} \tag{3.53}$$

$$\frac{d^2}{d\xi^2}\left(\sqrt{\frac{1-\beta}{1+\beta}}\right) = \omega_p^2\left(\frac{\beta}{1-\beta} + \frac{n_b}{n_0}\right) \tag{3.54}$$

Written here for simplicity under the hypothesis that the drive beam velocity is the speed of light. The derivation of equations (3.53) and (3.54) relies on the Maxwell-Vlasov system **[Noble 83, Rosenzweig 87a, Rosenzweig 87b]**.

Equation **(3.54)** can be expressed with the normalized potential **[Krall 91]**:

$$\frac{\partial^2\phi}{\partial\xi^2} = \frac{k_p^2}{2}\left[\frac{2n_b}{n_0} + \frac{1}{(1+\phi)^2} - 1\right] \tag{3.55}$$

(3.55) is the equation of generation of a one-dimensional nonlinear wakefield in a cold plasma by a non-evolving beam. It is easy to solve numerically equation **(3.55)** and compare the solution to the one of **(3.52)**. In Fig. 3.5 (b) the solution for an electron driver is displayed. The wakefield has the same properties as the laser driven one.

A qualitative description of plasma electron motion in three-dimensional waves for positron driven wakes will be given in Part II. The next section is dedicated to the model of plasma electron motion in three-dimensional laser or electron beam driven waves.

4. Nonlinear "Blow-out" regime

a. The Bubble regime

A model exists to predict the behaviour of three-dimensional plasma waves driven by an extremely intense laser or an electron driver. With increasing laser power available in the laser facilities around the world and high electron beam density in conventional accelerators, the nonlinear regime of wakefield acceleration, $a_0 \gg 1$, or $n_b \gg n_0$ became experimentally achievable. Drive beams do not just create small perturbations of the density but rather expel electrons out of a cavity (Fig. 3.6 (a) and (b)) in the plasma in this regime: this is the "blow-out" **[Sun 87, Pukhov 02]**.

The nonlinear "blow-out" regime is all the more interesting that from 2006 on, a phenomenological model provides several useful scalings of the characteristics of the accelerating cavity with the drive beam and plasma parameters. It is the first comprehensive three-dimensional theory of nonlinear plasma waves **[Lu 06a, Lu 06b]**.

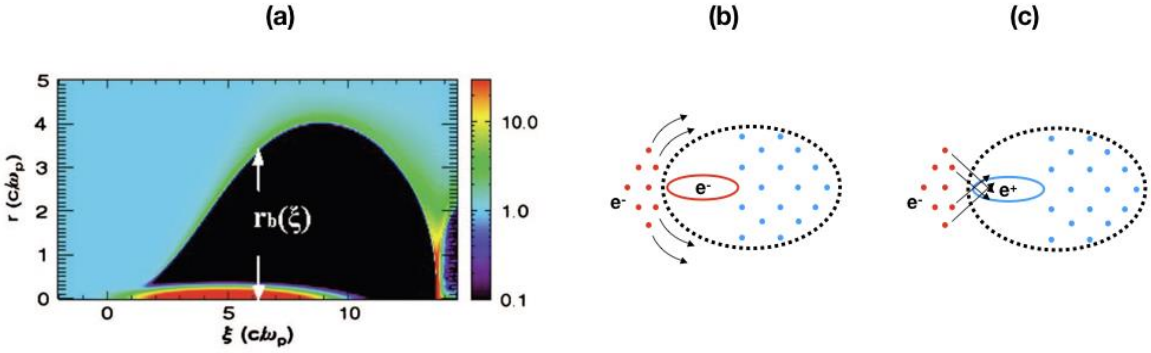

Figure 3.6: (a) Bubble half-cavity. The drive (red) clears all plasma electron from the bubble (black), a thin sheath of electrons circulates around the cavity (green) and crosses on the axis at the back of the bubble. Propagation to the left, from ***[Lu 06b]****. (b) Behavior of plasma electrons in the case of an electron driver: "blow-out" regime. (c) Behavior of plasma electrons in the case of a positron drive: "suck-in" regime* ***[Hogan 03]****.*

As said in the first paragraph, the model assumes that for very intense drive beams, all background electrons within a blow-out radius are totally expelled outward from the axis. These electrons then form a dense sheath surrounding an ion cavity, before crossing the axis and closing the cavity (see Fig 3.6 (a)). Beyond this sheath is a linear response region.

In addition, the "bubble model" predicts that when using an intense laser pulse as the driver, with a size matched to the condition $k_p w_0 = 2\sqrt{a_0}$, the cavity takes a quasi-spherical shape. This spherical shape gave to the model its name "bubble model". In fact, the model provides an ellipse equation for the shape of the cavity. It is then possible to retrieve from this equation an order of magnitude for the cavity length: $L \approx \sqrt{1 + \frac{\beta}{2k_S}} r_m$. The model also shows that this condition is the requirement for a stable optical guiding of the laser. Fulfilling this condition ensures therefore that acceleration can occur over a significant distance. Furthermore, the model provides also an approximate solution for the slope of the field E_z in the cavity $\frac{dE_z}{d\xi} \approx -\frac{1}{2}$.

Inside the cavity, there is a transverse focusing force for electrons due to the background ions, that scales as $F_\perp \propto -r$, r being the distance to the axis. The focusing force is purely linear in r and should not introduce abberations in principle, and thus should not lead to emittance growth.

b. Wavebreaking limit

It appears that the coherent motion of electrons in a plasma wave is limited, and the determination of this limit is of prime importance to physicists. It is important especially when it comes to applications of plasma based accelerators to high energy physics, for which a limitation in accelerating gradients is a major drawback.

When the amplitude of a plasma wave becomes higher than a limiting value, coherent motion of plasma electrons disappears. If some particle trajectories have a too high amplitude, they

may cross other particles trajectories. This is the situation when **wavebreaking** takes place. In 1D for instance, if plasma particles displacement occurs along axis Oz, wavebreaking means that plasma particles do not stay ordered along Oz as they were before the perturbation reaches them. The limit corresponds as well to the limit of the fluid approximation: when wavebreaking occurs, some plasma electrons share the same position but have different velocities.

The model derived here is a simple one-dimensional model **[Mori 90]**, and considers a cold plasma in the fluid approximation.

Starting with the case of a wave with a non-relativistic phase velocity, we consider the particle conservation equation, in one dimension. The change of variables $z(z_0,\tau) = z_0 + \zeta(z_0,\tau)$ and $t = \tau$, ζ being the fluid particle displacement from the initial position z_0, leads to:

$$\frac{\partial n_p}{\partial t} + \frac{\partial}{\partial z}\left(n_p v\right) = 0 \Longrightarrow \frac{\partial}{\partial \tau}\left(n_p\left(1 + \frac{\partial \zeta}{\partial z_0}\right)\right) = 0 \qquad \textbf{(3.56)}$$

$$n_p = \frac{n_0}{\left(1+\frac{\partial \zeta}{\partial z_0}\right)} \qquad \textbf{(3.57)}$$

Following the derivation from Ref. **[Mora 13]**, the density must stay positive and finite: this condition writes $\frac{\partial \zeta}{\partial z_0} > -1$. To obtain the expression of E we have to find a relation between ζ and E, using Maxwell-Gauss equation and equation (3.57):

$$\nabla \cdot E = -\frac{e\left(n_p - n_0\right)}{\epsilon_0} \Longrightarrow \frac{\partial E}{\partial z_0}\frac{1}{\left(1+\frac{\partial \zeta}{\partial z_0}\right)} = \frac{e}{\epsilon_0}\frac{n_0 \frac{\partial \zeta}{\partial z_0}}{\left(1+\frac{\partial \zeta}{\partial z_0}\right)} \qquad \textbf{(3.58)}$$

Which leads to the very simple relation: $E = \frac{e n_0 \zeta}{\epsilon_0}$. On the other hand, the change of variable turns Euler equation to:

$$\frac{\partial^2}{\partial \tau^2}\zeta = -\frac{e}{m}E = -\omega_p^2 \zeta \qquad \textbf{(3.59)}$$

Therefore, solutions for ζ and E are of the form: $\zeta = \zeta_0 \sin(\omega_p \tau - k z_0)$ and $E = E_0 \sin(\omega_p \tau - k z_0)$, the condition $\frac{\partial \zeta}{\partial z_0} > -1$ leads to $E_0 = \frac{e n_0 \zeta_0}{\epsilon_0} = \frac{m v_\phi \omega_p}{e}$, with $v_\phi = \frac{\omega_p}{k}$ the phase velocity of the wave.

The parameter $E_0 = \frac{m v_\phi \omega_p}{e}$ is the **non-relativistic wavebreaking limit**. It must be pointed out that wavebreaking occurs when there is no unique correspondence between the Lagrangian and Eulerian coordinates.

Replacing v_ϕ by c in E_0 gives a convenient order of magnitude of the accelerating gradient in a plasma wakefield. It appeared in formulas **(3.50)** and **(3.51)** for the field values in the linear regime of LWFA. Some of the plots of the fields in this thesis are normalized to $\frac{mc\omega_p}{e}$. In practical units, $\frac{mc\omega_p}{e}[V/m] = 96\, n_0^{1/2}[cm^{-3}]$ **[Dawson 59, Mori 90, Esarey 95]**. For a plasma with an electron density of $n_0 = 10^{17} cm^{-3}$, one gets $\frac{mc\omega_p}{e} = 30\ GV/m$ which is still two to three orders of magnitudes higher than the fields in conventional accelerators.

However, the phase velocity of the waves can become relativistic. A correction must be applied to the wavebreaking limitation of the electric field **[Mori 90]**. The maximum value for E in that case writes: $E_{0,r} = \frac{\omega_p mc}{e}\sqrt{2}\left(\gamma_\phi - 1\right)^{\frac{1}{2}}$, where γ_ϕ is defined with the phase velocity $\gamma_\phi = \left(1 - \left(\frac{v_\phi}{c}\right)^2\right)^{-1/2}$. This is the relativistic cold plasma wavebreaking limit. As said in the derivation for the non-relativistic case, when the plasma density wave is driven to an amplitude larger than this limit, the speed of the electrons can outrun the phase velocity of the wave and therefore a longitudinal crossing occurs, that is wavebreaking occurs.

Experimental physicists in plasma based acceleration rely on the theory presented in this chapter: beam propagation in a plasma, plasma wave excitation by a drive beam and acceleration regimes are key concepts. The experiment discussed in the next part takes place in this theoretical context. This experiment relied on a positron driven wakefield to accelerate particles from a second, distinct bunch of positrons.

Part II

Chapter 4

Plasma wakefield acceleration of positrons

The core experiment of my thesis is the first demonstration of the acceleration of a distinct bunch of positrons in a plasma wakefield accelerator. Part II will be dedicated to the presentation of the experiment and of its results. This chapter is dedicated to a more comprehensive introduction of **positron driven nonlinear plasma waves** as the experiment was accomplished, for technical reasons, with a positron driver instead of an electron or laser one. A presentation of the state of the art **experiments regarding positron acceleration** is given in the second section, followed by a **presentation of the SLAC and FACET** facilities and of their beam parameters.

Contents

1. Positron driven plasma wakefield

We evoked briefly in Part I the difference between positron and electron driven plasma wakefield, in the nonlinear regime. This difference was illustrated in Fig. 3.6 (b) and (c). Positron drive bunches pull plasma electrons inward instead of pushing them outward. The phenomenon is called the "suck-in regime" **[Lee 01].**

We focus now only on positron drivers. When the initial kick due to the driver is weak, then plasma electrons oscillate with a small amplitude around their initial positions. This is the linear regime of positron driven wakefields. The positron driven wakefield in this regime has the same analytic solution as the electron driven linear plasma wakefield. When the positron driver density increases, the force on plasma electrons becomes accordingly stronger, the motion induced to the electrons can cause them to reach and cross the axis as seen in Fig. 3.6 (c). This major difference has consequences on the wakefield that explain the difficulty to use positron driven nonlinear wakefield for plasma-based particle acceleration.

First, electrons from different initial radii cross the axis at different times, the on-axis compression is not optimal **[Lee 01, Sahai 15]**. This is due first to the different distances between the sucked-in electrons and the driver and second to the force each ring of electrons faces that decreases with the distance from the ring to the axis. Consequently, the compression area where electrons are densely pulled around the axis is not optimally localized. As a result, the wakefield is accordingly weaker: accelerating fields in a positron driven wakefield are weaker.

Second, in the wake of the driver, when plasma electrons undergo radial oscillations, accelerator cavities are formed. In the first cavity for instance, the focusing and accelerating region for positrons is very limited. For each period of the wave, this region lies at the back of the cavity. In fact, plasma electrons are being focused to the axis over a larger length as explained in the above paragraph. However, in the area where they are not being focused, there are unshielded background ions whose fields are defocusing for positrons **[Sahai 15]**. In Fig. 4.1 is drawn a positron driven nonlinear wakefield, with the focusing area for positrons highlighted. It is therefore very challenging to use a positron driven wave to efficiently accelerate an externally injected bunch of positrons.

In addition to these difficulties, it must be added that the process of creating a positron bunch,

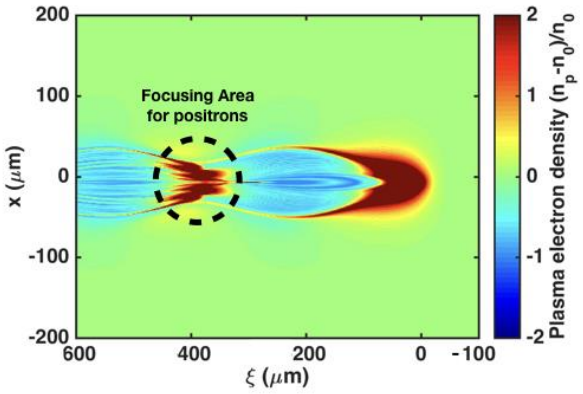

Figure 4.1: Plasma electron density in a positron wakefield from a PIC simulation. The code QuickPIC was used, with $n_0 = 10^{16}\ cm^{-3}$*, and a drive bunch of charge* $Q_{drive} = 480\ pC$ *and dimensions* $(\sigma_x, \sigma_y, \sigma_z) = (35\ \mu m, 25\ \mu m, 30\ \mu m)$*. The focusing and accelerating area is very limited, by contrast, the large blue area is very defocusing for positrons.*

detailed in section 3 is not energetically efficient compared to a laser pulse or an electron bunch. This is an important drawback to the use of positron driven waves in plasma wakefield experiments compared to laser or electron beam driven ones.

PWFA technology can be applied to colliders either as an "energy booster" to a conventional collider (also called "afterburner") or as a multi-staged PWFA accelerator **[Lee 02]** for an all-plasma collider. To stage plasma accelerator sections, synchronization between a drive and an externally produced beam is necessary. This is still a major challenge for the scientific community. Up to now, as it is accomplished in the experiment described in this chapter, for technical reasons the drive and the trailing bunch come from the same initial bunch that is reshaped.

2. Positron acceleration experiments

As said in the previous section, the acceleration of positrons is a crucial result for future plasma-based e^+/e^- colliders. However, plasma-based positron acceleration lags far behind electron acceleration **[Downer 14]** for the reasons listed above. Some experiments were already performed to study either acceleration in a positron driven wakefield itself or physical phenomena occurring to the positron drive bunch when it propagates in a plasma.

Regarding propagation and transverse forces acting on a positron bunch traversing a plasma, an experiment reported in 2003 **[Hogan 03]** studied the focusing effect of a $1.4\,m$-long plasma on a long positron beam ($\sigma_z = 3\,mm$), whose density was higher than the plasma electron density. The transverse effects of a positron wakefield can be more complicated due first to the incoherent convergence of plasma electrons toward the axis described in section 1. Furthermore, the transverse force is also impacted by the large quantity of surrounding electrons converging as opposed to the limited number of background ions inside the volume blown-out by an electron drive beam. The authors of this work showed a focusing of the tail of the beam (Fig. 4.2 (a)) and a clear dependence on the plasma density and identified an optimal density value.

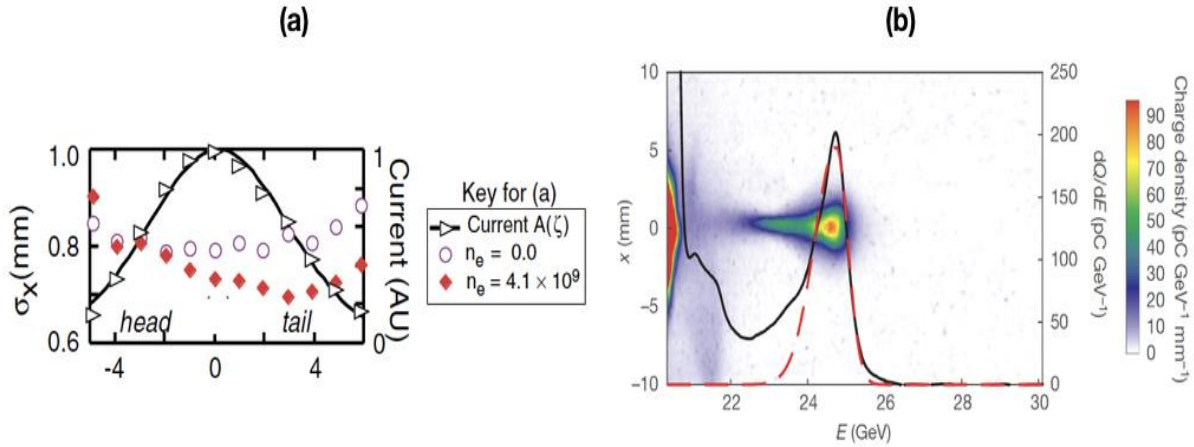

*Figure 4.2: (a) Transverse size in x of the bunch after the plasma. Red squares are with plasma, white circles are without plasma. A strong focusing of the tail occurs. From **[Hogan 03]**. (b) Accelerated positron bunch in a self-loaded positron PWFA experiment. From **[Corde 15]**.*

The first experimental demonstration of positron acceleration was accomplished concomitantly, and also at SLAC **[Blue 03]**. The experiment relied on a 1.5 mm-long positron bunch, in a 1.40 m −long plasma of density 2 10^{14} cm^{-3}. The authors showed a reasonable agreement between theory and experiment, proving that the front of the drive bunch deposits energy in the plasma while the positrons at the back of the bunch gain energy. The spectrum of the outgoing bunch is continuous in this experiment, with a maximal energy gain of about 85 MeV and an energy loss of 70 MeV, for an initial energy spread of 20 MeV. As concluded by the authors, this precursor work on acceleration opens prospects towards either a multiple plasma accelerator stages device or an extremely high gradient single stage also known as "afterburner" or "energy booster".

In the context of creating an "afterburner", positron driven waves can be used to increase the energy of some particles from the drive beam itself. However, in such a scheme, it is necessary to preserve emittance of the initial beam when accelerating some of its particles. The transverse force of a positron driven wakefield are not linear in r, and are dependent on the longitudinal coordinate ξ **[Lee 01]**. An experiment of 2008, accomplished at SLAC **[Muggli 08]** studied the consequences of the nonlinearity of the transverse forces on the emittance of a 700 μm-long beam in a plasma with a 5 $10^{14} cm^{-3}$ electron density. They observed an accumulation of accelerated positrons on a ring surrounding the axis during the acceleration, and an increase of the emittance of the beam during the interaction with the plasma.

More recently, an experimental result published in Nature **[Corde 15]**, demonstrated very high acceleration gradients for positrons, in a self-loaded plasma wakefield. Using a 1.4 10^{10} particles in the initial positron bunch and a plasma of density 8 10^{16} cm^{-3}, the authors demonstrated the acceleration of some positrons coming from the back of the bunch, forming an accelerated bunch with good properties as can be seen in Fig. 4.2 (b). The accelerated bunch had an energy spread of around 2%, a charge in the range $100 - 200$ pC, and an energy gain ranging from 3 GeV to 10 GeV. Such good properties were due to a phenomenon the authors identified through the comparison with numerical simulations: a longitudinal and transverse beam loading. Longitudinal beam loading is described in detail in the next chapter of the manuscript. This self-loaded scheme demonstrated the feasibility of an "energy booster" using positrons, with very high accelerating gradients.

3. SLAC and FACET Facilities

a. Accelerator facility

The PWFA experiments described in this chapter took place at SLAC National Accelerator Laboratory. The main SLAC accelerator is a linear radiofrequency accelerator located in Menlo Park, California. It operated for the first time in 1966. In 1972, an extension, SPEAR, opened. The new project consisted in the building of two storage rings, that were used to collide electrons and positrons of 3 GeV and to produce X-ray beams. A platform called Stanford Synchrotron Radiation Lightsource started in 1973. This platform was using the synchrotron radiation emitted by the particles moving in the rings for molecular imaging.

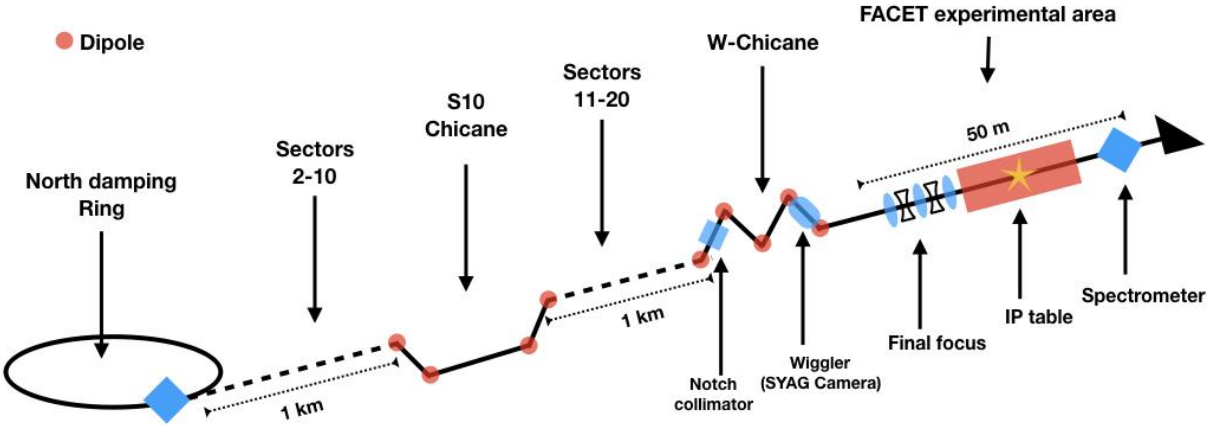

Figure 4.3: Schematic of the FACET beam line and of its main components

From 1980 until 1990, SPEAR was replaced by the Positron-Electron Project (PEP) that reused SPEAR rings and the linear accelerator to collide electrons and positrons with an energy of 29 GeV. PEP was upgraded in 1994 to become the PEP-II project, in which larger storage rings were built and sheltered the Babar experiment which aimed at demonstrating Charge Parity violation. The PEP-II system was in use until 2008.

The SLC (Stanford Linear Collider) was another experimental platform at SLAC, completed in 1987. It was an electron-positron collider that relied on SLAC 3-km-long linac to accelerate both kind of particles and then force them to collide thanks to two « arcs », curved final cavities. The center-of-mass energy of the colliding particles was 90 GeV. The SLAC hosted experiments for a decade.

From 2009 on, Linac Coherent Light Source (LCLS) became the main user facility operated at SLAC. LCLS was the first hard X-ray free electron laser in the world. In 2012, FACET, the Facility for Advanced aCcelerator Experimental Tests opened and provided the opportunity to work on advanced accelerator concepts such as PWFA schemes. The schematic of the current facility is depicted in Fig. 4.3.

After the shutdown of FACET in April 2016, LCLS-II, an X-ray free electron laser operating at MHz repetition rate and using superconducting technology, is being built and is expected to give first light in 2020. LCLS-II accelerator will use the first kilometer of the historical SLAC 3-km linac tunnel. In parallel, FACET is being upgraded to FACET-II, a new facility expected to provide state-of-the-art electron and positron beam parameters that could make many discoveries possible in the field of PWFA. FACET-II will use the second kilometer of the historical SLAC 3-km linac.

SLAC National Accelerator Laboratory is one of the ten laboratories of the US Department of Energy and is operated on its behalf by Stanford University. As said in the general introduction about particle accelerators of Chapter 1, SLAC led three of its users to be awarded a Nobel Price, in 1976, 1990 and 1995.

b. Beams and parameters

SLAC conventional accelerator can provide $20.35\ GeV$ electron or positron beams to the experimental area **[Erikson 84]**. The properties of the beams are listed in Fig. 4.4.

The process of producing electron or positron bunches has several steps that take place at different areas of the facility. An electron gun provides the initial bunches of electrons that are cooled down in the north damping ring. The bunches are then sent into the 2-km linac and are accelerated to $20.35\ GeV$. When the accelerator is setup to produce positrons, positrons are created from an electromagnetic shower that is generated by hitting a tungsten alloy target with a $20.35\ GeV$ electron beam previously accelerated in the linac. The electrons are accelerated in the two kilometres of the beamline at the end of which they hit the tungsten alloy target. Electron-positron pairs are created in an electromagnetic shower in the target. Positrons emerging from the target are captured and a positron return line transport them to the start of the accelerator where they are injected and cooled down in the south storage ring and then finally accelerated into the main linac to $20.35\ GeV$.

Parameter	Value
Beam charge	$2 - 3.5\ nC$
Beam central energy	$20.35\ GeV$
RMS energy spread	$\sim 1.5\%$
RMS longitudinal size	$30 - 50\ \mu m$
RMS transverse size	$\sim 30\ \mu m$
Normalized emittance (in transverse $x \times y$ dimensions)	$100 \times 10\ mm^2.mrad^2$
Drive beam energy (two-bunch configuration)	$20.55 \pm 0.25\ GeV$
Trailing beam energy (two-bunch configuration)	$20.05 \pm 0.15\ GeV$
Minimal interbunch distance	$\sim 100\ \mu m$

Figure 4.4: Beam parameters at FACET.

In the linear accelerator, klystrons provide the RF fields used to accelerate the particles. The $2\ km$-long straight line is where the acceleration takes place.

When it penetrates into the W-chicane area at the end of the accelerator, the particle beam can be reshaped to have a two-bunch longitudinal structure. This can be necessary for some experiments, such as the one described in the next chapter. In this section of the accelerator, successive dipoles and quadrupoles manipulate the beam. From a beam with an initial correlation between the energy of the particles and their longitudinal position, an energy-dependent transverse position (and therefore a correlation between longitudinal and transverse position) is given. After the first dipole, a tantalum bar can be inserted to block the central particles, those at the middle of the bunch energy range. The correlation between transverse position and energy is cancelled by the rest of the chicane. The minimum

longitudinal distance between the two bunches that can be created thanks to this technique is $\sim 100\ \mu m$. In our experiment, the drive beam energy was centred on $20.55\ GeV$, and the trailing on $20.05\ GeV$. Furthermore, for technical reasons, the drive beam was also the first beam in time to reach the experimental area. For the experiment described in this part, the two-bunch structure consists of a **first bunch, the drive bunch of energy $\mathbf{20.55 \pm 0.25\ GeV}$**, **followed** $100 - 150\ \mu m$ later by a **second bunch, the trailing, of energy $\mathbf{20.05 \pm 0.15\ GeV}$**.

In the W-chicane, a non-invasive energy spectrometer called SYAG is setup. This setup uses the synchrotron X-ray radiation produced by the horizontally-dispersed beam when it goes through a magnetic wiggler system composed of three dipoles deflecting the beam vertically. In particular, this energy spectrometer, combined with toroid charge diagnostics setup along the beamline, allows us to measure the charge in each of the two bunches and will be described in more details in Chapter 5.

Before the Interaction Point a final focus device composed of five quadrupole magnets focuses the beam to the transverse size indicated in Fig. 4.4 This section allows also to adjust the beta function of the beam at the entrance of the plasma.

c. Plasma source

To setup the PWFA experiments at FACET, it was necessary to setup a gas column, whose density could reach $10^{14} - 10^{17} cm^{-3}$ or even more. It was also necessary to employ a gas whose first ionization energy would be low (of a few eV) and whose second ionization potential would be much higher (a few tens of eV). Such a gas would ensure that when the plasma is generated by the passage of a laser in the gas, each atom releases exactly one electron.

FACET relies on a lithium plasma for most of the PWFA experiments. The first ionization potential of lithium is $5.4\ eV$ and the second $75.4\ eV$. Lithium vapor is contained during the experiments in a pressure heat-pipe oven, whose internal lithium pressure is controlled by the temperature of the vapour **[Muggli 99]**. It is necessary to maintain the gas at a high temperature to reach neutral densities of about $10^{16}\ cm^{-3}$. A temperature of around $900°C$ is needed, this was made possible by the plasma oven where the pressure is **[Mozgovoi 86]**:

$$P = \exp\left(-2.05\ln(T) - \frac{19.43}{T} + 9.50 + 0.75T\right)/(133 \cdot 10^6) \qquad \textbf{(4.1)}$$

where T is the temperature and P is the pressure in Torr. The density in the gas is therefore directly given by the performances of the oven **[Vafaei-Najafabadi 12]**, in Fig. 4.5 is depicted the temperature and the density profile along the length of a plasma oven. There is almost no density fluctuation in the plateau.

For the oven used in the experiments, the density plateau is $1.15\ m$ long, with a $15\ cm$ up or down ramps on each side. The **FWHM length** of the oven is therefore $\mathbf{1.30\ m}$.

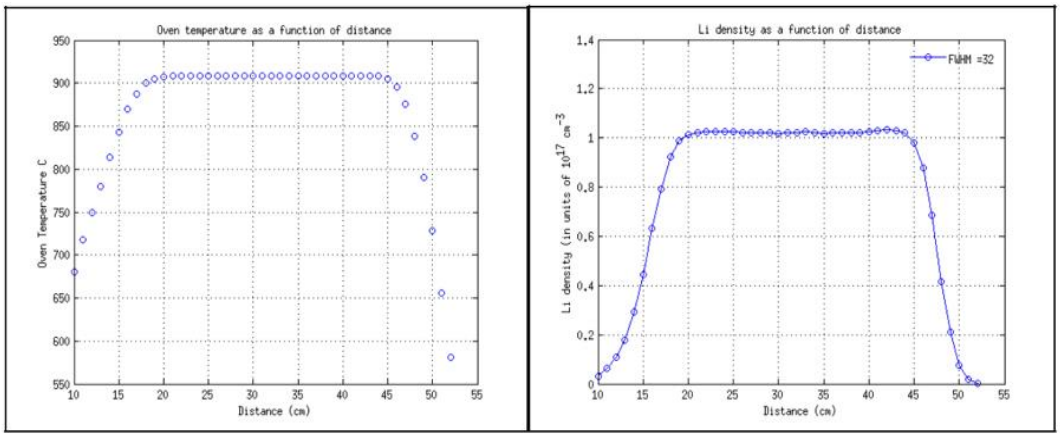

Figure 4.5: A plasma oven temperature profile (left) and density profile (right), from ***[Vafaei-Najafabadi 12]***

The plasma electron density can be established from the models of the ionization processes introduced in Chapter 1. A femtosecond TW laser pulse is focused on a line by an axicon over the full length of the oven to ionize the lithium vapor. With a lithium vapor, Multiphoton Ionization is the process to be taken into account. The ionization rate for an ionization potential U_I is given by the formula for Multiphoton Ionization, in a k-photon process **[Bruhwiler 03]**:

$$W(s^{-1}) = \sigma_k \left(\frac{I}{h\nu}\right)^k \qquad \textbf{(4.2)}$$

Where I is the flux of photon, ν is the photon frequency, and σ_k is the Multiphoton Ionization cross-section for a process with k photons. The electron density is given by $n_0 = n_{Li}(1 - \exp(-\int W dt))$. With a laser pulse containing $\sim 100\, mJ$ of energy, we can easily ionize all lithium atoms and reach $n_0 = n_{Li}$.

d. FACET laser systems

The laser system available for the PWFA experiments at FACET operates at $10\, Hz$, and has a central wavelength of $800\, nm$ **[Green 14]**. A schematic of the whole laser chain is depicted in Fig. 4.6.

The femtosecond laser chain begins with a Ti:Sapphire femtosecond oscillator, providing a $800\, nm$ beam at $68\, HMz$ with a $60\, nm$ bandwidth. Next in the chain is a Regenerative Amplifier that is setup to deliver a beam of $1\, mJ$, at a repetition rate of $10\, Hz$. A preamplifier increases the main beam energy up to $30\, mJ$ and is pumped by a YAG laser of $130\, mJ$, at $532\, nm$. The outgoing beam is then delivered to the main amplifier stage which consists of a Ti:Sapphire crystal pumped by two Thales SAGA YAG lasers of $1.8\, J$ at $532\, nm$. The amplified beam reaches an energy of up to $1\, J$ after the main amplifier and is not yet compressed.

The beam is transported over $28\, m$ from the laser room down to the Interaction Point Table. During transport, two telescopes focus the beam once each time, which can cause distortion of the beam profile. This is why a vacuum inferior to $10^{-5}\, Torr$ pressure is setup in the transport line. The compressor stands along the Interaction Point Table, and the pulses can be

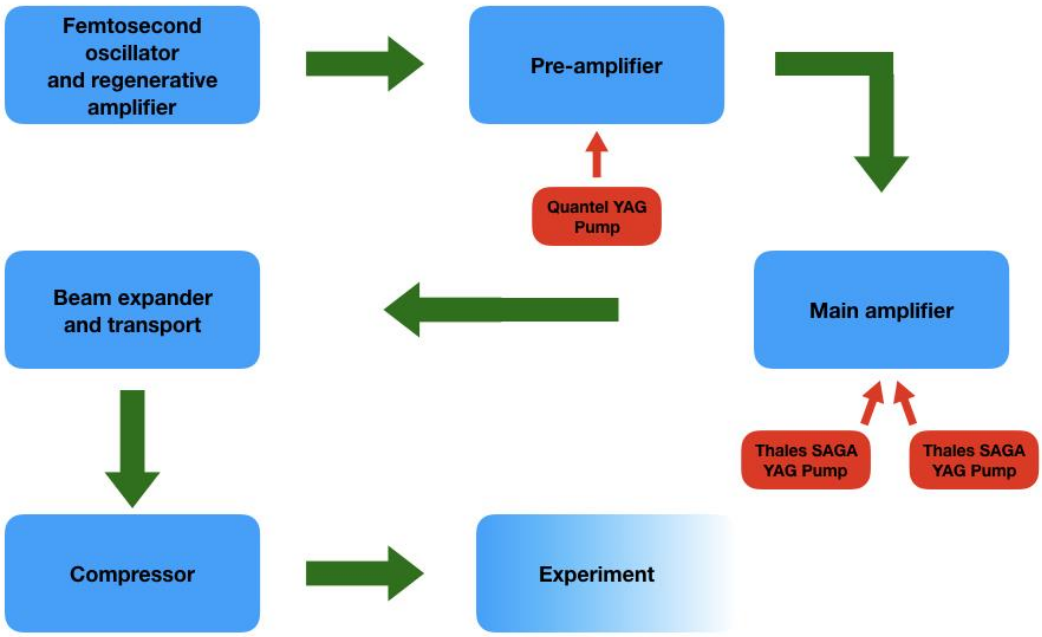

Figure 4.6: Schematic of FACET femtosecond laser systems

compressed down to 50 fs. However, to prevent self-phase modulation it is necessary to slightly modify the distance between the gratings in the compressor to have $100 - 200\ fs$ long pulses.

The laser pulse is synchronized with the linac to ionize the plasma around $100\ ps$ before the $e^{\pm}$ beam from the FACET accelerator passes in the oven. The maximum laser energy available after compression is of about $500\ mJ$. This energy is high enough to fully ionize a column of lithium vapor of $1.30\ m$ with a diameter of the order of $1\ mm$.

Previous results in the field of beam driven plasma wakefields were presented in chapter 4, along with the difficulties in accomplishing particle acceleration using positron driven wakefields. In the following, the experimental apparatus of the trailing positron bunch experiment will be described in details before the discussion regarding the results themselves is made.

Chapter 5

Acceleration of a distinct positron bunch in a plasma wakefield accelerator

The first section of this chapter is dedicated to a comprehensive description of the **experimental apparatus** that led to accelerate a distinct bunch of positrons. The different diagnostics are described in details. In the second section the **proof of acceleration** is given, along with results regarding **beam loading effects** occurring in the process. Last, a study of the **acceleration regime** in the experiment is accomplished and in particular, the existence of a transition from a very nonlinear to a quasilinear regime is discussed.

Contents

1. Experimental setup and diagnostics

a. Experimental setup

The experimental setup of the trailing positron bunch acceleration experiment is depicted in Fig. 5.1. On this schematic, the main process and all the associated diagnostics appear.

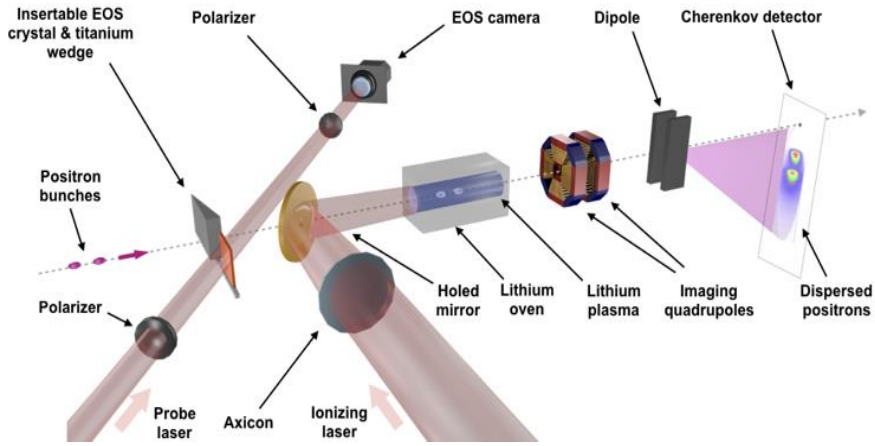

Figure 5.1: Experimental setup of the trailing positron bunch acceleration.

A femtosecond laser pulse is used to pre-ionize a column of plasma. After it exits the compressor, the laser pulse is focused on a line by an axicon, before being superimposed on the positron beamline by the holed mirror. The axicon angle determines the length of the focal line. In our case, the laser is focused on a line all along the plasma oven, and the peak intensity is approximately constant in the gas. As said in chapter 4, in the section dedicated to the plasma oven, the electron density is almost constant over 1.15 m, and two linear up and down ramps of 15 cm-long lay on both sides of the oven density profile. The FWHM of the oven is therefore approximately 1.30 m. The laser and axicon parameters used in the experiment are depicted on the table of Fig. 5.2.

Parameter	Value
Axicon angle	0.6°
Laser convergence angle	0.28°
Laser pulse energy in plasma	120 mJ
Laser peak power	0.6 TW
Bunch length in plasma	200 fs
Laser Intensity at plasma center	$\sim 2\ 10^{14}\ W\ cm^{-2}$

Figure 5.2: Axicon and laser beam parameters in the experimental area.

A schematic of the principle of an axicon lens is given in Fig. 5.3. Such an optic is used to obtain complex laser intensity distributions over large areas. In our experiment, an axicon was needed to produce a cylindrical plasma all along the plasma oven.

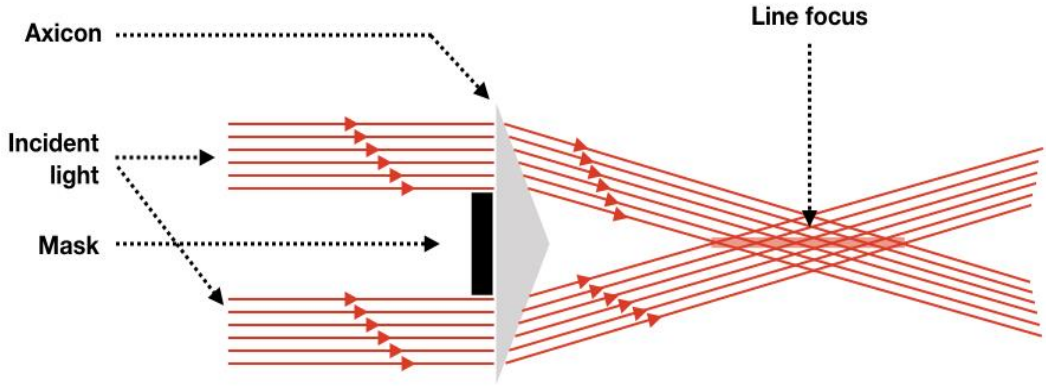

Figure 5.3: An axicon focusing an incident laser beam. In the transverse plane, the intensity profile is a Bessel function of order 0, $J_0(k\alpha r)$.

The on-axis intensity at a distance z from an axicon is the result of positive interference of the light emerging from a small annulus on the axicon. The analytic calculation shows that the intensity distribution in the transverse plane Oxy at distance z created by a plane wave going through the axicon is given by an order 0 Bessel function $J_0(k\alpha r)$, where α is the angle of the rays after the axicon (calculated from the axicon angle and material indices), k is the wavevector and r is the distance to the axis in the transverse plane. For simplicity, we consider here the case of a Gaussian beam incident on the axicon. The intensity after the optic in the case of a Gaussian beam illuminating the axicon is given by the formula:

$$I(r,z) = I_0 \left(4\pi^2\alpha^2 \frac{z}{\lambda}\right) \exp\left(-\frac{2(\alpha z)^2}{w_0^2}\right) J_0^2(k\alpha r) \qquad \textbf{(5.1)}$$

Where λ is the wavelength of the laser and w_0 and I_0 are respectively the waist and the on-axis intensity of the Gaussian beam illuminating the axicon.

In our setup, a mask blocks the light near the center of the optics, allowing to focus the light on a line starting at the beginning of the plasma oven for an appropriate choice of mask radius and axicon-plasma distance. This is why the axicon line focus in Fig. 5.3 begins at a distance from the optic.

In reality, the transverse shape of the FACET laser pulse is closer to a flat-top than a Gaussian beam. The laser intensity after the axicon can be approximated in this case by simply removing the exponential term in (5.1). The intensity of the laser pulse incident on the axicon is:

$$I_0 = \frac{E}{\pi r_0^2 \tau} \sim 5\ 10^{10}\ W\ cm^{-2} \qquad \textbf{(5.2)}$$

where $E = 120\ mJ$ is the laser energy, r_0 is the radius of the laser and $\tau = 200\ fs$ is the laser pulse duration.

On axis, the maximal intensity after the axicon obtained is:

$$I_{max} = I_0 \left(4\pi^2\alpha \frac{r_0}{\lambda}\right) \sim 2\ 10^{14}\ W\ cm^{-2} \qquad \textbf{(5.3)}$$

for a wavelength $\lambda = 800\ 10^{-9}\ m$ and a convergence angle $\alpha = 0.28°$.

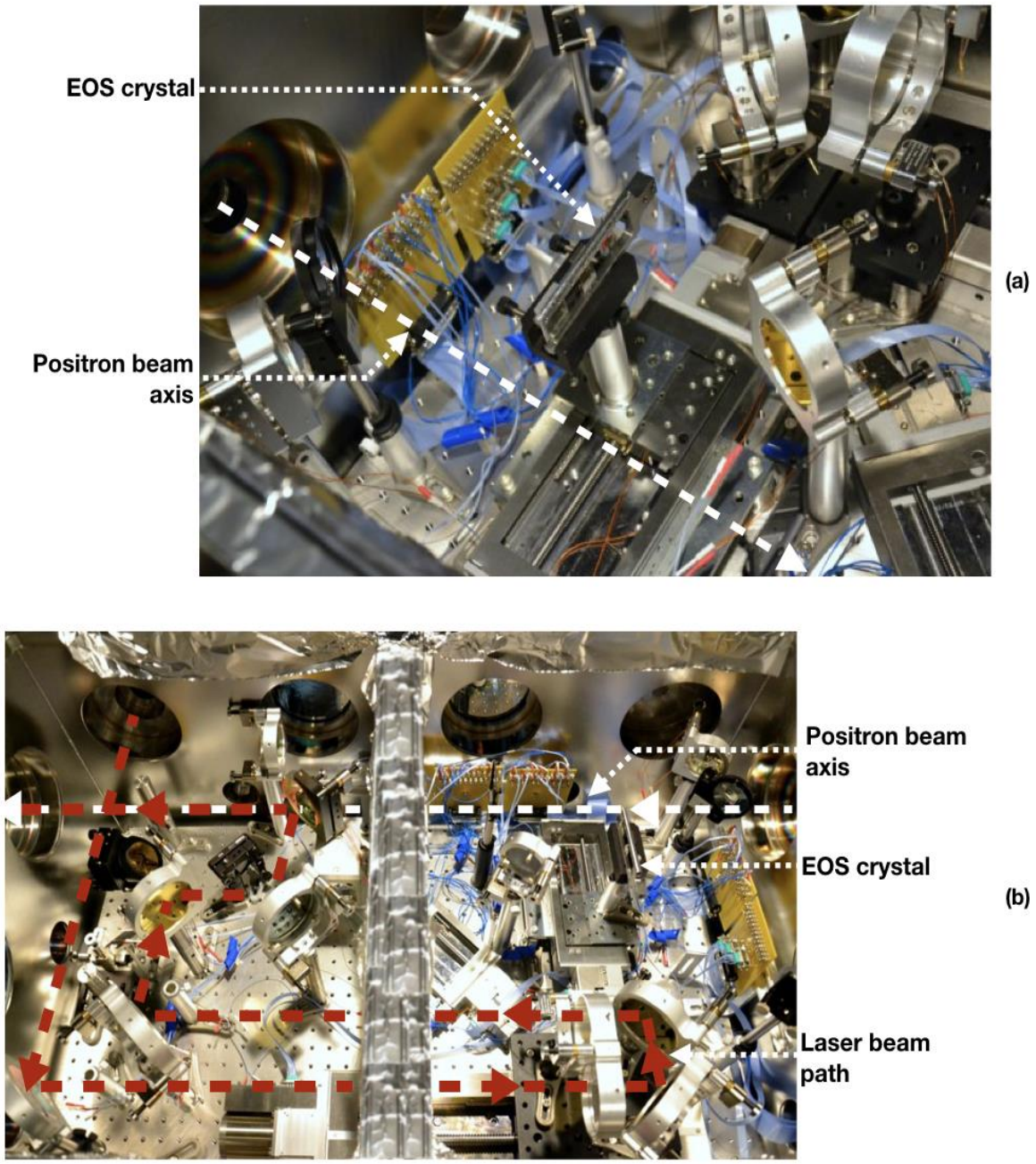

Figure 5.4: (a) EOS crystal and titanium wedge mount in the picnic basket. (b) Overview of the picnic basket with the positron beam and laser beam paths.

Such a peak laser intensity ensures that a mm-diameter column of lithium vapor is fully ionized all along the oven **[Green 14]**. The compressor has its own vacuum chamber, the rest of the optics: axicon, delay line, holed mirror are in a separate vacuum chamber called the picnic basket, and shown in Fig. 5.4 (b). The plasma oven is in the same volume as the picnic basket.

In the picnic basket is setup another diagnostic, the electro-optic sampler (EOS) that provides a direct longitudinal profile measurement of the positron beam. The two-bunch positron beam passes above the EOS crystal and modifies its properties, then goes through the holed mirror and enters the plasma, 100 ps after the laser pre-ionizes the gas. The beam-plasma interaction process can then take place.

As described in the section dedicated to the EOS diagnostics, a fraction of the main laser intensity is used as the EOS probe. This probe is synchronized with the passage of the bunches above the crystal. This probe is the laser beam on the bottom left of Fig. 5.1 that goes through the crystal.

The EOS crystal is setup on a mobile mount, and can be moved to be replaced by a Titanium wedge, used in the second part of the experiment to modify the emittance of the bunch. The mount is visible in Fig. 5.4 (a). The modification of the particle beam parameters when it passes through the metallic wedge is calculated in detail in section 3.

b. Energy spectrometer

The energy of the particles is measured by a Cherenkov light imaging spectrometer, appearing on the right, in Fig. 5.1. The details of this setup are given in Fig. 5.5 (a). First, a dipole magnet which has an equivalent length and field of $97.8\ cm$ and $0.8\ T$ deflects the positrons vertically, according to their energy. The particles then reach a device composed of two silicon wafers separated by a $5\ cm$ long air gap, and emit Cherenkov light when they move through the air in the gap as depicted in Fig 5.5 (a). The wafers have a 45° angle compared to the beam trajectory, so that the second wafer reflects the Cherenkov light that is then recorded by a camera **[Adli 15]**. The unmodified two-bunch beam spectrum leads to the image of Fig 5.5 (b) on the spectrometer.

The dispersion due to the dipole leads the particles to spread on the vertical dimension of the screen. The vertical position can then be related to the energy of the particles thanks to the following formula, where y is the vertical position along the screen, y_0 is the nominal position (position of the particles at energy E_0) and η_0 the dispersion from the dipole at the nominal beam energy E_0:

$$y = y_{E=\infty} - \eta_0 \frac{E_0}{E} \qquad \textbf{(5.4)}$$

Therefore, the energy can be expressed as:

$$E = \frac{E_0}{1-(y-y_0)/\eta_0} \qquad \textbf{(5.5)}$$

Equation **(5.4)** is nonlinear in y, the position along the screen. In Fig 5.5 (b), the conversion from the vertical coordinate to the energy axis has already been made, and the image was stretched accordingly.

In addition, error estimation is of prime importance in experimental plasma wakefield acceleration. FACET offers the possibility to acquire data at $10\ Hz$, therefore, it is extremely convenient to record a large amount of data when performing a parametric study. As a result, statistical errors can efficiently be reduced. However, systematic errors remain.

When using the Cherenkov light spectrometer system, the limitation in the resolution of the energy measurement can have two origins. Resolution can be limited by the Cherenkov optical system itself. The conceptual design of the spectrometer used at FACET leads to an estimation of the resolution of $76\ MeV$ **[Adli 15]**. Limitation in the resolution can also be due to the Betatron beam size in the vertical dimension, this resolution is estimated to be of the order of $50\ MeV$. A systematic error is induced when the calibration of the energy axis on the Cherenkov system camera is accomplished. However, when measuring energy differences, the

error on the origin of the axis cancels out and the remaining error is only due to the uncertainty on the dispersion η_0.

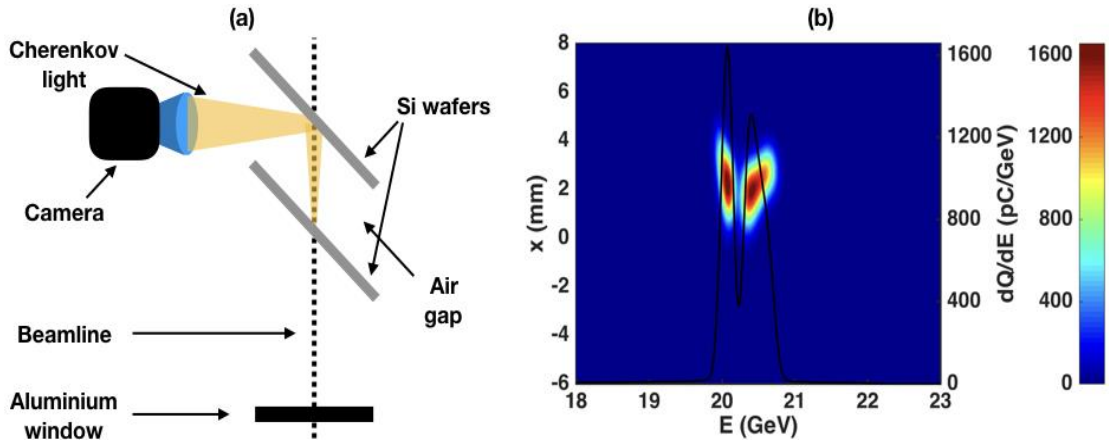

Figure 5.5: (a) Schematic (top view) of the Cherenkov light spectrometer. (b) A processed image from the spectrometer showing the two-bunch energy structure when no plasma is present. The vertical position on the Cherenkov screen is converted into the energy axis. The left y-axis is the horizontal position. The right y-axis is the integrated spectrum axis. The black plain line is the integrated spectrum that appears on the background image.

c. EOS diagnostic

The Electro-Optic Sampler diagnostic provides a measurement of the longitudinal profile of the beam before it passes through the plasma. As seen in Fig. 5.1, the EOS crystal is setup on a mount in the picnic basket, before the plasma.

The crystal is a 50 μm-thick GaP crystal standing a millimeter below the beam path. A probe laser beam passes through the crystal at an angle, with an adjustable delay relative to the positron beam passage **[Litos 11]**. The GaP electro-optic crystal birefringence property is modified by the sliced shaped electric field of the positron bunches **[Steffen 07]**. The femtosecond probe laser pulse passes through the crystal to sample its instantaneous properties. The modification of the crystal birefringence induced by the positron beam field in the crystal results in a relative phase delay between the two orthogonal components of the laser probe pulse. Two polarizers are used in the laser path, a first one before the crystal, with a main direction at a 45° angle relative to the crystal axis and a second one, located before the camera and after the crystal and aligned for laser extinction in the absence of a positron beam.

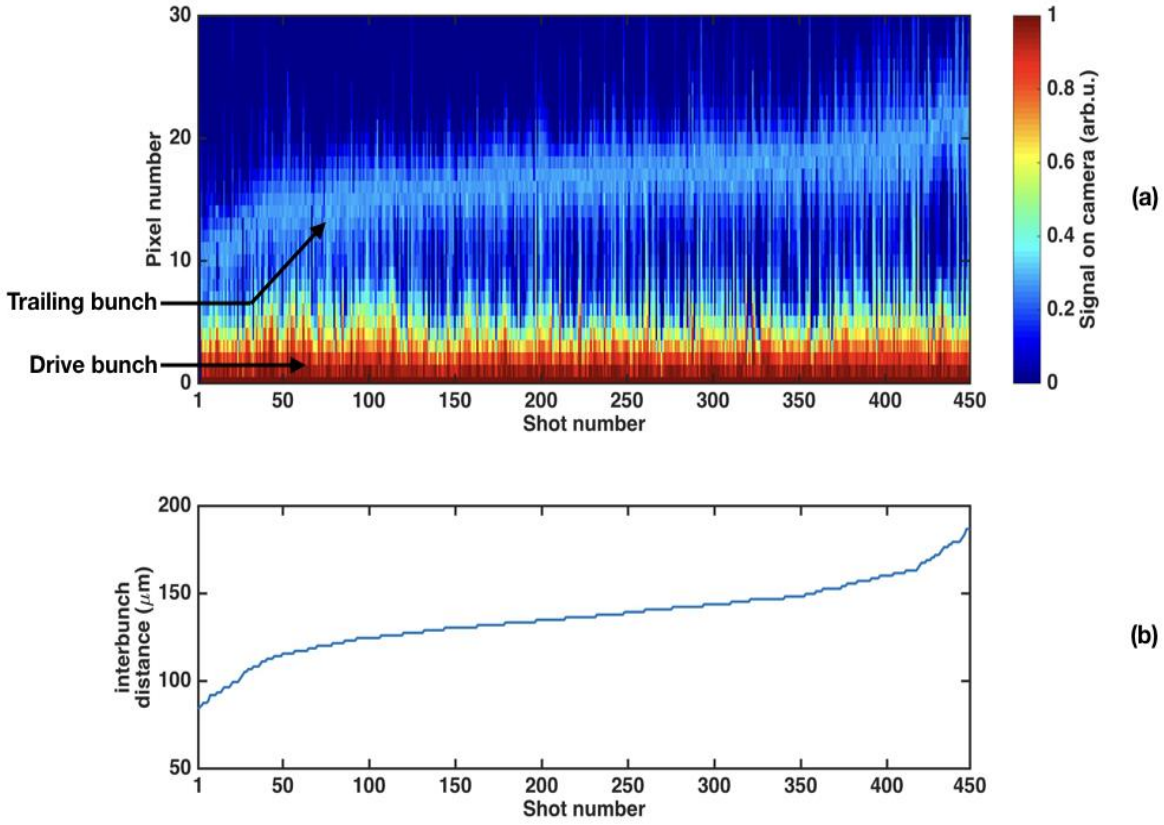

Figure 5.6: (a) Waterfall (columns of integrated signal) of the EOS signal measured during a dataset. The images are sorted by increasing interbunch distance. (b) Corresponding interbunch distance. Calibration of the EOS camera: $8.06\ \mu m\ px^{-1}$.

A higher laser signal on the detector is observed in the areas in which birefringence was modified by the positron beam electric field. Those areas correspond to a perfect synchronicity between beam field and probe pulse in the crystal. The two bunches (trailing and drive bunch) are not synchronized with the probe at the same position on the crystal, as the probe comes at an angle on the crystal. Therefore, the longitudinal profile of the positron beam can be reconstructed from a single measurement, with a temporal resolution of about $150\ fs$. An example of the measurement of the interbunch distance for a whole dataset is given in Fig. 5.6.

The longitudinal separation between the drive and the trailing bunch can be modified experimentally by varying the arrival time of the positron beam in the linear accelerator. The EOS diagnostic monitors the resulting change.

d. Beam charge diagnostics

Toroidal charge monitors are setup at 30 stations along the beam line of the SLAC linear accelerator. These devices act as current transformers, when the charged particles move through them. Their output signals allow to monitor the charge of the beam **[Larsen 71].** Close to the experimental area, the toroids have the highest precision and provide a measurement of the beam total charge with an accuracy of $\pm 0.1\%$. However, this technique does not permit to

monitor the charge in each of the two bunches composing the beam when the notch collimator is used to produce a two-bunch structure.

Another system, a non-invasive energy spectrometer, is used to monitor efficiently the charge distribution within the bunch. We refer to this system as the SYAG system. After the notch collimator, the two bunches have different energies: the drive bunch is centered on $20.55 \pm 0.25\ GeV$ and the trailing bunch is centered on $20.05 \pm 0.15\ GeV$. At the far end of the W-chicane, the beam is horizontally dispersed: there is a correlation between the energy of the particles and their transverse position. Then, a magnetic vertical wiggler leads the beam to produce synchrotron X-rays. A scintillating YAG screen collects the X-ray radiation due to the wiggling, reproducing the energy spectrum of the two-bunch beam. A camera records the signal on the screen for each shot, the energy spectrum of the two bunches leads to two distinct spots on the camera. The toroid monitors are used to calibrate this signal. As the result, the SYAG camera provides a direct measurement of the charge in each of the two bunches.

Beam charge is one of the parameters of the beam that fluctuate the most. These natural fluctuations can be useful, as they are used to identify correlations between the beam parameters and the parameters of the plasma acceleration. For example, it is possible to plot the energy peak of the accelerated bunch of positrons as a function of the initial trailing beam charge. The natural fluctuations ensure that the initial trailing beam charge spans the range $[150\ pC\ , 400\ pC]$.

e. Optical Transition Radiation (OTR) screens

A perfect alignment of the beam and of the laser axis in the plasma oven is necessary. As seen in Fig. 5.1, a holed mirror is setup on the beam line. The positron beam passes through the hole, and the laser is superimposed thanks to the mirror. Fine alignment is performed thanks to insertable thin OTR foils, which are set up on both sides of the plasma oven.

Optical Transition Radiation is a radiation emission process that occurs when relativistic charged particles pass from a medium to another one. In fact, the electric field of the bunch of particles in each of the media is not the same, and the difference gives birth to optical transition radiation **[Dolgoshein 93]**. In the experiment, the foils are setup at an angle of $45°$ compared to the beamline. A part of the OTR radiation is emitted on the front face of the foil, at $90°$ compared to the beam line, where a camera collects it. The alignment method in this experiment uses the cameras and motors mounted on the optics in the picnic basket to superpose the beam and the laser spots on the OTR camera screens on both sides of the oven.

f. Simulations

Numerical simulations play a major role in plasma-based acceleration studies. Regarding the experiment described in this section, a parametric study was accomplished before the experiment, using a particle-in-cell (PIC) code, to examine whether the experiment could work for a choice of parameters.

Simulations were performed using the particle-in-cell QuickPIC code **[Huang 06, An 13b]**. QuickPIC is a kinetic simulation code in which the quasi-static approximation is made. This hypothesis assumes that the particle beam is evolving slowly compared to the time scale of the plasma response.

In the simulations performed for the trailing positron bunch experiment, the simulation box moves at the speed of light in the beam propagation direction. The coordinate system used in this chapter is x, y (in the transverse plane) and $\xi = ct - z$ (in the longitudinal dimension). The simulation box has a size of $400 \times 400 \times 400\,\mu m^3$ (in x, y and ξ) divided into $512 \times 512 \times 1024$ cells.

In the simulations, the drive and trailing bunches initially have Gaussian profiles in all dimensions. In most simulations presented in this part, the initial r.m.s. spot sizes used are $\sigma_x \times \sigma_y = 35 \times 25\,\mu m^2$ and an r.m.s. bunch length of $\sigma_z = 30\,\mu m$ (for the drive beam) and $\sigma_z = 40\,\mu m$ (for the trailing beam) is always used.

Both bunches in the simulation have no initial energy spread and their central energies are $20.55\,GeV$ (for the drive bunch) and $20.05\,GeV$ (for the trailing bunch). These values correspond to the measurements accomplished on the Cherenkov spectrometer, without plasma, but neglecting the energy spread of the beams.

As will be seen on the experimental results, the charge of the bunches used in the simulations is chosen to be 50% of the charge measured experimentally. In fact, this reduced charge shows better agreement with the experimental data. This adjustment is justified by the presence of possibly large transverse tails in the positron charge distribution that do not take part in the interaction **[Litos 14]**. This is a consequence of the hypothesis of perfectly Gaussian bunches in the simulations.

2. Acceleration of a trailing positron bunch

a. Proof of acceleration

The demonstration of acceleration of a trailing positron bunch took place in several steps. As said earlier, the electron density of the plasma was chosen to be $10^{16}\,cm^{-3}$, the laser energy was set to $120\,mJ$, in order to ionize the whole $1.3\,m$-long oven. The positron beam has a two-bunch longitudinal shape, where the two bunches, the drive and the trailing are separated by $100\,\mu m$. The bunches are centered on the energies $20.05 \pm 0.15\,GeV$ (trailing bunch, second in time) and $20.55 \pm 0.25\,GeV$ (drive bunch, first in time).

Before the bunches pass in the oven, it was possible in the experiment to choose not to pre-ionize the gas by blocking the laser. In that case, the energy spectrum of the beam after the oven was unmodified. In fact, no interaction occurred. This unmodified spectrum can be used as a reference to illustrate energy gain or loss. In addition, it was also possible in the experiment to block any of the bunches, when the beam was being reshaped in the W-chicane. As a result, it was possible to send in the oven, either the two bunches, drive and trailing bunches, only the trailing or only the drive bunch.

One affirmation can be made already: causality implies that the trailing bunch (second bunch in time) cannot influence the drive bunch. The bunches propagate with an ultrarelativistic velocity, and only the drive bunch (or maybe the trailing bunch itself) can influence the spectrum of the trailing bunch.

As a result, the demonstration of the acceleration of particles from the trailing bunch, using a plasma density wave excited by the drive bunch requires:

1. To demonstrate that when the trailing only, or the drive bunch only is sent, some beam particles lose energy: they deposit energy in the plasma by exciting the density wave, but no acceleration is observed.
2. To demonstrate that when both bunches are sent, some beam particles reach an energy higher than the upper-limit energy of the drive beam.

The remark regarding causality, added to proposition 1. and 2., would demonstrate that if we observe accelerated particles in the experiment, then those particles must come from the trailing: if only the presence of both bunches give birth to particles above $20.8\ GeV$ then we can conclude that the demonstration is successful.

In Fig. 5.7 (a), two integrated spectra are displayed, when only the drive bunch was sent into the oven. When the plasma was preformed, some particles lost energy, but no acceleration was observed.

In Fig. 5.7 (b), two integrated spectra are displayed, when only the trailing bunch was sent into the oven. When the plasma was preformed, some particles lost energy, but no acceleration was observed.

In Fig. 5.7 (c), two integrated spectra are displayed, when both the trailing and the drive bunch were sent into the oven. When the plasma was preformed, some particles lost energy, and some particles reached an energy above $20.8\ GeV$. When the plasma was not preformed, no interaction occured, the spectrum was unchanged.

As a result, we can conclude that Fig 5.7 (a) and (b) demonstrate that proposition 1. is correct. In addition, Fig. 5.7 (c) and the remark regarding causality demonstrate that the drive beam deposits energy in the plasma wave and that particles from the trailing bunch extract it to reach

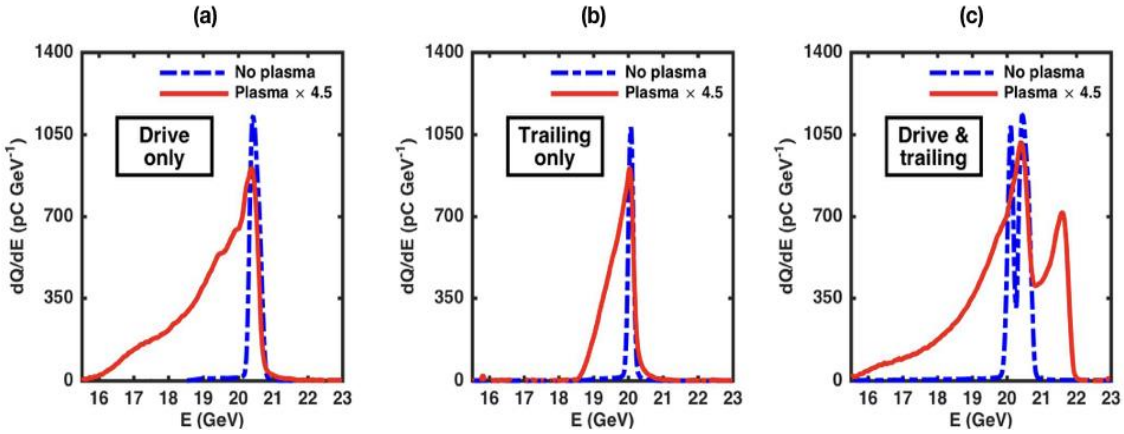

Figure 5.7: (a) Integrated spectra for a shot when only the drive bunch was sent into the plasma, with plasma (red plain line), without plasma (blue dashed line) (b) Integrated spectra for a shot when only the trailing bunch was sent into the plasma, with plasma (red plain line), without plasma (blue dashed line) (c) Integrated spectra for a shot when both bunches were sent into the plasma, with plasma (red plain line), without plasma (blue dashed line). Acceleration is clear with a secondary red peak on the right. From ***[Doche 17]***

energies above $20.8\ GeV$.

This result by itself is a first **accomplishment**: a distinct bunch of positrons had never been accelerated before in any type of plasma-based accelerators (beam-driven or laser-driven).

The shots displayed in Fig. 5.7 come from a stack of 500 shots for each case: the case in which the trailing bunch only is sent, the case in which the drive bunch only is sent and the case in which both bunches are sent. Fig. 5.7 (c) presents a successful acceleration of the trailing bunch. The accelerated bunch displayed in this figure has especially good properties. The r.m.s. energy spread associated to the fit of the peak is 1.0%. The charge contained in the peak is $85\ pC$ and the peak energy is $21.5\ GeV$. The initial trailing bunch energy was centered on $20.05\ GeV$, which corresponds to an energy gain of $1.45\ GeV$. Considering a plasma length of $1.3\ m$, this is an accelerating energy gradient of $1.12\ GeV\ m^{-1}$. The wake-to-bunch energy extraction efficiency can also be estimated from the data. This parameter is defined as the total amount of energy gained by all the particles in the trailing bunch with final energy above $20.8\ GeV$ relative to the total amount of energy lost by all the particles in the drive bunch with final energy below $19.9\ GeV$. It is estimated to be 40% for this shot of Fig. 5.7 (c). This parameter describes the fraction of the energy transferred to the plasma wake that is extracted by the trailing bunch.

Going further into the description of the acceleration mechanism, a physical process was observed in the data recorded during the experiment: beam loading of the wakefield.

b. Beam loading, theory and experimental observation

Theory

Beam loading is an effect due to the wakefield driven by the accelerated bunch itself. This physical process is not limited to the specific trailing positron bunch acceleration scheme performed at FACET. In a plasma wakefield, if the accelerating field is sampled by a particle beam, the wakefield driven by this accelerated bunch modifies the initial driven wakefield.

In conventional accelerators, the phenomenon of beam loading exists as well. In a conventional accelerating cavity, a bunch of particles surfing on the cavity radiofrequency field can drive a wakefield **[Ng 06]**.

In the linear theory of plasma wakefield acceleration, the calculation of the modified wakefield due to the drive beam and to the accelerated beam (in the experiment described in this chapter, due to the trailing beam) is straightforward: for the linearized equations, the wakefield is the sum of the wakefields due to each of the two bunches.

For a beam density:

$$n_b(\xi, r) = \left(n_d(\xi) + n_t(\xi)\right) \cdot \exp\left(-\frac{r^2}{2\sigma_r^2}\right)$$

where $n_d(\xi) = \frac{N_d}{(2\pi)^{3/2}\sigma_r^2\sigma_{z,d}} \cdot \exp\left(-\frac{\xi^2}{2\sigma_{z,d}^2}\right)$ and $n_t(\xi) = \frac{N_t}{(2\pi)^{3/2}\sigma_r^2\sigma_{z,t}} \cdot \exp\left(-\frac{(\xi-\xi_t)^2}{2\sigma_{z,t}^2}\right)$, equation (3.39) for instance, writes on axis:

$$E_z(0,\xi) = \frac{q}{2\epsilon_0} k_p^2 \int_{-\infty}^{\xi} \left(n_d(\xi) + n_t(\xi)\right) \cdot \cos\left(k_p(\xi - \xi')\right) d\xi' \int_0^{\infty} K_0\left(k_p r'\right) \exp\left(-\frac{r'^2}{2\sigma_r^2}\right) r' dr' \qquad \textbf{(5.6)}$$

An example of a loaded wakefield in the linear regime is shown in Fig. 5.8 (c). Two observations regarding this wakefield can be made. First, when the wakefield is not modified by beam loading as seen in Fig. 5.8 (a), the field is steep in the trailing bunch grey area. As a result, the maximal and minimal fields that the trailing particles face are very different from each other. In Fig. 5.8 (c), the difference between the maximum and minimum field in the grey area is lower. That is why, beam loading leads to a lower maximum accelerating field and to a lower energy spread of the accelerated bunch.

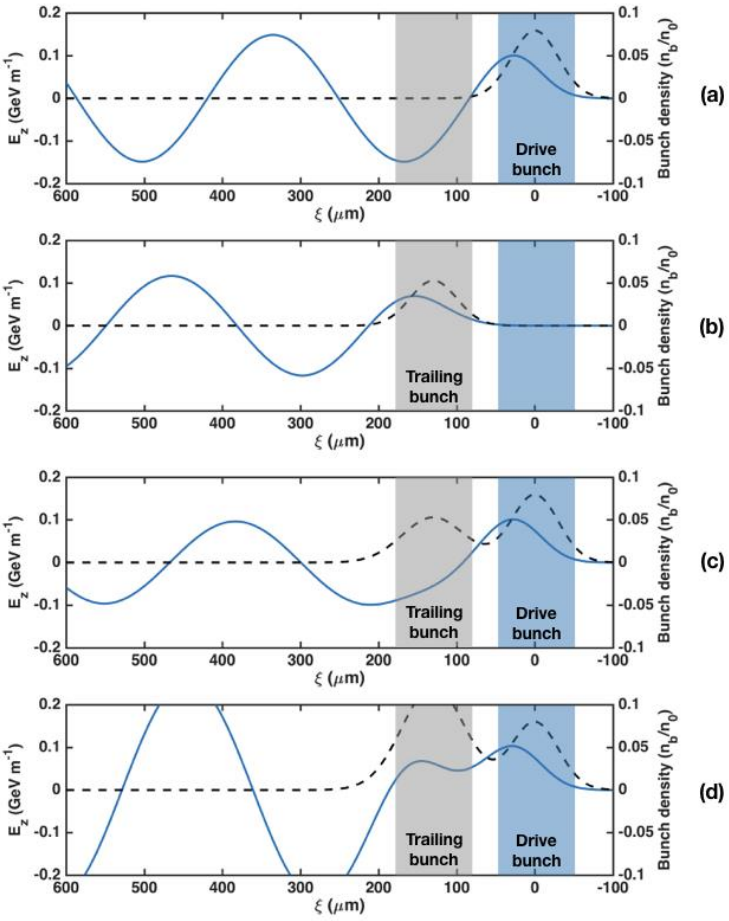

Figure 5.8: (a) E_z field on axis, in the linear regime of positron driven wakefield. $n_0 = 10^{16}\ cm^{-3}$, $N_{drive} = 3\ 10^8\ particles$. Drive beam at $\xi = 0$. (b) E_z field on axis. $n_0 = 10^{16}\ cm^{-3}$, $N_{trailing} = 2\ 10^8\ particles$. Trailing beam initially at $\xi = 130\ \mu m$. (c) E_z field on axis, with a loaded wakefield. $n_0 = 10^{16} cm^{-3}$. Drive beam at $\xi = 0\ \mu m$ and trailing beam at $\xi = 130\ \mu m$, the total wakefield is the superposition of the previous two. The wake is still accelerating at the trailing position (grey area), the wake is not optimally loaded. $N_{drive} = 3\ 10^8\ particles$ and $N_{trailing} = 2\ 10^8\ particles$. (d) E_z field on axis, with an overloaded wakefield: the wake becomes decelerating at the trailing position. $n_0 = 10^{16} cm^{-3}$. Drive beam at $\xi = 0\ \mu m$ and trailing beam at $\xi = 130\ \mu m$. $N_{drive} = 3\ 10^8\ particles$ and $N_{trailing} = 4.5\ 10^8\ particles$.

Beam loading of electron driven plasma waves was studied in details, it was shown **[Katsouleas 87]** that an accelerated bunch in an electron beam driven linear wakefield, whose current linearly increases with ξ leads to an almost flat field and therefore prevents energy spread growth during the acceleration process.

A nonlinear theory of beam loading in laser or electron driven wakefields also exists and was written by Tzoufras and al. **[Tzoufras 08]**. It describes in the very nonlinear, blow-out regime, the perturbation the accelerated beam makes to the cavity shape, and therefore to the fields. However, as explained earlier in the manuscript, there is no analytical theory of positron driven nonlinear plasma waves and of positron nonlinear beam loading.

However, an experimental study of beam loading in positron driven nonlinear waves, as we consider in this manuscript, would provide insights into the acceleration process.

Experiment

Two observables are particularly related to beam loading. The main observable is the **maximum energy**, as explained in the introduction, the maximum energy decreases when beam loading increases. The second observable is the energy spread of the accelerated beam. Without beam loading, the trailing bunch should face an E_z field rapidly varying with ξ from the front to the back of the bunch. However, as beam loading effects occur, the field becomes flatter, until it reaches an optimum (dependent on the trailing bunch current profile). If beam loading effects keep increasing, the field progressively becomes strongly reduced or even decelerating for the particles at the back of the trailing bunch: the wakefield becomes overloaded as shown in Fig. 5.8 (d).

During the experiment described in this section, the initial parameters of the beams slightly changed from a shot to another one. This was due to the natural fluctuations of the conventional accelerator. In particular, the compression of the beam, strongly related to the entrance time of the beam in the accelerator led the charge in each of the two bunches to fluctuate from a shot to another one. One dataset was particularly better than the others in terms of the energy spread of the accelerated beam, of the accelerated charge and peak energy. The quality of the data allowed to make a Gaussian fit of the accelerated beam, which is a repeatable and rigorous parameter measurement methods. From the EOS data of this dataset, the estimated mean interbunch distance was $100\ \mu m$, which is shorter than the usual value. This may be accounted for the better results of this dataset.

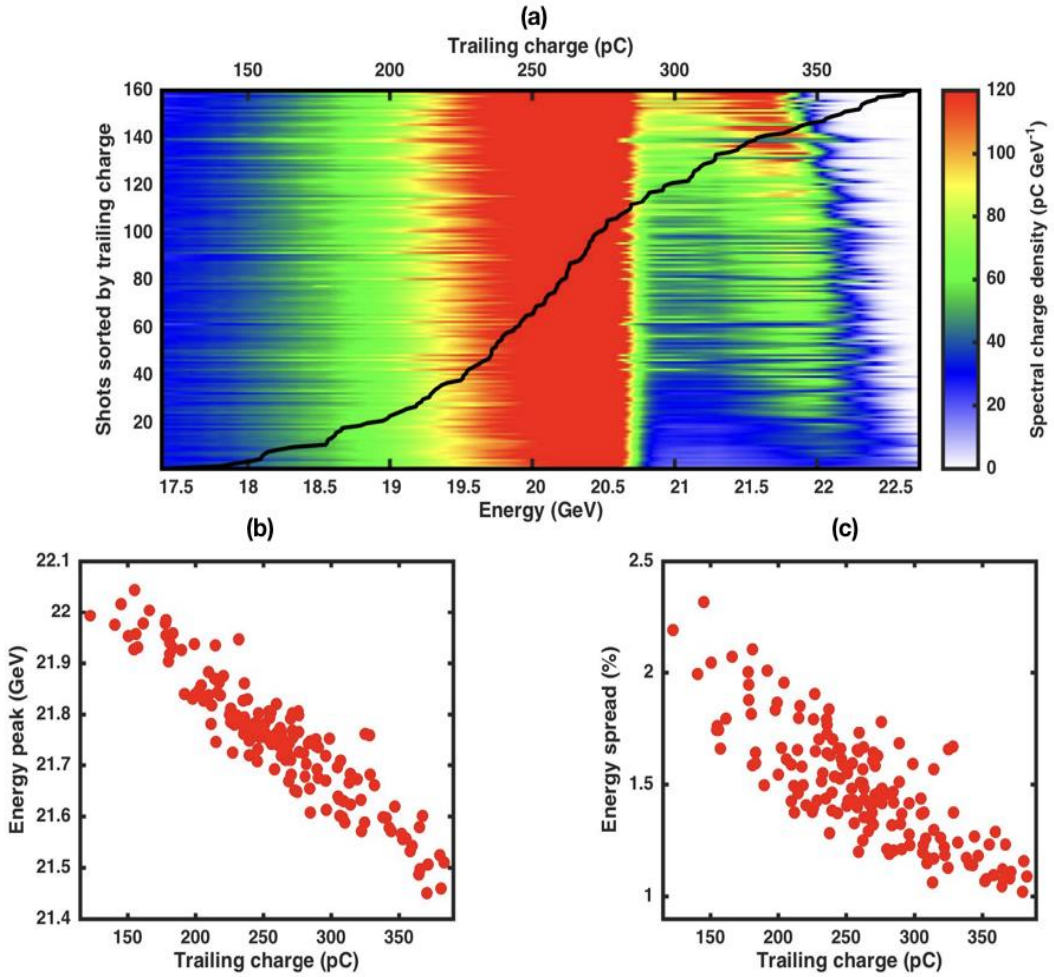

Figure 5.9: (a) Waterfall plot of the 160 spectra in which the beam loading effects are particularly visible. Each line is an integrated spectrum from the Cherenkov spectrometer. (b) Correlation between the trailing bunch charge and the peak energy of the accelerated bunch. (c) Correlation between the trailing bunch charge and the energy spread of the accelerated bunch.

The dataset is composed of 160 shots, that are displayed in Fig. 5.9 (a). Fig. 5.9 (a) is a waterfall plot of the spectrum of all the shots, sorted by increasing initial trailing bunch charge. The left y-axis is the shot number, the top x-axis represents the initial charge of the trailing bunch, while the bottom x-axis is the energy of the particles. Each horizontal line is an image of the spectrometer, integrated over the horizontal position, the dimension perpendicular to the dipole dispersion (vertical). Qualitatively, two correlations appear: the peak energy and the energy spread decrease with the initial trailing charge. The colorful waterfall plot is a first tool to identify this kind of correlations.

Going further into the quantification of the process, the trailing charge spanned in this dataset from 150 to 400 pC and the mean charge was 260 pC. The standard deviation was 55 pC. The average energy of the accelerated peak was 21.75 GeV, this is a 1.70 GeV gain on average, and the mean r.m.s. energy spread was 1.5%. On the waterfall plot depicted in Fig. 5.9 (a), energy spectra are sorted by increasing trailing bunch charge. Accelerated particles appear on the right, above 20.8 GeV (upper limit of the drive bunch). Two correlations can be seen: the peak

energy and the energy spread of the accelerated bunch decrease when the charge of the trailing bunch increases. The correlations with the trailing bunch charge are plotted in Fig. 5.9 (b) (for the energy of the accelerated peak) and Fig. 5.9 (c) (the energy spread is the width of the Gaussian fit of the peak). As the trailing bunch charge reaches its maximum value in the dataset, the energy spread decreases from 2% down to 1% while the energy gain reduces from 1.95 GeV to 1.45 GeV. Beam loading implies that the maximum longitudinal electric field is reduced as the charge of the trailing bunch is increased as demonstrated with Fig. 5.7 (c). Beam loading results also in a flattening of the electric field, both effects are observed and depicted in Fig. 5.9 (b) and (c).

The correlations of Fig. 5.9 (b) and (c) are coherent with a beam loading process. However, they may in principle be due to correlations of the peak energy and energy spread with the interbunch distance as well. By looking at Fig. 5.7 (a) we can guess the hypothetical effect of the interbunch distance on the peak energy and the energy spread. When the interbunch distance increases, the energy peak should increase as the maximum accelerating field seen by the trailing particles increases. On the other hand, the energy spread should decrease as the slope decreases "on top" of the E_z field oscillation. This is not the effect observed in Fig. 5.9 (b) and (c).

In addition, the data contain clear evidence that the interbunch distance is not correlated with the accelerated bunch parameters and with the initial trailing charge. In Fig. 5.10 (a) and Fig. 5.10 (b) can be seen plots of the peak energy and the energy spread as a function of the interbunch distance, no clear correlation is visible. Furthermore, in Fig. 5.10 (c) is the evidence that the trailing bunch initial charge is not correlated with the measured interbunch distance and that the clear correlations observed in Fig. 5.9 are not due to a coincidental correlation between interbunch distance and trailing charge in the incoming beam. These three clear results demonstrate that the initial trailing bunch charge alone is responsible for the correlation showed in Fig. 5.9.

Therefore, it is indeed only a modification of the initial beam charge that is to be accounted for the change in the peak energy and the energy spread of the accelerated positron bunch.

In the light of the theoretical models described in the beginning, we reached the conclusion that a clear beam loading phenomenon occurred during the acceleration process. The specific

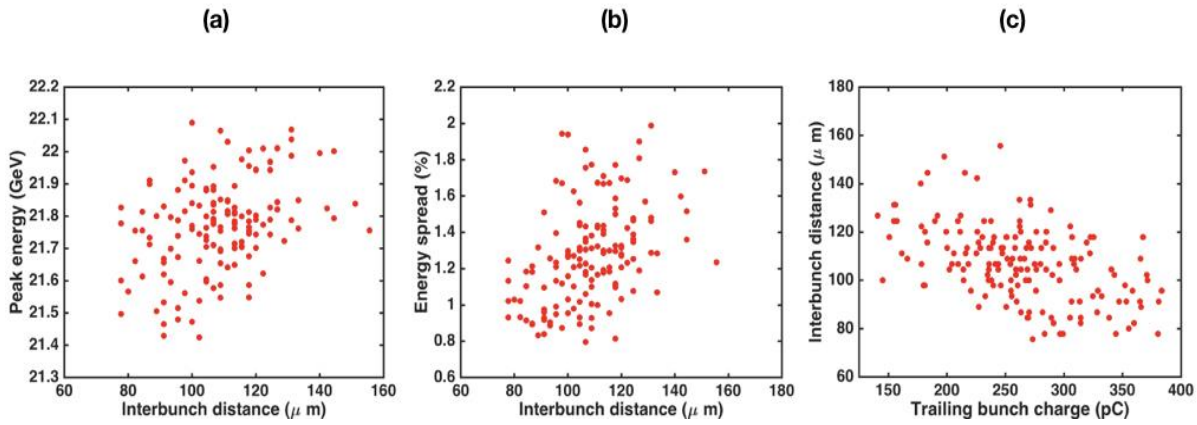

Figure 5.10: Absence of correlations with the interbunch distance. Plot of the peak energy of the accelerated bunch as a function of the interbunch distance (a), plot of the energy spread of the accelerated bunch as a function of the interbunch distance (b), plot of the interbunch distance of the accelerated bunch as a function of the trailing bunch charge (c).

parameters of the beams (low interbunch distance of order of $100\ \mu m$) during this dataset seem to explain the relatively good results. The acceleration of a distinct positron bunch has been accomplished.

However, the wakefield is expected to be very nonlinear in the result presented in this section. Therefore, this regime does not open the prospect of using a laser or electron driven wakefield to accelerate a distinct bunch of positrons. In fact, positron driven nonlinear wakefields are specific to positron drivers.

3. Acceleration regimes

In the electron or laser driven case, the transition from the linear to the nonlinear regime of wakefield driving has been studied both theoretically and experimentally. The parameters responsible for the regime transition were discussed. It appeared that the ratio n_b/n_0 plays a major role in the wakefield regime. When this ratio becomes much larger than 1, the regime becomes necessarily nonlinear **[Lu 05]**. Furthermore, another parameter was shown to be important in predicting the regime (relativistic versus non-relativistic), it is the normalized peak current of the drive bunch $\Lambda = 2I_p/I_A$ **[Lu 05, Lu 10]**. However, these results do not apply to positron drivers.

In fact, for positron driven waves, numerical simulations seemed to show that for an initial emittance achievable at FACET $\epsilon_x \times \epsilon_y = 100 \times 10\, mm^2.mrad^2$, whatever the drive beam initial diameter the beam would self-focus into the plasma and drive a nonlinear wakefield.

This section will be dedicated to the study of a wakefield regime transition. We will compare this experimental result with numerical simulations to show that initial emittance and beam diameter are both important parameters to reach a positron driven quasilinear wakefield.

a. Emittance manipulation system

A convenient method to modify the emittance of the beam when it enters the plasma relies on the insertion of a block of metal in the beam line to "spoil" the emittance just before the plasma oven. The system is visible in Fig. 5.1: a titanium wedge can be inserted in the beam, the variable thickness of the wedge allows to choose the degree of emittance spoiling.

Emittance growth when a charged particle beam goes through a dense material is a well described process. In fact, when a beam of charged particles crosses a dense block of matter, multiple scatterings of the particles in the beam occur. Therefore, the beam Twiss parameters and emittances are modified **[Reid 91, Olive 14]**.

The r.m.s. angle at which a particle will be scattered after traversing a thickness L of material is given by:

$$\theta_{rms}(L) = \frac{13.6\ MeV}{\beta cp[MeV]}\sqrt{\frac{L}{X_0}}\frac{9}{8}\left[1 + 0.038\ ln\left(\frac{L}{X_0}\right)\right] \qquad \textbf{(5.7)}$$

Where X_0 is the radiation length of the scattering material, for titanium, $X_0 = 3.56\ cm$. The material we consider in our experiment is Titanium as it is convenient to use and has a

radiation length which modifies the emittance of the beam by factors acceptable for our studies. In the following the subscript "Ti" indicates that the parameter value is given at the Titanium wedge position along the beam line, and the prime indicates that the Titanium effect has been taken into account. The Twiss parameters are modified according to the formulas:

$$\beta'_{Ti} = \frac{\beta_{Ti}}{\sqrt{1+\xi}} \quad \textbf{(5.8)}$$

$$\alpha'_{Ti} = \frac{\alpha_{Ti}}{\sqrt{1+\xi}} \quad \textbf{(5.9)}$$

$$\gamma'_{Ti} = \gamma_{Ti}\frac{1+\xi_0}{\sqrt{1+\xi}} \quad \textbf{(5.10)}$$

where

$$\xi = \frac{\theta^2_{rms}}{\epsilon/\beta_{Ti}} \text{ and } \xi_0 = \frac{\theta^2_{rms}}{\epsilon/\beta_0} \quad \textbf{(5.11)}$$

In formula (5.11), ϵ is the geometrical emittance, β_0 is the Twiss parameter β, taken at focus before spoiling the beam. The modification of the emittance is given by the formula:

$$\epsilon' = \epsilon\sqrt{1+\xi} \quad \textbf{(5.12)}$$

In the table of Fig. 5.11 are listed the modifications of the beam parameters due to the to presence of the Titanium wedge in the beam line. The wedge is setup $D = 156\ cm$ before the entrance of the plasma, in the picnic basket, but before the holed mirror, along the beam line. The mount was setup to insert the wedge at several fixed positions that correspond to the Titanium thicknesses given in the first column of the table.

Titanium Thickness (μm)	L/X_0	θ_{rms} (μrad)	$\theta_{rms} \cdot D$ (μm)	ϵ_x (μm)	ϵ_y (μm)
0	0	0	0	100	10
100	0.00281	27.5	45.9	171	34.3
139	0.00391	33.0	55.1	195	40.1
179	0.005	37.7	63.0	214	46.1
218	0.00613	42.2	70.5	234	51.3
257	0.00723	46.2	77.1	253	56
297	0.00834	49.9	83.4	270	60.3
382	0.0107	57.3	94.5	298	69.1

Figure 5.11: Titanium wedge thickness and modification of the beam parameters.

The emittances of the beam are therefore multiplied by factors of 1.7 to 3 in x and 3.4 to 7 in y. The Twiss parameters were modified also, these modifications were taken into account in the simulations. The corresponding experimental and numerical results will be introduced and discussed in the next section.

b. Nonlinear to quasilinear positron driven waves

Experimental results

When the beam emittance was increased, the beam-plasma interaction became accordingly weaker, and the accelerated bunch energy became closer to the drive bunch initial energy upper limit of $20.8\ GeV$. We had to use therefore, in order to quantify the energy gain, the maximum energy of the accelerated particles. The maximum energy was defined as the energy at which the accelerated spectrum crosses the $10\ pC\ GeV^{-1}$ threshold.

The comparison between the experimental results and the simulations is displayed in Fig. 5.12. This plot shows the maximum energy of the accelerated particles, as a function of the Titanium thickness. It shows that, in the experiment, the maximum trailing bunch energy decreases when the titanium thickness is increased. These experimental results show similar trends with particle-in-cell simulations.

A dataset was recorded to acquire these data. Each step contained 500 shots. The average interbunch distance measured on the EOS system was $135\ \mu m$. The initial charge in the beam was on average $480\ pC$ in the drive beam and $140\ pC$ in the witness bunch.

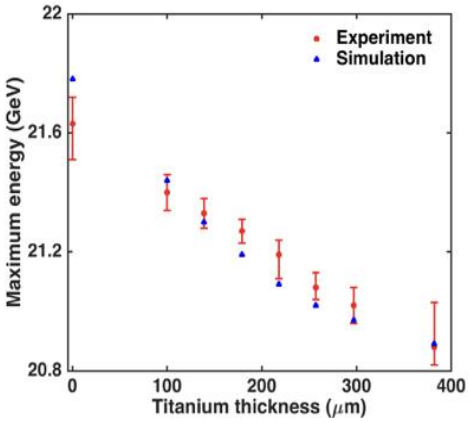

Figure 5.12: Maximum energy of the accelerated particles as a function of the titanium thickness.

Wakefield regime evolution

The plasma wakefield and its evolution are computed using the particle-in-cell code QuickPIC, with beam and plasma parameters similar to those of the experiment. The beam and the plasma wakefield evolve in the density up-ramp and in the first ten centimeters of the density plateau and then reach a quasi-steady state with negligible evolution.

In Fig. 5.13 is displayed the shape of the plasma wakefield in the middle of the plasma (at $z = 72.5\ cm$, i.e. after the quasi-steady state is reached), for emittances of $100 \times 10\ mm^2.mrad^2$ (no titanium), of $171 \times 34\ mm^2.mrad^2$ ($100\ \mu m$ of titanium), of $214 \times 46\ mm^2.mrad^2$ ($179\ \mu m$ of titanium) and of $270 \times 60\ mm^2.mrad^2$ ($297\ \mu m$ of titanium).

In the lower emittance cases Fig. 5.13 (a) and (b), the wake has a strong nonlinear structure. $n_{beam}/n_{plasma} = 14.2$ in (a) and $n_{beam}/n_{plasma} = 3.0$ in (b) for the drive bunch in the plasma. The longitudinal fields show very steep and asymmetric gradients and the shape of the transverse force (Fig. 5.13 (a)) strongly depends on the longitudinal coordinate $\xi = z - ct$. To be specific, the transverse wakefield is non-separable (it cannot be written as the product of a function of x and a function of ξ). The plasma wakefield in the ξy plane shows a nonlinear structure as well. In this regime, the accelerated bunch takes a specific arrowhead shape due to

the shape of the pseudo-potential **[Corde 15]**. The pseudo-potential well confines the trailing bunch in the transverse direction and permits its acceleration over the whole plasma length. Off-axis, the pseudo-potential well has two minimums that lead to a high trailing bunch density around these two positions. This is the source of the arrowhead shape.

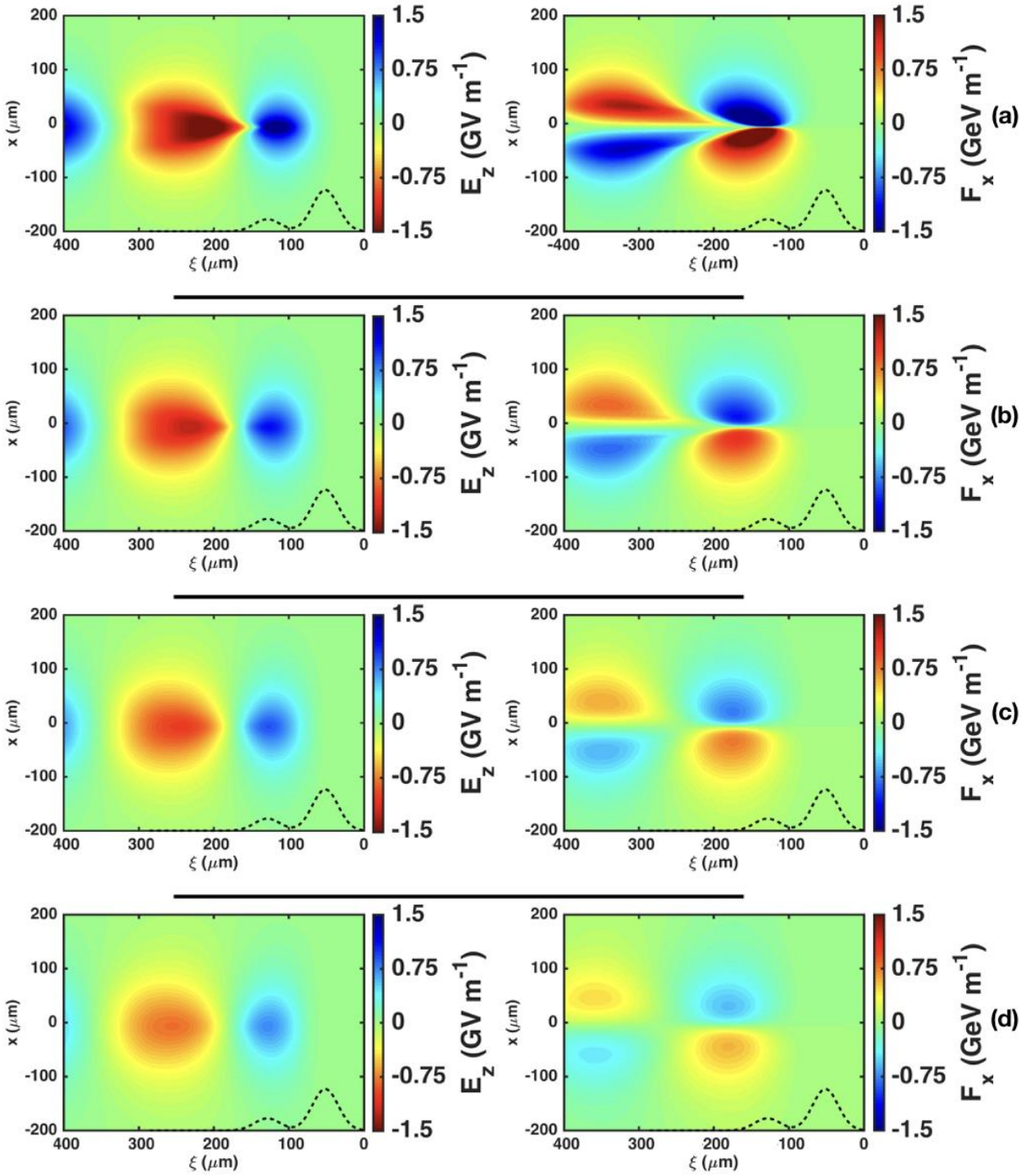

Figure 5.13: E_z field map (left) and transverse force F_x (right) after 72.5 *cm of propagation in the plasma, for the case without spoiling (a), with* 100 *μm of Titanium (b), with* 179 *μm of Titanium (c), with* 257 *μm of Titanium (d).*

In the higher emittance cases, Fig. 5.13 (c) and (d) the wakefield shows a quasi-linear structure. In addition, $n_{beam} / n_{plasma} = 1.9$ and $n_{beam} / n_{plasma} = 1.2$ for the drive bunch in the plasma. The maximum longitudinal electric field E_z is reduced from about 1.6 $GeVm^{-1}$ in Fig. 5.13 (a) to 0.8 $GeVm^{-1}$ in Fig. 5.13 (d). On this last figure, the wakefield is more regular and the transverse force takes a separable and sinusoidal form. Such a shape is characteristic of the linear regime of PWFA. The regime of Fig. 5.13 (d) is referred to as the **quasilinear regime**, similarly to what is used by the LWFA community to qualify wakefields driven by a laser pulse of $\boldsymbol{a_0}$~1 showing properties very close to the linear regime **[Schroeder 10]**.The quasilinear regime is interesting because of its more symmetrical properties for electrons and positrons, and its regularity may be an advantage for preserving positron beams quality during an acceleration to high energies **[Schroeder 10, Cros 16]**. In the experiment, acceleration of positrons from the trailing bunch was observed on the spectrometer over the whole range of achievable titanium thicknesses. However, when the emittance was progressively increased, the interaction of the beam with the plasma became accordingly weaker, and the energy of the accelerated bunch became close to the initial drive bunch energy, leading to a much less pronounced spectral peak on the spectrometer.

To conclude with this section, the use of a Titanium wedge allowed us to accomplish acceleration of a distinct positron bunch spanning nonlinear to quasilinear regimes. This is the first time that such a scheme is successfully demonstrated, and it also opens the prospect to accelerate an individual positron bunch from an independent laser or electron driver.

Regime transition and emittance

To search for a linear wakefield in the case of positron driven waves, numerical simulations seemed to show at first that when the emittance of the SLAC positron beam was used in the simulations $(\epsilon_x, \epsilon_y) = (100\ \mu m, 10\ \mu m)$, the beam would always self-focus, for any initial density. This evolution would always lead to a nonlinear wakefield regime. The previous paragraph showed that the spoiling of the beam led to accelerate particles first in a very nonlinear regime and progressively in a more linear one, until we could qualify the regime of "quasilinear". It seems that the emittance played a major role in this transition. A brief discussion regarding the regime transition and the role of emittance is therefore accomplished in this section.

In the experiment as it was performed at SLAC, the beam parameters at the plasma entrance were $(\sigma_x, \sigma_y) = (35\ \mu m, 25\ \mu m)$ and $(\epsilon_x, \epsilon_y) = (100\ \mu m, 10\ \mu m)$ in the absence of spoiling, with $(\alpha_x, \alpha_y) = (0, 0)$ (beam focus) at the entrance of the plasma. For the spoiled case ($297\ \mu m$ of titanium), the beam parameters at the plasma entrance were $(\sigma_x, \sigma_y) = (89\ \mu m, 86\ \mu m)$, $(\epsilon_x, \epsilon_y) = (270\ \mu m, 60\ \mu m)$ and $(\alpha_x, \alpha_y) = (-0.62, -2.70)$. We observed a change of the regime between the two parameters sets that is recalled in Fig. 5.14 (a) and (b).

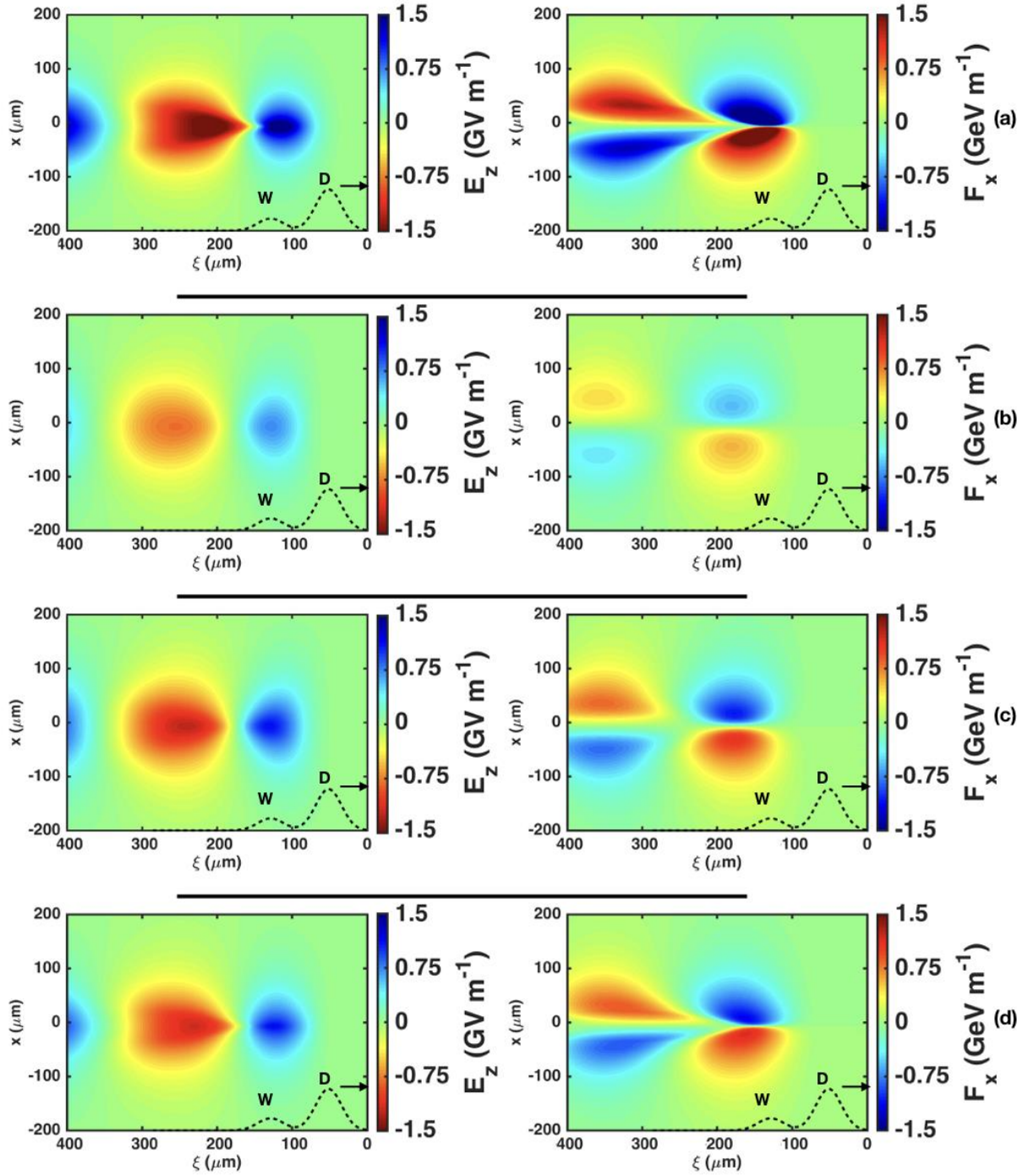

Figure 5.14: E_z field map (left) and transverse force F_x (right) after 72.5 cm of propagation in the plasma, for the four following cases: no spoiling (a), with 297 μm of Titanium (b), with the initial parameters $\sigma_x \times \sigma_y = 35 \times 25\ \mu m^2$ and $\epsilon_x \times \epsilon_y = 270 \times 60\ \mu m^2$ (c), with the initial parameters $\sigma_x \times \sigma_y = 89 \times 86\ \mu m^2$ and $\epsilon_x \times \epsilon_y = 100 \times 10\ \mu m^2$ (d).

We performed additional QuickPIC simulations to illustrate how the emittance is essential in this regime change. Two new sets of parameters were simulated. In the first set, the initial beam density (and therefore the initial beam sizes ($(\sigma_x, \sigma_y) = (35\ \mu m, 25\ \mu m)$) was kept constant, but the emittances were modified to fit the emittances values corresponding to 297 μm of Titanium $\left((\epsilon_x, \epsilon_y) = (270\ \mu m, 60\ \mu m)\right)$. In the second set, the initial emittances were kept constant $\left((\epsilon_x, \epsilon_y) = (100\ \mu m, 10\ \mu m)\right)$, but the initial beam density was varied by

setting the beam sizes to correspond to the values corresponding to $297\ \mu m$ of Titanium $\left((\sigma_x, \sigma_y) = (89\ \mu m, 86\ \mu m)\right)$. The four simulations are referred to as simulations A, B, C and D, and the corresponding beam parameters are listed in Fig. 5.15.

Simulation	Initial Size $(x \times y)$	Initial Emittance $(x \times y)$	FWHM Size at middle plasma	% charge in central spot	$\frac{n_{beam}}{n_0}$
A	$35 \times 25\ \mu m^2$	$100 \times 10\ \mu m^2$	$16 \times 4\ \mu m^2$	14.8	14.2
B	$89 \times 86\ \mu m^2$	$270 \times 60\ \mu m^2$	$61.5 \times 17.5\ \mu m^2$	17.9	1.2
C	$35 \times 25\ \mu m^2$	$270 \times 60\ \mu m^2$	$46 \times 15.5\ \mu m^2$	25.8	2.1
D	$89 \times 86\ \mu m^2$	$100 \times 10\ \mu m^2$	$31 \times 4.5\ \mu m^2$	10.2	4.8

Figure 5.15: Simulation parameters used to study the respective effects of emittance and initial beam density on the acceleration regime. The central spot sizes and charge percentage are calculated by taking into account all the particles initially in the drive bunch used in the simulation.

In simulation C corresponding to Fig 5.14 (c), increasing the emittance only (the initial beam density being kept constant) effectively led to a quasi-linear regime. The field map is very symmetrical and has a sinusoidal dependence in ξ. The longitudinal fields have a cosine-like shape. By contrast, simulation D, which corresponds to Fig 5.14 (d), where the initial beam density is decreased while the initial emittance is kept constant, the regime is still nonlinear but the field amplitude is reduced compared to case A, Fig 5.14 (a). The transverse force does not exhibit any sinusoidal shape and the variables ξ and x are not separable, this is still a nonlinear wakefield regime. As a result, increasing only the emittance as in C leads to a quasilinear regime. In fact, the large emittance prevents a strong self-focusing so that the beam reaches larger spot sizes and contains more charge in its central spot. Most of the charge spreads transversally and does not contribute to drive a strong wakefield as can be seen in the table of Fig. 5.15. In case D by contrast, the central spot has a lower relative charge than in C, but is also much smaller due to the strong self-focusing. Therefore, the drive bunch in case D can excite a more intense wakefield, and as a result, the regime remains nonlinear.

To conclude with this discussion, while the change in the initial beam density does have the effect of reducing the field amplitude, the emittance seems to be mainly responsible for the change of regime, from nonlinear to quasilinear.

The second part of the manuscript was dedicated to the trailing positron bunch experiment report. After a description of the context, SLAC facility was presented, and the results were discussed thoroughly. This experiment was serving the ambition of the plasma based acceleration research community to build a plasma based particle collider. The next chapter will be dedicated to an experiment that serves the same purpose: in order to facilitate research regarding beam driven wakefields, it would be convenient to accomplish such experiments in a small-scale university laboratory. This is why a hybrid LWFA-PWFA experiment was setup at LOA: it intended to use a laser produced electron beam to drive a plasma wakefield.

Part III

Chapter 6

Hybrid LWFA-PWFA experiment at Laboratoire d'Optique Appliquée

In this chapter I report on the first hybrid LWFA-PWFA experiment performed at LOA. The goal of this experiment was to study the interaction of an electron beam created by LWFA with a plasma and to see how it can be used for PWFA purpose. I first introduce the theory of physical processes involved in **Laser Wakefield Acceleration**. In the second section, I give a short presentation of the **Salle Jaune facility** in which LWFA experiments take place. The last section is dedicated to the **experimental setup** of the hybrid LWFA-PWFA and to the **results** obtained during the 2017 campaign.

Contents

1. Acceleration, trapping and injection of particles in plasma wakefield

Laser Wakefield Acceleration is a plasma-based scheme in which a plasma wave is excited by a very intense and ultrashort laser pulse. The theory of laser driven plasma waves was derived in Chapter 3. Unlike in some PWFA experiments (see Chapter 4 and 5) when LWFA experiments are performed in facilities such as the Salle Jaune at LOA, accelerated electrons, come from the plasma itself. Important physical processes related to LWFA experiments such as electrons trapping needs to be presented. The theory of injection is summarized below. It explains how some electrons can be trapped in the plasma wave and gain a substantive amount of energy.

a. Phase velocity of plasma density waves

It is important to recall first the wakefield velocity expression in the case of a LWFA scheme. In fact, the phase velocity of the plasma wave is a concept of prime importance to understand how some particles can be "trapped" inside the wakefield and increase their energy by staying in the accelerating E_z field. The 1D dispersion relation **(2.12)** provides the group velocity of the laser, and thus the phase velocity of the plasma wave. From the relation $\omega^2 = \omega_p^2 + k^2c^2$, one gets: $v_g = c\left(1 - \frac{\omega_p^2}{\omega^2}\right)^{1/2}$. The phase velocity of the laser is given by $c\left(1 - \frac{\omega_p^2}{\omega^2}\right)^{-1/2}$.

The phase velocity of the plasma wave is the group velocity of the laser. It is therefore smaller than c, and smaller than the velocity of the relativistic electrons produced in the LWFA experiments. Note that corrections of the phase velocity of the plasma wave in the case of very strong drivers **[Decker 94, Lu 07]** are required.

For instance, in a plasma of density $n_0 = 10^{19}\, cm^{-3}$, the group velocity of the laser is $\sim 0.997\, c$, by contrast, electrons whose energy is $100\, MeV$ have a velocity of $\sim c\,(1 - 1.3\ 10^{-5})$.

b. Acceleration, trapping and LWFA phase detuning

Trapping and acceleration of particles in the plasma wake

In 1D, the dynamics of particles in the wake can be simply described using the model shortly presented here. This model already gives insight into the physics and allows to understand behaviors that occur in 3D problems. Effects such as transverse motions, evolution of the laser driver or beam-loading require 3D PIC simulations. Starting from the equations of motion of a test electron in the phase space (ξ, γ), where $\beta = \frac{v}{c}$ and $\beta_p = \frac{v_p}{c}$ **[Esarey 95]**:

$$\frac{d\gamma}{dz} = -\frac{\partial \phi}{\partial \xi} \quad \textbf{(6.1)}$$

$$\frac{d\xi}{dz} = \frac{\beta_p}{\beta} - 1 \quad \textbf{(6.2)}$$

The Hamiltonian for a test electron can be calculated from these last two equations, it is given by **[Esarey 95, Esirkepov 06]**:

$$H(\xi, \gamma) = \gamma - \beta_p\sqrt{\gamma^2 - 1} - \phi(\xi) \quad \textbf{(6.3)}$$

Where $\phi(\xi)$ is the potential of the wakefield, oscillating between ϕ_{min} and ϕ_{max}. H does not depend explicitly on the variable z and it is therefore constant over the orbit of a test electron. The relation $H(\xi,\gamma) = H_0 = \gamma - \beta_p\sqrt{\gamma^2 - 1} - \phi(\xi)$ allows to draw the trajectory of a test electron in phase space. The phase portrait, i.e. the trajectory of particles in phase space, provides information about the electrons that can extract energy from the plasma wave. It is depicted in Fig. 6.1.

The phase portrait can be understood thanks to the study of the Hamiltonian. The Hamiltonian H has fixed points, corresponding to $\frac{\partial H}{\partial \xi} = 0$ and $\frac{\partial H}{\partial \gamma} = 0$. The fixed points are stable states of the system for $\phi = \phi_{max}$ and unstable for $\phi = \phi_{min}$, with each time $\gamma = \gamma_p = \left(1 - \beta_p^2\right)^{-1/2}$. A curve has a particular importance in the phase-space picture we consider: the **separatrix**. It distinguishes the closed orbits of trapped electrons and the open orbits of untrapped electrons that flow from the right to the left of the phase portrait. Both behaviors appear in Fig. 6.1 (b). The equation for the **separatrix** can be obtained from the relation:

$$H(\xi,\gamma) = H(\xi_{min},\gamma_p) \tag{6.4}$$

which can be solved to find the formula for $\gamma(\xi)$:

$$\gamma(\xi) = \gamma_p(1 + \gamma_p(\phi(\xi) - \phi_{min})) \pm \gamma_p\beta_p\left[\left(1 + \gamma_p(\phi(\xi) - \phi_{min})\right)^2 - 1\right]^{1/2} \tag{6.5}$$

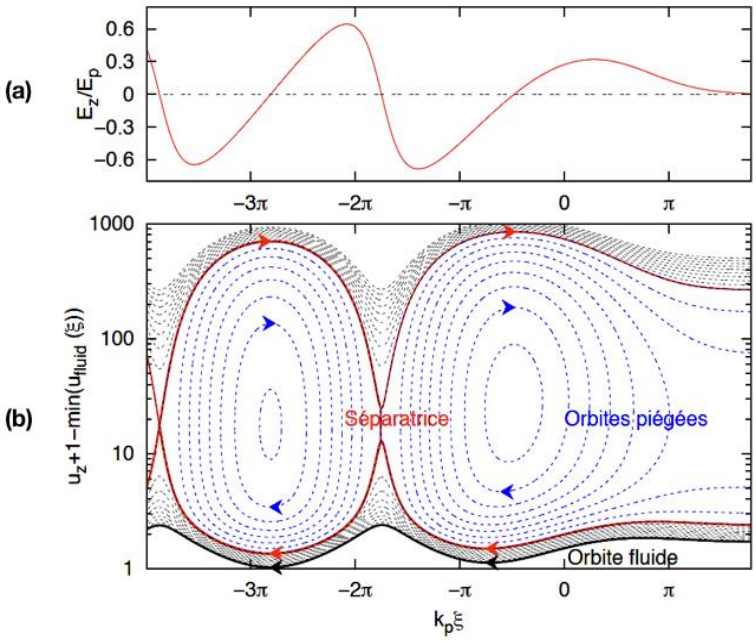

Figure 6.1: (a) Longitudinal electric field of a nonlinear laser driven wakefield (b) Phase portrait of the particles in the plasma. The separatrix (red line) distinguishes the trapped particles from the particles traversing the wakefield. The vertical coordinate is the speed. Figure from ***[Réchatin 10]****.*

In particular, the minimum and maximum energy for particles whose orbits are infinitesimally close to the separatrix are:

$$\gamma_{max,min} = \gamma_p(1 + \gamma_p \Delta\phi) \pm \gamma_p \beta_p \left[\left(1 + \gamma_p \Delta\phi\right)^2 - 1\right]^{1/2}$$

with $\Delta\phi = \phi_{max} - \phi_{min}$. The picture in phase space helps to understand how electrons can be trapped. When an electron is at $\xi = \xi_{max}$ with an energy higher than $\gamma_{min} mc^2$ and smaller than $\gamma_{max} mc^2$, it is simply trapped.

When one considers a thermal model for the plasma, it appears that a fraction of the electrons from the background, those whose energy is greater than the trapping energy, can be trapped **[Esarey 09].** However, this is not a reliable solution to produce high charge accelerated beams. Different concepts have been proposed and demonstrated to control and to improve electrons injection.

The maximum energy the accelerated particles can reach can be estimated using the expression of γ_{max} **[Esarey 95]**.

Phase detuning

Phase detuning is a fundamental limitation of Laser Wakefield Acceleration schemes. This limit comes from the difference between the phase velocity of laser driven plasma waves (approximately equal to the group velocity of the laser) and the speed of accelerated particles that becomes close to c as soon as their energy is of the order of mc^2.

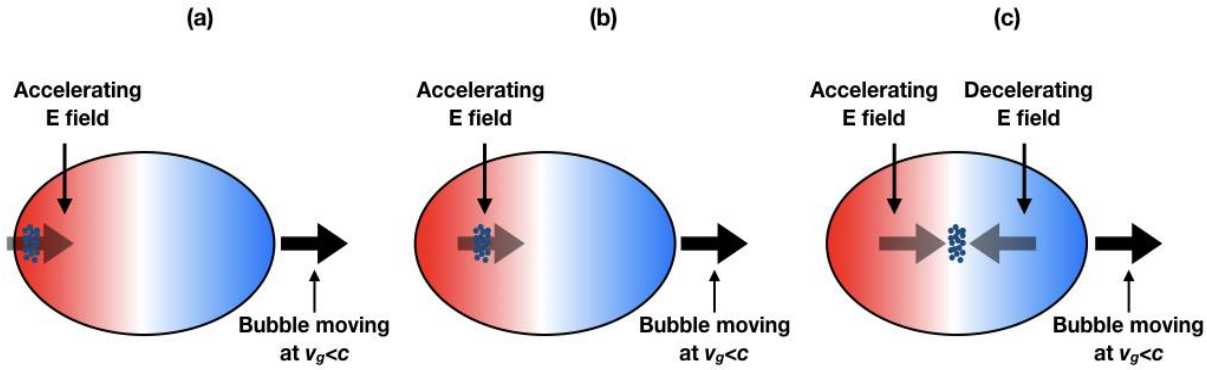

Figure 6.2: (a) In a laser produced wakefield, some particles (electrons) are injected at the back of the bubble, they face an accelerating wakefield. (b) Accelerated particles move faster than the plasma wave, they reach the end of the accelerating field. (c) The second half of the bubble forces the particles to decelerate, the maximal energy reached is limited: this is the dephasing limit.

If an electron is injected at the back of a plasma period, and remains trapped in the wakefield, it will be accelerated further. Its speed will become close to c and will outrun the speed of the plasma wave **[Joshi 84]**. The particle will eventually reach the front half of the plasma period where the field is no longer accelerating as depicted in Fig. 6.2. In the front half of the plasma period, the particle begins to decelerate, this phenomenon limits the maximum energy reached by the accelerated particles in LWFA schemes. For instance, in the linear regime, dephasing occurs after a time $t_d = L_d/c$ satisfying the relation $\left(v - v_p\right)t_d \approx \lambda_p/2$, under the approximation $v \approx c$. One gets $L_d \approx \gamma_p^2 \lambda_p \approx \lambda_p \sim 2\ mm$ for a density of $n_0 = 9.10^{18} cm^{-3}$,

where $\gamma_p = \left(1 - v_p^2/c^2\right)^{-1/2}$ **[Esarey 95, Esarey 96a]**. A correction has to be added in the case of non-linear plasma waves: $L_d \approx \frac{2\sqrt{a_0}\lambda_p^3}{3\pi\lambda^2}$ **[Lu 07]**.

A solution to this problem was found two decades ago **[Sprangle 01]**. It was suggested to spatially tailor the plasma density so that the accelerated bunch of electrons would see an accelerating field whose phase velocity is c. A successful experimental demonstration of this technique was accomplished at LOA **[Guillaume 15]**. The authors introduced a density step to reduce suddenly the plasma wavelength and therefore "force" the bunch to stay in an accelerating region for a longer time.

Phase detuning competes with two other limitations: laser diffraction and laser energy depletion in the plasma **[Esarey 96b]**. However, phase detuning remains probably the most serious challenge for applications of LWFA.

c. Injection techniques

Laser driven nonlinear wakefields are usually produced in plasmas whose densities are in the range $10^{18} - 10^{19}\ cm^{-3}$. Therefore, the corresponding plasma wavelengths are in the range $10 - 40\ \mu m$. In such wakefields, particles have to be injected in an area whose dimension is of the order of the plasma wavelength. Injection in such cavities is a real challenge. Several physical mechanisms leading to this process were studied and demonstrated, the most important ones are listed below.

Optical or ponderomotive injection

A scheme using a secondary laser pulse was proposed to inject electrons in a plasma wakefield driven by a primary intense laser **[Umstadter 96]**. A second, perpendicular laser beam forces a fraction of plasma electrons into motion thanks to its transverse ponderomotive force. These accelerated electrons are trapped in the wakefield driven by the primary laser. A similar scheme was suggested in the so-called colliding laser pulse scheme **[Esarey 97]** and experimentally demonstrated with a counter propagative beam **[Faure 06]** that has allowed to produce high quality electron beams with controllable parameters. It was shown that the beam energy and charge of the accelerated particles were controlled by changing the intensity and delay of the secondary laser pulse (the injection pulse) **[Rechatin 09]**. Optical injection can provide extremely stable, quasi-monoenergetic bunches of electrons. **[Rechatin 09]** accomplished it with two lasers of parameters $a_0 = 1.3$ and $a_1 = 0.4$, in a helium plasma of density $n_e = 7.5\ 10^{18} cm^{-3}$. The bunches, for a specific choice of synchronization position in the gas **[Rechatin 09]**, have a central energy of $206\ MeV$, with an energy spread of $14\ MeV\ \pm 3\ MeV$, and a total charge of $13\ pC$.

The colliding pulse optical injection scheme we just mentioned is responsible for a longitudinal injection of particles in the wakefield. Another optical-injection scheme was discovered through numerical simulations by LOA researchers **[Lehe 13**], but it relies on transverse optical injection. This scheme is expected to provide low emittance beams ($0.17\ mm.mrad$), higher charge ($50 - 100\ pC$) and a low energy spread as well (2 %).

Density downramp injection

An inhomogeneity in the plasma that sustains the density oscillations can be the source of local injection of particles. It occurs in the case of very non-linear plasma waves driven by a laser **[Bulanov 98]**. It was first demonstrated theoretically, and then studied experimentally. In this scheme, a density gradient is used to change locally the wake phase velocity to lower the threshold velocity required to inject plasma electrons into the wake **[Geddes 08]**.

Longitudinal self-injection

The injection schemes presented above are all controlled injection techniques. They rely on active and complex systems to inject electrons in the wakefields. The following two techniques are self-injection methods, they are simpler and therefore convenient to realize.

Longitudinal self-injection of electrons from the plasma background is a process similar to longitudinal wavebreaking in 1D. It is the result of the relativistic lengthening of the plasma wake that follows strong relativistic self-focusing effects. In this case, injected electrons are those that are the closest to the propagation axis before the perturbation of the plasma reaches them. Those electrons undergo the whole first period of the plasma wave, and when they reach the rear of the first bucket, i.e. the first period of the wave, their velocities exceed slightly the phase velocity of the plasma wave. Therefore, they are trapped and can gain energy from the wave. It was first observed and studied at LOA **[Corde 13]**. The experiment was accomplished in Salle Jaune, with a laser peak power of $30\ TW$. The main laser pulse which was driving the wakefield, contained $1\ J$ of energy, and lasted $35\ fs$. The laser parameter was then $a_0 = 1.4$. In the experiment, a gas cell of adjustable length was providing a plasma with a density of $n_0 = 10^{19}\ cm^{-3}$. Longitudinal injection was demonstrated to occur after a few hundred of micrometers at any plasma density and to stay dominant at lower density ($n_0 < 10^{19}\ cm^{-3}$). The charge of the longitudinally injected bunches is low $\sim 2 - 10\ pC$, the spectrum is quasi-monoenergetic and very stable shot to shot.

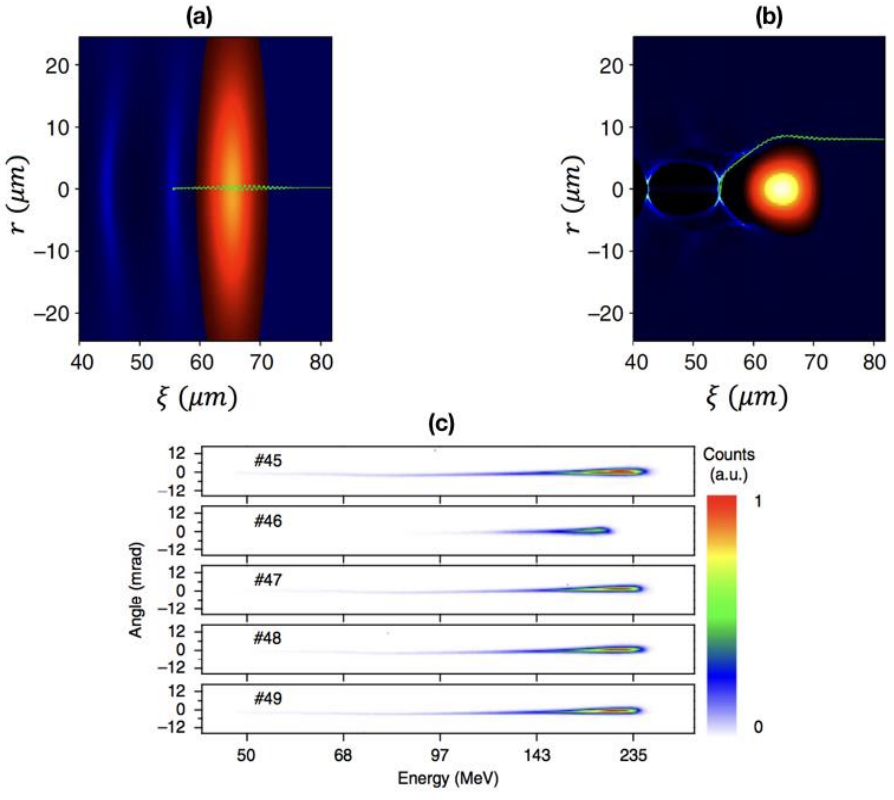

Figure 6.3: (a) Trajectory of a particle injected through longitudinal injection. (b) Example of a trajectory of a particle injected through transverse injection. (c) Example of longitudinal self-injected electron bunches. Figure from ***[Corde 13]***

The trajectories of trapped electrons in the wakefield, for the transverse and longitudinal self-injection cases, are depicted in Fig. 6.3 (a) and (b). Spectra obtained from the experiment of **[Corde 13]** with longitudinal self-injection are shown in Fig. 6.3 (c).

Transverse self-injection

Transverse self-injection is another self-injection scheme, that results in lower quality bunches that the previous one, and relies on a different type of wavebreaking. It can have three variants.

In the bubble regime, transverse self-injection can occur from electron moving backwards in the wave, inside the sheath. In fact, when those electrons cross the axis and contribute to close the bubble structure they can be trapped **[Lu 07]**. A trajectory is displayed in Fig. 6.3 (b). It was shown also that abrupt changes in the cavity frontier radius could lead to sudden trapping of electrons **[Kalmykov 09]**. In both cases, injected electrons are those that are far from the propagation axis (at a distance of about a cavity radius) before the arrival of the laser driver.

An experimental demonstration of a transverse self-injection process was accomplished at LOA **[Corde 12]** along with the longitudinal self-injection demonstration described in the previous paragraph. It was shown that transverse self-injection can occur with the same experimental parameters, but after a longer propagation of the laser in the gas. Transverse self-injection provides higher charge bunches, of order $50 - 100\ pC$, with a broad spectrum. The maximal electron energy in this experiment was $250\ MeV$ as well. The process has a low stability and is very sensitive to the shot-to-shot fluctuations of the laser intensity profile. The produced electron bunches have higher emittance compared to longitudinal self-injected ones.

Ionization injection

Generally speaking, ionization injection such as the one performed in a mixture of helium with a small percentage of nitrogen **[Pak 10, McGuffey 10]** uses the successive ionization thresholds of a large Z gas to inject particles in the wakefield. This process allows to ionize and release electrons near the peak intensity of the laser in the plasma, which can then be easily trapped by the wake as they are born inside the wake at an optimal location. However, ionization injection occurs mostly continuously in the wake, which implies a higher energy spread than other injection techniques.

These physical processes are necessary for LWFA experiments such as the one performed at Laboratoire d'Optique Appliquée. These LWFA experiments rely on the Salle Jaune facility that is described in details in the next section.

2. Salle Jaune facility

a. Facility

Salle Jaune is an experimental facility of rather modest dimensions compared to accelerators such as SLAC National Accelerator Laboratory. It consists of two rooms on top of each other, each of dimensions about $20 \times 30\ m$ drawn in Fig. 6.4 (a).

The facility relies on a $2 \times 50\ TW$ laser system. Two laser pulses containing each $1.5\ J$ named P1 and P2 are used. An additional beam named P3 with a lower energy is available and can be used as an optical probe for various diagnostics. The central wavelength of the main laser is $810\ nm$, and the bandwidth is $40\ nm$. The main system can operate at $1\ Hz$, however, data acquisition at full power is generally performed at 0.1 or 0.2 Hz. The pulses are compressed down to $30\ fs$, thanks to the Chirped Pulse Amplification technique described in the section dedicated to lasers. A picture of the laser chain is reported in Fig. 6.4 (b).

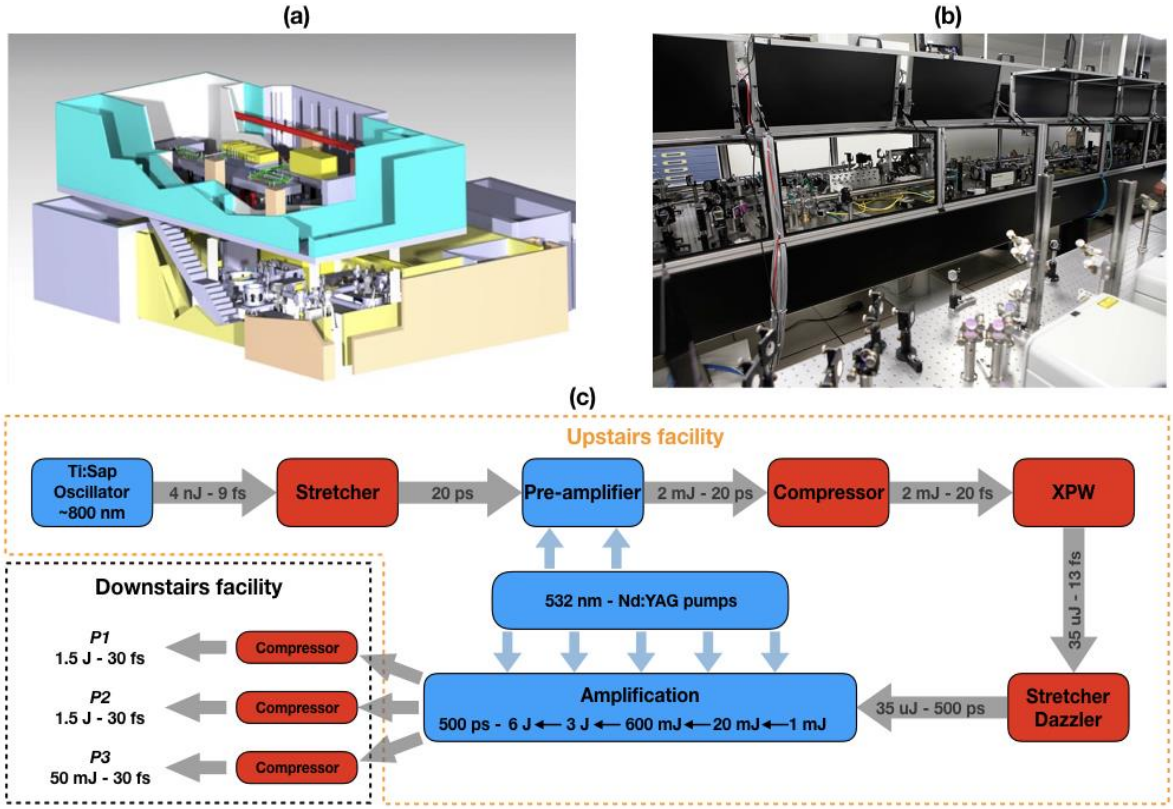

Figure 6.4: (a) 3D map of the Salle Jaune facility. Upstairs is most of the laser chain while the compressors and the experimental chambers are downstairs. (b) Picture of the laser chain. (c) Schematic of the whole laser chain, with the evolution of the beam parameters.

The laser chain (Fig. 6.4 (c)) begins with a Ti:Sapphire oscillator that provides a $9\ fs$ pulse with a nJ of energy. At that stage, the spectrum is broad and centred on $800\ nm$, the repetition rate is much higher than the final laser rate: $88\ MHz$. The pulse is then stretched temporally to reach a length of $20\ ps$, so that it can be amplified to a total power of $2\ mJ$. After this pre-amplification, a first compressor system brings the pulse back to $20\ fs$, and the rate is at that stage of $10\ Hz$. An XPW system filters the pulse: contrast is a key parameter to

ensure a good laser-plasma interaction. The contrast reached (at the end of the laser chain) thanks to the XPW is 10^{10}, $100\ ps$ before the main pulse and 10^{7}, $10\ ps$ before the pulse. After the XPW, the beam energy is reduced to $35\ \mu J$. The laser pulse is then stretched again to $500\ ps$ and enters a Dazzler system, an acousto-optic modulator that will manipulate its spectral phase. This setup is important to prevent the spectral shortening due to the main amplifier stage at the next step of the chain. Several $532\ nm$ Nd:YAG lasers pump the five amplification stages. The pulse is amplified at each stage, it is brought by the first stage to $1\ mJ$, then to $20\ mJ$ after the second. Successively, the pulse energy increases to $600\ mJ$, then $3\ J$ and finally $6\ J$. At the end of the amplification chain, the beam is divided into three beams, P1, P2 with the same energy, and P3 used as a probe containing very little energy. All these processes take place at the second floor of Salle Jaune. The beam is then transported downstairs by sets of afocal lenses systems, to enter the compressors. In the experimental chamber, the beams have a diameter of almost $6\ cm$ for P1 and P2 and $3\ cm$ for P3. The beams are compressed independantly to $25-30\ fs$, FWHM.

During the experiments as depicted in Fig. 6.5, P1 is focused thanks to a parabola, and P2 thanks to cylindrical lenses. The quality of the focal spots is corrected thanks to deformable mirrors for P1 and P2. This adaptive optics system relies on a phase-front sensor on which is imaged the surface of the deformable mirror. The HASO phase-front sensor measures the front aberrations and reconstructs it by using the decomposition of the phase transverse profile on Zernike polynomials. The deformable mirror can then compensate for each component on Zernike basis. As a result, the focal spot quality can be greatly improved. Around 60% of the beam total energy (total energy available in the experimental chamber) is contained in the focal spot.

The optics in the chain deteriorate when the beams are used at full power. As a result, the energy on target can be reduced from an experimental campaign to another one. When the optics in the chain are perfectly clean, about 60 % of the energy after the final amplification stage arrive in the experimental chamber where the target is.

LWFA experiments in Salle Jaune take place either in the cubic chamber ROSA, or in the circular chamber ZITA. A typical experiment setup is depicted in Fig. 6.5, for the circular chamber ZITA. This is a schematic of the 2017 hybrid LWFA/PWFA experiment in the circular chamber ZITA. As can be seen in Fig. 6.5:

P1 is the main beam that is used for LWFA. It is deflected by two mirrors onto an off-axis parabola. In the experiment depicted in this part, the parabola is a 1-m focal length parabolic mirror with a diameter of 6 *cm*.

P2 is used in the hybrid experiment as a pre-ionizing beam for the second gas jet. An optical elevator brings the beam up where two cylindrical lenses focus it in the second gas jet, along a line. P2 propagates in the second gas jet moving downwards from the top of the chamber, with a 10° angle. In the first experimental campaign described in this chapter, P2 was not used.

P3 is used as a probe beam for a side-view diagnostic. In the hybrid experiment, it is used with the Wollaston cube interferometer diagnostic system. P3 probes the interaction region in the horizontal plane, and is collimated with a diameter of 3 *cm*.

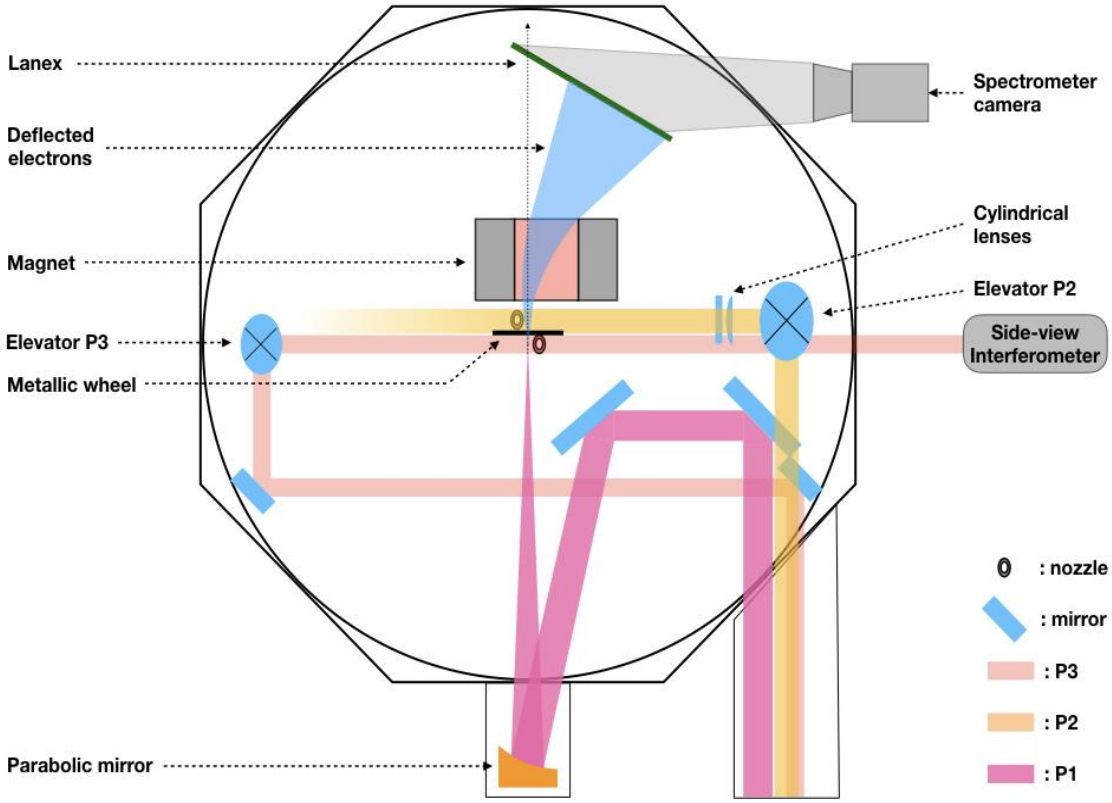

Figure 6.5: Schematic of the hybrid LWFA/PWFA experiment.

Two diagnostics are constantly used in the experiment in Salle Jaune. The first one, the Nomarski side-view interferometer, allows to monitor the laser and electron beam propagation in the gas jet targets. The second one, the electron spectrometer, is used to monitor the electron energy and divergence distributions.

b. Energy spectrometer

The electron spectrometer relies on a permanent dipole, a magnet whose field deflects the electron beam in the horizontal plane and on a Lanex screen that emits light when the electrons interact with it. The Lanex is a Kodak fine scintillating screen that measures $35 * 180\ mm^2$. A 16 $bits$ Hamamatsu camera is used to collect the light emitted by the Lanex after the particles reach it. In Fig. 6.6 (a) is a schematic of the setup, and Fig. 6.6 (b) and (c) illustrate two examples of electron spectra.

For a particle with an energy E at the exit of the gas jet, a simple code that solves the equation of motion of an electron in a B field allows to calculate the position at which the particle reaches the screen. The map of the B field must be known to draw the curve $s(E)$, position of the electron on the screen as a function of their energy. It is then possible to replace the x-axis of an image with the result $s(E)$. To do that, a calibration of the axis origin on the camera image is required. In addition, the magnet is setup on a translation stage, which allows to remove it and therefore to record the position on the screen that corresponds to un-deflected particles (that would correspond, in the presence of the dipole to infinite energy particles). The exact geometry of the setup is necessary to compute the curve $s(E)$. The resolution is calculated while supposing a constant divergence of 3 $mrad$ for all energies.

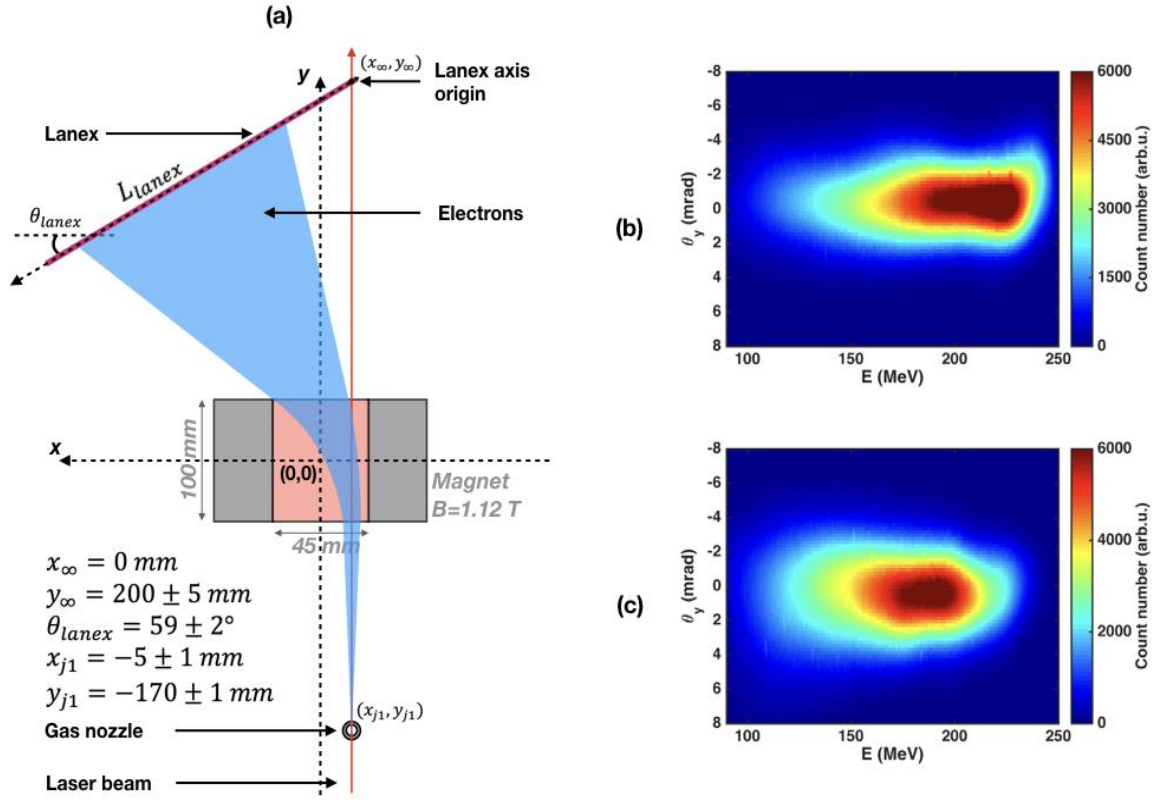

Figure 6.6: (a) Schematic of the spectrometer system. (b), (c) Examples of electron bunch spectra measured by the spectrometer. The images were processed: the energy axis is established thanks to a code which calculates the trajectories of the electrons in the field of the magnetic dipole.

Depending on the choice of setup, the Salle Jaune spectrometer allows to detect electrons of energy in the range $40 - 400\ MeV$.

The calibration of the Lanex light emission and light collection by the camera was accomplished in the laboratory in the past **[Glinec 06]** for the previous system of Salle Jaune. However, the calibration of the new Hamamatsu camera is yet to be done and will probably be accomplished during the next experimental campaign. For now, the number of counts on the camera chip will be used to quantify the signal intensity without at the moment the absolute value of the charge.

c. Side-view interferometer

During the experiments, the gas is delivered through a nozzle using a pulsed electro-valve. The density profile of the jet is determined by the shape of the nozzle, whereas the maximal density is given by the backing pressure. We use to measure the plasma density a single shot measurement method. This method relies on a Nomarski interferometer, based on the use of a Wollaston cube **[Small 72]**. The probe beam, P3, propagates horizontally, and exits the chamber where an imaging system composed of two lenses of focal length 60 *cm* projects it onto a CCD camera chip as depicted in Fig. 6.7 (a). The plane of the plasma is conjugated with the plane of the CCD chip. A Wollaston prism is setup just after the second lens and separates the components of the incoming light onto its two axes. Therefore, on the chip of

the camera appears a spot for each polarization component. The incoming light is projected by the first polarizer, before the Wollaston cube to obtain the same intensity on each of the two spots. From the second lens to the CCD chip the beams are collimated: they overlap on the camera. At that point, the light of the spots cannot interfere with each other as their polarization is orthogonal. That is why the second polarizer is setup and forms a 45° angle with each beam polarization. The beams emerging from the second polarizer can interfere.

The distance between the two focal spot centers is $a = \alpha . f_{L2}$ where alpha is the Wollaston cube angle (multiplied by the refractive indices difference), and f_{L2} is the focal length of the second lens. The inter-fringe distance is then given by the usual formula for interference from two coherent point-like sources interfering at infinity: $\delta = \lambda f_{L2}/a$. Fringe spacing can therefore be written as a function of the wavelength of the probe and the Wollaston angle only: $\delta = \lambda/\alpha$.

The choice of the lenses focal length was made to image a window of 1 cm^2 onto the 1 cm^2 CCD chip. The Wollaston angle was chosen to resolve spatially the plasma density gradient and ensure that at least 5 pixels are used for one inter-fringe spacing on the chip. For a probe at $\lambda = 800\,nm$, and a Wollaston with an angle of $\alpha = 1.5°$, a $14\,bits$, $4240 \times 2824\,pixels$ Point Grey camera, the resolution is of $\sim 10\,pixels/fringe$.

The gas flow is very slow compared to the passage of the 30 fs-long probe beam moving at the speed of light. When the probe samples the gas after the main beam (P1) created a plasma,

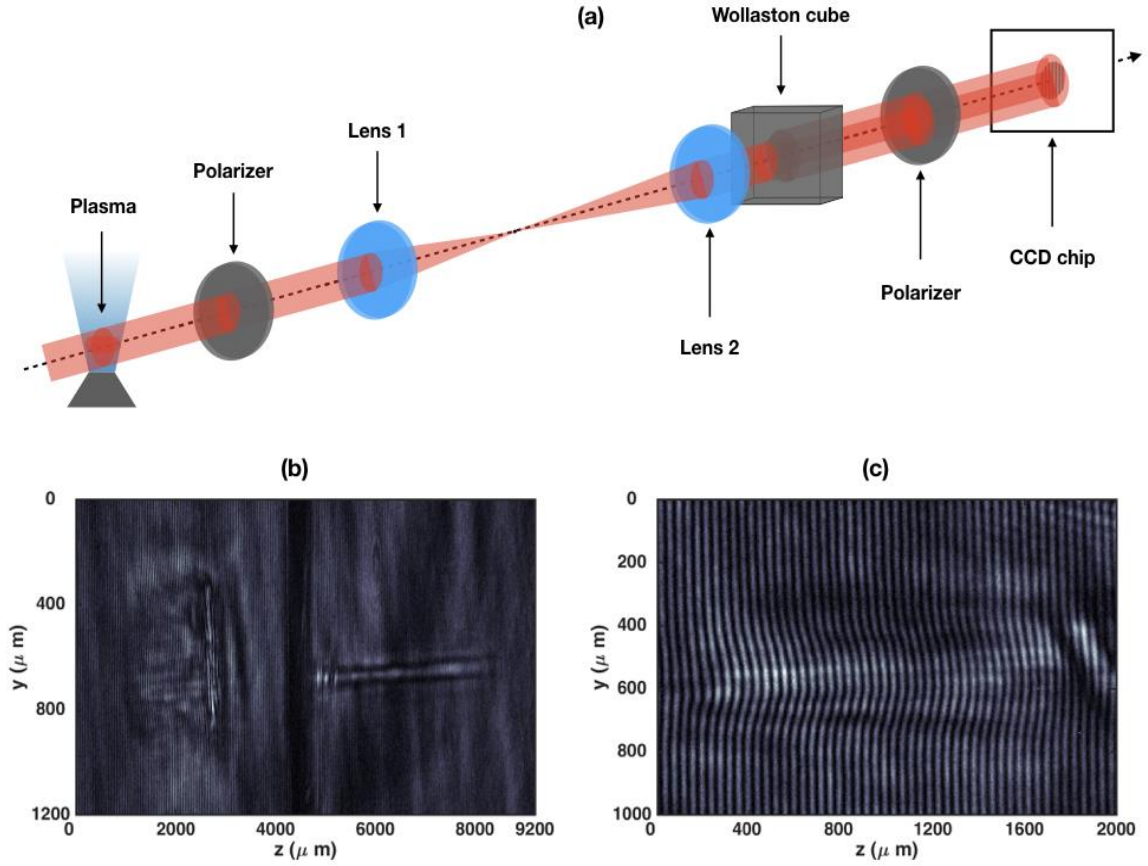

Figure 6.7: (a) Schematic of the side-view diagnostic. (b) Example of an image recorded on the camera. On the left, a plasma wakefield is created in the first jet (nozzles are not visible). The wheel intercepts the laser beam (center), and the electron beam ionizes a thin column of gas in the second jet (on the right). (c) Perturbations of fringe spacing in both jets allows to retrieve the plasma density.

the probe accumulates a phase shift in the area where ionization occurred. The plasma refractive index is given by the formula:

$$\eta = \sqrt{1 - n_e/n_c} \quad \textbf{(6.6)}$$

The fringe spacing on the camera chip depends on the plasma and gas refractive index. Under the hypothesis of an axi-symmetrical plasma, an Abel inversion algorithm allows to convert the phase shift axial profile to a plasma density radial profile **[Kalal 88]**. A rough estimate of the density can be reached using a simpler calculation. In Fig. 6.6 (c), the plasma channel is roughly $l = 250\ \mu m$ wide, and the pattern is shifted at the center of the channel over about two fringes. As a result, the phase difference at the center provides the equation:

$$\frac{2\pi}{\lambda}(\eta_{plasma} - 1)l = -2.2\pi \quad \textbf{(6.7)}$$

which gives an estimate of the density of the plasma: $n_e = 2.2\ 10^{19} cm^{-3}$. In this calculation, we made the hypothesis that the density was constant in the plasma column. This assumption is incorrect, however the peak density for a similar nozzle, and a backing pressure of $11\ bar$ can reach $2.6\ 10^{19}\ cm^{-3}$ **[Guillaume 15]** which is close to the estimation above.

3. Hybrid LWFA-PWFA experiment and results

a. Experimental setup

The experimental setup is depicted in Fig. 6.5. P1 is focused in the first gas jet and it produces an electron bunch by Laser Wakefield Acceleration. The second gas jet is aligned a few millimeters after jet one. Both nozzles are mounted on three-axis translation stages, gas jet positions can therefore be adjusted, for instance by moving gas jet two from touching jet one to at least $20\ mm$ downstream. Between the gas jets are placed two thin steel disks, screwed to each other and maintain a thin aluminum foil. The thickness of the foil will be varied in the following sections. The disks are mounted on a two-dimension translation stage and fixed to a goniometer to adjust its orientation. The adjustment of the position of the nozzles can be controlled thanks to the side-view diagnostic. An example of an image recorded on the camera is displayed in Fig. 6.7 (b).

The first run of the hybrid experiment aims at studying the interaction of the LWFA electron beam interacting with a gas jet. The thin foil located between the two gas jets is used to prevent laser interaction in the second gas jet. The effect of this foil on the electron beam propagation needs to be elucidated first. P2 is intended to ionize the second gas jet, before the electron beam passes in the preformed plasma. However, the study of this scheme will be pursued in future experimental campaigns.

b. Effects of the second gas jet on the electron beam

In this section, we describe the electron beam produced by the LWFA stage. We report then on the effect of the second gas jet on the spectrum of the electron beam, when no plasma was pre-formed in gas jet two.

Electron beam production and spectrum

Electron beam produced in the LWFA stage is performed by focusing the main laser beam (P1) into gas jet 1 to excite a nonlinear wakefield. A gas density of $\sim 2.10^{19} cm^{-3}$ was used, with $a_0 \approx 2.1$. Ionization injection is used in this experimental campaign with a gas mixture of 99% helium, 1% nitrogen. An example of a spectrum is given in Fig. 6.8 (a) and (b). The

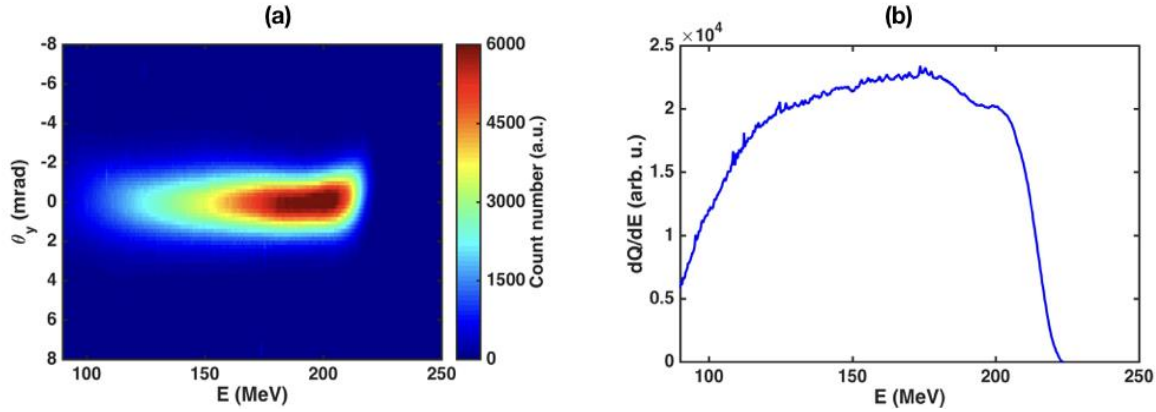

Figure 6.8: (a) Example of a spectrum recorded on the camera. Vertical axis is the divergence of the beam, in the direction of the dipole field. (b) Spectrum integrated over the whole vertical axis. (in arbitrary units)

spectrum has features common to most ionization injection schemes, it spreads here from $220\ MeV$ to $80\ MeV$ and is almost uniform over the whole range. In this section, the wheel is removed, and the second gas jet can be switched on or off. We characterize here the electron bunch created in the first jet.

Averaging over several shots, the mean maximal energy - defined as the highest energy at which some signal was recorded on the camera - was $215.60 \pm 5.23\ MeV$. The average peak energy was $182.04 \pm 5.56\ MeV$ in the dataset considered. The spectrum of Fig. 6.8 (a) belongs to the dataset used to produce these typical average values.

The calibration of the charge in the bunch, measured by the camera chip signal is yet to be accomplished. However, the charge measured in the same context, in Salle Jaune of LOA revealed bunch charge of the order of $50 - 100\ pC$ **[Guillaume 15]**.

The divergence in the transverse plane is assumed to be identical in x and y dimensions. However, it can only be measured in y, as the spectrometer deflects the particles in the x direction. The divergence on the screen appears as displayed in Fig. 6.8 (a). For the shot displayed, the divergence spans from $3.22\ mrad$ at $100\ MeV$ to $2.01\ mrad$ at $200\ MeV$ (FWHM).

The average beam energy values quoted above are unaffected by the second gas jet: without the second gas jet, the maximum and peak energies are $232.53 \pm 8.19\ MeV$ and $209.45 \pm 18.20\ MeV$. When the second gas jet is setup, those values become $237.31 \pm 5.55\ MeV$ and $221.66 \pm 6.41\ MeV$. The increase in the maximal energy can be explained for example by the beam self-generated deviation due to an asymmetry in its transverse profile.

The plasma in the second gas jet is ionized by the self-field of the LWFA electron bunch created in the first gas jet. Self-ionization of a neutral gas by a bunch of particles, in the

context of PWFA, has been widely studied **[Deng 03, Bruhwiler 03, Hogan 05, Zhou 07, An 07]**. However, the schemes considered in these articles are often different from the hybrid platform described in this section. First, the gas they consider is usually lithium or cesium, second, the neutral gas and particle bunch densities they consider are lower by at least an order of magnitude. Numerical results obtained considering the same scheme as us were reported **[Heinemann 17]**. In this last work, numerical simulations compared the wakefield driven in the second gas jet, when the gas was pre-ionized by a laser or self-ionized by the drive beam. First, this work showed that self-ionization occurred with a LWFA electron drive bunch comparable to ours. Second, the accelerating electric field in the wakefield driven by this bunch, although smaller in the self-ionized case than in the pre-ionized one, could reach $300\ GV/m$ at a gas density of $n_0 = 10^{19}\ cm^{-3}$. Such a study could be accomplished experimentally in Salle Jaune during the next experimental campaign in early 2018.

Effect of the second gas jet on the bunch spectrum

In this part, we consider shots for which the wheel contained a Mylar film of 13 μm. The wheel with the foil could be inserted to block the laser after the first stage. Several materials and thicknesses for the film were tried in the experiments. The choice of the thickness and the study of the material effect will be given in the next section.

When the wheel is inserted, the laser beam is blocked, and the electron beam can ionize a thin column of plasma in the second gas jet on its own, as shown in Fig. 6.6 (b). In addition, the second gas jet has a focusing effect, particularly strong at low energies. This effect can be seen in Fig. 6.9 (a) and (b). A quantification of this phenomenon is provided with Fig. 6.9 (c). On that plot, the red dots depict the divergence along the spectrum for the LWFA created electron bunches, when they pass through the wheel, but without the second gas jet. By contrast, the blue dots depict the bunch divergence, after the beam passes through the wheel, when the second gas jet is used.

The self-focusing phenomenon occurring when a bunch of particles - electrons or positrons – excites a plasma wakefield in a gas is a process studied for several decades, that was called from the beginning the plasma lens.

This phenomenon focused attention first in the context of setting up a final stage at the end of a conventional accelerator, to use the self-pinching effect to increase the luminosity of the particle source **[Chen 87]**. The principle of the self-focusing phenomenon is simple: when a charged particle bunch propagates in a gas, the front particles ionize the medium and excite a wakefield that is focusing for the bunch particles following. Head erosion usually occurs. Along the bunch will exist a progressively stronger focusing force that will reduce the global divergence of the beam. In the context of conventional accelerators, the plasma lens was studied theoretically **[Chen 87]** and experimentally **[Nakanishi 91, Ng 01]**.

The plasma lens phenomenon focused LWFA researchers' attention next. In fact LWFA produced electron bunches have fundamentally an extremely low emittance of order of $1\ mm.mrad$. When such bunches drift in free space, the finite energy spread of the particles they contain has the negative consequence of increasing the emittance of the beam. If a plasma based collider is created someday, several plasma stages distant from each other will have to successively accelerate the beams. It will therefore be important to collimate the bunches after each plasma cell before they propagate to the next. However, preserving the

emittance implies that the lenses operate on the emerging beam over the first few millimeters when they are transversally short. Quadrupoles used in conventional facilities are not strong enough to provide the accelerating gradients needed to focus LWFA beams. The plasma lens technique could in principle accomplish this.

The major drawback of self-focusing is the inhomogeneity of the force along the bunch. Two schemes in the context of LWFA were suggested to exploit the advantages of the plasma lens technique while getting rid of the drawbacks. The schemes were proposed theoretically **[Lehe 14]**, and a first demonstration was accomplished at LOA **[Thaury 15**]. Both schemes rely on a two-jet setup. However, these schemes rely on the wakefield driven by a laser bunch in the second jet whose transverse field is used to refocus the electron beam emitted in the first jet. This is incompatible with the concept of the hybrid LWFA/PWFA project.

The focusing phenomenon reported in this section is the "conventional plasma lens" technique quoted above, that was reported in conventional facilities **[Nakanishi 91]**.

In the experiment described in this chapter, the laser is blocked by a Mylar foil after the first jet, only the particle beam is responsible for the focusing effect in the second stage. It is therefore a scheme comparable to the original plasma lens design. The comparison accomplished in Fig. 6.9 (c) ensures that the focusing effect is an interaction between the electron beam and the plasma: the laser is blocked by the wheel, only the electrons and the

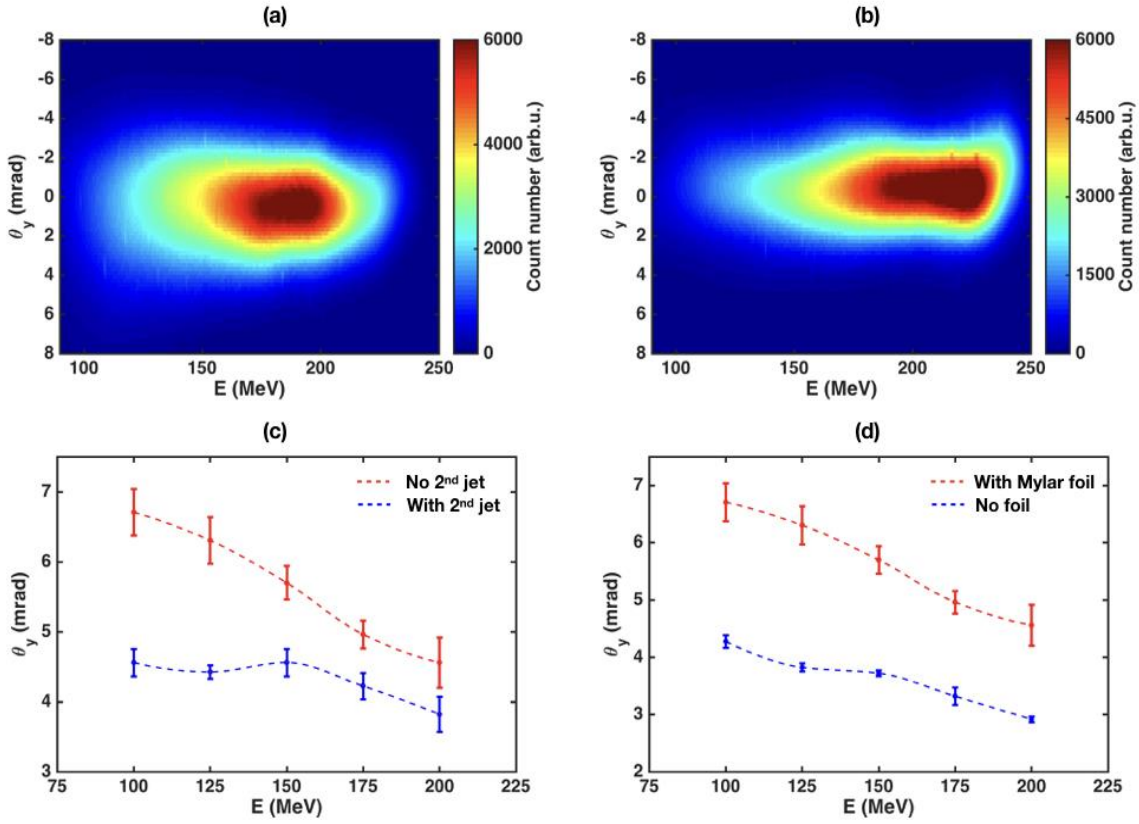

Figure 6.9: (a) Example of an electron bunch spectra, for a shot with a Mylar window to block the laser, but no gas in the second jet. (b) Same, but with gas in the second jet. (c) Divergence of the beam on the spectrometer as a function of the particles energy. The focusing effect of the second gas jet is visible. (d) Divergence of the beam on the spectrometer as a function of the particles energy. This is an evidence of the defocusing effect of the Mylar foil.

gas interact in jet 2. The effect is the strongest at $100\ MeV$, where the divergence is reduced by 32 %. At higher energy, $200\ MeV$, the divergence is only reduced by 16 %.
The maximal energy of the beam is slightly modified as said in the previous section. With the Mylar foil and without the second gas jet, the maximal energy is $E_{max} = 232.53 \pm 8.19\ MeV$. When the second gas jet is added, the measured maximal energy is $E_{max} = 237.31 \pm 5.5\ MeV$.

The magnetic field gradients in the transverse plane can be estimated. Starting from the simple model of an electron of the bunch whose initial energy is $100\ MeV$ ($\gamma \sim 198$), at the distance $\sigma_{x,rms}$ from the axis facing a focusing and constant field, we can estimate B. The particle speed is nearly c, and is not modified during the motion. The deflection of this particle is supposed to be $\theta_0 \sim 1\ mrad$ (reduction of the beam divergence at $100\ MeV$ is $\sim 2\ mrad$ in Fig. 6.9 (c)). We suppose as well that the field is constant for this electron along the length $l = 3\ mm$ of the second jet. The equation of motion is:

$$\frac{d\vec{v}}{dt} = \omega_c \vec{v} \times \vec{u}_B, \qquad \textbf{(6.8)}$$

where $\omega_c = \frac{qB}{\gamma m_e}$. It has the solution:

$$\vec{v} = c \begin{pmatrix} cos(\omega_c t) \\ sin(\omega_c t) \end{pmatrix}, \qquad \textbf{(6.9)}$$

leading to $\omega_c t_0 = \theta_0$ at the exit of the second jet. This particle propagates along $l = 3\ mm$, assuming the deviation is very small, we have the relation: $ct_0 = 3\ mm$. This leads to the value of B seen by this electron:

$$B = \frac{\gamma m_e c \theta_0}{ql} \qquad \textbf{(6.10)}$$

The numerical application gives: $B = 0.74\ T$. Assuming a beam with an initial divergence of $6\ mrad$, that propagates $2\ mm$ between the jets, the transverse size is $12\ \mu m$ when the bunch enters the plasma lens. The B field is null on axis, and has an amplitude of $0.74\ T$ at the edge of the bunch. The corresponding transverse magnetic gradient is therefore $|\nabla B| = 6.2 \cdot 10^4\ T\ m^{-1}$. This is two orders of magnitude higher than the highest performance permanent magnets transverse gradients ($\sim 500\ T\ m^{-1}$) **[Thaury 15]**.

To conclude, it is clear that an interaction happens between the electron beam and the second gas jet. However, no energy deposition is seen yet. Furthermore, another comment must be made: the wheel itself has a defocusing effect at all energies. This effect can be seen in Fig. 6.9 (d). The blue dots depict the divergence along the spectrum for the LWFA created electron bunch, with the Mylar foil. The red dots depict the bunch divergence, when the wheel is inserted. The effect is almost constant: at $100\ MeV$ and at $200\ MeV$, the divergence is increased by 36 %. The origin of the defocusing effect will be studied in the next section.

c. Effects of the foil on the electron beam

In this part, we study the effect of the wheel on the electron beam. We use Aluminum foils with tens of micrometers thicknesses, or a Mylar foil, with a thickness of $13\ \mu m$.

When a charged particle beam traverses matter, multiple scattering occurring in the material leads to an increase in the divergence. This phenomenon is characterized by the radiation length of the material. The radiation length of Aluminum is $8.897\ cm$ **[PDG 17]**, and the

radiation length of Mylar is $50.3\ cm$ **[Adler 06]**. The scattering angle due to the foil is non-negligible. The corresponding additional angles are reported in Fig. 6.10.

Material	Thickness	$\theta_s(E = 150\ MeV)$
Mylar	$13\ \mu m$	$0.28\ mrad$
Aluminum	$8\ \mu m$	$0.56\ mrad$
Aluminum	$15\ \mu m$	$0.79\ mrad$
Aluminum	$30\ \mu m$	$1.2\ mrad$
Aluminum	$60\ \mu m$	$1.7\ mrad$

Figure 6.10: Scattering angles due to the effect of the foil. Only the angles at $E = 150\ MeV$ are given here.

These additional angles will be automatically subtracted to the measured data during image processing from now on. The studies below aim at identifying other effects that could explain the increase of the divergence.

At that point, the remaining "scattering" of the electron beam due to the foil can have three origins. It could be an effect of the plasma in front of the foil and/or it could be a volumetric plasma effect in the foil, or it could be due to the reflection of the laser bunch on the foil. Setting up the wheel at a 45° angle should verify the first hypothesis. The second hypothesis, related to the volume, should be verified by a parametric study of the foil thickness and material. Following the last conjecture, the "scattering" effect could be located on the surface of the wheel, where laser-foil interaction could give birth to chaotic electromagnetic fields at the surface. Varying the distance between the foil and the first jet should reduce the scattering. If this last hypothesis is valid, the defocusing effect should decrease rapidly as the gas jet-foil distance increases.

First was accomplished the study of the hypothesis of a plasma effect, by changing the orientation of the wheel. An example of the side-view diagnostic is displayed in Fig. 6.11 (a) to illustrate the modification of the setup for this test. The plot of Fig. 6.11 (b) does not show any difference with or without the angle given to the wheel.

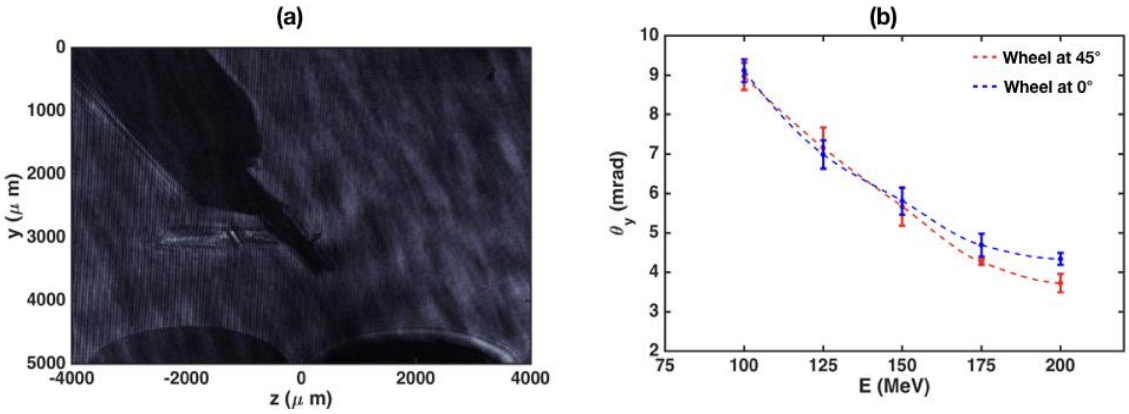

Figure 6.11: (a) Side-view image that displays the 45° oriented wheel. (b) Plot of the divergence of the beam as a function of the energy of the particle. No effect of the 45° wheel is seen, compared to the 0° usual one.

The conclusions of the volumetric effect study are more likely to show an effect on the divergence of the beam. Fig. 6.12 reports on the divergence of the beam as a function of energy for different Aluminum thicknesses of the wheel, and for a Mylar foil as well. Several plots are showed that correspond to different distances between the first gas jet and the wheel. The reference position is chosen as the position where the foil touches the downstream edge of the first nozzle. At each position, it seems that the thickness of that material correlates slightly with the scattering effect. In fact, the curves show on each plot that the defocusing grows as the Aluminum thickness increases. In addition, using a Mylar foil instead of an Aluminum one seems to increase the effect at the closest position (Fig. 6.12 (a) and (b)).

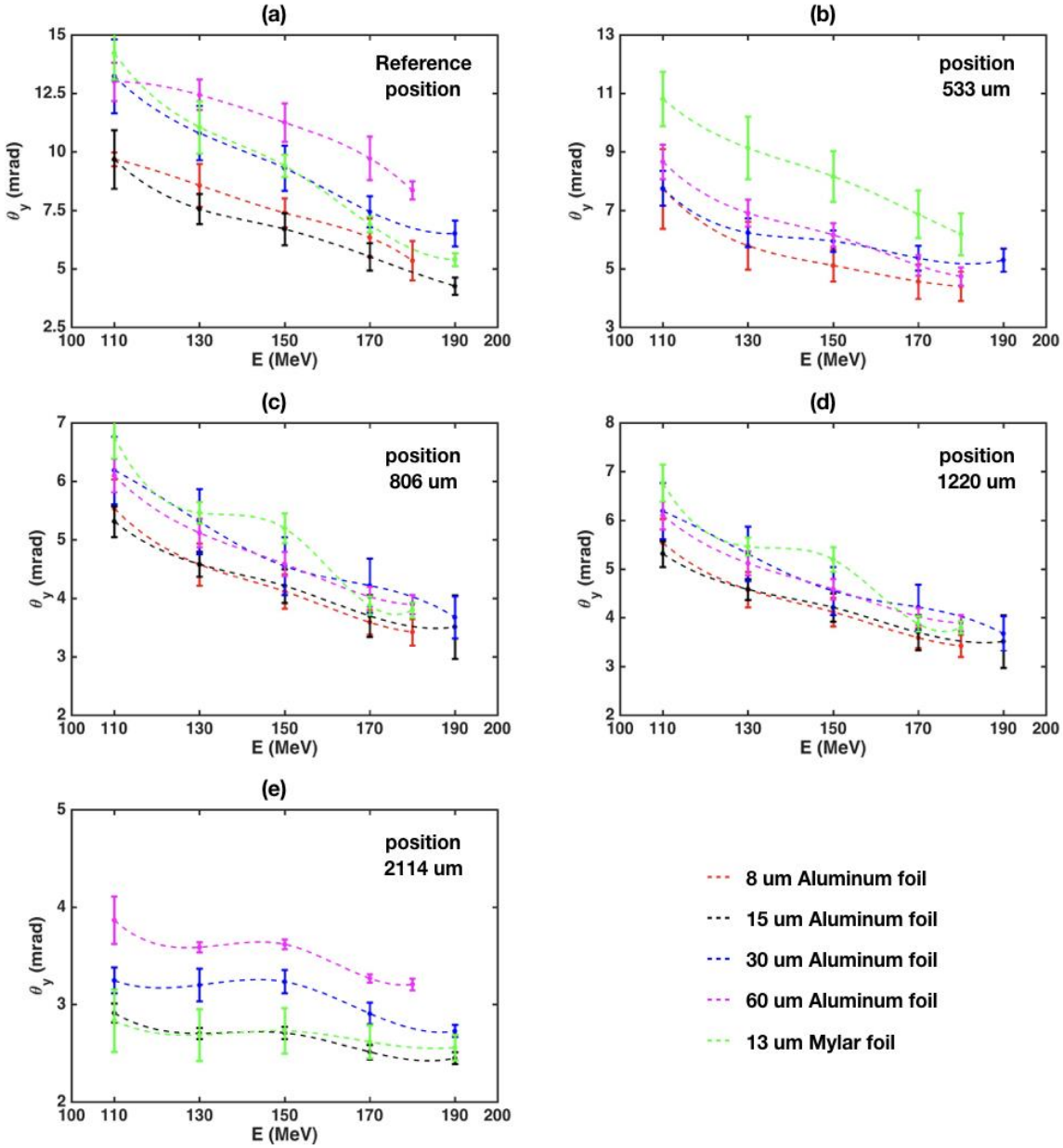

Figure 6.12: Plots of the divergence evolution for different materials and thicknesses of the foil in the wheel. Each image corresponds to a distinct nozzle-foil distance. (a) Reference position (b) 533 *μm between the foil and the reference position. (c)* 806 *μm between the foil and the reference position. (d)* 1220 *μm between the foil and the reference position. (e)* 2114 *μm between the foil and the reference position.*

The errorbars in Fig. 6.12. are quite large. Data analysis reveals that more data is required to draw a perfect conclusion regarding the material and foil thickness influence. It is clear that the effect of the thickness is non-negligible.

As a conclusion for this second study, we can say that the effect of the volume of the foil exists, but is modest. A larger amount of data would bring clearer datas regarding the volumic effects in the foil. During the experimental campaign, the amplitude of the defocusing effect seemed to be larger, this is why the last parametric study is likely to bring positive and clear results.

The last study, related to the effect of the distance between the foil and the first jet is reported in Fig. 6.13. Fig. 6.13 (a) and (b) for an aluminum foil with different thicknesses. The reference position is chosen as it was made in the measurements reported in Fig. 6.12: the position for which the foil touches the downstream edge of the first nozzle. As can be seen, the trend is similar for all thicknesses. Generally speaking, the divergence at $120\ MeV$ and at $160\ MeV$ increases very slightly with the thickness of the foil. In addition, when the distance increases, the scattering of the electron beam decreases rapidly.

When the foil is made of Mylar, the behavior is more chaotic. In Fig. 6.13 (c), are reported the measurements at $120\ MeV$ and at $160\ MeV$ for a Mylar foil. Two steps seem to appear on this graph, when the distance between the foil and the first jet outruns $700\ \mu m$, a clear reduction of the scattering effect occurs, and the effect is almost constant for longer distances.

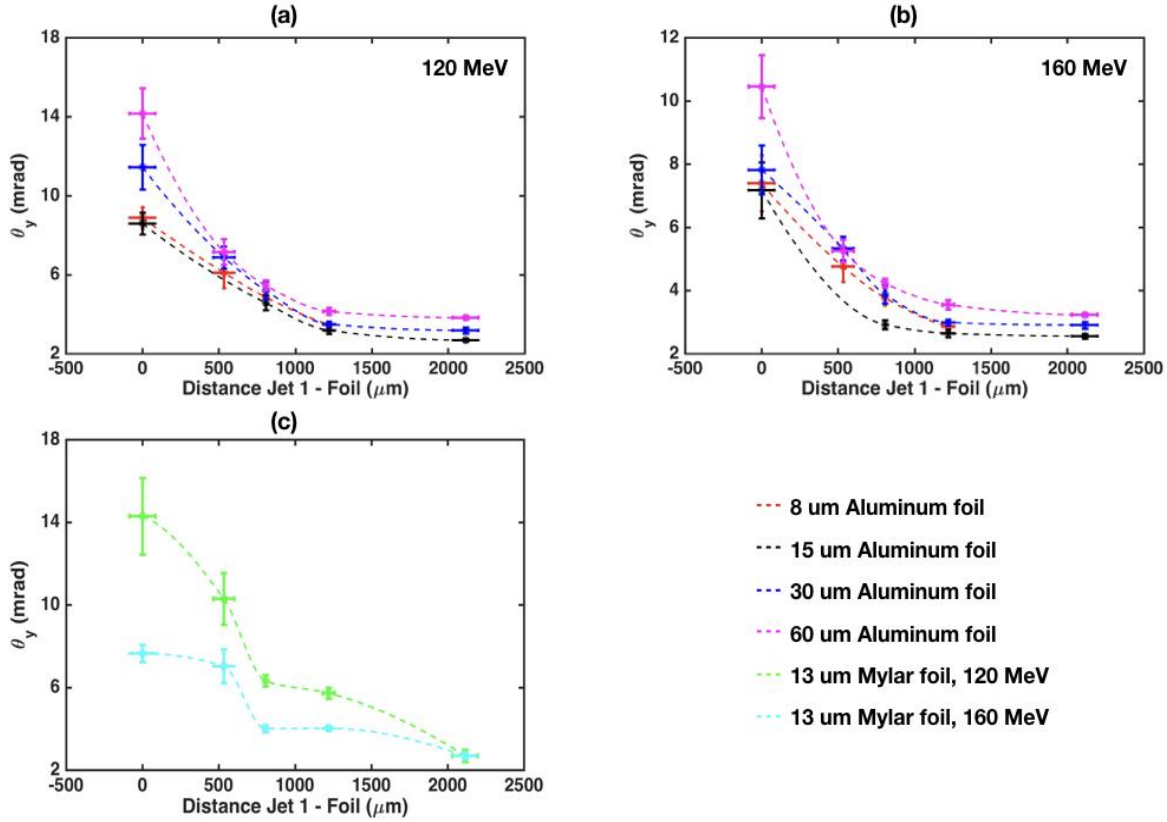

Figure 6.13: Plots of the divergence evolution for different materials and thicknesses of the foil in the wheel. (a) Aluminum foil of different thicknesses. The divergence is measured at $120\ MeV$. *(b) Aluminum foil of different thicknesses. The divergence is measured at* $160\ MeV$. *(c) Mylar foil, divergence at* $120\ MeV$ *and at* $160\ MeV$.

The main conclusion of Fig. 6.13 is the following: the strong decrease of the divergence with the distance illustrates that the plasma-foil interaction plays a role in the deterioration of the beam properties. This effect is much greater than the influence of the material or of the thickness of the foil blocking the laser.

To conclude, a first characterization of the hybrid LWFA-PWFA was accomplished in this chapter. The results of the last section illustrate the difficulty to build a two-stage LWFA-PWFA experiment. An evidence of the electron bunch – second gas jet interaction was obtained. In addition, a parametric study of the scattering effect of the wheel was realized. This led to rather complex results and seems to indicate that laser-foil interaction at the surface of the material is responsible for the effect. This conclusion opens the prospect of several interesting new experiments to explore further this laser-foil interaction. We will discuss these prospects in the general conclusion of the manuscript.

Chapter 7

Decoupling of LWFA electron acceleration and Betatron radiation in a two-stage experiment

As an introduction to **radiation emission by electrons** in LWFA experiments we will first recall the origin of radiation emission by charged particles, we will then briefly introduce the main concepts and the formalism of **Betatron emission** by LWFA electron bunches. The second section will be dedicated to the **simulation results regarding the decoupling** of electron acceleration and X-ray emission in a two-stage LWFA-PWFA scheme. In fact, for reasons that will be discussed in details, the two-stage scheme is promising to enhance the usual Betatron emission of LWFA experiments. The last section will be dedicated to the corresponding **experimental campaign performed at LOA in 2016** that aimed at realizing this conceptual scheme.

Contents

1. Betatron X-ray radiation in LWFA experiments

a. Radiation from charged particles

The origin of radiation by accelerated charged particles can be understood by a simple picture **[Khan 08, Ferri 16]**. Electromagnetic emission fundamentally comes from the finite speed at which information (electric and magnetic fields here) propagates, the speed of light c. Considering a single particle in vacuum, at rest, an observer could feel its electric field everywhere in space. If the particle is moving at a constant speed, the observer could always switch to the particle reference frame, in which the particle is not moving.

Let's consider a particle initially at rest. If the particle starts moving, a change of its electric field in all space should be felt. However, this information needs to propagate from the particle to the observer at the speed of light. The retarded information – the sudden change in the position of the charged particle and of its electric field - propagates toward the observer. This propagating perturbation is the electromagnetic radiation emitted by the particle. This is illustrated in Fig. 7.1 (a). This simple picture shows the link between acceleration of charged particles and emission of radiation. In the following the exact formulas for the radiation will be introduced first and the process that explains why LWFA-produced electron bunches emit radiation second.

In the following, we consider the fields generated by a relativistic particle P. t' is the time, in the laboratory frame, at which the particle emitted some radiation, that propagated at speed c and reached the observer at position $M(\vec{\boldsymbol{r}}_M)$ at time t. t' is referred to as the retarded time, and is before time t at which the radiation is received by the observer. The four-vector positions for P the particle and M the observer are $\boldsymbol{r}_P = (ct', \vec{\boldsymbol{r}}_{\boldsymbol{P}}(t'))$ and $\boldsymbol{r}_M = (ct, \vec{\boldsymbol{r}}_{\boldsymbol{M}})$. The retarded time t' is a function of $\vec{\boldsymbol{r}}_{\boldsymbol{P}}$ and t. All the conventions are summarized in Fig. 7.1 (b). It is written $t'(\vec{\boldsymbol{r}}_{\boldsymbol{P}}, t)$ and fulfills the so-called light cone condition:

$$c(t - t') = |\vec{\boldsymbol{r}}_{\boldsymbol{M}} - \vec{\boldsymbol{r}}_{\boldsymbol{P}}(t')| = R(t') \qquad \textbf{(7.1)}$$

Equation **(7.1)** leads to:

$$\frac{\partial t}{\partial t'} = 1 - \boldsymbol{n}(t') \cdot \boldsymbol{\beta}(t') \qquad \textbf{(7.2)}$$

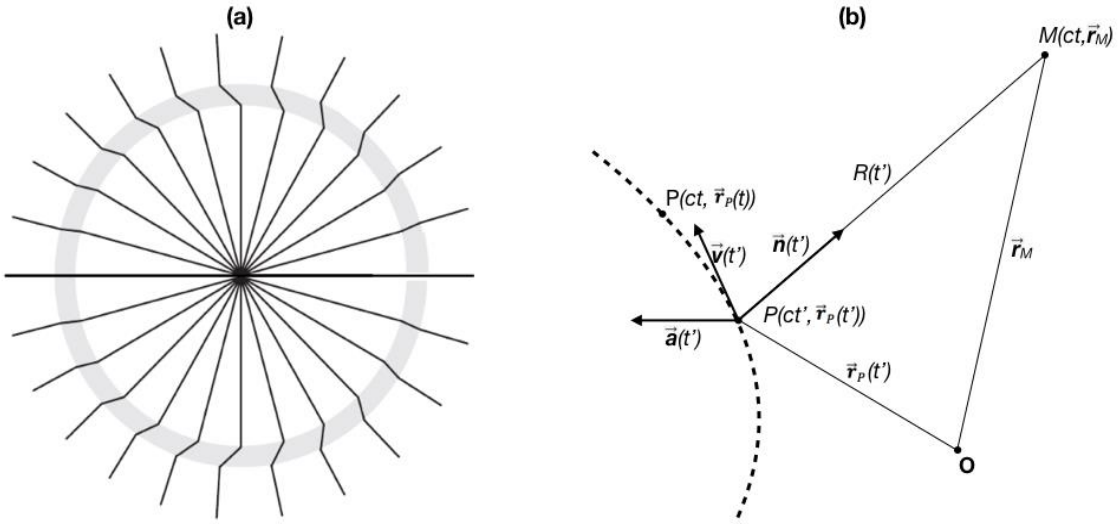

Figure 7.1: (a) Perturbation of the electric field propagating from a charged particle. (b) Definition of the retarded time t' and of various notations.

Where $\boldsymbol{\beta} = \boldsymbol{v}/c$ and $\boldsymbol{n}$ is the unit vector collinear to $\vec{r}_M - \vec{r}_P(t')$. The wave equation, written in terms of the electromagnetic four-potential $\boldsymbol{A}^\alpha = (\phi/c, \boldsymbol{A})$ and of the four-current $\boldsymbol{J}^\alpha = (c\rho, \boldsymbol{J})$, reads in the Lorentz gauge ($\partial_\mu \boldsymbol{A}^\mu = 0$):

$$\left(\frac{1}{c^2}\frac{\partial^2}{\partial t^2} - \nabla^2\right)\boldsymbol{A}^\mu = \mu_0 \boldsymbol{J}^\mu \qquad \textbf{(7.3)}$$

where $\phi, \boldsymbol{A}, \rho, \boldsymbol{J}$ are the usual scalar potential, vector potential, charge density and charge current density. Using the Green function of **(7.3)**, the solution of this inhomogeneous linear differential equation for the four-current associated to a single accelerated electron, described by its four-position $\boldsymbol{r}_P$ and four-velocity u^α, can be expressed as **[Jackson 62]**:

$$A^\mu(\boldsymbol{r}) = -\frac{e}{4\pi\epsilon_0 c}\frac{u^\mu(t')}{u(t')\cdot[\boldsymbol{r}-\boldsymbol{r_P}(t')]} \qquad \textbf{(7.4)}$$

where $\boldsymbol{r}$ is the four-vector position at which the four-potential is evaluated (i.e. the position of the observer). This formula is called the Liénard-Wiechert potential. Using the light cone condition **(7.1)** and the definition of the $\boldsymbol{E}$ and $\boldsymbol{B}$ fields in terms of the potentials, one can reach the following expressions, where all terms are expressed as a function of t':

$$\boldsymbol{E}(r,t) = -\frac{e}{4\pi\epsilon_0}\left[\frac{\boldsymbol{n}-\boldsymbol{\beta}}{\gamma^2(1-\boldsymbol{\beta}\cdot\boldsymbol{n})^3 R^2} + \frac{1}{c}\left(\frac{\boldsymbol{n}\times[(\boldsymbol{n}-\boldsymbol{\beta})\times\dot{\boldsymbol{\beta}}]}{(1-\boldsymbol{\beta}\cdot\boldsymbol{n})^3 R}\right)\right]_{t'} \qquad \textbf{(7.5)}$$

$$\boldsymbol{B}(r,t) = \frac{1}{c}[\boldsymbol{n} \times \boldsymbol{E}]_{t'} \qquad \textbf{(7.6)}$$

In **(7.5)** and **(7.6)**, $\dot{\boldsymbol{\beta}} = d\boldsymbol{\beta}/dt$ is the acceleration and γ is the Lorentz factor of the particle, defined as $\gamma = (1-\beta^2)^{-1/2}$.

The first term in **(7.5)** does not depend on the acceleration of the radiating electron, it is a static term that decreases fast with the distance $\propto 1/R^2$. This term is sometimes said "quasi-coulombian" as it shares similarities with the expression of the electric field created by a charged particle at rest. The second term in the expression of $\boldsymbol{E}$ is particularly interesting as it depends on the acceleration of the radiating electron. This term represents the electromagnetic field generated by the acceleration of the particle. The term only decreases with the scaling $\propto 1/R$.

If the distance R is much bigger than the size of the radiation source (the spatial extent covered by the trajectories of a bunch of particles for example) and the wavelength of the radiation, then the second term in formula **(7.5)** is dominant. In addition, in that case $\boldsymbol{n}$ can be considered as a constant, and the following approximation can be used:

$$R(t') \approx R_0 - \boldsymbol{n}\cdot\boldsymbol{r_P}(t') \qquad \textbf{(7.7)}$$

It is possible from **(7.5)** and **(7.6)**, to reach the expression of the radiated energy per unit of solid angle and frequency by the particles of a LWFA electron bunch. The definition of Poynting vector, the vector transporting the energy of the electromagnetic field, is:

$$\boldsymbol{\Pi} = \frac{\boldsymbol{E}\times\boldsymbol{B}}{\mu_0} = \epsilon_0 c|\boldsymbol{E}|^2\boldsymbol{n} \qquad \textbf{(7.8)}$$

(7.8) leads to the formula for the radiation power received by an observer in the direction $\boldsymbol{n}$ and in a solid angle $d\Omega$:

$$\frac{dP(t)}{d\Omega} = |A(t)|^2 = \left|\sqrt{c\epsilon_0}R\boldsymbol{E}(t)\right|^2 \qquad \textbf{(7.9)}$$

The integration over time of this expression leads to the total energy radiated per unit of solid angle:

$$\frac{dI}{d\Omega} = \int_{-\infty}^{\infty} \left|\sqrt{c\epsilon_0} R \boldsymbol{E}(t)\right|^2 dt = \int_{-\infty}^{+\infty} \left|\sqrt{c\epsilon_0} R \boldsymbol{E}(\omega)\right|^2 d\omega = 2\int_{0}^{+\infty} \left|\sqrt{c\epsilon_0} R \boldsymbol{E}(\omega)\right|^2 d\omega \quad \textbf{(7.10)}$$

Where the second equation is justified by Parseval-Plancherel's theorem, and the factor of 2 in the last equation arises from considering only positive frequencies. As a result,

$$\frac{d^2 I}{d\Omega d\omega} = 2\left|\sqrt{c\epsilon_0} R \boldsymbol{E}(\omega)\right|^2 \quad \textbf{(7.11)}$$

which can be expressed easily using the Fourier Transform of $\boldsymbol{E}(t)$:

$$\boldsymbol{E}(\omega) = -\frac{e}{4\pi\epsilon_0}\frac{1}{cR_0}\frac{1}{\sqrt{2\pi}}\int_{-\infty}^{+\infty} e^{\frac{i\omega}{c}(ct' + R_0 - \boldsymbol{n}\cdot\boldsymbol{r}_P)} \frac{\boldsymbol{n}\times[(\boldsymbol{n}-\boldsymbol{\beta})\times\dot{\boldsymbol{\beta}}]}{(1-\boldsymbol{\beta}\cdot\boldsymbol{n})^2} dt' \quad \textbf{(7.12)}$$

Injecting **(7.12)** into **(7.11)** leads to the general formula for the radiated energy, per unit of solid angle and frequency:

$$\frac{d^2 I}{d\Omega d\omega} = \frac{e^2}{16\pi^3 c\epsilon_0}\left|\int_{-\infty}^{+\infty} e^{\frac{i\omega}{c}(t' - \boldsymbol{n}\cdot\boldsymbol{r}_P)} \frac{\boldsymbol{n}\times[(\boldsymbol{n}-\boldsymbol{\beta})\times\dot{\boldsymbol{\beta}}]}{(1-\boldsymbol{\beta}\cdot\boldsymbol{n})^2} dt'\right|^2 \quad \textbf{(7.13)}$$

This formula gives the expression of the radiation emitted by an electron, in the direction of observation $\boldsymbol{n}$, as a function of the particle position, velocity, and acceleration. This formula is only valid for an observer far from the source. Four important aspects of this expression characterize the radiation emitted by accelerating charged particles **[Corde 13]**:

If $\dot{\boldsymbol{\beta}} = 0$, then the radiated energy is null. In addition, the dominance of the term containing $\dot{\boldsymbol{\beta}}$ in our calculation indicates that the acceleration is responsible for the electromagnetic field far from the charged particle.

The radiated power is maximum for $\boldsymbol{\beta} \parallel \boldsymbol{n}$, and for $\beta \approx 1$. Relativistic electrons will radiate much more energy than non-relativistic particles, by several orders of magnitude. In addition, the theory of special relativity teaches us that the radiation is emitted in the direction of propagation, in a cone of angle $\Delta\theta \sim 1/\gamma$.

Knowing the scalings $\dot{\beta}_{\parallel} \propto F_{\parallel}/\gamma^3$ and $\dot{\beta}_{\perp} \propto F_{\perp}/\gamma$, we can conclude that transverse forces will be much more efficient than longitudinal ones to force relativistic electrons to produce radiation.

Last, the phase term can lead us to the frequency of the radiation a wiggling electron will produce: $\omega_{e-wig.} = \omega_{X-rays}/2\gamma^2$. This formula illustrates the interest of manipulating very relativistic particle beams: $\omega_{e-wig.}$ is the electron oscillation frequency, and ω_{X-rays} is the frequency of the emitted radiation.

b. Radiation in LWFA experiments

Moving now to the purpose of this theoretical presentation, X-ray radiation have many applications, for instance for medical imaging or non-destructive testing. In previous paragraphs, we saw that forcing relativistic particles to wiggle transversally is a very efficient way to produce X-ray radiation. Based on this principle, Betatron X-ray production in LWFA is one of the most promising schemes towards the realization of a high-brilliance high-energy X-ray source, this is why many X-ray studies are accomplished in the context of LWFA.

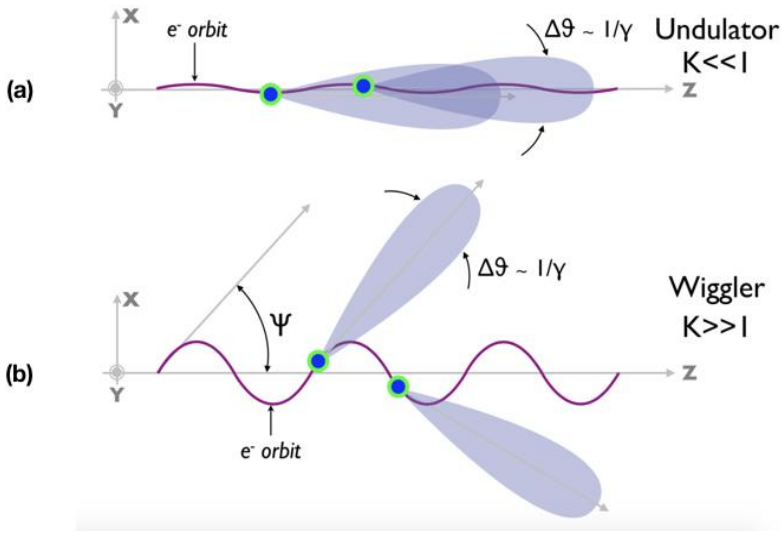

Figure 7.2: (a) Electron trajectory and X-ray emission cone in the undulator regime. (b) Electron trajectory and X-ray emission cone in the wiggler regime. Figure from ***[Corde 13]****.*

Before introducing the natural source of transverse oscillations of LWFA electrons, we start with a presentation of an important concept regarding these transverse oscillations: the regime of oscillations, that can be either **wiggler** or **undulator**. We define ψ as the maximal angle between the velocity of the particle and the main axis of propagation. The fundamental parameter to distinguish and define the two regimes is $K = \psi\gamma = \psi/\Delta\theta$, where γ is the energy of the electrons. It can be shown that if the transverse oscillation has a spatial periodicity λ_u, the emitted radiation is also periodic with the wavelength: $\lambda = \frac{\lambda_u}{2\gamma^2}\left(1 + \frac{K^2}{2} + \gamma^2\theta^2\right)$, where θ is the angle of emission. When $K \ll 1$, the regime is undulator and when $K \gg 1$ the regime is wiggler. The specificities of the two regimes are summarized on the schematic of Fig. 7.2. The spectrum always contains the fundamental frequency $\omega = 2\pi c/\lambda$ and in some cases harmonics of this frequency. In the undulator regime, only the fundamental frequency will be present. In the wiggler case, harmonics will be contained up to a critical frequency ω_c.

In the bubble regime of LWFA, the plasma cavity can act as a wiggler. The electrons accelerated in the ion cavity also face a restoring focusing force which forces them to oscillate around the main propagation axis. The dynamic of the electrons in the cavity is slightly more complicated than the transverse oscillation described above, with fixed periodicity, amplitude and particle energy. In particular, the Betatron amplitude, the frequency of oscillation and the particle energy depend on time. Similarly, the transverse positions of the particles depend only on time, and not on the longitudinal coordinate. But the discussion is still relevant in the context of Betatron radiation, by considering that the properties of the radiation needs to account for the instantaneous oscillation amplitude, oscillation frequency and particle energy. The amplitude of the Betatron oscillation scales as $A \propto \gamma(t)^{-1/4}$ while the frequency of the Betatron oscillation scales as $\omega_\beta \approx \omega_p/\sqrt{2\gamma(t)} \propto \gamma^{-1/2}$.

The theoretical description is more complex for electrons that radiate while being accelerated, which is the case relevant for practical LWFA experiments like the ones performed at LOA.

The model shows in particular that the number of emitted photons in an oscillation period depends very weakly over γ, while the radiated energy is strongly dependent on γ, as the frequency of the photon increases quickly with γ. As a result, the energy contained in the observed radiation is dominated by the contribution from the radiation emitted by particles at the end of their acceleration, when they have the highest energy. For a LWFA-produced bunch, it usually is when dephasing occurs.

The first demonstration of Betatron electron oscillations in a bubble ion cavity and Betatron X-ray production was accomplished in the context of PWFA. A plasma wakefield was driven with an electron bunch of 1.8×10^{10} particles in a preformed plasma of density $1.7 \times 10^{14}\ cm^{-3}$ **[Wang 02]**. The beam electrons oscillated in the transverse field as well and were responsible for X-ray emission. The oscillation parameter was $K = 16.8$ and the peak spectral brightness was $7 \times 10^{18}\ photons/s/mrad^2/mm^2/0.1\ \%\ BW$ at $14.2\ keV$ in this experiment.

The first experiment relying on a LWFA-produced electron bunch was accomplished at LOA **[Rousse 04]**. The Salle Jaune $50\ TW$ laser system was used to produce electrons from a $3\ mm$ long helium gas jet providing a plasma density of $10^{19}\ cm^{-3}$. The bunch of electrons emerging from the gas was deflected by a $1\ T$ permanent dipole magnet, and a CCD camera placed on axis detected the Betatron X-ray light emitted by the electron bunch during its acceleration in the ion cavity. The peak spectral brightness was $2 \times 10^{22}\ photons/s/mrad^2/mm^2/0.1\ \%\ BW$.

As said in the general introduction of the manuscript, several applications rely on bright, spatially-coherent X-ray sources. Maximizing the production of X-ray light in LWFA experiments is one of the main efforts from the laser-plasma acceleration community. In fact, Betatron X-ray light could be a convenient and technically superior method of imaging. However, its main disadvantage comes from the relatively low total energy radiated by the source and the energy of the produced photons, which need to be increased to make this state-of-the-art technique really efficient for a broad range of application experiments. The scheme presented in the following is a promising attempt to bring the current performances of X-ray plasma sources to the next level, both in terms of brightness and spectral range.

2. Design and numerical characterization of a two-stage hybrid LWFA-PWFA X-ray source

A comprehensive numerical study of a new scheme was accomplished by researchers from LOA, as a part of a project that aimed at decoupling the LWFA production of an electron beam and the generation of X-ray light through Betatron oscillations. The theoretical work was published in a recent article **[Ferri 17]**, this section introduces its main results.

a. Motivations for a decoupled scheme

As explained in the first section, electrons in a LWFA experiment emit a so-called Betatron X-ray radiation during their acceleration in the ion cavity. The radiation originates from the transverse oscillations of the charged particles, around their main axis of propagation. In the bubble regime of LWFA, the particles wiggle and emit radiation with a broadband photon energy spectrum that extends up to the critical energy $E_c = \hbar\omega_c \propto \gamma^2 n_e r_\beta$. Due to its very short fs duration, micrometer source size and natural synchronization with the laser system,

this radiation source is very promising for many applications such as high-resolution imaging or temporally-resolved absorption spectroscopy.

For application purposes, it is necessary to use very high energy X-ray photons. The energy of Betatron photons produced in LWFA is still rather low. This photon energy limitation comes from the dephasing limit that prevents the Lorentz factor of the LWFA-produced electrons from growing further. The dephasing length scales as $\boldsymbol{L_{deph} \propto n_e^{-3/2}}$ with the plasma density, therefore, a lower gas density is more suitable for optimizing LWFA acceleration of electrons and reaching higher electron energy. However, a stronger transverse wiggling (higher transverse acceleration, higher K) and a shorter Betatron oscillation period favor Betatron radiation, which necessitates a higher plasma density. The shorter Betatron oscillation period at high plasma density simply results from the higher plasma frequency, a parameter that scales as $\boldsymbol{\omega_p \propto n_e^{1/2}}$. The stronger wiggling results from the higher transverse restoring force that scales as $\boldsymbol{\omega_p^2 \propto n_e}$. Electron energy gain and strong wiggling have an opposite behavior relative to the plasma density of the gas in which they occur. This explains why decoupling electron acceleration and Betatron X-ray generation is very promising. In fact, both a high-energy gain and a strong wiggling could occur in a two-stage scheme, relying on two gas jets with different plasma densities independently optimized for electron acceleration and Betatron production.

The theoretical design described above would rely experimentally on a two gas-jet setup. The first jet would have a low density and be the source of relativistic electrons. While the second jet, with a much higher density, would allow to optimize the production of Betatron radiation. The scheme is depicted in Fig. 7.3. By using such a scheme, Betatron radiation is produced by high-energy electrons accelerated in the first jet and wiggling in the high-density plasma of the second jet. In fact, because of dephasing and laser depletion limits at high plasma densities, it is expected that the interaction in the second jet occurs in the PWFA regime, the laser being quickly depleted and the electron beam exciting the wakefield itself. The use of the PWFA regime here is very interesting as it is much more favorable at high plasma densities, not being limited by dephasing and laser depletion. In this case, this optimized scheme for Betatron radiation can be referred to as a two-stage hybrid LWFA-PWFA X-ray source.

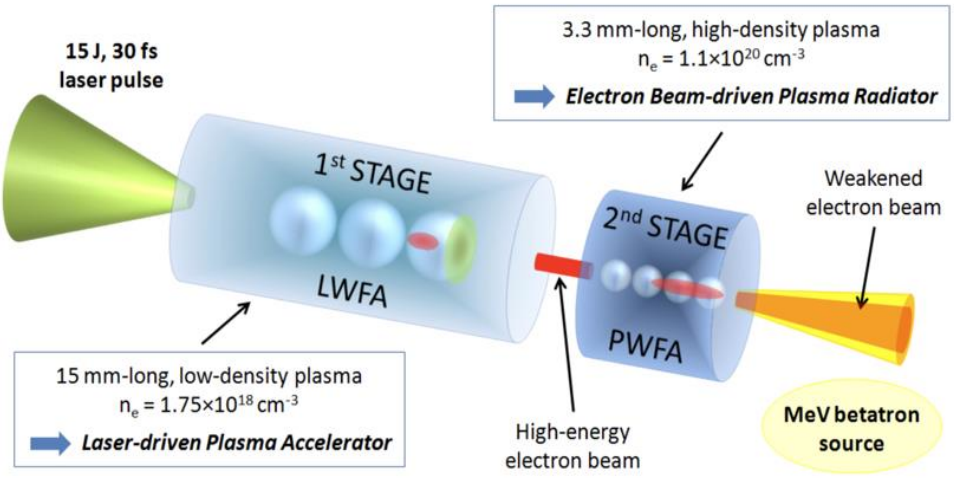

*Figure 7.3: Schematic of the two-stage LWFA-PWFA scheme for X-ray production. Figure from **[Ferri 17]**.*

b. Numerical results

The article **[Ferri 17]** relies on a numerical study of the two-stage hybrid Betatron source described above. The simulation of the LWFA stage was considering a $500\ TW$ laser pulse, containing $15\ J$ of energy in a $30\ fs$ (FWHM) duration and focused to a spot size of $23\ \mu m$ (FWHM) at the entrance of a plasma with an electron density of $1.75 \times 10^{18}\ cm^{-3}$. The plasma has a linear entrance ramp of $200\ \mu m$. The laser wavelength is $\lambda = 800\ nm$ and $a_0 = 6$ at the vacuum focus. From theoretical scaling laws, the dephasing length was estimated to be $15.3\ mm$.

The simulation shows that after 15 mm of propagation, an electron beam is obtained with an energy spectrum peaked at $1.8\ GeV$ and with $5\ nC$ of charge above $350\ MeV$. The length of the bunch is $30\ \mu m$ (FWHM) in the longitudinal dimension.

The simulation of the first stage was accomplished thanks to the CALDER-CIRC quasi-cylindrical code, using a box of $3200 \times 200\ cells$, with spatial steps of $\Delta z = 0.25\ c/\omega_0$, $\Delta r = 4c/\omega_0$. The time step was chosen as $\Delta t = 0.249\ \omega_0^{-1}$.

The electron bunch was sent after its acceleration up to the dephasing limit into the second stage. In the second stage (PWFA), the plasma density was set to $1.1 \times 10^{20}\ cm^{-3}$ with a $25\ \mu m$ linear entrance ramp.

The simulation in the second stage was accomplished with the 3D CALDER code, using a simulation of $800 \times 200 \times 200\ cells$. The spatial steps were $\Delta z = 0.5\ c/\omega_0$, $\Delta x = \Delta y = 0.5\ c/\omega_0$. The time step was chosen as $\Delta t = 0.288\ \omega_0^{-1}$.

The simulation showed a maximum radiated power of $50\ GW$ in the second stage, and a produced photon beam containing a total energy of $140\ mJ$. The critical energy of the photon beam was $E_c = 9\ MeV$, and the photon energy spectrum was peaked at $1\ MeV$.

In comparison, a simulation was run with the usual single-stage LWFA setup, with a plasma density of $10^{19}\ cm^{-3}$ and with the same laser parameters as the two-stage hybrid simulation. In this case, both electron acceleration and Betatron radiation occur in the same LWFA stage and are therefore not decoupled. This reference simulation led to a photon energy spectrum peaked at $30\ keV$ and to a photon beam containing in total $7.5\ mJ$ of energy. The comparison with the two-stage result is outstanding. The choice of laser parameters, although realistic, fully exploit the potential of the two-stage concept, in particular because it allows to use widely different plasma densities in the two stages of the hybrid LWFA-PWFA scheme.

In the two-stage scheme, the laser to X-ray and gamma-ray beam conversion efficiency was as high as 0.9 %. The divergence of the X-ray beam was $14 \times 15\ mrad^2$ (FWHM), and under the hypothesis that the source (the e^- bunch) was $2\ \mu m$ wide, the brilliance of the source was $B = 4.4\ 10^{23} photons/s/mm^2/mrad^2/0.1\%\ BW$ at $1\ MeV$.

Those figures are indeed very promising. It suggests that it is possible to reach even higher brilliance and to produce photon beams with higher photon energy from the Betatron X-ray source. The laser considered here is a $0.5\ PW$ laser pulse, which exceeds what is available with the laser system at LOA, however, many facilities in the world are either already available or will open soon with this class of lasers.

3. Experiment in Salle Jaune at LOA

An attempt was made at LOA to accomplish the experimental decoupling of the LWFA production of electrons and of the Betatron X-ray emission. The setup was the same as the one presented in Fig. 6.7, only the foil between the two jets was removed.

The experiment relied on the Salle Jaune laser system at LOA that delivers laser pulses with $50\ TW$ peak power, $30\ fs$ (FWHM) pulse duration and with $1.5\ J$ of energy. The backing pressure of the gas jet could be setup manually by adjusting the pressure in the supply gas pipe. P_1 is the backing pressure of the first jet and P_2 is the backing pressure of the second jet. Ionization injection was used for injecting electrons in the first jet and to increase the reproducibility and shot-to-shot stability of the LWFA accelerator stage, as well as for its simplicity. The first jet was therefore using a gas mixture with 99% helium and 1% nitrogen. The second jet, where Betatron radiation is expected to be produced by electrons accelerated in the first jet, was using pure helium.

The X-ray emission was detected by a Quad-RO Princeton instrument X-ray CCD camera with indirect detection. The camera indirectly detects X-ray photons with energies ranging from a few keV to a few 100s keV using a Gd_2O_2S:Tb scintillator screen and a 1:1 fiber optic coupler in front of a low-noise visible CCD camera with quantum efficiency of 70% at 550 nm. Each X-ray photon incident on the scintillator has a probability to interact with the scintillator through photoelectric absorption, scattering or electron-positron pair production and to deposit energy in the scintillator. A fraction of the deposited energy is converted to photons emitted at $\sim 550\ nm$ and detected by the visible CCD camera, giving a count value on the camera proportional to the energy deposited in the scintillator. The detector size is a square of $50 \times 50\ mm^2$, containing $2084 \times 2084\ pixels$, each pixel being of dimension $24 \times 24\ \mu m^2$. The camera was setup along the beam line axis, at the exit of the vacuum chamber. A $75\ \mu m$ mylar window allowed the X-ray beam to exit the vacuum chamber. The gas jet to mylar window distance was $73\ cm$, and the Quad-RO camera was located $2.5\ cm$ after the window in open air and was protected by a $500\ \mu m$ beryllium window.

As discussed earlier, the interest of the two-stage scheme relies on the independent control of the plasma density of each stage, which can be varied experimentally through the jet backing pressures P_1 and P_2. Therefore, the experiment had to rely on the optimization of electron acceleration and Betatron radiation using P_1 and P_2. All the other parameters (laser focus, compression, third order spectral phase, laser and jet positioning…) would also need to be optimized to obtain the best electron beam parameters possible.

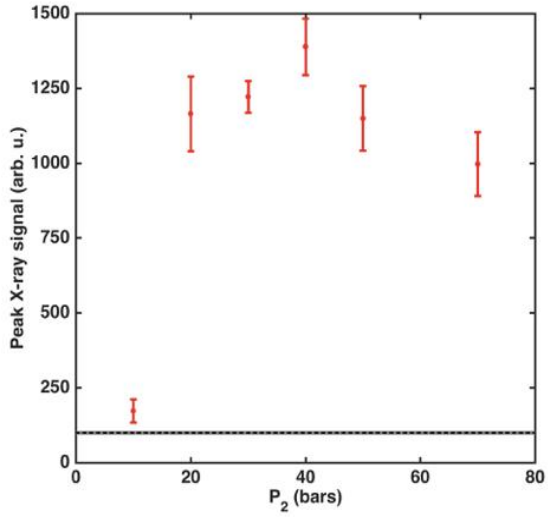

Figure 7.4: Plot of the peak X-ray signal in count number measured on the X-ray CCD camera as a function of the backing gas pressure of the second jet. The black dashed line is the level of Betatron radiation using the first jet only, with $P_1 = 17\ bars$, corresponding to the optimization of the electron beam parameters. Calibration of the camera signal is to be accomplished at LOA in 2018.

The main result of this work is presented in Fig. 7.4. The laser parameters and the first gas jet backing pressure had been optimized to reach the best electron beam parameters (highest electron energy and highest total charge). The optimized backing pressure for jet 1 was $P_1 = 17\ bars$. The X-ray radiation due to Betatron oscillations occurring in the first gas jet are drawn as a dashed line with the standard error displayed by a grey box. The level of X-ray signal with the first jet only is $99 \pm 6\ counts$ on the X-ray CCD camera. The optimized electron beam typically contains of the order of 100 pC of charge with a maximum electron energy in the $150 - 200\ MeV$ range. Keeping $P_1 = 17\ bars$ and using the second gas jet, Fig. 7.4 shows that the peak X-ray signal can be strongly increased and reaches a maximum when the backing pressure in the second jet P_2 is $40\ bars$. Starting from $99 \pm 6\ counts$ generated in the first jet alone, the X-ray signal grows to $1390 \pm 94\ counts$ when the pressure in the second jet is optimized at $P_2 = 40\ bars$, which corresponds to an impressive increase by a factor of 14. An example of a shot for the highest signal (for which parameters were $P_1 = 17\ bars$ and $P_2 = 40\ bars$) and for the reference signal (for which parameters were $P_1 = 17\ bars$ and $P_2 = 0\ bars$) is shown in Fig. 7.5. The triangular shapes on the figure are aluminum filters set up in front of the screen, initially intended to be used to evaluate the spectrum of the X-ray beam.

However, this result was obtained by optimizing the laser and jet 1 parameters for the best electron beam parameters. The same can be repeated but optimizing the X-ray signal instead,

and then optimizing both P_1 and P_2 in order to obtain the highest X-ray signal from the two-stage scheme. The best X-ray signal, $3880 \pm 307\ counts$, is obtained for $P_1 = 17\ bars$ and $P_2 = 41{,}5\ bars$. The scan of P_2 for $P_1 = 17\ bars$ is displayed in Fig. 7.6 (a), the red data points corresponding to the two-stage results and the black dashed line to the single-stage (jet 1 only, jet 2 switched off) result with $P_1 = 17\ bars$ (X-ray signal of $1020 \pm 45\ counts$). This value differs from the single-stage result of Fig. 7.4 and is mainly due to a different setting of the laser focus when optimizing the Betatron X-ray radiation directly instead of the electron beam parameters.

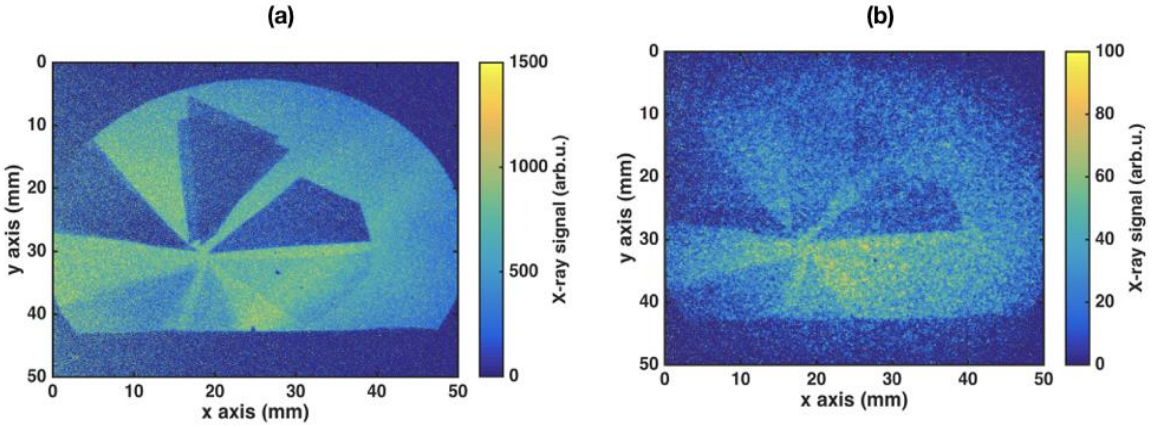

Figure 7.5: (a) X-ray signal on the CCD chip, parameters for this shot were $P_1 = 17\ bars$ and $P_2 = 40\ bars$ (highest signal in Fig.7.4). (b) X-ray signal on the CCD chip, parameters for this shot were $P_1 = 17\ bars$ and $P_2 = 0\ bars$ (reference signal in Fig.7.4).

Finally, to compare the two-stage scheme to the reference single-stage scheme, the single-stage scheme should be optimized for the highest Betatron X-ray radiation, even if this configuration is not favorable for the two-stage scheme. The result is reported in Fig. 7.6 (b), for different values of P_1, showing an optimum at $P_1 = 25\ bars$. This optimized pressure for the single-stage Betatron source is higher than the setting $P_1 = 17\ bars$ used for optimizing the two-stage Betatron source, which is expected since in that case X-rays come from electrons oscillating in the wakefield driven by the laser in P_1, and a higher pressure in the first jet implies a stronger wiggling of electrons, and therefore a higher X-ray signal. This comes at the expense of the electron beam quality, which can be strongly degraded. The black dashed line in Fig. 7.6 (b) show the X-ray signal from the optimized two-stage source, which is about two times higher than the X-ray signal from the optimized single-stage source.

Under the light of this experimental study, several conclusions can be made. The results presented in Fig. 7.4 clearly demonstrate the ability to decouple electron acceleration and Betatron radiation production. Indeed, for $P_1 = 17\ bars$ and $P_2 = 40\ bars$, electron acceleration is well optimized in the first stage (jet 1) and Betatron X-ray radiation originates at 93% from the second stage (jet 2). The two processes, acceleration and radiation production, are well decoupled as intended. However, the increase by a factor of 14 in Fig. 7.4 cannot be considered as a source improvement compared to the usual single-stage source, where acceleration and radiation production are coupled. The experimental data of Fig. 7.6 (b) shows instead that, when comparing the optimized two-stage source to the optimized single-stage source, the X-ray signal is increased by a factor of 2.

To conclude, the decoupling of electron acceleration and Betatron X-ray radiation production was experimentally demonstrated with attractive results. The X-ray source signal was increased by a factor of 2 using the two-stage scheme, which is already a promising result if it can be further improved by a better coupling between the two stages and with improved laser parameters and possibly higher electron charges, a possibility currently being investigated in Salle Jaune by correcting for laser chromatic aberrations. The numerical work of section 2 relied indeed on better laser parameters than the one available at LOA, for which the two-stage scheme is the most interesting as the difference in plasma density between the two stages is very important (two orders of magnitude). The real potential for the hybrid two-stage scheme has not been fully demonstrated yet experimentally, and certainly requires experiments at PW laser facility, where the expected gain is much higher.

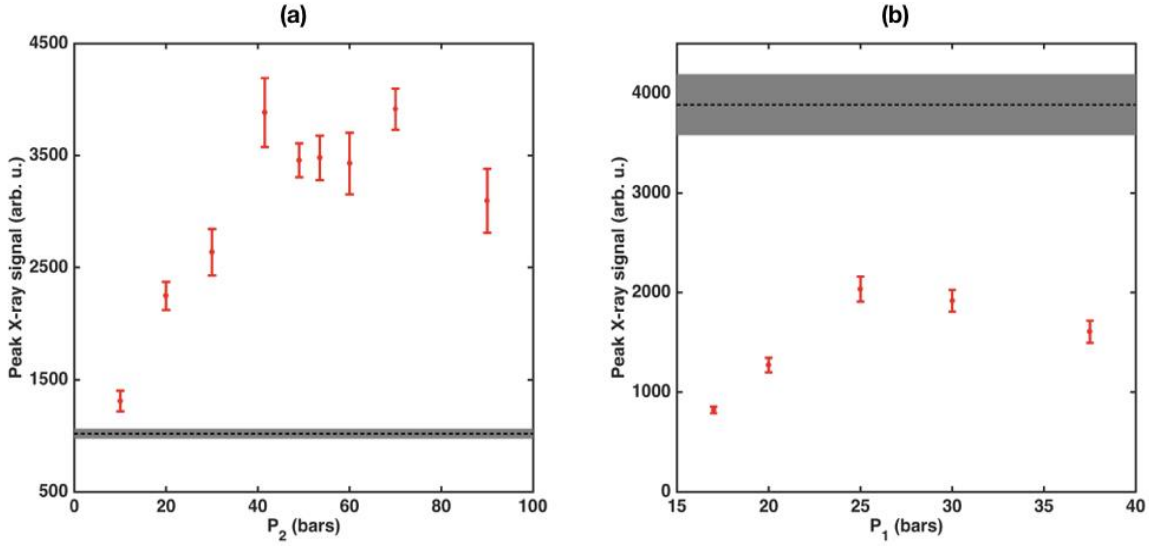

Figure 7.6: (a) Plot of the peak X-ray signal in count number as a function of the backing pressure of the second gas jet, for $P_1 = 17\ bars$. The black dashed line is the count level when only jet 1 is switched on, also for $P_1 = 17\ bars$. (b) Plot of the peak X-ray signal in count number as a function of the backing pressure in the first gas jet, with the second jet switched off and for laser and jet 1 parameters optimized for the highest X-ray signal. The black dashed line shows the count level of the fully-optimized two-stage X-ray source ($P_1 = 17\ bars$ and $P_2 = 41{,}5\ bars$), which is twice higher than the single-stage optimum. A calibration of the X-ray signal is to be accomplished again in 2018 at LOA.

Conclusion

Summary of the results

This section is a summary of the main results of my thesis.

I reported the first demonstration of the acceleration of a distinct positron bunch in a Plasma Wakefield Accelerator. Such a demonstration was challenging as the focusing and accelerating phase range for positrons in a positron driven wakefield is short. Even though the experiment was hard to accomplish, a clear proof of acceleration was reported along with a proof of longitudinal beam-loading that provided an insight into the energy transfer from the wave to the trailing bunch. In this experiment, the initial $350\ pC$ trailing bunch, initially at $20.05\ GeV$, extracted energy from the wakefield to lead to a typical accelerated bunch that contained $85\ pC$, and had a peak energy of $21.50\ GeV$. An energy gain of $1.45\ GeV$ was obtained. This represents an accelerating gradient of $1.12\ GeV\ m^{-1}$.

Two regimes of acceleration are of interest for the community of PWFA, the nonlinear "bubble regime" and the linear or quasilinear regime. The former is not favorable for positron acceleration because in this regime, the behavior of plasma electrons is not symmetric to their motion in electron driven waves. In addition, producing positron beam drivers is not energetically favorable. This is why PWFA positron acceleration would highly benefit from a regime in which a positron bunch extracts the energy of a laser driven or electron driven wakefield. The use of the universal quasilinear regime – that relies on a similar wakefield for laser, electron and positron drivers – was considered but never demonstrated for positrons. I brought in chapter 5 a clear evidence of the realization of such a regime. By increasing the emittance of the drive bunch, we overcame the tendency of positron drivers to evolve toward a nonlinear regime. A good agreement between numerical simulations and experimental results sustained the evidence that acceleration of trailing positrons was occurring in a quasilinear wakefield.

In chapter 6, I reported the results of the first experimental attempt to explore a hybrid compact approach. The corresponding M-PAC project aims at creating a LWFA-PWFA two-stage experiment. Such a scheme would rely on the production of LWFA electron bunches in a first gas jet, and then use these electron bunches to drive wakefields in the gas jet of the second stage. The first experimental campaign of the project provided the proof that the LWFA electron bunches can interact with the second stage gas jet. In fact, a clear self-focusing effect was seen in the second stage, with a reduction of the divergence of the electron beam spanning from 32% at $100\ MeV$ to 16 % at $200\ MeV$. This result provides an experimental demonstration of a beam-driven wakefield in the second stage. In addition, the two stages were separated by a thin foil that blocked the laser driving the wakefield of the first stage. A side effect of this thin foil is the defocusing of the electron bunch. I contributed to the study of this effect by conducting experimental tests that allowed us to exclude some

physical interpretations, such as the reflected laser ponderomotive force or instabilities within the bulk of the foil, and to propose a credible origin for this effect, related to the existence of strong electromagnetic fields at the surface of the material affecting the electron beam.

Last, in chapter 7, I report on the experimental confirmation of the theoretical work of Julien Ferry. His theoretical and numerical proposal suggested a scheme that exploits the advantages of a two-stage hybrid LWFA-PWFA scheme to produce high energy and bright Betatron X-rays from an LWFA beam. In fact, a two-stage setup allows to decouple the acceleration of LWFA electrons – favorable in plasmas with an electron density of $10^{18}\ cm^{-3}$or lower – and the Betatron oscillations of the electrons, favorable in plasmas with an electron density of $10^{20}\ cm^{-3}$ or higher. I reported the results of the experiment accomplished at LOA to illustrate this concept, with the $50\ TW$, $30\ fs$ laser pulse of Salle Jaune that produced LWFA bunches with broadband electron energy spectra with a maximum energy of $200\ MeV$. The laser parameters available at LOA allowed us to clearly decouple electron acceleration and Betatron X-ray production, with an enhancement of the X-ray emission by a factor of 2 compared to the optimized single-stage Betatron X-ray source.

Future prospects

These results have opened many promising prospects: they brought a confirmation of the scientific advances the plasma accelerator community is making towards an all plasma collider. They also suggest several new studies, in the project of building the hybrid LWFA-PWFA platform.

Acceleration of a distinct positron bunch: towards a plasma-based electron-positron collider. For the prospects of applying plasma-based accelerator technology to high-energy physics, it is crucial that not only electrons are successfully accelerated to high energies in plasmas, but also its antimatter counterpart, the positron. In the context of plasma-based positron acceleration, the experimental work of **[Corde 15]** demonstrated the possibility to accelerate positrons in a nonlinear plasma wakefield at high field and with high energy transfer efficiency from the wake to the accelerated positrons. The work relied on a single positron bunch sent into the plasma, and has opened the prospect for an "afterburner" or "energy booster" to an existing conventional linear electron-positron collider. However, performing drive-trailing two-bunch experiments in which a trailing positron bunch extracts the energy deposited in the plasma by a drive bunch is of paramount importance if one wants to accelerate from the start a distinct bunch of positrons in multiple plasma accelerator modules, thereby opening the prospect for an all plasma collider. The demonstration of the acceleration of a distinct positron bunch in plasma-based particle accelerators, reported in this thesis, is now accomplished.

Because the use of positron bunches to drive plasma waves is not energetically favorable, our demonstration should be extended to electron and laser drivers. In the quasilinear regime, this should be straightforward as the plasma response is nearly symmetrical in this case. After the shutdown of the FACET facility, the advanced accelerator test facility is being upgraded to FACET-II to deliver much better beam parameters and new capabilities, and the possibility to deliver pairs of electron drive bunch and positron trailing bunch with longitudinal separation of less than 100 μm is being considered. This would allow for the experimental study of positron bunch acceleration in electron-driven plasma wakes.

Proposing a plasma-based collider scheme whose final beam parameters match all the requirements of a high-energy particle collider remains an extreme challenge in 2017. Two ordeals will have to be overcome: the issues of **emittance** and **charge conservation** along acceleration, for both positron and electron beams, while keeping high wall-plug energy efficiency. Preserving ultralow emittance is a particularly challenging task for positrons. The nonlinear regime allows for high efficiency, but the transverse force experienced by the positrons is not linear with the radial coordinate, which leads to emittance growth unless the positron bunch has a radial equilibrium distribution. Such transverse equilibrium distribution, accounting for the self-consistent wakefields (that is, beam loading), is slice-dependent, non-separable and highly nontrivial. While the quasilinear regime is promising for positrons, the charge of the accelerated ultralow emittance positron bunch is limited to prevent the collapse of the positron bunch leading to nonlinear beam loading. This sets strong limits on the energy efficiency that can be achieved. Another alternative for positron acceleration is the hollow plasma channel (a tube of plasma), allowing to suppress the transverse focusing force inside the channel, thereby opening the prospect for emittance preservation at ultralow emittance. But hollow plasma channels suffer from very strong transverse instabilities, and solutions for their mitigations have to be found. Achieving **simulatenously** the preservation of ultralow emittance and high energy efficiency in plasma-based positron acceleration will certainly be the most challenging milestone of the next decade.

A hybrid LWFA-PWFA platform: PWFA studies in small facilities. The cost and footprint of conventional accelerator facilities is a major barrier to particle beam applications and plasma acceleration experiments. The realization of a hybrid LWFA-PWFA two-stage experiment would offer the possibility to run plasma wakefield acceleration of electrons in a small size facility such as Salle Jaune at Laboratoire d'Optique Appliquée. Other groups in the world are also considering the development of such two-stage hybrid LWFA-PWFA setup **[Chou 16]**.

In our setup, a thin foil between the two gas stages blocks the laser driving the wakefield in the first stage, ensuring that the electrons alone interact in the second stage. In comparison to other experimental designs that use a large distance between the two stages (typically 5 to 10 mm) to ensure the wakefield in the second stage is driven by the electron beam (PWFA) and not by the laser pulse (LWFA), using the thin foil offers the prospects of a much more compact setup with sub-mm distance between the LWFA and PWFA stages, and hence a much better coupling of the electron beam into the second stage. But the potentially detrimental effect of the thin foil, which is observed to be largely superior in experiments than the multiple angle scattering prediction, is a very important effect that needs to be studied and understood before considering the physics of beam-plasma interaction in the second stage. While the experimental tests we have conducted allowed us to exclude some physical interpretations and to put experimental constraints on physical models, a theoretical and numerical study is now necessary and is underway in our group at LOA. From my analysis of chapter 6, the effect of strong electromagnetic fields at the surface of the foil on the electron beam is a potential candidate for the development of a physical model, and will be investigated in further details in the near future.

Last, the beam-plasma interaction occurring in the second jet must be improved, with the prospect of observing energy loss or gain of the particles in the electron beam. The effect of **pre-ionizing the plasma** in the second stage will be considered, and can potentially lead to substantial improvements in the beam-plasma interaction, as the ionization of the plasma by

the electron beam itself is known to have important limitations, in particular related to the beam head erosion. The **use of quasi-monoenergetic** shock-injected electron bunches could also bring some new information. The optimization of the hybrid LWFA-PWFA platform could also strongly benefit from in-situ optical visualization of the beam-driven wakefield and of its magnetic fields, using optical shadowgraphy snapshots with 5 fs probe laser pulse and using Faraday measurements of the magnetic field.

Plasma-based X-ray sources. Among the applications of plasma-based particle beam acceleration, X-ray source production focuses the attention from multiple communities. In fact, X-ray radiation is a fundamental tool for bioimaging, material science and atomic physics. The unique properties of plasma based X-ray sources make them unrivaled choices for use in high resolution X-ray phase contrast imaging. The scheme suggested and studied theoretically by Julien Ferri **[Ferri 17]** showed very promising prospects for plasma-based Betatron X-ray sources. Its experimental investigation with the parameters of the laser system of Salle Jaune at LOA brought a first proof of principle for this scheme. Accomplishing a new experimental campaign could however bring more impressive results. The very promising laser to X-ray **energy transfer efficiency** of the order of 1 % in Julien Ferri's work should be **demonstrated experimentally**, by using a **laser power** closer to the numerical choice of the article, 0.5 *PW*, an order of magnitude higher than the laser power in Salle Jaune. Doing so, one could exploit the full potential of this two-stage hybrid scheme for the first time.

In the context of plasma-based acceleration research, my thesis contributed to the scientific journey towards innovative plasma technologies for particle accelerators and X-ray sources. Even though many challenges are still to be overcome before producing particle beams with parameters matching colliders requirements, the accomplishments of the recent years invite to remain optimistic regarding the promises plasma-based acceleration has brought. Some researchers even suggest that a plasma-based collider could be built within decades **[Esarey 16]**. On a shorter time scale, the Betatron X-ray source or the Compton source **[Ta Phuoc 12]** already offer unique opportunities for bioimaging, atomic physicists and material scientists to accomplish convenient and low cost experimental campaigns. The Betatron source properties make it already feasible for a commercial development. An optimized two-stage scheme - reported in my thesis - could bring the available performances of such a system to the next level.

Bibliography

[Adli 13] Adli, E., Delahaye, J-P., Gessner, S. J., Hogan, and al., *A beam driven plasma-wakefield linear collider: from Higgs Factory to Multi-TeV,* SLAC-PUB-15426, 2013.

[Adli 15] Adli, E., Gessner, S., J., Corde, S., Hogan, and al., *Cherenkov light-based beam profiling for ultrarelativistic electron beams*, Nuclear instruments and methods in physics research A, **783**, 35-42, 2015.

[Agostini 68] Agostini, P., Barjot, G., Bonnal, J.F., Mainfray, G., and al., *U-5-Multi-photon ionization of hydrogen and rare gases*, IEEE journal of quantum electronics, **4**, 667-669, 1968.

[Akhiezer 56] Akhiezer, A. I. and Polovin, R. V., *Theory of wave motion of an Electron Plasma*, Journal of Experimental and Theoretical Physics, **30**, 915-928, 1956.

[An 13] W. An, V. K. Decyk, W. B. Mori, and T. M. Antonsen Jr., *An improved iteration loop for the three-dimensional quasi-static particle-in-cell algorithm: QuickPIC*, J. Comput. Phys. **250**, 165-177, 2013.

[An 13b] An, W., Zhou, M., Vafaei-Najafabadi, N., Marsh, K. and al., *Strategies for mitigating the ionization-induced beam head erosion problem in an electron-beam-driven plasma wakefield accelerator*, PRSTAB, **16**, 101301, 2013.

[Bethe 57] Bethe H. A. and Saltpeter E. E., *Quantum Mechanics of One- and Two-Electron Atoms*, Elsevier, 103, 1957.

[Ben-Ismaïl 11] Ben-Ismaïl, A., Lundh, O., Rechatin, C., Lim, J., K., and al., *Compact and high-quality gamma-ray source applied to 10 µm-range resolution radiography*, Applied Physics Letters, **98**, 264101, 2011.

[Blue 03] B. E. Blue, C. E. Clayton, C. L. O'Connell, F.-J. Decker, and al., *Plasma-wake acceleration of an intense positron beam*, Physical Review Letters, **90**, 214801, 2003.

[Blumenfeld 07] Blumenfeld, I., Clayton C. E., Decker, F., Hogan, and al., *Energy doubling of 42 GeV electrons in a meter-scale plasma wakefield accelerator*, Nature, **445**, 741, 2007.

[Bourjaily 04] Bourjaily, J., L., *Classical Electrodynamics*, Physics 505, 2004.

[Bruhwiler 03] Bruhwiler, D., L. and Dimitrov, D., A., *Particle-in-cell simulations of tunnelling ionization effects in plasma-based accelerators*, **10**, 2022, 2003.

[Bulanov 97] Bulanov, S., V., Pegoraro, F., Pukhov, A., M. and Sakharov, A., S., *Transverse-wake wave breaking*, Physical Review Letters, **78**, 4205-4208, 1997.

[Bulanov 98] S. Bulanov, N. Naumova, F. Pegoraro and J. Sakai, *Particle injection into the wave acceleration phase due to nonlinear wake wave breaking*, Physical Review E, **58**, 2856-2860, 1998.

[Cartz 95] Cartz, L., *Nondestructive testing*, ASM International, 1995.

[Corde 12] S. Corde, C. Thaury, A. Lifschitz, G. Lambert, and al., *Observation of longitudinal and transverse self-injections in laser-plasma accelerators*, Nature Communications, **4**:1501, 2012.

[Corde 13] S. Corde, K. Ta Phuoc, G. Lambert, Fitour, and al., *Femtosecond x rays from laser-plasma accelerators*, Reviews of modern physics, **85**, 34-6861, 2013.

[Corde 15] S. Corde, E. Adli, J. M. Allen, W. An, and al., *Multi-gigaelectronvolt acceleration of positrons in a self-loaded plasma wakefield*, Nature, **524**, 442-445, 2015.

[Coutard 37] Coutard, H., *The results and methods of treatment of cancer by radiation*, Annals of surgery, Paris, France, **106**, 584-598, 1937.

[Christophilos 64] Christophilos, N.C., Hester, R. E., Lamb, W. A. S. and Reagan, D. D., *High-current linear induction accelerator for electrons*, Review of Scientific Instruments **35**, 886, 1964.

[Chen 85] Chen, P., Dawson, J. M., Huff, R. W. and Katsouleas, T., *Acceleration of electrons by the interaction of a bunched electron beam with a plasma*, PRL, **54**, 693-696, 1985

[Chen 89] Chen, P. and Rosenzweig, J., *Beam optics of a self-focusing plasma lens*, Physical Review D, **39**, 7, 1989.

[CLIC 12] *CLIC*, CLIC Conception design reports, 2012.

[Cros 16] Cros, B., *Plasma physics: Compact coupling for a two-stage accelerator*, Nature, 530, 165-166, 2016.

[Dalla 93] Dalla, S. and Lontano, M., *On the maximum longitudinal electric field of a large amplitude electron plasma wave excited by a short electromagnetic radiation pulse*, Physics letters A, 456-461, 1993.

[Dalla 94] Dalla, S. and Lontano, M., *Large amplitude plasma wave excitation by means of sequences of short laser pulses*, Physical Review E, **49**, 1819-1822, 1994

[Dawson 59] Dawson, J., *Nonlinear electron oscillations in a cold plasma*, Physical Review, **113**, 383-387, 1959.

[Debye 23] *P. Debye and E. Hückel, The theory of electrolytes. I. Lowering of freezing point and related phenomena, Physikalische Zeitschrift, 24, 185–206, 1923.*

[Deng 03] Deng, S., Barnes, C., Clayton, C., O'Connel, C. *and al., Plasma wakefield acceleration in self-ionized gas or plasma, Physical Review E, **68**, 047401, 2003.*

[Decker 94] Decker, C., D. and Mori, W., B., *Group velocity of large amplitude electromagnetic waves in a plasma*, Physical Review Letters, **72**, 490-493, 1994.

[Doche 17] Doche, A., Beekman, C., Corde, S., Allen, and al., *Acceleration of a trailing positron bunch in a plasma wakefield accelerator*, Scientific Reports, **7**:14180, 2017.

[Dolgoshein 93] Dolgoshein, B., *Transition radiation detectors*, Nuclear instruments and methods in physics research A, **326**, 434-469, 1993.

[Döpp 16] Döpp, A., Guillaume, E., Thaury, C., Lifschitz, and al., *A bremsstrahlung gamma-ray source based on stable ionization injection of electrons into a laser wakefield accelerator*, Nuclear instruments and methods in physics A, **830**, 515-519, 2016.

[Downer 14] Downer, M., Zgadzaj, R., News and views, 2014 Editor's choice, Nature, **515**, 40-41, 2014.

[Erikson 84] Erikson, R., SLAC Linear Collider Design Handbook SLAC-R-714 http://www.slac.stanford.edu/pubs/slacreports/slac-r-714.html, 1984.

[Esarey 95] Esarey, E. and Pilloff, M., *Trapping and acceleration in nonlinear plasma waves*, Physic of Plasmas, **2**, 1432-1436, 1995.

[Esarey 96a] Esarey, E., Shadwick, B. A., Schroeder, C., B. and W. P. Leemans, *Nonlinear pump depletion and electron dephasing in laser wakefield accelerators*, AIP Conference Proceedings 737, 578, 2004.

[Esarey 96b] Esarey, E., Sprangle, P., Krall J. and Ting, A., *Overview of plasma-based accelerator concepts*, IEEE transactions on plasma science, 24, 252-288, 1996.

[Esarey 97] Esarey, E., Sprangle, P., Krall, J. and Ting, A., *Self-focusing and guiding of short laser pulses in ionizing gases and plasmas*, IEEE journal of quantum electronics, **33**, 1879-1914, 1997.

[Esarey 09] Esarey, E., Schroeder, C., B. and Leemans, W., P., *Physics of laser-driven plasma-based electron accelerators*, Review of Modern Physics, **81**, 1229, 2009.

[Esirkepov 06] Esirkepov, T., Bulanov, S., V., Yamagiwa and M., Tajima, T., *Electron, positron and photon wakefield acceleration: trapping, wake overtaking and ponderomotive acceleration*, Physical Review Letters, **96**, 014803, 2006.

[Fainberg 56] Fainberg, I. B., *The use of plasma waveguides as accelerating structures in linear accelerators*, Ukrainian academy of science, Kharkov.

[Faure 04] Faure, J., Glinec, Y., Pukhov, A., Kiselev, S. and al., *A laser-plasma accelerator producing monoenergetic electron beams*, Nature, **431**, 541–544, 2004.

[Faure 06] Faure, J., Rechatin, C., Norlin, A., Lifschitz, and al., *Controlled injection and acceleration of electrons in plasma wakefields by colliding laser pulses*, Nature, **444**, 737–739, 2006.

[Faure 07] Faure, J., *Accélération de particules dans les plasmas*, 2007.

[Ferri 16] Ferri, J., *Etude des rayonnements Bétatron et Compton dans l'accélération par sillage laser*, thesis, 2016.

[Fourmaux 11] Fourmaux, S., Corde, S., Ta Phuoc, K., Lassonde and al., *Single shot phase contrast imaging using laser-produced Betatron x-ray beams*, Optics Letters, **36**, 2426-2428, 2011.

[Frederico 16] Frederico, J., *Theory and measurements of emittance preservation in Plasma Wakefield Acceleration*, Thesis manuscript, 2016.

[Geddes 04] Geddes, C. G. R., Toth, C., van Tilborg, J., Esarey, and al., *High-quality electron beams from a laser wakefield accelerator using plasma-channel guiding*, Nature, **431**, 538–541, 2004.

[Geddes 08] C. G. R. Geddes, K. Nakamura, G. R. Plateau, Cs. Toth, and al., *Plasma-density-gradient injection of low absolute-momentum-spread electron bunches*, Physical Review Letters, **100,** 215004, 2008.

[Geraci 00] Geraci, A., A., Witthum, D., H., *Transverse dynamics of a relativistic electron beam in an underdense plasma channel*, Physics of plasmas, **7**, 8, 2000.

[Gibney 15] Gibney, E., *CERN's next director-general on the LHC and her hopes for international particle physics*, News: Q&A, Nature, 2015.

[Gibbon 05] Gibbon, P., *Short pulse laser interaction with matter*, an introduction, Imperial College Press, 2005.

[Glinec 06] Glinec, Y., Faure, J., Guemnie-Tafo, A., Malka and al., *Absolute calibration for a broad range single shot electron spectrometer*, Review of scientific instruments, **77**, 103301, 2006.

[Gorbunov 97] Gorbunov L., Mora, P and Antonsen T. M., *Quasistatic magnetic field generated by a short laser pulse in an underdense plasma*, Phys. Of Plasmas, **4**, 4358-4368, 1997.

[Green 14] Green, S., Z., Adli, E., Clarke, C., I., Corde, S. and al., *Laser ionized preformed plasma at FACET*, Plasma physics and controlled fusion, **56**, 084011, 2014.

[Guillaume 15] Guillaume, E., Döpp, A., Thaury, C., Ta Phuoc, and al., *Electron rephrasing in a laser wakefield accelerator*, Physical Review Letters, **115**, 155002, 2015.

[Heinemann 17] Heinemann, T., Hidding, B., Assman, R., Martinez de la Ossa, A. and al., *Investigating the key parameters of a staged laser- and particle driven plasma wakefield accelerator experiment*, Proceedings of IPAC 2017, 2017.

[Hogan 03] Hogan, M., Clayton, C., Huang, C., Muggli and al., *Ultrarelativistic-positron-beam transport through meter-scale plasmas*, Physical Review Letters, **90**, 20, 2003.

[Hogan 05] Hogan, M., Barnes, C., Clayton, Decker, F. and al., *Multi-GeV energy gain in a plasma-wakefield accelerator*, Physical Review Letters, **95**, 054802, 2005.

[Huang 06] C. Huang, V. K. Decyk, M. Zhou, W. Lu and al., *QuickPIC: a highly efficient fully parallelized PIC code for plasma-based acceleration*, J. Comput. Phys. **217**, 658-679 (2006).

[Humphries 85] Humphries, S., *Principles of Charged Particle Acceleration*, 1st Edition, Wiley, 1985.

[Humphries 02] Humphries, S., *Charged Particle Beams*, 2nd Edition, Wiley, 2002.

[ILC 07] ILC press, *ILC reference design report*, 2007 2007.

[Ising 24] Ising, G., *Prinzip einer Methode zur Herstellung von Kanalstrahlen hoher Voltzahl. In: Arkiv för Matematik*, Astronomi och Fysik, **8**, 1-4, 1924.

[Jackson 62] Jackson, J. D., *Classical Electrodynamics*, 3rd Edition, Wiley, 1962.

[Joshi 84] Joshi, C., Mori, W., B., Katsouleas, T., Dawson, and al., *Ultrahigh gradient particle acceleration by intense laser-driven plasma density waves*, Nature, **311**, 525, 1984.

[Joshi 03] Joshi, C., Blue, B., Clayton, C., Dodd, E. and al., *High energy plasma science with an ultrarelativistic electron beam*, Physics of plasmas, **9**, 1845, 2002.

[Joshi 03] Joshi, C. and Katsouleas, T., *Plasma accelerators at the energy frontier and on tabletops*, Physics today, 47-53, 2003.

[Kalal 88] Kalal, M. and Nugent, K, *Abel inversion using fast Fourier transforms*, Applied optics, **27**, 1956–1959, 1988.

[Kalmykov 09] Kalmykov, S., Yi, S. A., Khudik, V. and Shvets, G., *Electron self-injection and trapping into an evolving plasma bubble*, Physical Review Letters, **103**, 135004, 2009.

[Katsouleas 86] Katsouleas, T., *Physical mechanism in the plasma wake-field accelerator*, Physical Review A, **33**, 2056-2064, 1986.

[Katsouleas 87] Katsouleas, T., Wilks, S., Chen, P., Dawson, J., Su, J., *Beam loading in plasma accelerators*, Particle accelerators, **22**, 81-99, 1987.

[Keinigs 86] Keinigs, R. and Jones, M. E., *Two-dimensional dynamics of the plasma wakefield accelerator*, Phys. Fluids **30,** 252-263, 1987.

[Keldysh 65] Keldysh, L., *Ionization in the field of a strong electromagnetic wave*, JETP, 20:1307, 1965.

[Kerst 40] Kerst, D. W., *Acceleration of Electrons by Magnetic Induction*, Physical Review, **58**, 841, 1940.

[Khan 08] Khan, S., *Free-electron lasers*. Journal of Modern Optics 55, **21**, 3469–3512, 2008.

[Kim 13] Kim, H. T., Pae, K. H., Cha, H. J., Kim, I. J., and al., *Enhancement of electron energy to the multi-GeV regime by a dual-stage laser-wakefield accelerator pumped by petawatt laser pulses*, Physical Review Letter, **111**, 165002, 2013.

[Klein 08] Klein, E., *Electron-beam therapy: dosimetry, planning and techniques, Principles and practice of radiation oncology*, 5th edition, 2008.

[Krall 91] Krall, J., Joyce, G. and Esarey, E., *Vlasov simulation of very-large-amplitude-wave generation in the plasma wakefield accelerator*, Physical Review A, **44**, 10, 1991.

[Kruer 88] Kruer, W., *The physics of laser-plasma interactions*, Westview Press, 1988.

[Larsen 71] Larsen, R., S., *Toroidal charge monitoring systems*, SLAC-PUB-**947**, August 1971.

[Lawrence 32] Lawrence, E. O., Livingston, M. and Stanley, M., *The Production of High Speed Light Ions Without the Use of High Voltages*, Physical Review, **40**, 19-35, 1932.

[Leemans 14] W. P. Leemans, A. J. Gonsalves, H. S. Mao, K. Nakamura, and al., *Multi-GeV electron beams from capillary-discharge-guided subpettawatt laser pulses in the self-trapping regime*, Physical Review Letters **113**, 245002, 2014.

[Lee 01] Lee, S., Katsouleas, T., Hemker, R., G., Dodd, E., S. and Mori, W., B., *Plasma-wakefield acceleration of a positron beam*, Physical Review E, **64**, 045501, 2001.

[Lee 02] Lee, S., Katsouleas, T., Muggli, P. and Mori, W. and al., *Energy doubler for a linear collider*, PRSTAB, **5**, 011001, 2002.

[Lehe 13] Lehe, R., Lifschitz, A., Davoine, X., Thaury, C. and Malka, V., *Optical transverse injection in laser-plasma acceleration*, Physical Review Letters, **111**, 085005, 2013.

[Lejeune 80] C. Lejeune and J. Aubert, *Emittance and Brightness: Definitions and Measurements*, Applied Charged Particle Optics, Academic Press, New York, A-159, 1980.

[Levin 05] Levin, W., Kooy, H., Loeffler, J., S. and Delaney, T., F., *Proton beam therapy*, British journal of cancer, **93**, 849-854, 2005.

[LHC 12] *Observation of a new particle in the search for the Standard Model Higgs boson with the ATLAS detector at the LHC*, Physics Letters B, **716**, 1-29, 2012.

[Litos 11] Litos, M., Bionta, M. R., Dolgashev, V., A., England, R., J., and al., *Evaluation of temporal diagnostic techniques for two-bunch facet beam*, SLAC publication, **14419**, 2011.

[Litos 14] M. Litos, E. Adli, W. An, C. I. Clarke, and al., *High-efficiency acceleration of an electron beam in a plasma wakefield accelerator*, Nature, **515**(7525), 92-95, 11, 2014.

[Litvak 69] Litvak, A., *Finite-amplitude wave beams in a magnetoactive plasma*, JETP, **30**, 2, 1969.

[Lu 05] Lu, W., Huang, C., Zhou, M., Mori, W. and Katsouleas, T., *Limits of linear plasma wakefield theory for electron or positron beams*, Physics of plasmas, **12**, 063101, 2005.

[Lu 06a] Lu, W., Huang, C., Zhou, M., Mori, W. B. and Katsouleas, T., *Nonlinear theory for relativistic plasma wakefields in the blowout regime*, Physical Review Letters, **96**, 165002, 2006.

[Lu 06b] Lu, W., Huang, C., Zhou, M., Tzoufras, and al., *A nonlinear theory for multidimensional relativistic plasma wave wakefields*, Physics of plasmas, **13**, 056709, 2006.

[Lu 07] Lu, W., Tzoufras, M., Joshi, C., Tsung, F. and al., *Generating multi-GeV electron bunches using single stage laser wakefield acceleration in a 3D nonlinear regime*, PRSTAB, **10**, 061301, 2007.

[Lu 10] Lu, W., An, W., Zhou, M., Joshi, C. and al, *The optimum plasma density for plasma wakefield excitation in the blowout regime*, New Journal of Physics, **12**, 085002, 2010.

[Maine 88] Maine, P., Strickland, D., Pessot, M. and Mourou, G., *Generation of ultrahigh Peak Power pulses by chirped pulse amplification*, IEEE Journal of quantum electronics, **24**, 398-403, 1988.

[Malka 02] Malka, V., Fritzler, S., Lefebvre, E., Aleonard, and al., *Electron acceleration by a wakefield forced by an intense ultrashort laser pulse*, Science, **298**, 1596-1600, 2002.

[Malka 08] Malka, V., Faure, J., Gauduel, Y., Lefebvre, and al., *Principles and applications of compact laser-plasma accelerators*, Nature Physics, **4**, 448-453, 2008.

[Mangles 04] Mangles, S. P. D., Murphy, C. D., Najmudin, Z., Thomas, A. G. R., Collier, J. L., and al., *Monoenergetic beams of relativistic electrons from intense laser-plasma interactions*, Nature, **431**(7008), 535–538, 2004.

[McGuffey 10] McGuffey, C., Thomas, A., Schumaker, W., Matsuoka, T., Chvykov, and al., *Ionization induced trapping in a Laser wakefield accelerator*, Physical Review Letter, **104**, 025004, 2010.

[Mehrling 12] Mehrling, T., Grebenyuk, J., Tsung, F. S., Floettmann, K. and Osterhoff, J., *Transverse emittance growth in staged laser-wakefield acceleration*, Physical Review ST Accelerators and Beams, 15:111303, 2012.

[Michel 06] Michel, P., Schroeder, C.B., Shadwick, B. A., Esarey, E. and Leemans W. P., *Radiative damping and electron beam dynamics in plasma-based accelerators*, Physical Review E, 74:026501, 2006.

[Mora 13] Mora, P., *Introduction aux plasmas créés par laser*, Editions de l'école Polytechnique, 2013.

[Mori 90] Mori, W. B. and Katsouleas, T., *Wavebreaking of longitudinal plasma oscillations*, Physica Scripta, **30**, 127-133, 1990.

[Mozgovoi 86] Mozgovoi, A., G., Novikov, I., I., Pokrasin, M., A. and Roschupkin, V., V., *The saturated vapour pressure of lithium, Sodium, Potassium, Rubidium and Cesium*, High temperatures, high pressures, **19**, 425-430, 1987.

[Muggli 99] Muggli, P., Marsh, K., A., Wang, S., Clayton, C., E., and al., *Photo-ionized lithium source for plasma accelerator applications*, IEEE transactions on plasma science, **27**, 3, 1999.

[Muggli 01] Muggli, P., Lee, S., Katsouleas, T., Assman, and al., *Collective refraction of a beam of electrons at a plasma-gas interface*, PRSTAB, **4**, 091301, 2011.

[Muggli 08] Muggli, P., Blue, B., E., Clayton, C., E., Decker, F., and al., *Halo formation and emittance growth of positron beams in plasmas*, Physical Review Letters, Physical Review Letters, **101**, 055001, 2008.

[Myers 90] Myers, S., *The LEP collider from design to approval and commissioning*, CERN Press 1990.

[**Nakanishi 91]** Nakanishi, H., Yoshida, Y., Ueda, T., Kozawa, T. and al., *Direct observation of plasma-lens effect*, **66**, 1970, 1991.

[Neal 68] Neal, R., B., *The two-miles Stanford Accelerator, New York, W.A. Benjamin, Inc., 59,* 1968.

[Ng 01] Ng, J., Chen, P., Baldis, H. and Bolton, P., *Observation of plasma focusing of a 28.5 GeV positron beam*, Physical Review Letters, **87**, 244801, 2001.

[Ng 06] Ng, K., Y., *Physics of intensity dependent beam instabilities*. World Scientific Publishing, 108, 2006.

[Noble 83] Noble, R., J., in Proceedings of the 12th International Conference on High Energy Accelerators, 1983.

[Olive 14] Olive K.A. and al. (Particle Data Group), Chinese Physics C, **38**, 090001, 2014.

[Pak 10] A. Pak, K. A. Marsh, S. F. Martins, W. Lu, and al., *Injection and trapping of tunnel-ionized electrons into laser-produced wakes*, Physical Review Letters, **104**, 025003, 2010.

[Pommarel 17] Pommarel, L., Vauzour, B., Mégnin-Chanet, F., Bayart, E., and al., *Spectral and spatial shaping of a laser-produced ion beam for radiation-*

biology experiments, Physical Review Accelerators and Beams, **20**, 2, 2017.

[Pukhov 02] Pukhov, A. and Meyer-Ter-Vehn, J., *Laser wake field acceleration: the highly non-linear broken-wave regime*, Applied physics B, **74**, 355-361, 2002.

[Pusey 00] Pusey, W. A., *Roentgen rays in the treatment of skin diseases and for the removal of hair. Journal of cutaneous diseases including syphilis*, William & Wood.,**18**: 302–318, 1900.

[Rax 05] Rax, J.-M., *Physique des plasmas*, Ed. Dunod, 2005.

[Réchatin 09] Réchatin, C., Faure, J., Ben-Ismail, A., Lim, and al., *Controlling the phase-space volume of injected electrons in a laser-plasma accelerator*, Physical Review Letters, 102, 164801, 2009.

[Réchatin 10] Réchatin, C., *Accélération d'électrons dans l'interaction laser-plasma : développement et caractérisation d'un injecteur optique*, 2010.

[Reid 91] Reid, M., B., *Electron beam emittance growth in thin foils: a Betatron function analysis*, Journal of Applied physics, 70, 7185, 1991.

[Reiser 08] Reiser, M., *Theory and design of charged particle beams*, 2nd edition, Wiley-VCH, 2008.

[Rosenzweig 87a] Rosenzweig, J. B., *Nonlinear plasma dynamics in the plasma Wakefield Accelerator*, Physical Review Letters, 58, 6, 1987.

[Rosenzweig 87b] Rosenzweig, J. B., *Nonlinear plasma dynamics in the plasma Wake-field Accelerator*, IEEE transactions on plasma science, PS-15, 2, 1987.

[Rosenzweig 88] Rosenzweig, J. B., D. B. Cline, B. Cole, H. Figueroa, and al., *Experimental Observation of Plasma Wake-Field Acceleration*, Physical Review Letters, **61**(1), 98-101, 7, 1988.

[Rosenzweig 89a] Rosenzweig, J, Schoessow, P., Cole, B., Ho, C, and al., *Experimental measurement of non-linear plasma wakefields*, physical review A, **39**, 1586-1589, 1989.

[Rosenzweig 89b] Rosenzweig, J., B., Chen, P., *Beam optics of a self-focusing plasma lens*, Physical Review D, **39**, 7, 1989.

[Rousse 04] Rousse, A., Ta Phuoc, K., Shah, R., Pukhov, A., and al., *Production of a keV x-ray beam from synchrotron radiation in relativistic laser-plasma interaction*, Physical Review Letters, **93**, 13, 2004.

[Ruth 85] R. D. Ruth, A. W. Chao, P. L. Morton, and P. B. Wilson, *A Plasma Wake Field Accelerator*, Particle Accelerators, **17**, pages 171, 1985.

[Sahai 15] Sahai, A., A., Katsouleas, T., *Optimal positron-beam excited plasma wakefields in hollow and ion-wake channels*, arXiv:1512.08013v1, 2015.

[Schroeder 10] Schroeder, C. & al. *Physics considerations for laser-plasma linear colliders*, Phys. Rev. Special Top. 13, 101301 (2010).

[Small 72] Small, R., D., Sernas, V., A. and Page, R., H., *Single beam Schlieren interferometer using a Wollaston prism*, Applied Optics, **11**, 4, 1972.

[Sprangle 87] Sprangle, P., Tang, C.M. and Esarey, E., *Relativistic self-focusing of short pulse radiation beams in plasmas*, **15**, 145-153, 1987.

[Sprangle 90] Sprangle, P., Esarey, E. and Ting, A., *Nonlinear interaction of intense laser pulses in plasmas*, Physical review A, **41**, 8, 1990.

[Sprangle 92] Sprangle, P., Esarey, E., Krall, J., Joyce, G., *Propagation and guiding of intense laser pulses in plasmas*, Physical Review Letters, **69**, 2200, 1992.

[Sprangle 01] Sprangle, P., Hafizi, B., Penano, J., R., Hubbard, R., and al., *Wakefield generation and GeV acceleration in tapered plasma channels*, Physical Review E, **63**, 056405, 2001.

[Steffen 07] Steffen, B. R. *Electro-optic methods for longitudinal bunch diagnostics at flash*, Thesis, 2007.

[Strickland 85] Strickland, D. and Mourou, G. *Compression of amplified chirped optical pulses*, Optics Communications, **55**, 447-449, 1985.

[Sun 87] Sun, G., Ott, E. and Lee, Y. C., *Self-focusing of short intense pulses in plasmas*, Physics of Fluids, **30**, 526, 1987.

[Tajima 79] T. Tajima and J. M. Dawson, *Laser Electron Accelerator*, Physical Review Letters, **43**, 267, 1979.

[Teychenné 94] Teychenné, D., Bonnaud, G. and Bobin, J., *Oscillatory relativistic motion of a particle in a power-law sinusoidal-shaped potential well*, Physical review E, **49**, 3254-3263, 1994.

[Thaury 14] Thaury, C., Guillaume, E., Döpp, A., Lehe, R. and al., *Demonstration of relativistic electron beam focusing by a laser-plasma lens*, Nature communications, **6**, 6860, 2015.

[Thwaites 06] Thwaites, D., I. and Tuohy, J., B., *Back to the future: the history and development of the clinical linear accelerator*, Physics in medicine and biology, **51**, 343-362, 2006.

[Trump 37] Trump, J.G. and Van de Graaff, R.J., *Design of a million-volt X-ray Generator for cancer treatment and research*, Journal of Applied Physics, **8**, 602, 1937.

[Tzoufras 08] Tzoufras, M., Tsung, F., S., Vieira, J. and Fonseca, R., A., *Beam loading in the nonlinear regime of plasma-based acceleration*, Physical Review Letters, **101**, 145002, 2008.

[Umstadter 96] Umstadter, D., Kim, J., K. and Dodd, E., *Laser injection of ultrashort electron pulses into wakefield plasma waves*, Physical Review Letters, **76**, 2073-2076, 1996.

[Vafaei-Najafabadi 12] Vafaei-Najafabadi, N., Shaw, J., L., Marsh, K., A., Joshi, C., Hogan, M., J., *Meter scale plasma source for plasma wakefield experiments*, AIP conference proceedings, **1507**, 650, 2012.

[Van de Graaf 33] Van de Graaf, R., J., Compton, K., T. and Van Atta, L., C., *The electrostatic production of high voltage for nuclear investigations*, Physical Review, **43**, 149, 1933.

[Veksler 44] Veksler, V. I., *A new method of accelerating relativistic particles*, Compte rendus de l'académie des sciences de l'URSS, 43, 346-348, 1944.

[Wang 13] Wang, X. M., Zgadzaj, R., Fazel, N., Li, Z. Y., and al., *Quasi-monoenergetic laser-plasma acceleration of electrons to 2 GeV*, Nat. Commun **4**, 1988 (2013).

[Wang 02] Wang, S., Clayton, C. E., Blue, B., Dodd, and al., *X-ray emission from Betatron motion in a plasma wiggler*, Physical Review Letters, **88**, 135004, 2002.

[Whittum 91] Whittum, D., W., Sharp, W., M., Yu, S., S., Lampe, M. and Joyce, G., *Electron-hose instability in the ion-focused regime*, **67**, 8, 1991.

[Zhou 07] Zhou, M., Clayton, C., Huang, C., Joshi, C. and al., *Beam head erosion in self-ionized plasma wakefield accelerators*, Procedings of PAC07, 2007.

Résumé en Français

Cette thèse porte principalement sur l'accélération de particules par ondes de sillage excitées par un faisceau de particules. C'est une thèse de recherche expérimentale, durant laquelle trois expériences ont eu lieu. Ces expériences avaient chacune un but précis, mais toutes se trouvent dans le cadre de l'accélération de particules dans des sillages plasma. Une partie de ce travail se place notamment dans le large projet de construire un jour un collisionneur de particules reposant sur la technologie d'accélération plasma, et d'exploiter les particularités de cette technologie pour les applications scientifiques d'une telle machine.

Ondes de sillage excitées par un faisceau de particules

Les accélérateurs de particules sont des inventions scientifiques aux multiples applications rappelées au début du manuscrit. Quelques exemples sont donnés, tels que le traitement du cancer, l'imagerie médicale, le contrôle non destructif ou plus fondamental, l'étude des constituants de la matière par la collision de particules de très haute énergie. Cette dernière application nécessite d'utiliser des particules d'énergie toujours plus haute pour sonder des constituants toujours plus petits de la matière. Le coût et la taille des derniers collisionneurs suggèrent qu'il faille apporter une nouvelle technologie pour permettre à la recherche fondamentale de poursuivre son développement. L'accélération par onde de sillage plasma permettrait d'augmenter les gradients d'accélération de particules. En effet, lorsque cette technologie est utilisée, les champs accélérateurs sont soutenus par des plasmas qui ne sont pas sujets à la limite de claquage électronique.

L'accélération de particules par onde de sillage est un domaine de recherche qui a déjà connu plus de cinquante ans de développement. Cette technologie repose sur le principe d'envoyer un faisceau pour perturber la densité d'électrons dans un plasma, et créer ainsi des champs accélérateurs dans le sillage de ce faisceau. Ces champs peuvent être exploités pour accélérer des particules. La théorie de l'excitation d'ondes de sillage possède des solutions analytiques dans le cas d'une faible perturbation exercée sur les électrons du plasma, c'est-à-dire dans le cas linéaire. Ces solutions ont la même forme pour une excitation par un faisceau laser ou par un faisceau de particules chargées positivement ou négativement. Ces résultats sont dérivés dans le manuscrit, et les différences entre les cas d'excitation par laser ou par un faisceau sont mises en avant. Dans le cas non-linéaire, il n'y a pas de solution analytique, en revanche des simulations numériques permettent de comprendre le comportement des électrons du plasma lorsqu'un sillage non-linéaire est créé. Ce comportement du plasma diffère entre les faisceaux de particules chargées positivement et les autres faisceaux excitateurs. Ces différences expliquent le retard que l'accélération de positrons et l'usage d'ondes de sillages excitées par des faisceaux de positrons ont sur l'accélération d'électrons.

Le résultat majeur de mon travail de thèse a été la démonstration de l'accélération d'un faisceau distinct de positron. Il s'agissait d'un résultat espéré par la communauté scientifique pour avancer vers un collisionneur électron-positron reposant sur la technologie plasma. Dans l'expérience, les ondes de sillages ont été excitées par un premier faisceau de positron. L'accélération d'un second paquet dans le sillage a été démontrée dans un régime non-linéaire, propre aux faisceaux de positrons, mais également dans un régime d'accélération quasi-linéaire, commun à tous les types de faisceaux excitateurs. Cela ouvre notamment la perspective d'utiliser des ondes de sillage laser pour accélérer des positrons.

Réaliser une expérience d'accélération par onde de sillage plasma dans un laboratoire universitaire

L'expérience précédente comme la plupart des expériences d'accélération par onde de sillage excitées par faisceau s'est déroulée dans un accélérateur conventionnel : le Stanford Linear Accelerator. Il s'agit d'un établissement employant plusieurs centaines de personnes et qui a nécessité un investissement de plus d'un milliard de dollars. La taille et le coût de ces centres de recherche limitent les scientifiques dans leurs recherches. C'est pourquoi une avancée majeure serait de rendre possible les expériences d'accélération par onde de sillage excitées par faisceaux dans un laboratoire universitaire. Le projet M-PAC et l'expérience réalisée durant ma thèse en 2017 avaient cet objectif.

L'expérience reposait sur un premier étage d'accélération par onde de sillage laser (LWFA), après lequel une feuille d'aluminium bloquait le faisceau laser. Après cette feuille, un deuxième étage d'interaction plasma était positionné, et était composé d'un jet de gaz dans lequel le faisceau d'électron créé au premier étage excitait une onde de sillage.

Les résultats de cette expérience et les premiers obstacles sont présentés et analysés dans ce manuscrit. Ce travail expérimental va se poursuivre au Laboratoire d'Optique Appliquée à partir de 2018.

Les applications des faisceaux de particules produits par sillage laser

L'accélération d'électrons par onde de sillage s'accompagne de l'émission de rayons X. En particulier les ondes de sillage laser permettent de produire dans des laboratoires tels que le Laboratoire d'Optique Appliquée des sources de rayons X au potentiel intéressant pour les applications médicales ou industrielles.

L'expérience conduite en 2016 et présentée dans la dernière partie du manuscrit proposait d'utiliser un schéma hybride pour optimiser l'émission de rayonnement. Le montage expérimental reposait à nouveau sur deux étages, composés de deux jets de gaz. Le premier jet fournissait du gaz à une pression modeste, ce qui favorise la production d'électrons de haute énergie lors d'une accélération par onde de sillage laser. Le second jet avait une pression plus forte, ce qui permettait d'obtenir une émission de rayon X plus intense, et composée de photons de plus haute énergie.

Le découplage de l'accélération des particules et de la production des rayons X est donc un schéma prometteur qui a été démontré durant la campagne expérimentale de 2016. Par ailleurs, le système reposant sur deux jets de gaz a permis d'obtenir un doublement de la quantité globale de rayon X émis.

Conclusions et perspectives de ce travail

L'expérience principale de mon travail de thèse, l'accélération d'un paquet distinct de positron dans une onde de sillage excitée par un faisceau ouvre plusieurs perspectives pour la

communauté scientifique. Il serait maintenant intéressant de parvenir à accélérer un paquet de positrons en excitant une onde plasma avec un laser ou un paquet d'électrons. Mais il est aussi important de travailler à présent à la préservation de la qualité du faisceau durant l'accélération ou encore de travailler à augmenter la charge accélérée. Ces défis sont les prochaines étapes avant de pouvoir se rapprocher d'un faisceau comparable à celui d'un accélérateur conventionnel.

L'expérience hybride LWFA-PWFA a montré qu'il fallait comprendre le détail des phénomènes physiques qui bloquent actuellement les performances du second étage d'interaction faisceau-plasma. Un travail de simulation numérique est sans doute nécessaire. Par ailleurs d'autres conditions sont peut-être intéressantes, par exemple une pré-ionisation du second étage ou l'usage de faisceaux mono-énergétiques pour obtenir une interaction plus claire, peuvent apporter de nouveaux résultats à cette étude expérimentale.

Enfin, le schéma de découplage de l'accélération d'électrons et de production de rayons X dans un système à deux étages laisse également la place à de nouvelles campagnes expérimentales. Il serait utile à la communauté scientifique d'étudier et de démontrer la grande efficacité de transfert énergétique prévue dans l'article théorique relatif à ce schéma. Il serait également intéressant d'effectuer cette expérience avec un système laser aussi performant que celui proposé par les théoriciens, pour obtenir une émission de rayonnement plus intense et des rayons X de plus forte énergie, et ainsi exploiter le schéma de découplage en profondeur.

université PARIS-SACLAY | ÉCOLE DOCTORALE Ondes et Matière (EDOM)

Titre : Accélération de particules dans des ondes de sillage plasma excitées par faisceaux de particules

Mots clés : Plasmas, ondes dans les plasmas, ondes électromagnétiques, interaction laser matière, accélération par sillage plasma, code Quick PIC (Particle in Cell).

Résumé : Les accélérateurs par onde de sillage plasma produites par faisceaux de particules (PWFA) ou par faisceaux laser (LWFA) appartiennent à un nouveau type d'accélérateurs de particules particulièrement prometteur. Ils permettent d'exploiter des champs accélérateurs allant jusqu'à plusieurs centaines de gigaélectronvolts par mètre alors que les dispositifs conventionnels se limitent à cent mégaélectronvolts par mètre. Dans le schéma d'accélération par onde de sillage plasma, ou par onde de sillage laser, un faisceau de particules ou une impulsion laser se propage dans un plasma et créé une structure accélératrice dans son sillage : c'est une onde de densité électronique à laquelle sont associés des champs électromagnétiques dans le plasma. L'un des principaux résultats de cette thèse a été la démonstration de l'accélération par onde de sillage plasma d'un paquet distinct de positrons. Dans le schéma utilisé, un plasma de lithium était créé dans un four, et une onde plasma était excitée par un premier paquet de positrons (le pilote ou faisceau excitateur) et l'énergie était extraite par un second faisceau (le trailing ou faisceau témoin). Un champ accélérateur de $1{,}12\ GeV/m$ a ainsi été obtenu durant l'expérience, pour une charge accélérée typique de 85 pC. Nous montrons également ici la possibilité d'utiliser différents régimes d'accélération qui semblent très prometteurs. Par ailleurs, l'accélération de particule par sillage laser permet quant à elle, en partant d'une impulsion laser femtoseconde de produire un faisceau d'électron quasi-monoénergétique d'énergie typique de l'ordre de 200 MeV. Nous présentons les résultats d'une campagne expérimentale d'association de ce schéma d'accélération par sillage laser avec un schéma d'accélération par sillage plasma. Au cours de cette expérience un faisceau d'électrons créé par laser est refocalisé lors d'une interaction dans un second plasma. Une étude des phénomènes associés à cette plateforme hybride LWFA-PWFA est également présentée. Enfin, le schéma hybride LWFA-PWFA est prometteur pour optimiser l'émission de rayonnement X par les électrons du faisceau de particule crée dans l'étage LWFA de la plateforme. Nous présentons dans un dernier temps la première réalisation expérimentale d'un tel schéma et ses résultats prometteurs.

Title: Particle acceleration with beam driven wakefield

Keywords: Plasmas, plasma and electromagnetic waves, laser-matter interaction, Plasma Wakefield Acceleration, Quick PIC (Particle in Cell) code.

Summary: Plasma wakefield accelerators (PWFA) or laser wakefield accelerators (LWFA) are new technologies of particle accelerators that are particularly promising, as they can provide accelerating fields of hundreds of gigaelectronvolts per meter while conventional facilities are limited to hundred megaelectronvolts per meter. In the Plasma Wakefield Acceleration scheme (PWFA) and the Laser Wakefield Acceleration scheme (LWFA), a bunch of particles or a laser pulse propagates in a plasma, creating an accelerating structure in its wake: an electron density wake associated to electromagnetic fields in the plasma. The main achievement of this thesis is the very first demonstration and experimental study in 2016 of the Plasma Wakefield Acceleration of a distinct positron bunch. In the scheme considered in the experiment, a lithium plasma was created in an oven, and a plasma density wave was excited inside it by a first bunch of positrons (the drive bunch) while the energy deposited in the plasma was extracted by a second bunch (the trailing bunch). An accelerating field of $1.12\ GeV/m$ was reached during the experiment, for a typical accelerated charge of 85 pC. In the present manuscript is also reported the feasibility of several regimes of acceleration, which opens promising prospects for plasma wakefield accelerator staging and future colliders. Furthermore, this thesis also reports the progresses made regarding a new scheme: the use of a LWFA-produced electron beam to drive plasma waves in a gas jet. In this second experimental study, an electron beam created by laser-plasma interaction is refocused by particle bunch-plasma interaction in a second gas jet. A study of the physical phenomena associated to this hybrid LWFA-PWFA platform is reported. Last, the hybrid LWFA-PWFA scheme is also promising in order to enhance the X-ray emission by the LWFA electron beam produced in the first stage of the platform. In the last chapter of this thesis is reported the first experimental realization of this last scheme, and its promising results are discussed.

Université Paris-Saclay
Espace technologique / Immeuble Discovery
Route de l'Orme aux merisiers RD 128 / 91120 Saint-Aubin, France